

SEISMOLOGY OF THE BRAIN

Characterizing brain mechanics using MRI

Marius Burman Ingeberg

Seismology of the brain:

characterizing brain mechanics using MRI

Marius Burman Ingeberg

Seismology of the brain: characterizing brain mechanics using MRI

PhD Thesis, Utrecht University, The Netherlands
© 2026 Marius Burman Ingeberg

ISBN: 978-94-6534-263-4
DOI: 10.33540/3460
Cover design: Duy Phan
Printing & layout: Proefschriftmaken.nl

The research described in this thesis was funded by Netherlands Organization for Scientific Research (NWO), grant number 18674.

Financial support of the publication of this thesis was generously provided by ChipSoft and Alzheimer Nederland.





Seismology of the brain:

characterizing brain mechanics using MRI

Seismologie van de hersenen:

karakterisering van de hersenmechanica met MRI
(met een samenvatting in het Nederlands)

Proefschrift

ter verkrijging van de graad van doctor aan de
Universiteit Utrecht
op gezag van de
rector magnificus, prof. dr. ir. W. Hazeleger,
ingevolge het besluit van het College voor Promoties
in het openbaar te verdedigen op

vrijdag 1 mei 2026 des middags te 2:15 uur

door

Marius Burman Ingeberg

geboren op 6 mei 1995
te Norrfjärden, Zweden

Promotoren:

Dr. ir. J.J.M. Zwanenburg
Dr. E.W.W. van Houten

Beoordelingscommissie:

Prof. dr. E.T. van Bavel
Prof. dr. G.J. Biessels
Prof. dr. T. van Leeuwen
Dr. ir. C.M.W. Tax
Prof. dr. B.K. Velthuis

Contents

Chapter 1	Introduction	9
Chapter 2	Estimating the viscoelastic properties of the human brain at 7T MRI using intrinsic MRE and nonlinear inversion	35
Chapter 3	Evaluating the performance and repeatability of poroelastic and poroviscoelastic models in intrinsic MR elastography	75
Chapter 4	Evidence for the ultra-soft brain provided by uniqueness in intrinsic MR elastography	111
Chapter 5	Exploring the role of vascular factors and tissue properties in pulsatile brain deformation	133
Chapter 6	Alignment of cardiac-induced brain tissue strain with global boundary conditions and local microstructure: potential effects of anisotropy	167
Chapter 7	Discussion	199
Appendix	Dutch summary	221
	Publications	227
	Acknowledgements	230
	Curriculum Vitae	233

We might say that the earth has a spirit of growth,
and its flesh is the soil,
its bones the arrangement and connection of rocks of which the mountains are composed,
its cartilage the tufa, and its blood the springs of water.

The pool of blood which lies around the earth's heart is the ocean,
and its breathing…
the ebb and flow of the sea…
and the seat of the earth's soul is in the fires.

Leonardo da Vinci, Codex Leicester, 1510



Chapter 1

General Introduction

1 The human brain

The brain has often been referred to as one of the most complex systems known in the universe. Consisting of tens to hundreds of billions of cells that are interconnected through trillions of connections, the brain remains one of the greatest scientific frontiers. It not only gives rise to our conscious experience but also orchestrates every facet of our behavior, cognition, and bodily functions, shaping who we are and how we interact with the world around us. Given the complexity of the brain, there are countless ways in which its functions can be impaired or altered - which we call pathology. In the case of the brain, pathology is particularly painful as it can affect the mind. When cognitive functions are compromised, the individual not only loses their mental abilities, but also their sense of self, often causing immense emotional distress for both the person and their loved ones. There is therefore enormous value in understanding such pathology, for both the affected and unaffected. However, you can't fully understand pathology without first understanding physiology, or normal function.

Due to the vast complexity of the brain, there are many ways of making sense of it. Psychology, neuroscience, and neurochemistry are just a few examples of fields that try to understand the brain in distinct ways, all with important perspectives and insights. This thesis aims to deepen the understanding of the brain by investigating its mechanical aspects. Such aspects are related to its underlying structure, function, and the complex interactions between its various components. It is therefore important to first understand what the brain consists of, how it is organized, and what roles its different parts play in maintaining normal function.

2 The brain from micro to macro

The brain primarily consists of several major types of cells: neurons, glial cells, vascular cells, and epithelial cells. Neurons transmit information throughout the system by either electrical or neurochemical means, while glial cells play an active role in maintaining the health and integrity of the brain. Neurons have axons that can reach lengths of up to several decimeters, allowing them to transmit electrical signals over long distances, while their dendrites receive incoming signals from other neurons. Glial cells generally consist of a cell body and different extensions depending on the cell type, such as astrocytes, oligodendrocytes, and microglia. Astrocytes provide, among many other functions, structural support in the brain by extending into a branched network surrounding neurons and blood vessels, acting like a scaffold. Oligodendrocytes produce myelin, a fatty substance that wraps around the axons of neurons, insulating them and allowing for faster transmission of electrical signals. Microglia are the brain's immune cells, responsible for

clearing debris, fighting infections, and maintaining overall brain health. Ependymal cells line the brain ventricles and contribute to cerebrospinal fluid production, while specialized choroid plexus epithelial cells secrete and regulate cerebrospinal fluid. Vascular cells, including endothelial cells, pericytes, and smooth muscle cells, form the blood vessels that deliver oxygen and nutrients to the brain and interact closely with astrocytic endfeet to maintain the blood-brain barrier.

Around these cells is the extracellular matrix, a complex network of proteins, carbohydrates, and other molecules that exist outside of the cells, providing structural support. Interstitial fluid fills the spaces within this extracellular environment, acting as a medium for the exchange of nutrients, waste, metabolites, and signaling molecules between cells. Together, these components form the structural and functional foundation of the brain. Figure 1 shows the distribution of cells, myelin, and blood vessels in a 1 mm^3 sample of human temporal cortex obtained with serial section electron microscopy.

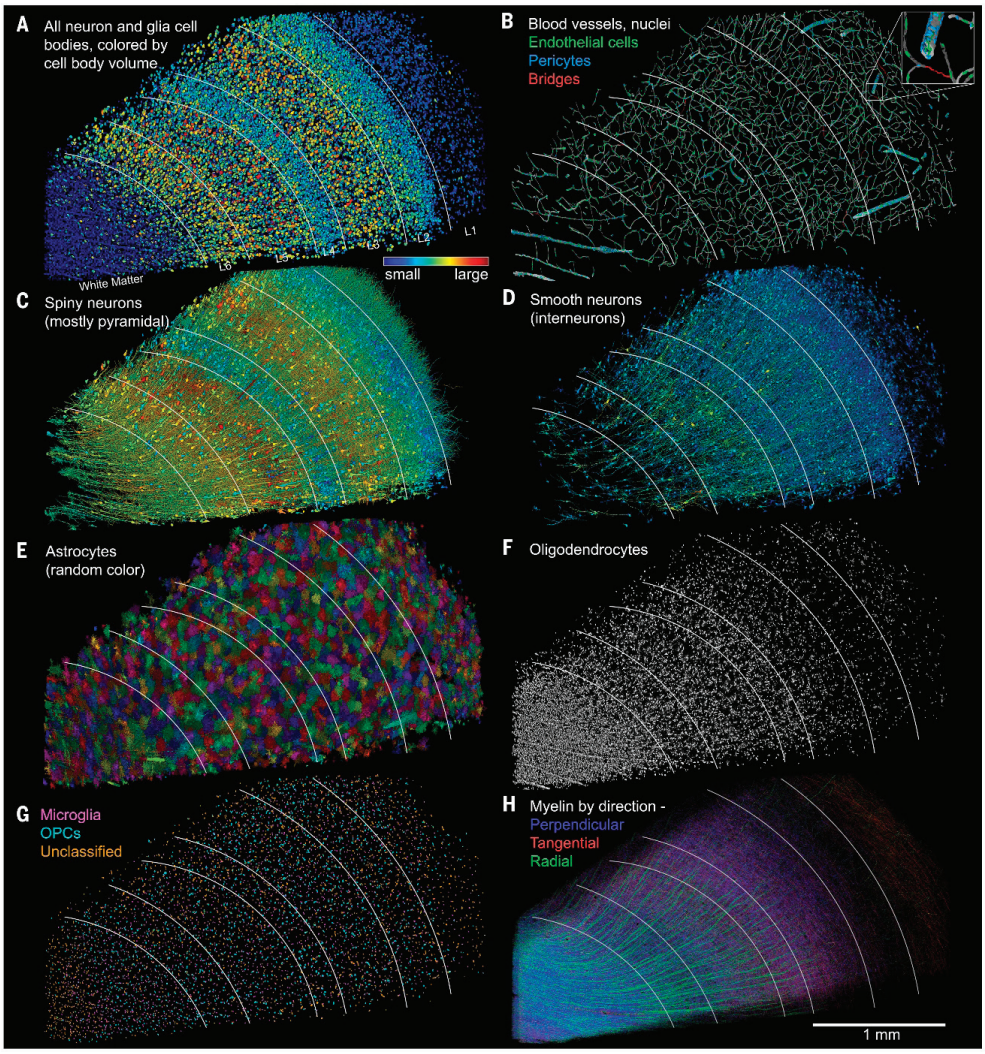


Figure 1: Distribution of cells, myelin, and blood vessels in a 1 mm^3 sample of human temporal cortex, obtained with serial section electron microscopy. These images reveal the intricate architecture that forms the microstructure of the human brain. Neurons are represented by subtypes such as pyramidal cells and interneurons, glial cells include astrocytes, oligodendrocytes, microglia, and oligodendrocyte precursor cells (OPCs), and other cell types include vascular cells such as endothelial cells and pericytes. Figure adapted from Shapson-Coe et al., (2024), Fig. 4, reprinted with permission from American Association for the Advancement of Science.

On a macroscopic scale, the brain is composed of two major tissue types - gray matter and white matter - which can be distinguished with the naked eye. Gray matter contains neuronal cell bodies along with glial cells and is primarily involved in information processing. White matter consists mainly of myelinated axons and glial cells, supporting

communication between brain regions. While this gray-white distinction forms the basic structural framework, distinct brain regions within gray matter arise from variations in cellular composition, cortical layer architecture, and local myelination patterns, each supporting specialized functions. For example, the cerebral cortex, forming the brain's outer layer, is critical for memory, language, and perception, while the underlying white matter connects cortical and subcortical regions to enable coordinated activity. The brain can be further subdivided into numerous distinct regions, reflecting functional specialization; its cellular and extracellular organization adapts to these regional demands, resulting in areas with differing mechanical and structural properties (Budday et al., 2020).

In order to function, the cells need to be supplied with oxygen and nutrients which is done through the cerebrovascular system. Blood is pumped from the heart into the brain through the carotid and vertebral arteries and is distributed through a vast network of arteries that envelop the brain. These arteries lead into penetrating arteries that dive deeper into the brain tissue and branch out into smaller vessels. This microvasculature interpenetrates the entirety of the brain tissue through an extensive capillary network that is deeply intertwined with the cellular structure. For example, the entire surface of these capillaries is ensheathed by astrocytic endfeet, which help regulate blood-brain barrier function and support nutrient exchange. The microvasculature eventually flows into veins, which converge into larger venous structures, ultimately draining into the jugular veins and returning the blood to the heart. Depending on the type and size of blood vessels, they have distinct mechanical properties related to the structure and function of their vessel walls. In a broader context, the density and characteristics of the underlying microvasculature also plays a role in the overall mechanical characteristics of the brain tissue itself.

Because the brain is both a highly sensitive and vital organ, it is enclosed within the neurocranium, which serves as a protective shield against external forces. In addition to the cranium, the brain is further protected by the cerebrospinal fluid (CSF)**,** a clear liquid that surrounds the brain and spinal cord. CSF circulates through the subarachnoid space and the brain's ventricles, which are fluid filled cavities within the brain, providing a buffer against mechanical shock and helping to remove waste products from the brain and to transport signaling molecules. The cranium also plays an important role in maintaining normal intracranial pressure, which is the pressure exerted by fluids such as blood and CSF within the skull. Together, the cranium and CSF work to safeguard the brain, ensuring its stability and optimal performance in regulating vital bodily functions. Figure 2 illustrates the major macroscopic components of the brain.

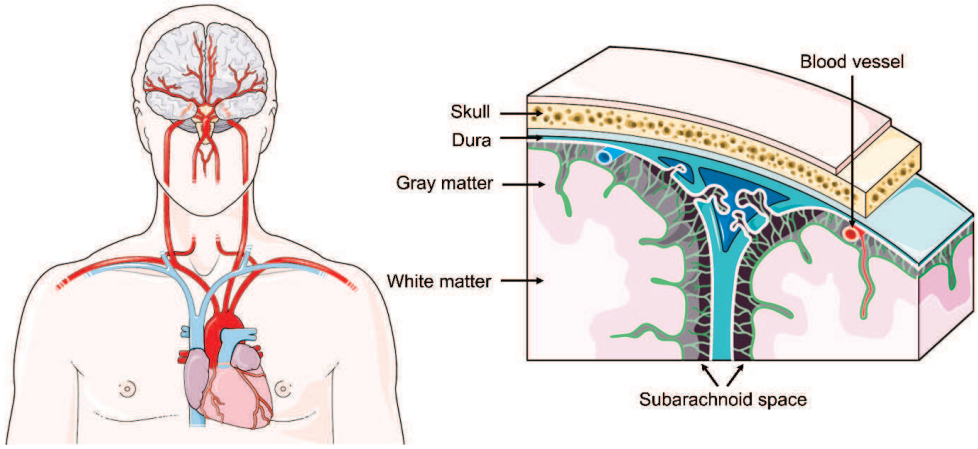


Figure 2: Macroscopic anatomy of the brain. The left panel illustrates the major arteries supplying blood to the brain from the heart, while the right panel provides a magnified view highlighting key anatomical structures.

3 Brain mechanics and pathology

A healthy brain functions like a finely tuned orchestra, where each component plays a crucial role in maintaining overall health and stability. However, any disruption to this delicate system - whether due to injury, disease, or degeneration - can profoundly impact cognitive and physical well-being, sometimes leading to severe disability or death. Many of these pathologies manifest as structural changes, which in turn alter the brain's mechanical properties. Because brain structure and function are tightly coupled, these mechanical changes can reflect underlying functional alterations, sometimes even preceding detectable symptoms. This makes mechanical measurements a potentially sensitive biomarker for early pathological changes.

Neurodegenerative diseases serve as a clear example of this, as even the name would suggest. The degeneration of neurons and their supporting structures leads to progressive loss of function, disrupting communication pathways and impairing essential cognitive and motor processes. In Alzheimer's disease, for example, one of the most noticeable structural changes is the widespread shrinkage of the brain due to progressive loss of neurons and synapses (Blinkouskaya & Weickenmeier, 2021; Murphy et al., 2019). This also manifests as tissue softening, with different regions of the brain showing distinct softening patterns (Yin et al., 2018). Parkinson's disease also manifests as distinct structural changes across the brain, often in the form of neural loss and brain tissue atrophy (Prakash et al., 2016). Multiple sclerosis (MS), on the other hand, is characterized by the loss of myelin, the protective sheath that surrounds axons. This demyelination disrupts nerve signal transmission, leading to axonal damage and eventual degeneration, which

contributes to permanent disability. In addition to the loss of myelin, MS also results in neurodegeneration that extends to gray matter atrophy, further impairing cognitive and motor functions.

Cerebral small vessel disease (CSVD) primarily affects the brain's arterioles, small veins, and capillaries. These microvascular changes, including thickening of vessel walls, endothelial dysfunction, and pericyte loss, can compromise the blood-brain barrier, contributing to both reduced blood supply (ischemia) and fluid accumulation in the tissue (edema) (Sun et al., 2021). The disease manifests as white matter lesions, areas of damaged myelin and axons resulting from these vascular insults, and lacunar infarcts, which are small strokes in deep brain regions caused by blockage of small vessels. White matter is particularly susceptible because its long axonal tracts are supplied by small penetrating vessels that are easily affected by microvascular disease. Chronic reductions in blood flow can also lead to metabolic stress in neurons and glial cells, further contributing to tissue damage. Damage to glial cells, such as astrocytes and oligodendrocytes, and changes in the extracellular matrix may additionally alter the mechanical properties of the affected tissue. Over time, these structural alterations contribute to general brain atrophy, reducing overall brain volume. Together, these changes affect the mechanical characteristics of the brain, influencing its stiffness (Chojdak-Łukasiewicz et al., 2021; De Guio et al., 2020), and are associated with functional impairments such as cognitive decline and increased risk of stroke.

Another clear example of pathology that affects the underlying brain structure is brain tumors. Cancer greatly alters the microstructure of the brain, disrupting normal cellular organization, connectivity, and function. As tumors grow, they infiltrate and replace healthy neuronal and glial cells. They also stimulate the formation of new blood vessels, which are often leaky and disrupt tissue osmotic balance, resulting in edema. These changes contribute to axonal damage, demyelination, and loss of structural integrity. When a tumor originates from glial cells, it is classified as a glioma, comprising approximately 75% of all malignant brain tumors (Lv et al., 2022). Microstructural alterations lead to macroscopic changes in tissue stiffness, as seen in gliomas, which are typically softer than the surrounding healthy brain tissue. Understanding brain tumor mechanical stiffness is potentially important for presurgical planning, as it can guide surgical approach, instrument selection, and resection strategy (Bunevicius et al., 2020). Several other pathologies also impact the mechanical characteristics of the brain, including traumatic brain injury (TBI) (Yin et al., 2018), stroke (Xu et al., 2013), and hydrocephalus (Fattahi et al., 2016; Murphy et al., 2020). Moreover, the brain undergoes structural changes throughout the entire life span, which can be measured as a progressive softening in later age (Hiscox et al., 2021; Sack et al., 2011). Even conditions typically regarded as affecting only cognitive function, such as depression, can lead to measurable structural alterations (Zhang et al., 2018).

4 Assessing brain mechanics

Because brain structure and function are tightly coupled, virtually all neurological diseases involve alterations in the brain's microstructure. For this reason, techniques that allow for the assessment of the microstructure or the mechanical state of the brain are critically important. These methods are essential not only for understanding the underlying mechanisms of disease but also for diagnosing and evaluating the extent and severity of various conditions. However, there are a few challenges when measuring such properties. First, the brain is encased within the skull, making it difficult to access with external measurement tools. Second, given the brain's critical and sensitive nature, any instruments used to assess its properties must be non-invasive or minimally invasive to prevent harm. For these reasons, imaging approaches such as Magnetic Resonance Imaging (MRI) and Computed Tomography (CT) become highly valuable, as they provide non-invasive means of assessing the brain's microstructure and mechanical state. These imaging techniques allow for detailed visualization of the brain's anatomy, revealing subtle changes that may indicate the presence of disease or damage.

MRI, in particular, is widely used for its versatility. Depending on the acquisition sequence, it can measure a range of brain tissue properties, from macrostructural features such as cortical thickness to microstructural characteristics such as tissue water content and water diffusion, as well as physiological parameters like cerebral blood flow. This versatility allows MRI to capture a range of microstructural changes that occur in various neurological conditions. However, these standard MRI measurements are not specific for mechanical properties and cannot directly characterize, for example, tissue stiffness.

To evaluate the mechanical properties of a material, an applied force is typically required to induce a reaction. This principle is commonly applied in mechanical testing, where various forces are applied to a material, and the resulting deformation or response is measured. By analyzing how the material reacts to these forces, its mechanical properties can be determined. For example, in a compression test, a material is compressed under a known force, and the amount of deformation is measured to calculate its stiffness. However, generating such forces inside the closed system of the skull is inherently challenging.

5 The pulsating brain

In the brain, as the heart beats, pulsatile pressure waves are transmitted through the carotid and vertebral arteries, eventually entering the microvasculature. To accommodate for the increase in blood volume, the microvessels swell and consequently stretch

elastically which displaces the surrounding tissue (Feinberg & Mark, 1987; Greitz et al., 1992). This causes pulsatile motions throughout the brain, commonly referred to as cerebral arterial pulsations (CAP). These pulsations are not just a side effect of cardiac pulsation, but seemingly play an important role in brain health. For example, CAPs have been proposed as a key driver of the recently discovered glymphatic system, where they induce oscillatory CSF flow that aids the removal of waste products (Nedergaard, 2013). Furthermore, abnormal brain pulsatility is often related to disease processes, and can be an important biomarker for pathologies such as cerebral small vessel disease (Shi et al., 2020) and dementia (Chung et al., 2017).

These brain pulsations manifest as mechanical waves that travel through the brain tissue. Therefore, the brain is always reacting to certain forces, in principle making it possible to characterize its mechanical properties without the use of external vibration sources. This is analogous to seismology, where seismologists analyze naturally occurring waves - such as those generated by earthquakes - to infer the mechanical properties of the Earth's interior. Although the displacements induced by brain pulsations are extremely small - on the order of a micrometer (comparable to the size of a red blood cell) - they are surprisingly remarkable when scaled up. If the brain were the size of the Earth, these pulsations would correspond to movements roughly the height of Mount Everest. In addition to these relatively large motions, MRI characterization of cardiac driven brain pulsations has additional advantages. First, in contrast to traditional seismology, where sensors are sparsely distributed across the earth's surface, MRI provides measurement data throughout the entire brain volume. Second, brain pulsations are highly regular, occurring approximately once a second, providing rich temporal data sets at any time and thus making the characterization problem much more practical than traditional seismology.

Although these pulsations are relatively large when viewed through the Earth metaphor, the blood-cell-sized displacements they induce in the brain remain extremely small. Accurately detecting such minute motions requires highly sensitive imaging techniques. While there are various flavors of phase encoding techniques in MRI that are able to quantify displacements, the *Displacement Encoding with Stimulated Echoes* (DENSE) (Aletras et al., 1999) technique has been shown to be particularly well-suited for measuring brain pulsations (Adams et al., 2020; Sloots et al., 2021; Soellinger et al., 2009; Williamson et al., 2020a). Briefly, phase encoding techniques quantify displacement by tracking the phase shifts induced by motion in the presence of spatially varying magnetic fields. Through stimulated echoes, DENSE allows for longer mixing times between the encoding and decoding gradients. This extended time allows signal phase shifts from small displacements to accumulate more effectively, enabling motion sensitivities that are much lower than the imaging resolution. Velocities as low as only a few µm/s can be detected by this approach (Magdoom et al., 2019; Williamson et al., 2020a).

By acquiring data throughout the cardiac cycle, DENSE enables a detailed temporal characterization of brain tissue displacement. Typically, measurements are performed in three orthogonal directions - anterior-posterior, right-left, and head-foot - to capture the full 3D motion profile. DENSE therefore offers a means to completely and precisely quantify intrinsic mechanical waves induced by CAP, enabling the characterization of brain mechanics without the need for externally generated vibrations. Figure 3 presents an example of DENSE measurements from a single subject, illustrating both axial views of peak displacement maps as well as displacement curves over the cardiac cycle for all motion encoding directions.

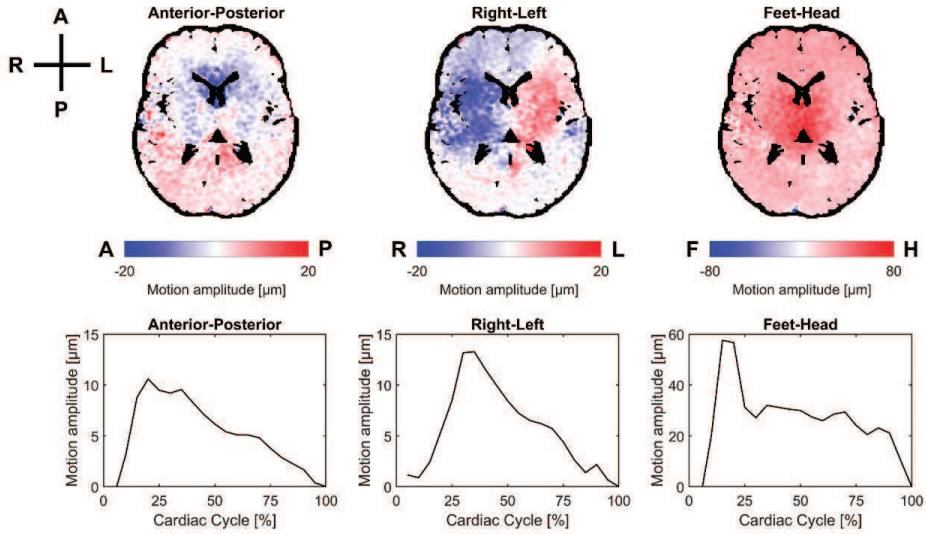


Figure 3: Example of DENSE measurements from a single subject. The top panels show axial views of approximate peak displacements for each motion encoding direction. The displacement maps reveal inward-directed motion, primarily oriented downward. The panels at the bottom illustrate the corresponding mean displacement curves over the cardiac cycle: for the anterior region of the brain in (left), the right hemisphere in (middle), and the entire brain in (right). The bold letters indicate anatomical directions: A = anterior, P = posterior, R = right, L = left, F = feet, H = head.

6 Strain tensor imaging

One aspect of brain mechanics is its dynamic behavior, which can be characterized by analyzing how the tissue deforms over time using techniques like DENSE. Accurately quantifying these deformations requires computing spatial derivatives of the displacement field, which are highly sensitive to noise. Therefore, achieving a high signal-to-noise ratio (SNR) in displacement maps is essential for accurately characterizing tissue deformation. Recent studies have demonstrated that the DENSE sequence, combined with 7T

MRI, provides sufficient SNR for this purpose (Adams et al., 2020; Sloots et al., 2021). This approach enables the computation of the voxel-wise 3D strain tensor, which characterizes the stretch and shortening of a voxel along three orthogonal directions. Performing an eigenvalue decomposition on the strain tensor provides the three principal strain directions where only pure stretch or compression takes place, with no effective shear strain. The corresponding eigenvalues represent the strains along these directions and are referred to as the principal strains. The first principal strain represents the direction of dominant stretch, and the third principal strain represents the direction of dominant shortening.

Two more properties related to brain dynamics can be directly calculated from the strain tensor, volumetric strain and octahedral shear strain (OSS). Volumetric strain quantifies the net expansion or compression of a given voxel and is thought to be related to the swelling or contraction of the microvasculature (Adams et al., 2020; Hirsch et al., 2013). OSS instead reflects the deformation of a voxel, regardless of net expansion or compression. Larger OSS indicate significant overall deformation, while zero shear strain represents isotropic expansion or compression of a voxel. Here, the words expansion and compression are used in place of to stretch and shortening denote that these are volumetric changes, rather than directional quantities as for the principal strains. Examples of the discussed strain quantities are displayed in Figure 4.

These four quantities together provide rich information about the dynamic behavior of the tissue throughout the brain may prove to be important markers for various pathological conditions. However, even though previous studies provided repeatable property maps with consistent patterns between subjects (Adams et al., 2020; Sloots et al., 2021), the underlying mechanisms contributing to each property remain largely unknown due to their novelty. While different pathology could result in unique identifiable "fingerprints", a more complete understanding of the biophysical and physiological origins of these parameters is necessary to interpret them accurately. Part of this thesis aims to advance the understanding of these dynamic parameters by examining their relationship with underlying biomechanical properties of brain tissue.

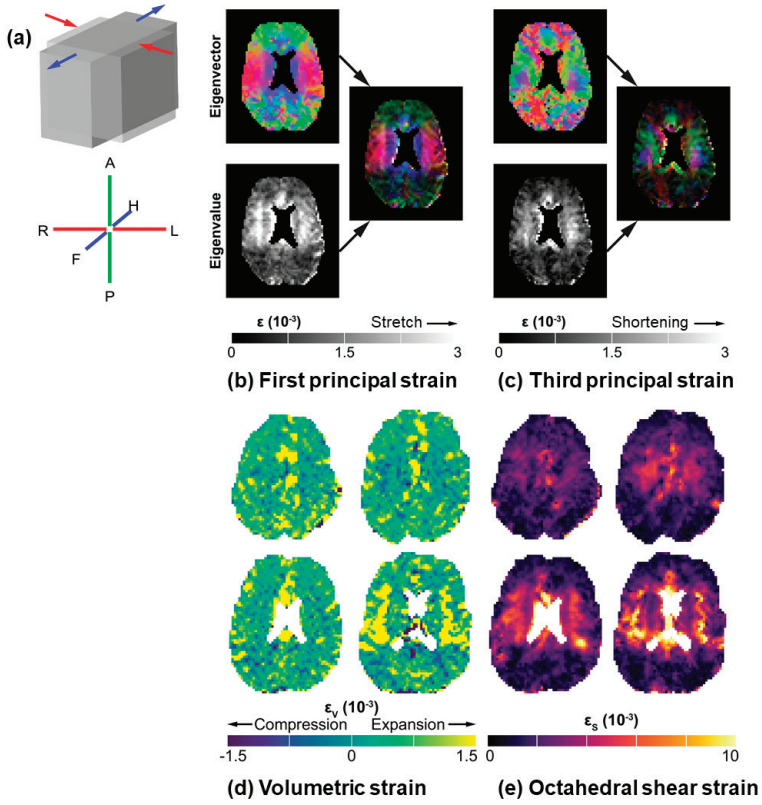


Figure 4: (a) Visualization of a deformed voxel stretching in one dimension (blue arrows) while compressing in the perpendicular direction (red arrows), illustrating the Poisson effect. Figures (b) and (c) illustrate the direction and magnitude of the largest stretch (first principal strain) and largest shortening (third principal strain), respectively, in each voxel. In the top row, the direction of the eigenvector in each voxel is visualized using a directionally encoded color (DEC) scheme. In the bottom row, gray-scale maps depict the magnitude of the corresponding principal strain. Multiplying each eigenvector by its corresponding eigenvalue produces an intensity-modulated color map. Example maps of volumetric strain and octahedral shear strain are shown in (d) and (e), respectively. Figure reproduced from Sloots et al., (2021), Fig. 2 and Fig. 3, licensed under CC BY.

7 Intrinsic Magnetic Resonance Elastography

In addition to characterizing the dynamic behavior of the brain during brain pulsations, the mechanical properties of the tissue itself can be assessed using a technique known as Intrinsic Magnetic Resonance Elastography (iMRE). This is analogous to the traditional mechanical testing described in section 1.4, where the force is generated by brain pulsations, and the resulting deformations can be measured using DENSE MRI. However, while

mechanical testing generally involves well-controlled experiments with approximately known conditions, iMRE presents a more complicated situation. There are two main reasons for this complexity. First, the external forces applied to the tissue are not directly measured and must be inferred from the observed displacements using the wave equation, which balances elastic and inertial forces. Second, brain tissue exhibits complex, heterogeneous, and nonlinear mechanical behavior, rather than behaving like a simple, homogeneous elastic material such as a steel beam.

Given these challenges, the tissue's underlying mechanical properties can be estimated through non-linear inversion (NLI) techniques. Here, the term inversion refers to the process of deriving the tissue's mechanical properties from the measured displacement fields, and non-linear refers to the non-linear relationship between the measured displacements and underlying mechanical properties when trying to infer these properties. While computationally cheap direct inversion approaches are possible, they are considerably more sensitive to noise and thus NLI provides an accurate and robust option for mechanical property characterization in a wide range of conditions. With NLI, finite element models of the tissue volume of interest are generated based on anatomical MR images. The goal is to iteratively minimize the differences between the measured displacement data and the computational mechanical model, which relates the displacement fields to the underlying mechanical properties. This is done by minimizing an objective function

$$\Phi = \sum_{i=1}^{N_m} \left(u_{m(i)} - u_c(\theta)_i\right)^2,$$

where u_m are the measured displacements, u_c are the model displacements, θ are the underlying mechanical properties and N_m are the number of measurement locations. Once converged, the solution provides a spatially resolved estimation of the tissue's mechanical properties, allowing for a more detailed characterization of its biomechanical behavior under physiological conditions.

The recovered mechanical properties depend on the choice of computational model. Traditionally, either a purely elastic or a viscoelastic model is used. In the elastic model, the material responds instantaneously to applied forces, with no energy dissipation. The key parameter in this case is the shear modulus G, which quantifies tissue stiffness by relating shear stress to shear strain. In contrast, a viscoelastic model accounts for time-dependent behavior, allowing for energy dissipation. Here, the shear modulus is expressed as a complex quantity $G^* = G' + iG''$, reflecting both the tissue's elastic stiffness and its viscous damping properties. The real part of G^* is called the storage modulus (G') and represents the elastic component of the material. The imaginary part of G^* is called the loss modulus (G'') and characterizes the viscous component and reflects energy dissipation.

Mechanical shear waves can also be externally generated using a variety of actuator setups. When combined with MRI, this principle forms the basis of conventional Magnetic Resonance Elastography (MRE) (Mariappan et al., 2010). In MRE, steady-state mechanical vibrations - typically in the frequency range of 20-100 Hz - are applied to the brain using pneumatic, piezoelectric, or other actuator systems. An example experimental setup is shown in Figure 5. The resulting wave propagation is then imaged and analyzed to estimate tissue mechanical properties. Because MRE relies on externally applied vibrations, it artificially affects the mechanical state of the brain (see section 8) and therefore offers a different view of brain mechanics than iMRE. In the context of this thesis, MRE serves as an important point of reference, while the primary focus remains on intrinsic, pulsation-driven measurements.

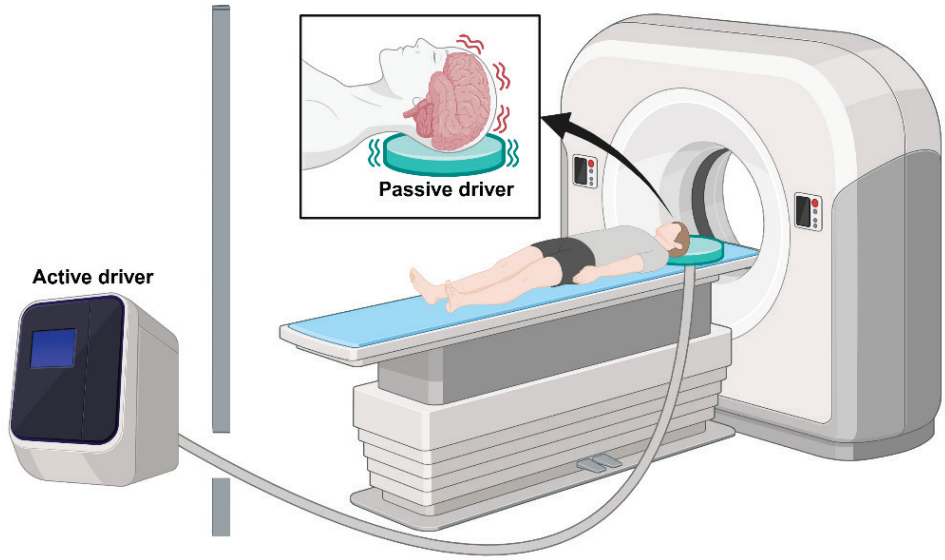


Figure 5: Schematic view of an example experimental setup for MRE. The subject's head is positioned on a pillow-like passive driver, which transmits vibrations received from an active driver. The displacement fields induced by the vibrations can then be captured using phase-contrast imaging techniques.

A key feature of iMRE is its ability to non-invasively obtain quantitative measurements of mechanical properties. This is especially important for the brain, given its inaccessibility, but iMRE has also been applied to other organs such as the liver (Baradaran Najar et al., 2025), where traditional MRE is used to detect liver fibrosis (Pepin et al., 2022). Elastography can be thought of as an extension of palpation - a technique that has been a cornerstone of medicine for centuries. Where clinicians use palpation to detect lesions based on their differential stiffness compared to surrounding tissues, MRE provides a quantitative

map of tissue mechanics. Abnormal tissues can exhibit stiffness up to 100 times greater than normal tissue (Kruse et al., 2008), highlighting the potential value of such measurements iMRE also provides full 3D coverage of the tissue of interest, which can be challenging with techniques like ultrasound elastography, especially when imaging larger or deeper tissue regions. Furthermore, the resulting mechanical property descriptions are spatially resolved, enabling the characterization of regional profiles that could predict e.g. tumor pathology through mechanical phenotyping (Mirzakhel et al., 2024). Importantly, the mechanical property descriptions provided by iMRE directly reflect the underlying microstructure of the tissue in question. This makes iMRE a valuable tool for investigating the mechanisms underlying disease. It can also aid in the diagnosis of pathological conditions and in evaluating their severity.

iMRE was first suggested in 2012 by Weaver et al., who used a multiphase phase contrast gradient echo sequence in a 3 T scanner. This approach provided a maximum sensitivity of 2.5 cm/s, which is considerably larger than the micrometer-scale brain pulsations. Nonetheless, the shear modulus was successfully reconstructed for six subjects using both an elastic model and a poroelastic model, laying the foundation for exploring brain mechanics through naturally occurring physiological motions. Using a different approach, Zorgani et al. (2015) computed the shear wavelength (which is related to shear modulus) in two subjects by applying seismic noise correlation. Here, a single-shot echo planar gradient echo sequence was used in a 1.5 T scanner, with a sensitivity just above 1 cm/s. Although more sensitive than the initial attempt, a sensitivity of 1 cm/s still exceeds the scale of brain pulsations, leaving significant potential for noise and limiting the precision of the measurements. Despite the initial successes, both approaches yielded relatively noisy results and lacked anatomical detail in the resulting parameter maps, which likely contributed to the limited exploration of iMRE as a technique for measuring brain mechanics. Accurate measurements of the intrinsic brain pulsations thus served as a major challenge for iMRE.

As described earlier, the ability to have high sensitivity to small displacements is the strength of the DENSE sequence, making it an excellent candidate for the use in iMRE, as explored in this thesis. In contrast to sensitivities on the order of cm/s, previous work that employed DENSE to measure brain pulsations used sensitives reaching on the order of micrometers (Adams et al., 2019; Reese et al., 2002; Sloots et al., 2021). At this level, it is even possible that peak displacements of less than 100 πm exceed the sensitivity limits, leading to phase wraps during phase encoding (Sloots et al., 2021). Additionally, further increases in sensitivity can introduce diffusion-related signal attenuation, which may compromise the accuracy of the displacement measurements (Williamson et al., 2020b). These considerations suggest that current implementations are approaching the practical sensitivity limit, where an optimal trade-off between SNR, measurement accu-

racy, and phase wrapping must be considered. Incorporating the DENSE sequence into iMRE represents an important advancement in achieving accurate reconstructions that are both sensitive and resilient to noise.

8 Poroelastic iMRE

Another important factor in accurately reconstructing mechanical properties is the choice of material model used for characterization. In traditional MRE, brain tissue is often represented by a viscoelastic model. However, given that brain tissue consists of a matrix of neurons and glial cells surrounded by extracellular fluid and permeated by an extensive vascular network, poroelastic models provide a more comprehensive representation of its mechanical behavior. Poroelastic models describe a biphasic medium with an elastic matrix permeated by a porous network filled with a viscous *pore fluid* - a description matching the structural characteristics of brain tissue. A visual representation of poroelastic models in the context of biological tissues can be seen in Figure 6.

The predominance of viscoelastic models in traditional MRE arises from the use of high-frequency external vibrations, under which the mobility of the pore fluid is substantially reduced, effectively suppressing porous effects. In more technical terms, the fluid equilibrium time is much longer than the actuation period, causing the tissue to behave in a manner that can be approximated as viscoelastic rather than poroelastic. These high-frequency vibrations also tend to increase the apparent stiffness of the tissue (Herthum et al., 2021; Parker, 2014). Furthermore, while poroelastic models can capture fluid-solid interactions more comprehensively, their higher complexity increases the risk of modeling errors and places greater demands on signal-to-noise ratio and spatial resolution. Consequently, the simpler viscoelastic model remains a practical and appropriate choice under typical MRE conditions (McGarry et al., 2015).

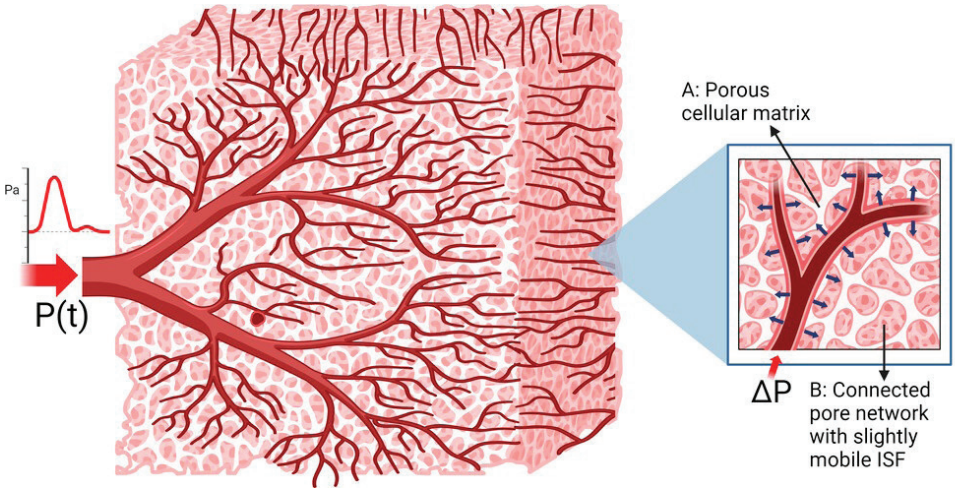


Figure 6: Poroelastic models describe a material composed of an elastic solid matrix permeated by a connected pore network, which is saturated with a viscous fluid. In biological tissues, both the interstitial space between cells and the blood vessels can be considered part of this porous domain. Figure adapted from (McGarry et al., 2025), Fig. 1, licensed under CC BY.

An advantage of iMRE is that porous effects are fully present at the low frequencies associated with the cardiac pressure pulse, in contrast to the effects observed in traditional MRE, where actuation frequencies are typically greater than 20 Hz. This low-frequency excitation in iMRE enables a more accurate assessment of the brain's poroelastic properties. This includes the distinction between the fluid and solid compartments rather than treating the brain as a single, continuous medium. Not only does this offer the possibility of a more accurate representation of the tissue compartments, but it may also provide unique insight into fluid compartments, such as the vasculature. In this context, the property that characterizes the fluid compartment is referred to here as fluid permeability (sometimes reported in the literature as hydraulic permeability or hydraulic conductivity), which reflects how easily fluid flows through the porous medium. This approach has the potential to differentiate vascular and tissue and tissue contributions in pathological conditions, such as neurodegenerative disease and cerebrovascular disease, where the underlying causes are often unclear.

Just as da Vinci envisioned the Earth as a living body - its rocks as bones, its waters as blood, its breath the tide - the human brain can be envisioned as the earth. This is at the core of this thesis, where techniques traditionally used in seismology are instead employed in the brain, giving rise to *seismology of the brain*. By analyzing the propagation of intrinsic mechanical waves generated by cardiac pulse, iMRE and STI can non-invasively probe the brain's mechanical properties, providing a unique perspective on its structure and dynamical behavior. This leads to the two-fold aim of this thesis:

1. To develop intrinsic Magnetic Resonance Elastography (iMRE) using precise measurements of brain pulsations enabled by the increased sensitivity of the DENSE sequence, and to assess the performance of the approach.
2. To explore underlying biological and physiological mechanisms in relation to mechanical property measurements to better understand their role in brain function and pathology.

9 Thesis outline

Chapter 2 introduces *in vivo* iMRE using the DENSE sequence and 7 T imaging, employing a viscoelastic model. Test-retest repeatability is assessed through comparisons of mechanical properties across repeated scans. The chapter also evaluates the sensitivity of regional mechanical property maps and compares these values to traditional MRE measurements obtained from a publicly available atlas at an actuation frequency of 50 Hz.

Chapter 3 investigates the application of poroelastic and poroviscoelastic models in the context of iMRE. Their performance and test-retest repeatability are directly compared. The chapter further examines the influence of two frequencies (approximately 1 Hz and 2 Hz) on estimated material properties by analyzing the first and second harmonic of the cardiac pulse. Finally, we demonstrate that fluid permeability can be reconstructed on a voxel-wise basis, providing a more localized representation than previous global estimates.

Chapter 4 builds on the finding from **Chapter 3** that the brain is considerably softer than previously assumed. This shift in understanding suggests that, during brain pulsations, elastic and inertial forces may be more balanced than previously recognized. In this chapter, we demonstrate that this is indeed the case, and that this balance enables the recovery of unique solutions in viscoelastic inversion - thereby addressing a major limitation identified in **Chapter 2**.

Chapter 5 explores the role of pulse pressure, vascular effects, and tissue properties in volumetric and octahedral shear strain. This exploration is possible as iMRE is able to provide direct estimates of tissue stiffness, and thus this chapter involves measurements obtained in **Chapter 3**. Here, we show that both metrics are driven by a complex interplay of factors, with volumetric strain showing stronger associations with vascular effect, and octahedral shear strain appearing more closely related to tissue stiffness.

Chapter 6 investigates the effects of global boundary conditions and local microstructure on the principal directions of stretch and shortening during brain pulsations. We dem-

onstrate that the stretch patterns are predominantly governed by the global boundary conditions of the system, whereas the shortening patterns are more strongly influenced by the underlying microstructure. Additionally, we show that the microstructure of white matter potentially exhibits signs of mechanical anisotropy.

Chapter 7 brings together the findings of this thesis, placing them in a broader context and offering interpretations and insights. It considers potential future directions before presenting the final conclusions.

10 References

Adams, A. L., Kuijf, H. J., Viergever, M. A., Luijten, P. R., & Zwanenburg, J. J. M. (2019). Quantifying cardiac-induced brain tissue expansion using DENSE. *NMR in Biomedicine*, *32*(2), e4050. https://doi.org/10.1002/nbm.4050

Adams, A. L., Viergever, M. A., Luijten, P. R., & Zwanenburg, J. J. M. (2020). Validating faster DENSE measurements of cardiac-induced brain tissue expansion as a potential tool for investigating cerebral microvascular pulsations. *NeuroImage*, *208*, 116466. https://doi.org/10.1016/j.neuroimage.2019.116466

Aletras, A. H., Ding, S., Balaban, R. S., & Wen, H. (1999). DENSE: displacement encoding with stimulated echoes in cardiac functional MRI. *Journal of Magnetic Resonance (San Diego, Calif. : 1997)*, *137*(1), 247–252. https://doi.org/10.1006/jmre.1998.1676

Baradaran Najar, A., Gilbert, G., Karam, E., Volniansky, A., Fohlen, A., Barat, M., Montagnon, E., Castel, H., Giard, J.-M., Nguyen, B. N., Cloutier, G., Tang, A., & Van Houten, E. (2025). MR Elastography for Classification of Focal Liver Lesions Using Viscoelastic Parameters: A Pilot Study Based on Intrinsic and Extrinsic Activations. *Journal of Magnetic Resonance Imaging : JMRI*, *61*(6), 2525–2540. https://doi.org/10.1002/jmri.29633

Blinkouskaya, Y., & Weickenmeier, J. (2021). Brain Shape Changes Associated With Cerebral Atrophy in Healthy Aging and Alzheimer's Disease. *Frontiers in Mechanical Engineering*, *7*. https://doi.org/10.3389/fmech.2021.705653

Budday, S., Ovaert, T. C., Holzapfel, G. A., Steinmann, P., & Kuhl, E. (2020). Fifty Shades of Brain: A Review on the Mechanical Testing and Modeling of Brain Tissue. *Archives of Computational Methods in Engineering*, *27*(4), 1187–1230. https://doi.org/10.1007/s11831-019-09352-w

Bunevicius, A., Schregel, K., Sinkus, R., Golby, A., & Patz, S. (2020). REVIEW: MR elastography of brain tumors. *NeuroImage. Clinical*, *25*, 102109. https://doi.org/10.1016/j.nicl.2019.102109

Chojdak-Łukasiewicz, J., Dziadkowiak, E., Zimny, A., & Paradowski, B. (2021). Cerebral small vessel disease: A review. *Advances in Clinical and Experimental Medicine*, *30*(3), 349–356. https://doi.org/10.17219/acem/131216

Chung, C.-P., Lee, H.-Y., Lin, P.-C., & Wang, P.-N. (2017). Cerebral Artery Pulsatility is Associated with Cognitive Impairment and Predicts Dementia in Individuals with Subjective Memory Decline or Mild Cognitive Impairment. *Journal of Alzheimer's Disease*, *60*(2), 625–632. https://doi.org/10.3233/JAD-170349

De Guio, F., Duering, M., Fazekas, F., De Leeuw, F.-E., Greenberg, S. M., Pantoni, L., Aghetti, A., Smith, E. E., Wardlaw, J., & Jouvent, E. (2020). Brain atrophy in cerebral small vessel diseases: Extent, consequences, technical limitations and perspectives: The HARNESS initiative. *Journal of Cerebral Blood Flow and Metabolism : Official Journal of the International Society of Cerebral Blood Flow and Metabolism*, *40*(2), 231–245. https://doi.org/10.1177/0271678X19888967

Fattahi, N., Arani, A., Perry, A., Meyer, F., Manduca, A., Glaser, K., Senjem, M. L., Ehman, R. L., & Huston, J. (2016). MR Elastography Demonstrates Increased Brain Stiffness in Normal Pressure Hydrocephalus. *American Journal of Neuroradiology*, *37*(3), 462–467. https://doi.org/10.3174/ajnr.A4560

Feinberg, D. A., & Mark, A. S. (1987). Human brain motion and cerebrospinal fluid circulation demonstrated with MR velocity imaging. *Radiology*, *163*(3), 793–799. https://doi.org/10.1148/radiology.163.3.3575734

Greitz, D., Wirestam, R., Franck, A., Nordell, B., Thomsen, C., & Ståhlberg, F. (1992). Pulsatile brain movement and associated hydrodynamics studied by magnetic resonance phase imaging.

The Monro-Kellie doctrine revisited. *Neuroradiology*, *34*(5), 370–380. https://doi.org/10.1007/BF00596493

Herthum, H., Dempsey, S. C. H., Samani, A., Schrank, F., Shahryari, M., Warmuth, C., Tzschätzsch, H., Braun, J., & Sack, I. (2021). Superviscous properties of the in vivo brain at large scales. *Acta Biomaterialia*, *121*, 393–404. https://doi.org/10.1016/j.actbio.2020.12.027

Hirsch, S., Klatt, D., Freimann, F., Scheel, M., Braun, J., & Sack, I. (2013). In vivo measurement of volumetric strain in the human brain induced by arterial pulsation and harmonic waves. *Magnetic Resonance in Medicine*, *70*(3), 671–683. https://doi.org/10.1002/mrm.24499

Hiscox, L. V., Schwarb, H., McGarry, M. D. J., & Johnson, C. L. (2021). Aging brain mechanics: Progress and promise of magnetic resonance elastography. *NeuroImage*, *232*, 117889. https://doi.org/10.1016/j.neuroimage.2021.117889

Kruse, S. A., Rose, G. H., Glaser, K. J., Manduca, A., Felmlee, J. P., Jack, C. R., & Ehman, R. L. (2008). Magnetic resonance elastography of the brain. *NeuroImage*, *39*(1), 231–237. https://doi.org/10.1016/j.neuroimage.2007.08.030

Lv, K., Cao, X., Wang, R., Du, P., Fu, J., Geng, D., & Zhang, J. (2022). Neuroplasticity of Glioma Patients: Brain Structure and Topological Network. *Frontiers in Neurology*, *13*, 871613. https://doi.org/10.3389/fneur.2022.871613

Magdoom, K. N., Zeinomar, A., Lonser, R. R., Sarntinoranont, M., & Mareci, T. H. (2019). Phase contrast MRI of creeping flows using stimulated echo. *Journal of Magnetic Resonance*, *299*, 49–58. https://doi.org/10.1016/j.jmr.2018.12.009

Mariappan, Y. K., Glaser, K. J., & Ehman, R. L. (2010). Magnetic resonance elastography: a review. *Clinical Anatomy (New York, N.Y.)*, *23*(5), 497–511. https://doi.org/10.1002/ca.21006

McGarry, M. D. J., Johnson, C. L., Sutton, B. P., Georgiadis, J. G., Van Houten, E. E. W., Pattison, A. J., Weaver, J. B., & Paulsen, K. D. (2015). Suitability of poroelastic and viscoelastic mechanical models for high and low frequency MR elastography. *Medical Physics*, *42*(2), 947–957. https://doi.org/10.1118/1.4905048

McGarry, M., Sowinski, D., Tan, L., Weaver, J., Zwanenburg, J. J. M., & Paulsen, K. (2025). In vivo magnetic resonance imaging of the interstitial pressure gradients pgMRI using a pulsatile poroelastic computational model. *Interface Focus*, *15*(1). https://doi.org/10.1098/rsfs.2024.0044

Mirzakhel, Z., Reddy, G. A., Boman, J., Manns, B., Veer, S. ter, & Katira, P. (2024). "Patchiness" in mechanical stiffness across a tumor as an early-stage marker for malignancy. *BMC Ecology and Evolution*, *24*(1), 33. https://doi.org/10.1186/s12862-024-02221-6

Murphy, M. C., Cogswell, P. M., Trzasko, J. D., Manduca, A., Senjem, M. L., Meyer, F. B., Ehman, R. L., & Huston, J. (2020). Identification of Normal Pressure Hydrocephalus by Disease-Specific Patterns of Brain Stiffness and Damping Ratio. *Investigative Radiology*, *55*(4), 200–208. https://doi.org/10.1097/RLI.0000000000000630

Murphy, M. C., Huston, J., & Ehman, R. L. (2019). MR elastography of the brain and its application in neurological diseases. *NeuroImage*, *187*, 176–183. https://doi.org/10.1016/j.neuroimage.2017.10.008

Nedergaard, M. (2013). Garbage Truck of the Brain. *Science*, *340*(6140), 1529–1530. https://doi.org/10.1126/science.1240514

Parker, K. J. (2014). A microchannel flow model for soft tissue elasticity. *Physics in Medicine and Biology*, *59*(15), 4443–4457. https://doi.org/10.1088/0031-9155/59/15/4443

Pepin, K. M., Welle, C. L., Guglielmo, F. F., Dillman, J. R., & Venkatesh, S. K. (2022). Magnetic resonance elastography of the liver: everything you need to know to get started. *Abdominal Radiology (New York)*, *47*(1), 94–114. https://doi.org/10.1007/s00261-021-03324-0

Prakash, K., Bannur, B., Chavan, M., Saniya, K., Sailesh, K., & Rajagopalan, A. (2016). Neuroanatomical changes in Parkinson's disease in relation to cognition: An update. *Journal of Advanced Pharmaceutical Technology & Research*, *7*(4), 123. https://doi.org/10.4103/2231-4040.191416

Reese, T. G., Feinberg, D. A., Dou, J., & Wedeen, V. J. (2002). Phase contrast MRI of myocardial 3D strain by encoding contiguous slices in a single shot. *Magnetic Resonance in Medicine*, *47*(4), 665–676. https://doi.org/10.1002/mrm.10111

Sack, I., Streitberger, K.-J., Krefting, D., Paul, F., & Braun, J. (2011). The Influence of Physiological Aging and Atrophy on Brain Viscoelastic Properties in Humans. *PLoS ONE*, *6*(9), e23451. https://doi.org/10.1371/journal.pone.0023451

Shapson-Coe, A., Januszewski, M., Berger, D. R., Pope, A., Wu, Y., Blakely, T., Schalek, R. L., Li, P. H., Wang, S., Maitin-Shepard, J., Karlupia, N., Dorkenwald, S., Sjostedt, E., Leavitt, L., Lee, D., Troidl, J., Collman, F., Bailey, L., Fitzmaurice, A., … Lichtman, J. W. (2024). A petavoxel fragment of human cerebral cortex reconstructed at nanoscale resolution. *Science (New York, N.Y.)*, *384*(6696), eadk4858. https://doi.org/10.1126/science.adk4858

Shi, Y., Thrippleton, M. J., Blair, G. W., Dickie, D. A., Marshall, I., Hamilton, I., Doubal, F. N., Chappell, F., & Wardlaw, J. M. (2020). Small vessel disease is associated with altered cerebrovascular pulsatility but not resting cerebral blood flow. *Journal of Cerebral Blood Flow & Metabolism*, *40*(1), 85–99. https://doi.org/10.1177/0271678X18803956

Sloots, J. J., Biessels, G. J., de Luca, A., & Zwanenburg, J. J. M. (2021). Strain Tensor Imaging: Cardiac-induced brain tissue deformation in humans quantified with high-field MRI. *NeuroImage*, *236*, 118078. https://doi.org/10.1016/j.neuroimage.2021.118078

Soellinger, M., Rutz, A. K., Kozerke, S., & Boesiger, P. (2009). 3D cine displacement-encoded MRI of pulsatile brain motion. *Magnetic Resonance in Medicine*, *61*(1), 153–162. https://doi.org/10.1002/mrm.21802

Sun, Z., Gao, C., Gao, D., Sun, R., Li, W., Wang, F., Wang, Y., Cao, H., Zhou, G., Zhang, J., & Shang, J. (2021). Reduction in pericyte coverage leads to blood-brain barrier dysfunction via endothelial transcytosis following chronic cerebral hypoperfusion. *Fluids and Barriers of the CNS*, *18*(1), 21. https://doi.org/10.1186/s12987-021-00255-2

Weaver, J. B., Pattison, A. J., McGarry, M. D., Perreard, I. M., Swienckowski, J. G., Eskey, C. J., Lollis, S. S., & Paulsen, K. D. (2012). Brain mechanical property measurement using MRE with intrinsic activation. *Physics in Medicine and Biology*, *57*(22), 7275–7287. https://doi.org/10.1088/0031-9155/57/22/7275

Williamson, N. H., Komlosh, M. E., Benjamini, D., & Basser, P. J. (2020a). Limits to flow detection in phase contrast MRI. *Journal of Magnetic Resonance Open*, *2–3*, 100004. https://doi.org/10.1016/j.jmro.2020.100004

Williamson, N. H., Komlosh, M. E., Benjamini, D., & Basser, P. J. (2020b). Limits to flow detection in phase contrast MRI. *Journal of Magnetic Resonance Open*, *2–3*, 100004. https://doi.org/10.1016/j.jmro.2020.100004

Xu, Z. S., Lee, R. J., Chu, S. S., Yao, A., Paun, M. K., Murphy, S. P., & Mourad, P. D. (2013). Evidence of Changes in Brain Tissue Stiffness After Ischemic Stroke Derived From Ultrasound-Based Elastography. *Journal of Ultrasound in Medicine*, *32*(3), 485–494. https://doi.org/10.7863/jum.2013.32.3.485

Yin, Z., Romano, A. J., Manduca, A., Ehman, R. L., & Huston, J. (2018). Stiffness and Beyond: What MR Elastography Can Tell Us About Brain Structure and Function Under Physiologic and Pathologic Conditions. *Topics in Magnetic Resonance Imaging : TMRI*, *27*(5), 305–318. https://doi.org/10.1097/RMR.0000000000000178

Zhang, F., Peng, W., Sweeney, J. A., Jia, Z., & Gong, Q. (2018). Brain structure alterations in depression: Psychoradiological evidence. *CNS Neuroscience & Therapeutics*, *24*(11), 994–1003. https://doi.org/10.1111/cns.12835

Zorgani, A., Souchon, R., Dinh, A.-H., Chapelon, J.-Y., Ménager, J.-M., Lounis, S., Rouvière, O., & Catheline, S. (2015). Brain palpation from physiological vibrations using MRI. *Proceedings of the National Academy of Sciences of the United States of America*, *112*(42), 12917–12921. https://doi.org/10.1073/pnas.1509895112



Chapter 2

Estimating the viscoelastic properties of the human brain at 7T MRI using intrinsic MRE and nonlinear inversion

Marius Burman Ingeberg[1], Elijah Van Houten[2], Jaco J.M Zwanenburg[1]

[1]Translational Neuroimaging Group, Center for Image Sciences, University Medical Center Utrecht and Utrecht University, Utrecht, The Netherlands
[2]Université de Strasbourg, CNRS, INSERM, ICube, UMR7357, Strasbourg, France.

Original work published in Human Brain Mapping:

Burman Ingeberg M, Van Houten E, Zwanenburg JJM. Estimating the viscoelastic properties of the human brain at 7 T MRI using intrinsic MRE and nonlinear inversion. Hum Brain Mapp. 2023 Dec 15;44(18):6575-6591. doi: 10.1002/hbm.26524. Epub 2023 Nov 1. PMID: 37909395; PMCID: PMC10681656.

Author Contribution Statement:

Marius Burman Ingeberg was responsible for conceptualization, methodology, software development, investigation, formal analysis, data management, and visualization, and wrote the original draft of the manuscript. Eli van Houten contributed to conceptualization, provided supervision and resources, and reviewed and edited the manuscript. Jaco Zwanenburg contributed to conceptualization, secured funding, provided resources and supervision, and reviewed and edited the manuscript.

Abstract

Introduction

Intrinsic actuation Magnetic Resonance Elastography (MRE) is a phase-contrast MRI technique that allows for *in vivo* quantification of mechanical properties of the brain by exploiting brain motion that arise naturally due to the cardiac pulse. The mechanical properties of the brain reflect its tissue microstructure, making it a potentially valuable parameter in studying brain disease. The main purpose of this study was to assess the feasibility of reconstructing the viscoelastic properties of the brain using high-quality 7T MRI displacement measurements, obtained using Displacement Encoding with Stimulated Echoes (DENSE) and intrinsic actuation. The repeatability and sensitivity of the method for detecting normal regional variation in brain tissue properties was assessed as secondary goal.

Method

The displacement measurements used in this analysis were previously acquired for a separate study, where eight healthy subjects (27 ± 7 years) were imaged with repeated scans (spatial resolution approx. 2 mm isotropic, temporal resolution 75 ms, motion sensitivity 0.35 mm/2π for displacements in Anterior-Posterior and Left-Right directions, and 0.7 mm/2π for Feet-Head displacements). The viscoelastic properties of the brain were estimated using a subzone based non-linear inversion scheme.

Results

The results show comparable consistency to that of extrinsic MRE between the viscoelastic property maps obtained from repeated displacement measurements. The shear stiffness maps showed fairly consistent spatial patterns. The whole-brain repeatability coefficient (RC) for shear stiffness was 15.1% relative to the mean whole-brain stiffness, and the damping ratio RC was 45.9% relative to the whole-brain damping ratio. The shear stiffness maps showed similar statistically significant regional trends as demonstrated in a publicly available atlas of viscoelastic properties obtained with extrinsic actuation MRE at 50 Hz. The damping ratio maps showed less consistency, likely due to data-model mismatch of describing the brain as a viscoelastic material under low frequencies.

Conclusion

While artifacts induced by fluid flow within the brain remain a limitation of the technique in its current state, intrinsic actuation based MRE allow for consistent and repeatable estimation of the mechanical properties of the brain. The method provides enough sensitivity to investigate regional variation in such properties in the normal brain, which is likely sufficient to also investigate pathological changes.

1 Introduction

Magnetic resonance elastography (MRE) (Muthupillai et al., 1995) is a phase-contrast MRI technique that allows for *in vivo* quantification of mechanical properties within any tissue. It shows potential as an additional contrast mechanism in the assessment and diagnosis of pathologies that affect tissue microstructure (Glaser et al., 2012; Hiscox et al., 2016; Rouvière et al., 2006; Yin et al., 2007). Recently, there has been increasing interest in applying MRE to the brain, for two principal reasons. First, MRE may provide an additional perspective into brain function, given recent studies demonstrating the link between tissue mechanics and neuronal activity (Barnes et al., 2017a; Forouhandehpour et al., 2021; Goriely et al., 2015a; Lan et al., 2020; Schwarb et al., 2016). Secondly, it provides a non-invasive approach to constructing detailed maps of the mechanical properties of the brain, which has previously been exceedingly difficult. Additionally, it allows for the quantification of mechanical properties while the brain is within its natural environment. In contrast, *ex vivo* attempts at quantifying such properties faces many challenges due to the inconsistent nature of extracted soft tissue, leading to contradictory results (Budday et al., 2020).

Typically, MRE uses a mechanical actuator to produce mechanical waves within the tissue of interest in order to produce displacements that can be imaged using phase-contrast techniques. The resulting displacement fields can then be used to reconstruct the mechanical properties of the tissue via various types of *inversion*, or image reconstruction. As previously shown, it is possible to reconstruct the mechanical properties of the brain without the use of an extrinsic driver (Herthum et al., 2021; Hirsch et al., 2013; Weaver et al., 2012; Zorgani et al., 2015). This approach is referred to as "intrinsic actuation" and uses the brain motions that arise naturally due to the cardiac pulse, which can be measured given a sufficiently sensitive MRI acquisition. Intrinsic actuation MRE has a few important benefits. First, it eliminates the necessity of external actuators, significantly simplifying the method of acquisition, which in turn increases the availability of the method. Second, it circumvents the problem of poor shear wave penetration through the skull (Weaver et al., 2012). Finally, the use of the cardiac pulse signal for MRE actuation leads to a mechanical profile of the brain in its *natural* state, rather than in an artificial vibration state.

Since the first attempts at intrinsic actuation MRE, there has been significant improvement to the acquisition of cardiac-induced brain deformation. Initial intrinsic acquisition methods employed traditional phase-contrast velocity measurements, which are not very sensitive to the low velocities of brain tissue motion during the cardiac cycle, which are typically below 1 mm/s. Over time, MRI sequences dedicated to quantifying cardiac-induced brain tissue motion emerged, enabling more sensitive measurements. Specifically, the acquisition sequence Displacement Encoding with Stimulated

Echoes (DENSE), originally developed for measuring motion in the myocardium (Aletras et al., 1999), can be adapted to measure subtle brain tissue motion (Reese et al., 2002; Soellinger et al., 2009). This sequence has recently been further optimized and adapted to exploit the benefits of 7T MRI. (Adams et al., 2019, 2020; Sloots et al., 2020, 2021). Such data, however, has not yet been tested in reconstructing the mechanical properties of the brain. The main purpose of this work is thus to assess the feasibility of reconstructing the mechanical properties of the brain using 7T displacement measurements, obtained using DENSE acquisition and intrinsic actuation. As secondary goals, we want to verify that the repeatability of the DENSE measurements is maintained after inversion as well as exploring the sensitivity of the method for detecting normal variation in brain tissue properties. This is done by conducting a regional analysis where we compare regional mechanical properties to those provided in a publicly available atlas (in standard-space) of viscoelastic properties obtained with extrinsic actuation (which we denote as the *extrinsic viscoelastic property atlas in standard space*, or *EVPASS*) (Hiscox et al., 2020).

2 Method

2.1 Utilized brain motion data

The displacement measurements used in this analysis were previously acquired by Adams et al. in 2020. Details of their method of acquisition and data processing can be found in the original paper (Adams et al., 2020). We will briefly summarize the method and resulting data in the following section. Subjects gave written-informed consent for participation in this study, which was approved by the ethical review board of our institution.

Eight healthy young subjects (3 females, mean age: 27 ± 6 years) were imaged using the DENSE sequence in a 7T MR scanner (Philips Healthcare), where a 3D EPI readout scheme was used. Repeated scans were performed to assess the repeatability of the measurements, with the subjects exiting the scanner for a maximum of 10 minutes between scans. A pulse oximeter was used to sync the DENSE measurements to the cardiac cycle by means of retrospective gating. The acquired resolution was 1.95 mm × 1.95 mm × 2.2 mm, with 20 phases (time points) reconstructed per cardiac cycle. Three acquisitions were performed with displacement encoding (D_{ENC}) sensitivity of 0.35 mm, 0.175 mm, and 0.175 mm in the FH, AP, and RL directions, respectively (i.e. displacement D_{ENC} causes a phase shift of π). The acquisition time for a heart rate of 60 beats/min was 2:24 min per motion encoding direction. T1-weighted images were also obtained during both scans, with an acquired resolution of 0.93 mm × 0.93 mm × 1.0 mm. The Computational Anatomy Toolbox (Jena University Hospital, Departments of Psychiatry and Neurology) extension for SPM12 (Wellcome Trust Centre for Neuroimaging, University College Lon-

don) was used to create a brain tissue mask that excludes large blood vessels. The toolbox was additionally used to generate gray matter (GM) and white matter (WM) probability maps, as well as cerebrospinal fluid (CSF) probability maps from T1-weighted images. Larger intracranial blood vessels induced high intensities in the T1-weighted images, affecting the segmentation. They were consequently removed from the GM and WM probability maps using morphological area opening. Additionally, physiological motion that is not synchronized with the triggering device results in inter-shot phase variability and consequently artifacts. Such artifacts were detected through the use of SNR maps, which were obtained by dividing the magnitude image at the end of the cardiac cycle (which contained the majority of artifacts) by the temporal standard deviation. The SNR maps could then be thresholded to create artifact-free masks, which were combined with the GM and WM masks using logical conjunction. A more detailed description of the above-mentioned methodology can be found in the original article (Adams et al., 2020).

AP and FH magnitude images were rigidly registered to the RL magnitude images (Klein et al., 2010) to account for subject motion between the three acquisitions, as described before (Adams et al., 2020). The last RL image of the cardiac cycle was then registered to the T1-weighted image for each subject, using non-linear registration. All images were then transformed to the T1-weighted image orientation and resolution using the non-linear registration parameters obtained from the RL to T1 registration and linear interpolation. All image registrations were performed using Elastix (Klein et al., 2010).

2.2 Mechanical property estimation

The mechanical properties were estimated using a subzone based non-linear inversion (NLI) scheme (McGarry et al., 2012; Van Houten et al., 1999, 2001). In order to perform such inversions, quadratic hexahedral finite element models (FEM) of the subject's brains are generated from the respective displacement measurements, where an isotropic mesh size of 2.0 mm was used. The reconstruction is formulated as a constrained optimization task where the objective is to minimize the difference between the measured tissue displacements and displacements obtained using the computational finite element model.

A viscoelastic model of the brain is used, which recovers the complex shear modulus $G^* = G' + iG''$, where G' is the shear storage modulus and G'' is the shear loss modulus. Additionally, the lambda-modulus, $\lambda = \frac{2\nu G^*}{1-2\nu}$, where ν is the Poisson ratio, is recovered with a 20 cm isotropic mesh resolution, such that one single value for λ is recovered for the entire brain volume. The equation of motion for a heterogeneous viscoelastic material expressed in the frequency domain is given by

$$\nabla \cdot G^* \left(\nabla \mathbf{U} + \nabla \mathbf{U}^T\right) + \nabla(\lambda \nabla \cdot \mathbf{U}) = -\rho\omega^2 \boldsymbol{U} + F, \qquad (1)$$

with ***u*** being the 3D complex-valued motion amplitude, ρ the density, ω the actuation frequency, and F the body forces (which are assumed to be 0 such that $F = 0$). As discussed more thoroughly by McGarry et al. (2019), the elastic forces on the left-hand side of equation (1) are much larger than the inertial forces described by the right-hand side. Equation (1) therefore reduces to

$$\nabla \cdot G^*\left(\nabla \mathbf{U} + \nabla \mathbf{U}^T\right) + \nabla(\lambda \nabla \cdot \mathbf{U}) \sim 0. \qquad (2)$$

All terms on the left-hand side of equation (2) contain G^*, which means that a constant multiplier g_0 can be factored out as $G^* = g_0 G_0^*$ and $\lambda = g_0 \lambda_0 = \frac{2\nu G_0^*}{1-2\nu}$, such that

$$g_0\left[\nabla \cdot G_0^*\left(\nabla \mathbf{U} + \nabla \mathbf{U}^T\right) + \nabla(\lambda_0 \nabla \cdot \mathbf{U})\right] \sim 0. \qquad (3)$$

Because g_0 is arbitrarily scalable and has no effect on the solution, it is only possible to recover relative distributions of G^* for the low frequencies exhibited in intrinsic actuation. Due to this effect, a lower bound of 100 Pa is applied to G^* and λ to ensure non-negative solutions.

The FEM property distributions are updated iteratively such that the model displacements approach the measured displacements. A subzone size of 20 mm^3 with 15% overlap between zones was used, and 800 global iterations were performed for each subject in order to assure convergence. The hexahedral finite element meshes contained (mean ± std) 157730 ± 15420 nodes. Finally, the shear stiffness $\tilde{\mu} = 2|G^*|^2/(G' + |G^*|)$ and the damping ratio $\xi = G''/2G'$ are computed and reported to stay consistent with literature. The shear stiffness $\tilde{\mu}$ has been denoted with a tilde to reflect the non-unique, relative nature of these intrinsic actuation viscoelastic solutions.

2.3 Fluid flow artifact removal

The DENSE protocol is tuned to measure small tissue deformations. Consequently, large motions from fluid flow within the brain, such as larger blood vessels and CSF, can give incorrect values when measured, potentially inducing artifacts. Such artifacts can appear in mechanical property distributions as large *hotspots*, perturbing the results in the vicinity of the artifact. The majority of such hotspots appear in the periphery of the brain around the subarachnoid space which contains large quantities of CSF. As the cardiac-induced brain pulsations have the lowest amplitudes in such areas, the areas with large motions due to CSF can be determined with more certainty.

A heuristic method to deal with such hotspots in the periphery was implemented by masking voxels in the DENSE measurements that contained unreasonably high displacements. The masking of fluid-flow dominated voxels was optimized by simultaneously minimizing masking of brain tissue in two ways. First, the masking was spatially limited to the peripheral area of the brain as it contained the vast majority of fluid flow related

hotspots. Secondly, a suitable threshold for a) the spatial extent of what is defined as the periphery and b) for the threshold motion amplitude for masking, was empirically determined by performing a number of trial runs with variable settings for multiple subjects. The settings which appeared to have the most reasonable trade-off between removal of erroneous fluid flow related displacement measurements and unwanted removal of voxels representing true tissue displacement measurements were found to be: a periphery defined by a 5-voxel deep layer (i.e., 5 mm) around the exterior boundary of the brain and a masking threshold of eight times the standard deviation of the displacement distribution within the brain. Any *stranded* voxels that ended up disconnected from the bulk of the brain volume were removed, and an additional one layer of voxel erosion was performed on the resulting mask.

2.4 Regional analysis

Regional differences within the brain were evaluated to explore the capability of the method to assess normal regional variation in tissue mechanical parameters. We investigated the variation in shear stiffness and damping ratio in the same regions of interest as is done in the EVPASS for reference. These regions are divided over cortical GM, subcortical GM, and white matter tracts (WMT), and were obtained from various standard-space MNI atlases, specified below.

2.4.1 Gray matter

The MNI-ICBM2009c nonlinear symmetric 1mm atlas (Manera et al., 2020) was used to identify cortical and subcortical GM. The cortical GM ROIs include the following 12 regions: cuneus (CN), fusiform gyrus (FSG), inferior temporal cortex (ITC), lateral occipital cortex (LaO), lingual occipital cortex (LiO), precuneus (PCN), postcentral cortex (POST), rostral middle frontal cortex (RMF), precentral cortex (PRE), superior frontal cortex (SFC), superior parietal cortex (SPC), and superior temporal cortex (STC). Similarly, the six subcortical GM ROIs include the amygdala (AM), caudate (CA), hippocampus (HC), pallidum (PA), putamen (PU), and thalamus (TH). Each regional mask was individually eroded by 1 voxel to obtain a more conservative estimate of the locations of the regions, thereby avoiding partial volume effects that occur at the boundaries.

2.4.2 White matter

Twelve WMT ROIs were identified, eight of which were obtained from the JHU-ICBM-tracts 2 mm atlas, thresholded at 25%. These include the anterior thalamic radiation (ATR), corticospinal tract (CST), major forceps (FMa), minor forceps (FMi), inferior frontal occipital fasciculus (IFOF), inferior longitudinal fasciculus (ILF), superior longitudinal fasciculus (SLF), and uncinate fasciculus (UN). The other four regions were obtained from the JHU-ICBM-labels 2 mm atlas, including corpus callosum (CC), corona radiata (CRa), fornix

(FX), and posterior thalamic radiation (PTR). Each regional mask was individually eroded by 1 voxel.

2.4.3 Global regions of interest

Each global region of interest was also investigated separately, where the cortical GM and subcortical GM masks were created by combining all investigated cortical and subcortical GM regions respectively. GM probability distributions were additionally used in combination with the regional masks, with a threshold of 90%. WM masks were generated by thresholding the white matter probability masks at 90%.

2.4.3 Region extraction

To extract the regions from the shear stiffness and damping ratio maps, the T1-weighted images (which were in the same space as the DENSE magnitude images) of each subject were non-linearly registered to the MNI-ICBM2009c non-linear average template, using Elastix (Klein et al., 2010). Two levels of resolution were used, with 250 iterations per resolution. Prior to the non-linear registration, each T1-weighted image was aligned to the MNI template by first performing a rigid registration for 100 iterations for 4 levels of resolution, followed by an affine registration for 200 iterations for one level of resolution. The resulting transformation matrices were then applied to the shear stiffness and the damping ratio distributions as well as grey and white matter probability distributions using nearest neighbor interpolation. Additionally, the JHU-ICBM atlases were interpolated to the resolution of the MNI-ICBM2009c non-linear average template using nearest neighbor interpolation such that the parameter distributions and all atlases have the same resolution. Each atlas was then used to identify each ROI in the shear stiffness and damping ratio distribution for each subject. Repeated scans are averaged such that there is only one data point per subject.

2.4.4 Statistical analysis

Post hoc pairwise comparisons were performed to examine regional differences in the shear stiffness and damping ratio by using General Linear mixed models. Bonferroni corrections were used to counteract the multiple comparisons problem. A value of $p < 0.05$ was used as the threshold for statistically significant effects. All statistical analyses were performed using the glmm package for R.

2.5 Atlas comparison

To assess differences between the extrinsic and intrinsic actuation approaches more thoroughly, the shear stiffness and damping ratio templates presented in the EVPASS, obtained by averaging spatially normalized parameter maps from 134 participants, were compared voxel-by-voxel with the equivalent mean distributions presented in this analysis. To do so, the EVPASS distributions were interpolated using nearest neighbor

interpolation to match the resolution of the MNI-ICBM2009c template. To account for the arbitrary scaling factor of the intrinsic results, all distributions were normalized by their global mean value throughout the brain volume, and maps representing the voxel-wise differences were obtained by computing the ratio between the respective distributions. Finally, the difference in regional variation of the shear stiffness and damping ratio between the two approaches was explored by directly comparing the regional means obtained in the intrinsic analysis presented here with the ones presented in the EVPASS. This was done by plotting the regional means obtained with both methods together. Due to the difference in scaling between the two methods, the y-axes are scaled using global mean values throughout the brain volume such that the relative values can be evaluated.

2.6 Repeatability analysis

To assess the repeatability of the measurements, a voxel-wise Bland-Altman analysis (Bland & Altman, 1986) was performed on each subject for the shear stiffness and damping ratio. The analysis was performed in MNI space to assess the repeatability in the cortical GM, the subcortical GM, and the WM separately using the global ROI masks. A subject-wise Bland-Altman analysis was additionally performed for the mean shear stiffness and damping ratio in each global ROI. Finally, the repeatability coefficient (RC) and coefficient of variation (CV) were calculated for each subject and global ROI.

3 Results

3.1 Mechanical property distributions

The viscoelastic property maps were successfully reconstructed in all subjects, including the repeated scans. The total change in property values between final iterations of the non-linear inversion was less than 0.053% for all subjects. An average of 3.45% (2.35% - 6.13%) of the total amount of voxels per subject were masked to suppress fluid flow artifacts. Figure 1 shows a representative axial slice in one subject of the shear stiffness and the damping ratio, along with the equivalent slice in the repeated scan which has been co-registered to the original scan. The equivalent axial slices for all subjects are presented in Figure S1 (shear stiffness) and Figure S2 (damping ratio). Consistent spatial patterns can be observed throughout the property maps, and general structural features of the brain can be identified. The shear stiffness maps of the repeated scans show strong structural similarity to that of the original scans, while the damping ratio distribution generally exhibits more variability. Though the property maps are generally symmetric (average difference between symmetric brain regions was 0.2% for the shear stiffness and 6.5% for the damping ratio), they remain affected by the existence of hotspots, as no fluid flow masking was applied to the interior of the brain volume. The mean lambda modulus

(single value per brain) over all subjects was 100.34 ± 0.27 Pa for the initial scans, and 100.22 ± 0.12 Pa for the repeated scans.

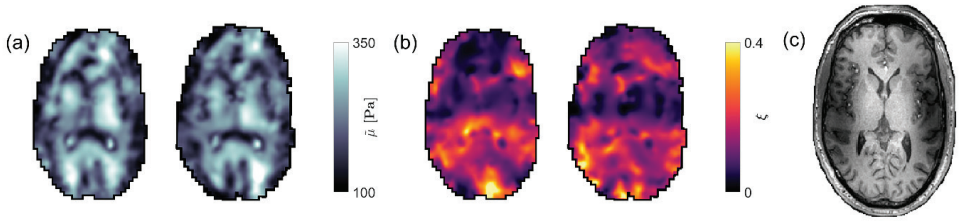


Figure 1. Representative axial slices of the (a) shear stiffness, μ̃, and the (b) damping ratio, ξ, for one subject along with repeat scans that have been co-registered to the initial scan. A T1-weighted image of the equivalent slice is shown in (c). Consistent spatial patterns can be observed throughout the property maps, and the repeated scans show strong structural similarity to that of the original scans, especially for the shear stiffness. The damping ratio maps show some consistency between repeated scans but only limited similarity to the anatomical scan, likely due to data-model mismatch and the noise propagation of the two reconstructed parameters, G′ and G″ into this composite parameter (see Discussion). The dark regions observed in the shear stiffness maps largely correspond to CSF-tissue boundaries. Large-valued hotspots can be seen in the repeated scan of the shear stiffness map, and in the original scan of the damping ratio map. The shear stiffness has been denoted with a tilde to the relative nature of the recovered solutions (see Methods).

3.2 Regional analysis

The mean over all subjects and repeats for the μ̃ and ξ spatial distributions are shown in Figure 2, where each image has been registered to the MNI-ICBM2009c non-linear template. The MNI-ICBM2009c template is also included in Figure 2 for visual comparison. The shear stiffness distribution shows high symmetry, clear spatial patterns, and large regional variability in all presented slices. Many structures of the brain can be identified that largely match anatomical structures seen in the MNI template. Some hotspots can be observed, such as in the lower left and top right regions in (k). The damping ratio distributions generally show less symmetry and spatial definition. Due to the masking of voxels containing fluid flows in the motion data, the boundaries of the finite element models used in NLI reconstruction can differ between subjects. For this reason, discretization artifacts can be observed along the periphery of the brain, particularly in the coronal slices (j, o).

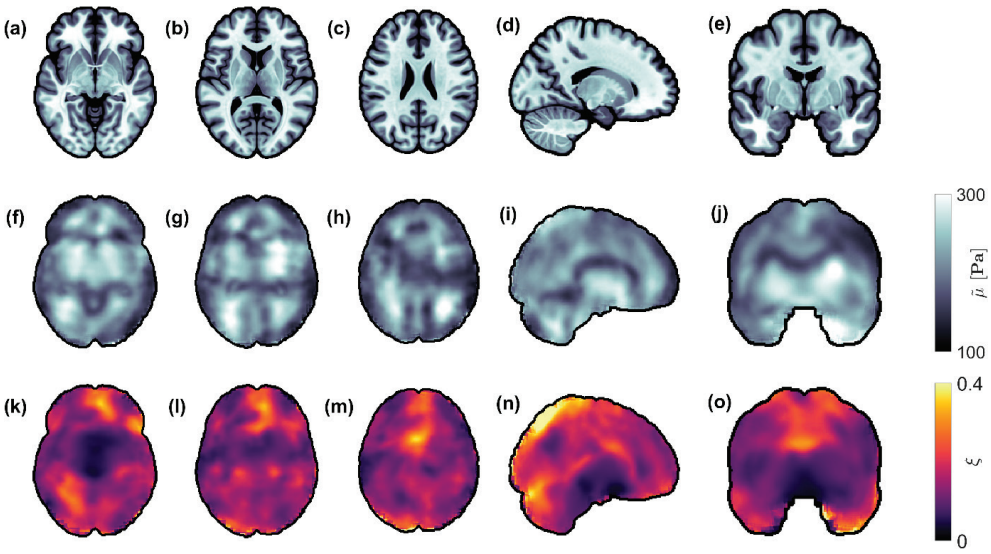


Figure 2. Transverse (a, b, c), sagittal (d), and coronal (e) anatomical representations of the brain in common space (MNI-ICBM2009c template), and respective shear stiffness (f-j) and damping ratio (k-o) maps, obtained from averaging over all subjects and repeats. Each individual parameter map has been registered to the MNI-ICBM2009c brain atlas. The shear stiffness distributions display clear spatial patterns and large regional variability, where many features of the brain can be identified. The damping ratio distributions exhibit less spatial definition. Discretization artifacts can be observed along the boundary of the brain due to the masking of voxels containing fluid flow. The shear stiffness has been denoted with a tilde to the relative nature of the recovered solutions.

3.2.1 Global regions of interest

The mean and standard deviation over all subjects within each global ROI are provided in Table 1. The shear stiffness showed regional differences that were consistent between subjects, as visualized in plot (a) of Figure 3. Likewise, the damping ratio is presented in plot (b) of Figure 3. The pairwise comparisons of each ROI are presented as significance charts for (c) the shear stiffness and (d) the damping ratio.

Table 1: Mean and standard deviation of stiffness parameters in global ROIs.

	$\tilde{\mu}$ [Pa]	ξ
Global	208 ± 14	0.162 ± 0.042
WMT	217 ± 15	0.154 ± 0.043
Subcortical GM	233 ± 24	0.106 ± 0.039
Cortical GM	200 ± 14	0.173 ± 0.053

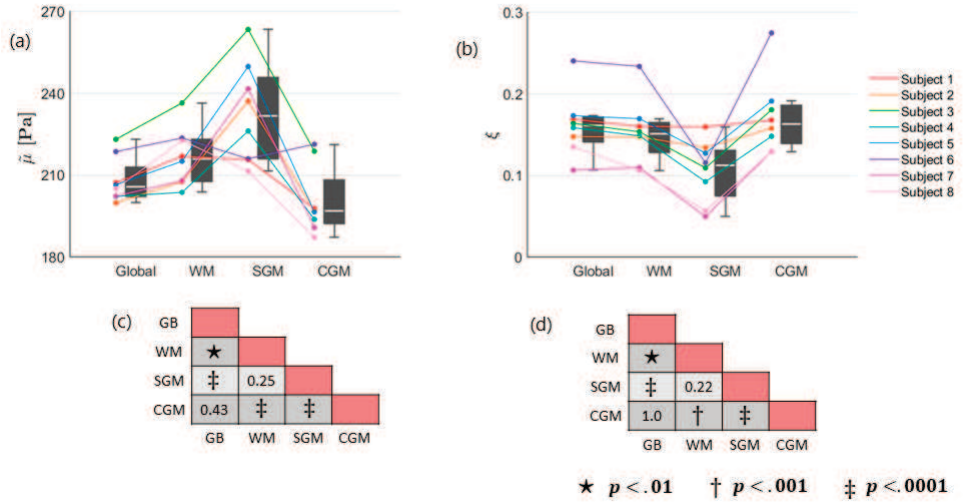


Figure 3: Boxplots alongside individual trend lines for each subject and significance charts in selected global ROIs for (a) shear stiffness, μ̃, and (b) damping ratio, ξ. Each dot represents the mean within one region for one subject. The white line within the boxplots corresponds to the median and the upper and lower end of the boxplots represent the 25th and 75th quartiles. The whiskers illustrate the maximum and minimum values that are not outliers, where outliers are values which lie at least *1.5*IQR* away from the upper or lower quartiles. The significance charts for the (c) shear stiffness and (d) damping ratio were determined by utilizing a general linear mixed model and performing a post-hoc analysis which was adapted for multiple comparisons using Bonferroni correction. Regions that are significantly different are indicated with bold text, and the symbols: ⋆, †, or ‡, depending on their level of significance. The shear stiffness has been denoted with a tilde to indicate the relative nature of the recovered solutions.

3.2.2 White matter tracts

The mean and standard deviation over all subjects within each WMT region are provided in Table 2. The shear stiffness showed regional differences that were consistent between subjects, as visualized in plot (a) of Figure 4. Likewise, the damping ratio is presented in plot (b) of Figure 4 but exhibits overall less consistent regional differences between subjects. The pairwise comparisons of each ROI are presented as significance charts for (c) the shear stiffness and (d) the damping ratio.

Table 2: Mean and standard deviation of stiffness parameters in WMT ROIs.

	$\tilde{\mu}$ [Pa]	ξ
Corpus callosum	207 ± 16	0.187 ± 0.072
Corona radiata	219 ± 16	0.158 ± 0.054
Minor forceps	231 ± 29	0.196 ± 0.092
Superior longitudinal fasciculus	213 ± 24	0.119 ± 0.025
Anterior thalamic radiation	245 ± 25	0.090 ± 0.035
Inferior frontal-occipital fasciculus	219 ± 12	0.154 ± 0.087
Corticospinal tract	236 ± 21	0.153 ± 0.064
Inferior longitudinal fasciculus	239 ± 17	0.123 ± 0.051
Posterior thalamic radiation	236 ± 19	0.092 ± 0.026
Major forceps	252 ± 34	0.140 ± 0.057
Fornix	268 ± 45	0.058 ± 0.028
Uncinate fasciculus	230 ± 32	0.920 ± 0.070

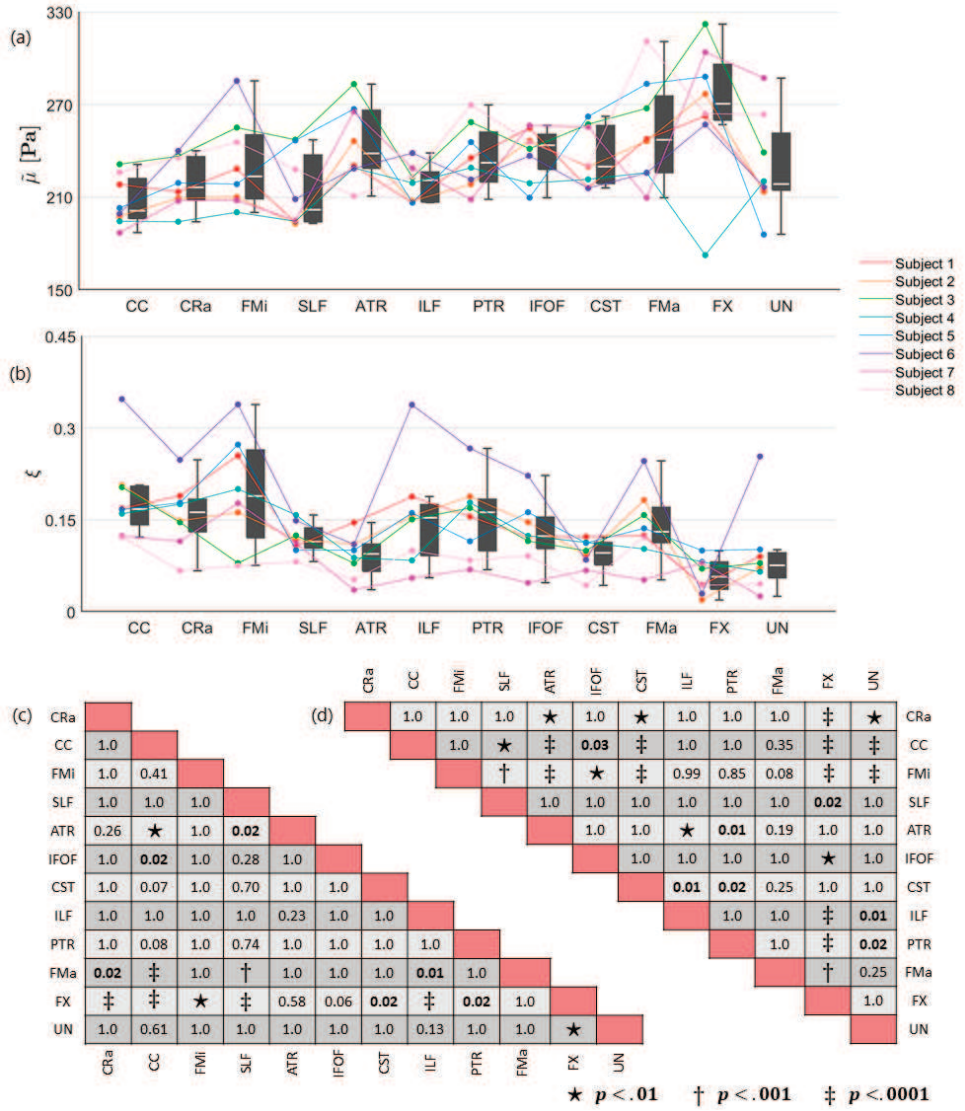


Figure 4: Boxplots alongside individual trend lines for each subject and significance charts in selected WMT ROIs for (a) shear stiffness, μ̃, and (b) damping ratio, ξ. Each dot represents the mean within one region for one subject. The regions are sorted by number of voxels such that the largest regions appear on the left. The white line within the boxplots corresponds to the median and the upper and lower end of the boxplots represent the 25th and 75th quartiles. The whiskers illustrate the maximum and minimum values that are not outliers, where outliers are values which lie at least 1.5 · IQR away from the upper or lower quartiles. The significance charts for the (c) shear stiffness and (d) damping ratio were determined by utilizing a general linear mixed model and performing a post-hoc analysis which was adapted for multiple comparisons using Bonferroni correction. Regions that are significantly different are indicated with bold text, and the symbols: ⋆, †, or ‡, depending on their level of significance. The shear stiffness has been denoted with a tilde to indicate the relative nature of the recovered solutions. The abbreviations for the regions can be found in the legend of Table 2.

3.2.3 Cortical Gray matter

The mean and standard deviation over all subjects within each cortical GM region are provided in Table 3. The shear stiffness showed regional differences that were consistent between subjects, as visualized in plot (a) of Figure 5. Likewise, the damping ratio is presented in plot (b) of Figure 5 but exhibits overall less consistent regional differences between subjects. The pairwise comparison of each ROI is presented as significance charts for (c) the shear stiffness and (d) the damping ratio.

Table 3: Mean and standard deviation of stiffness parameters in cortical GM ROIs.

	$\tilde{\mu}$ [Pa]	**ξ**
Superior frontal cortex	191 ± 15	0.198 ± 0.057
Superior temporal cortex	186 ± 9	0.142 ± 0.037
Rostral middle frontal cortex	173 ± 17	0.106 ± 0.024
Lateral occipital cortex	200 ± 23	0.157 ± 0.089
Inferior temporal cortex	208 ± 12	0.183 ± 0.078
Precuneus	206 ± 15	0.210 ± 0.094
Fusiform gyrus	222 ± 23	0.212 ± 0.094
Lingual occipital cortex	214 ± 23	0.182 ± 0.079
Superior parietal cortex	236 ± 35	0.297 ± 0.140
Precentral cortex	193 ± 14	0.140 ± 0.027
Postcentral cortex	192 ± 12	0.162 ± 0.037
Cuneus	195 ± 20	0.176 ± 0.073

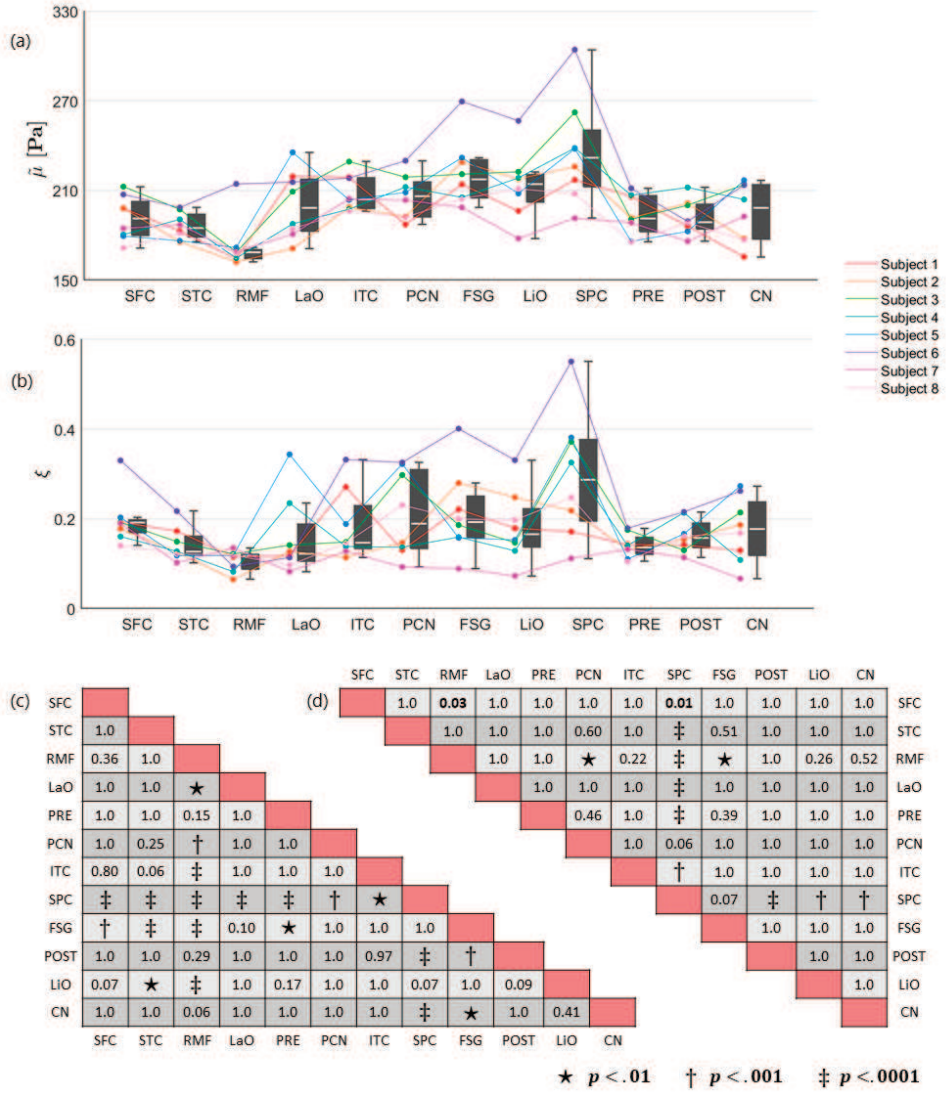


Figure 5: Boxplots alongside individual trend lines for each subject and significance charts in selected cortical GM ROIs for (a) shear stiffness, μ̃, and (b) damping ratio, ξ. Each dot represents the mean within one region for one subject. The regions are sorted by number of voxels such that the largest regions appear on the left. The white line within the boxplots corresponds to the median and the upper and lower end of the boxplots represent the 25th and 75th quartiles. The whiskers illustrate the maximum and minimum values that are not outliers, where outliers are values which lie at least 1.5 · IQR away from the upper or lower quartiles. The significance charts for the (c) shear stiffness and (d) damping ratio were determined by utilizing a general linear mixed model and performing a post-hoc analysis which was adapted for multiple comparisons using Bonferroni correction. Regions that are significantly different are indicated with bold text, and the symbols: ⋆, †, or ‡, depending on their level of significance. The shear stiffness has been denoted with a tilde to indicate the relative nature of the recovered solutions. The abbreviations for the regions can be found in the legend of Table 3.

3.2.4 Subcortical gray matter

The mean and standard deviation over all subjects within each subcortical GM region are provided in Table 4. The shear stiffness showed regional differences that were consistent between subjects, as visualized in plot (a) of Figure 6. Likewise, the damping ratio is presented in plot (b) of Figure 6 but exhibits overall less consistent regional differences between subjects. The pairwise comparisons of each ROI are presented as significance charts for (c) the shear stiffness and (d) the damping ratio.

Table 4: Mean and standard deviation of stiffness parameters in subcortical GM ROIs.

	$\tilde{\mu}$ [Pa]	ξ
Thalamus	232 ± 32	0.117 ± 0.055
Putamen	274 ± 20	0.090 ± 0.047
Caudate	208 ± 13	0.119 ± 0.048
Hippocampus	204 ± 22	0.121 ± 0.045
Pallidum	277 ± 28	0.074 ± 0.037
Amygdala	224 ± 46	0.075 ± 0.036

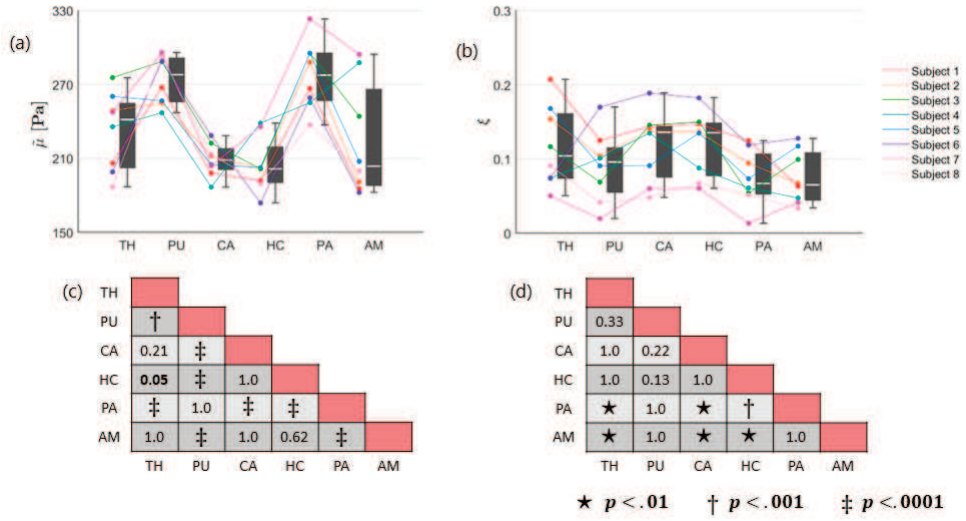


Figure 6: Boxplots alongside individual trend lines for each subject and significance charts in selected subcortical ROIs for (a) shear stiffness, $\tilde{\mu}$, and (b) damping ratio, ξ. Each dot represents the mean within one region for one subject. The regions are sorted by number of voxels such that the largest regions appear on the left. The white line within the boxplots corresponds to the median and the upper and lower end of the boxplots represent the 25th and 75th quartiles. The whiskers illustrate the maximum and minimum values that are not outliers, where outliers are values which lie at least 1.5·IQR away from the upper or lower quartiles. The significance charts for the (c) shear stiffness and (d) damping ratio were determined by utilizing a general linear mixed model and performing a post-hoc analysis which was adapted for multiple comparisons using Bonferroni correction. Regions

that are significantly different are indicated with bold text, and the symbols: ⋆, †, or ‡, depending on their level of significance. The shear stiffness has been denoted with a tilde to indicate the relative nature of the recovered solutions. The abbreviations for the regions can be found in the legend of Table 4.

3.3 Atlas comparison

Figure 7 shows the mean shear stiffness and damping ratio in each ROI for the intrinsic data presented in this analysis in addition to the extrinsic data presented in the EVPASS. The intrinsic shear stiffness maps generally showed similar spatial patterns and regional differences as in the extrinsic case. The majority of disagreement is found in the cortical GM, with the superior parietal cortex exhibiting inverse behavior between the methods. For the damping ratio, the similarity of spatial patterns and regional differences were less evident, and many large differences between the methods can be observed. Spearman's rank correlation coefficient for all regions was calculated to be 0.74 for the shear stiffness and -0.13 for the damping ratio.

The overall agreement in the shear stiffness and damping ratio maps is mapped in Figure 8, where the voxel-wise ratios between the mean distributions reported in Figure 2 and the distributions presented in the EVPASS are presented. Here it is also evident that the majority of disagreement in the shear stiffness maps is located in the outer regions of the brain, especially toward the top and back of the brain. Some spatial patterns of disagreement can also be observed throughout the bulk of the brain. The damping ratio maps show extensive areas of significant disagreement in all shown slices, principally along the region of the falx cerebri and the separation of the two hemispheres. Some disagreement due to discretization effects from fluid flow masking can also be seen in slices (d, e) and (i, j) at the bottom of the brain.

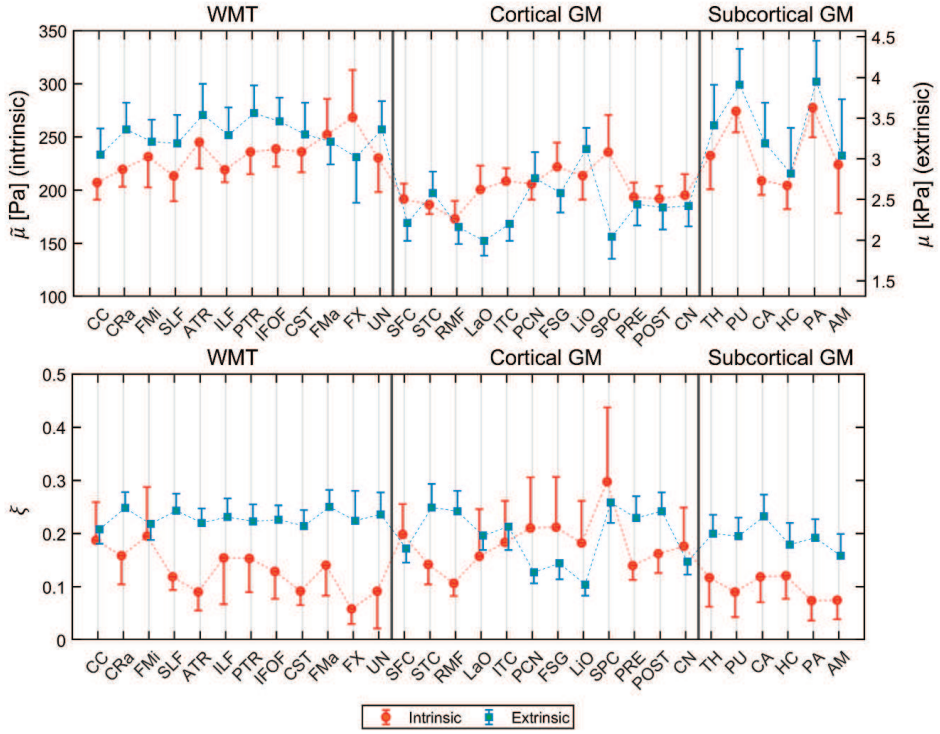


Figure 7: The mean shear stiffness, μ̃, (top) and damping ratio, ξ, (bottom) over all regions presented in this intrinsic analysis and the EVPASS. The whiskers represent the standard deviation in each ROI. The right-hand axis of the shear stiffness is scaled using global mean values throughout the brain volume such that the relative values between the intrinsic and extrinsic analyses can be evaluated. The shear stiffness has been denoted with a tilde to the relative nature of the recovered solutions. The thicker vertical lines were added as visual aid creating sections for white matter tracts (WMT), cortical GM and subcortical GM.

Abbreviations: CRa, corona radiata; CC, corpus callosum; FMi, minor forceps; SLF, superior longitudinal fasciculus; ATR, anterior thalamic radiation; IFOF, inferior frontal-occipital fasciculus; CST, corticospinal tract; ILF, inferior longitudinal fasciculus; PTR, posterior thalamic radiation; FMa major forceps; FX, fornix; UN, uncinated; SFC, superior frontal cortex; STC, superior temporal cortex; RMF, rostral middle frontal cortex; LaO, lateral occipital cortex; PCN, precuneus; SPC, superior parietal cortex; FSG, fusiform gyrus; LiO, lingual occipital cortex; POST, postcentral cortex; ITC, inferior temporal cortex; CN, cuneus. TH, thalamus; PU, putamen, CA, caudate; HC, hippocampus; PA, pallidum; AM, amygdala.

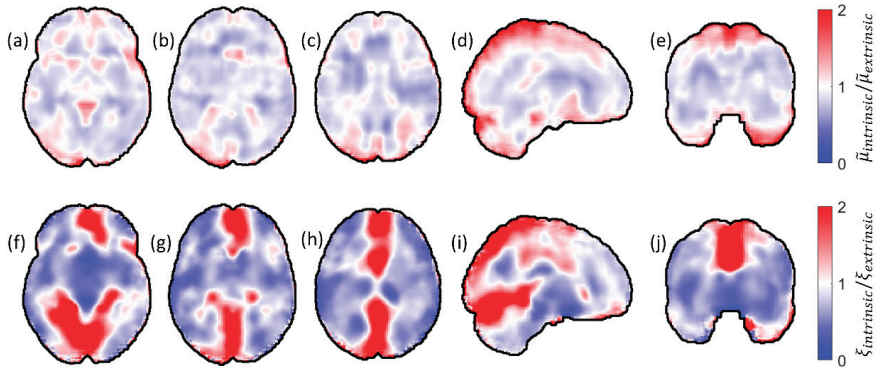


Figure 8: Transverse (a, b, c), sagittal (d), and coronal (e) slices of voxel-wise shear stiffness difference maps of the mean distributions presented in this analysis and those presented in the EVPASS that is based on extrinsic actuation with 50 Hz (Hiscox et al., 2020). The respective slices are also shown for the damping ratio in (f-j). Each distribution is normalized by the global mean value throughout the brain volume. Red and blue areas correspond to regions of relatively higher and lower values respectively in the mean parameter maps obtained with intrinsic actuation.

3.4 Repeatability

A summary of a comparison between the initial and repeated measurements is presented in Figure 9, which captures the representative features of the voxel-wise Bland-Altman plots for each subject. Each analysis is done in the cortical GM, subcortical GM, and WM separately. Most of the error bars in Figure 9 show symmetry in the length of the whiskers, suggesting significantly stable means between repeated measurements. Some variability is observed in the length of the whiskers between subjects, and probably reflects the difference in data quality due to variation in subject motion. The full voxel-wise Bland-Altman plots for all subjects are shown in Figure S3-S8 in the supplementary files.

Bland-Altman plots of the mean shear stiffness and damping ratio in the different global ROIs are presented in Figure 10 alongside the upper and lower limits of agreements. The root-mean-square error in shear stiffness was 15 Pa in cortical GM, 30.3 Pa in subcortical GM, 20.7 Pa in WM, and 16.0 in the whole brain. Similarly, the root-mean-square error in damping ratio was 0.051 in cortical GM and 0.025 in subcortical GM, 0.038 WM, and 0.038 in the whole brain for the damping ratio The RC for shear stiffness was 29.3 Pa in cortical GM, 59.3 Pa in subcortical GM, 40.6 Pa in WM, and 31.4 Pa for the whole brain. For the damping ratio, the RC was 0.10 in cortical GM, 0.05 in subcortical GM, 0.07 in WM, and 0.07 for the whole brain. The median CV for shear stiffness was 5.2% ± 2.8% in cortical GM, 2.5% ± 7.9% in subcortical GM, 4.0% ± 5.1% in WM, and 2.8% ± 4.0% for the whole brain. For the damping ratio, the median CV was 16.2% ± 9.4% in cortical GM, 15.1% ± 15.6% in subcortical GM, 13.2% ± 11.1% in WM, and 14.6% ± 8.7% for the whole brain.

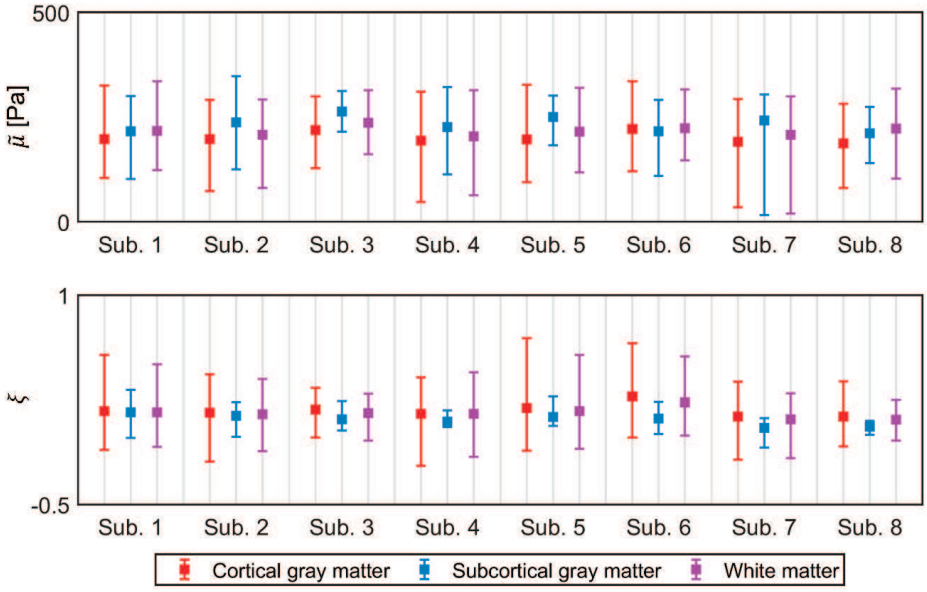


Figure 9. Summarized representation of a voxel-wise analysis of the repeated measurements for the cortical GM, subcortical GM and WM in each subject. The error bars represent summarized Bland-Altman plots where the dot indicates the mean over all voxels for the two measurements. The whiskers represent the upper and lower limits of agreement, defined as b ± 1.96·std where the bias b is the mean of the voxel-wise differences between measurements. An asymmetry in length of the whiskers in one error bar reflects a difference in the mean between the repeated scans. Most error bars show symmetry in the length of the whiskers, suggesting significantly stable means between repeated measurements. Some variability is observed in the length of the whiskers between subjects, and probably reflects the difference in data quality due to variations in subject motion. The shear stiffness has been denoted with a tilde to the relative nature of the recovered solutions.

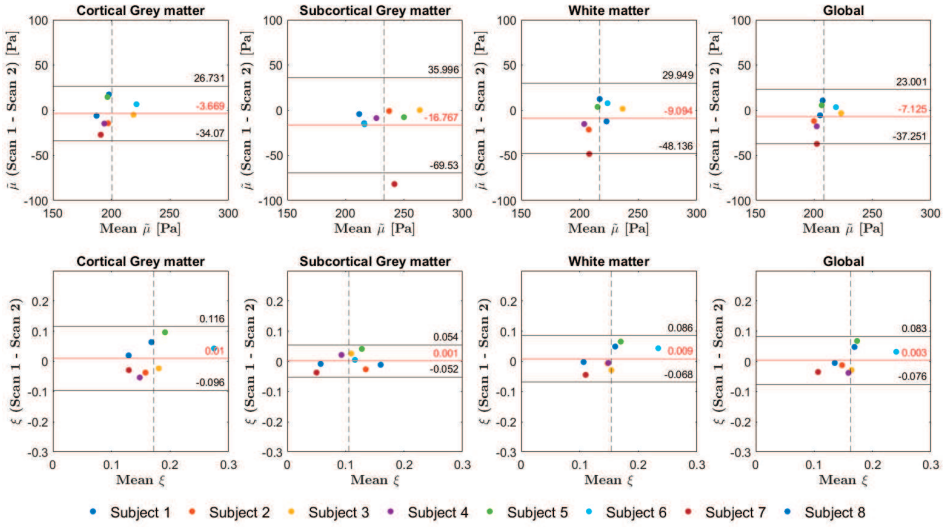


Figure 10*:* Bland-Altman plots of the mean shear stiffness (top row) and damping ratio (bottom row) in cortical GM, subcortical GM, WM, and global ROIs for all subjects. The horizontal red line represents the bias *b* which is the mean of the differences between the two measurements. The upper and lower horizontal black lines represent the upper and lower limits of agreement respectively, defined as $b \pm 1.96 \cdot \text{std}$. The vertical dashed line indicates the mean over all subjects.

4 Discussion

This work investigated the feasibility of utilizing intrinsic actuation-MR elastography in the brain based on 7T DENSE MRI measurements. The results demonstrated notable consistency between the viscoelastic property maps obtained from repeated displacement measurements. The shear stiffness maps showed fairly consistent spatial patterns. A voxel-wise analysis performed separately in the grey and white matter demonstrated good repeatability of the method in both tissue types. Additionally, we assessed the ability of the method to detect normal regional variation in tissue stiffness, which potentially can serve as a proxy of expected differences between patients and controls. This was investigated by performing a regional analysis for different grey and WM ROIs, where various subregions within white matter tracts (WMT), cortical GM, and subcortical GM were distinguished based on their viscoelastic properties. Finally, we explored how results obtained with the intrinsic actuation approach related to those obtained with extrinsic actuation by directly comparing the measurements reported in this analysis with those presented in the EVPASS (Hiscox et al., 2020). The shear stiffness maps showed generally good agreement between the two methods while the damping ratio maps exhibited significantly more disagreement, as indicated by Spearman's rank correlation coefficient.

A significant increase of anatomical detail compared to previous attempts at intrinsic actuation-based elastography could be seen in all presented stiffness maps (McGarry et al., 2019; Weaver et al., 2012; Zorgani et al., 2015), more than could be achieved by using higher field strength alone. Rather, the optimization of the acquisition sequence seemingly has a noticeable effect on the sensitivity. The first attempt at intrinsic MRE (Weaver et al., 2012) used a multiphase phase contrast gradient echo sequence in a 3 T scanner which allowed for a maximum sensitivity of 2.5 cm/s. Since then, there have only been two additional attempts at reconstructing mechanical property maps using the intrinsic MRE method (McGarry et al., 2019; Zorgani et al., 2015). Zorgani et al. employed a single-shot echo planar gradient echo sequence in a 1.5 T scanner and used seismic noise correlation to characterize the tissue mechanics, resulting in a sensitivity slightly above 1 cm/s. McGarry et al. used the Philips QFLOW sequence in a 3 T scanner with a sensitivity of 2.5 cm/s, leading to a considerable increase in detail in the shear stiffness maps compared to the initial two attempts. Although only one shear stiffness map was presented by McGarry et al., its quality suggests that intrinsic MRE could also be viable on 3 T scanners. In contrast to the lower sensitivities of the previous intrinsic MRE attempts, the DENSE sequence in its current implementation allows for a sensitivity of around 1 mm/s, which implies almost an order of magnitude higher SNR and helps explain the vast improvement of detail in the parameter maps. The lack of further exploration of the intrinsic elastography method can probably be attributed to the significant noise seen in the parameter maps of the initial two attempts. The demonstration of the stability of the parameter maps between repeated measurements as presented in this work might therefore renew interest in intrinsic elastography.

The shear stiffness maps were found to be generally symmetric, with the average difference between symmetric brain regions being 0.2% for the shear stiffness and 6.5% for the damping ratio. Asymmetries observed in these results in regions that show good agreement across the repeated images are most likely due to data-model mismatch between the measured displacement field and the purely viscoelastic model. This is due to the viscoelastic model not being able to provide a mechanism for relative fluid-tissue movement. In regions where such fluid-tissue interaction is significant, the optimization-based reconstruction process will determine effective parameter values which provide the best possible interpretation of this phenomenon in the context of the viscoelastic parameters, i.e. either effective stiffness or effective damping effects. A poroelastic brain model, such as those presented in previous work for MRE with extrinsic activation (McGarry et al., 2019, 2015; Perriñez et al., 2010; Sowinski et al., 2021), would be able to correctly account for this relative fluid-tissue movement and thus reduce such asymmetries.

We found that the shear stiffness is on average 9% higher in WM compared to cortical GM, which is in line with multiple previous studies (Braun et al., 2014; Hiscox et al., 2020;

Johnson, McGarry, Gharibans, et al., 2013; Weickenmeier et al., 2016), that consistently report higher shear stiffness in WM compared to GM. Despite the fact that there is general agreement that WM is stiffer, the ratio between grey and white matter stiffness varies substantially across studies. This could be explained by the fact that the shear stiffness tends to exhibit considerable regional variation across the entire brain as reported before (Budday et al., 2020; Hiscox et al., 2020). Such regional variability tends to be much larger than the average difference between global GM and WM, which implies that one WM- or GM value is a poor metric in this case. This effect can also be observed in our results, where the shear stiffness can vary by up to 60% (pallidum and rostral middle frontal cortex) between various ROIs. There are multiple factors that could contribute to such stiffness variability. Not only is the mechanical structure of the brain likely adapted to regionally varying functional demands (Budday et al., 2020), but also fluid-based effects like perfusion probably contribute to the tissue stiffness (Hetzer et al., 2018). Variability in stiffness parameters between different brain regions is clearly observed in the cortical GM, the subcortical GM, and the WMT. Most subjects follow similar trends in regional shear stiffness with occasional outliers, likely due to *hotspot*-like artifacts that tend to appear sporadically throughout the property maps. The intra-subject variance tends to increase for the smallest regions, which is particularly clear for the uncinate and fornix, which are on average 59 and 92 voxels in size, respectively. Additionally, the variance seems to increase for regions in close vicinity to the ventricles, such as the minor forceps, possibly due to remaining partial volume effects with CSF.

The relative shear stiffness between WMTs shows generally high correspondence to the EVPASS. As is observed in the atlas, the vast majority of investigated WMTs exhibit higher shear stiffness than the global WM (217 ± 15 Pa), with the exceptions being the superior longitudinal fasciculus and the corpus callosum. We also observe the corona radiate being stiffer than the corpus callosum, which is in line with multiple previous studies (Budday et al., 2017a; Hiscox et al., 2020; Johnson, McGarry, Gharibans, et al., 2013). We observe very similar regional trends for the shear stiffness in the subcortical GM with those found in extrinsic actuation. The pallidum and putamen are found to have the highest shear stiffness in the subcortical GM, something that has been observed across multiple MRE studies (Hetzer et al., 2018; Hiscox et al., 2020; Johnson et al., 2016). The relative regional shear stiffness in the cortical GM shows generally lower correspondence to the equivalent regions presented in the EVPASS. For example, the superior parietal cortex displays an inverted behavior, where it exhibits the largest shear stiffness in our results and second to lowest stiffness in the EVPASS. There are multiple factors that might play a role in these discrepancies, the first of which being that the low-resolution finite element mesh implemented in NLI treats the complex geometry exhibited due to gyri and sulci in the cortical GM as a single continuum (Hiscox et al., 2020). As discussed above, the periphery of the brain is also the area of largest uncertainty, as fluid flow due to CSF might introduce arti-

facts despite a significant portion of the CSF being masked. Additionally, the application of fluid flow masks itself might introduce some uncertainty as it affects the geometry of the finite element models used in NLI due to certain nodes being excluded.

The voxel-wise difference distributions shown in Figure 8 reveal some larger regions of disagreement between intrinsic and extrinsic actuation. The most pronounced differences are along the periphery of the brain, particularly towards the top back of the brain. Part of the reason might be that each subject is masked prior to inversion and then registered to standard space in both our work and in the EVPASS. The edges of the property maps therefore become somewhat different between subjects, leading to increased uncertainty. Furthermore, such regions tend to contain larger amounts of CSF and larger blood vessels. The differences might therefore be an effect of how fluid and fluid-tissue partial volume effects get treated differently in the two approaches. Some inherent variance also follows from the relatively limited sample size used in this analysis particularly also the existence of hotspots might bias certain regions towards higher shear stiffness. It is also possible that the stiffening effect of the brain under the common actuation frequencies used in extrinsic MRE may have a regional dependence due to the heterogeneous mechanical structure of the brain. To the authors' knowledge, this effect has not yet been examined and could be a subject for future investigation. As can be seen in Figure 7, there seems to be in general less variability in shear stiffness across brain structures when using intrinsic MRE, potentially due to this effect. It could, however, also be a result of limited regional sensitivity of intrinsic MRE.

The voxel-wise Bland-Altman analysis further establishes the repeatability of intrinsic-based elastography. There is certain dissimilarity in some measurements, which is likely to mainly due to the hotspots. This is particularly clear in Subject 7, where hotspots span large parts of the center of the shear stiffness map in the repeated scan (Figure S1) and is consequently reflected in the length of the bottom whisker in the summary plot of the voxel-wise Bland-Altman analysis (Figure 9). Such hotspots consequently have an effect on the statistics, resulting in large standard deviations in the root-mean-square error, the RC and the CV. Although a large portion of hotspots were successfully removed by masking high-displacement voxels in the displacement data induced by fluid flow, a considerable number still remained of which the origin is uncertain. Indeed, there are many areas within the bulk of the brain that contain additional CSF structures and larger blood vessels, which our current heuristic filtering method ignored as masking such voxels would result in gaps in the finite element model mesh. Other possibilities of the origin of hotspots include artifacts in displacement data due to motion-induced phase inconsistencies in the multishot (segmented) 3D EPI readout scheme (Adams et al., 2020; Soellinger et al., 2009) or data-model mismatch. Noisy data could also be a source of

hotspots, but that is less likely given the high SNR of the motion maps with the used 7T imaging method.

Despite the uncertainty introduced by hotspots, our method shows comparable repeatability to that of extrinsic MRE, as reported by Svensson et al. in 2021. They used a 3T scanner and a gradient echo sequence with a vibration frequency of 50 Hz to image the brains of 15 healthy subjects. Using FEM reconstruction, they report a whole-brain RC of 9.6% ± 2.3% relative to the mean whole-brain shear stiffness, and an upper and lower limit of agreement of 9.6% and 6.2% respectively. We report a whole-brain RC of 15.1% relative to the mean whole-brain stiffness, and an upper and lower limit of agreement of 11.0% and 17.8% respectively. Both the RCs and the upper limits of agreement show relatively good agreement, given the difference in number of subjects. The lower limit of agreement presented here is considerably larger, which can be largely attributed to the hotspots present in the second scan of Subject 7. Svensson et al. along with other groups has also looked into the CV as a metric of repeatability. In our case, CV measurements are of limited value given that we only have two repeats per subject, but the whole-brain median CV for shear stiffness across all subjects of 2.7% still compares well with the values ranging from 0.67% to 4.1% reported in literature (Herthum et al., 2022; Huang et al., 2019; Johnson et al., 2016; Murphy et al., 2013; Svensson et al., 2021).

In contrast to the shear stiffness distributions repeatedly showing consistent brain structure and general agreement with the EVPASS, the damping ratio distributions display a more inconsistent, ambiguous structure. This is especially apparent when comparing the RC between the two quantities, where it was 15.1% for the shear stiffness and 45.9% for the damping ratio when expressed as a percentage of the global shear stiffness and damping ratio respectively. These inconsistencies can in part be explained by the fact that the damping ratio is composed of two reconstructed parameters, G' and G", which yields unfavorable noise propagation from both parameters. Moreover, data-model mismatch could also affect the damping ratio when trying to model the brain under low frequencies as a viscoelastic material. As been discussed by McGarry et al. (McGarry et al., 2019, 2015), the choice of material model is significantly dependent on the actuation frequency, where poroelastic effects are more important under the low frequencies used in intrinsic actuation. Instead, the simpler viscoelastic model is more appropriate for the higher frequencies of extrinsic actuation, where the poroelastic effects diminish. It is thus plausible that the inconsistencies observed in the damping ratio are due to data-model mismatch, as it is a purely viscoelastic quantity. Shifting towards the use of a poroelastic brain model in intrinsic MRE may be the next step in resolving such inconsistencies (McGarry et al., 2019).

Although the performance of the intrinsic MRE approach looks promising on many levels, there are some limitations. The occurrence of hotspots throughout the stiffness parameter distributions introduces inconsistency across the measurements. However, recent developments in the optimization of the DENSE sequence (Sloots et al., 2021) might offer significant improvement in not only general noise, but also in sensitivity to brain tissue motion. This could significantly help diminish the number of artifacts that arise due to fluid flow. Such improvement to the DENSE sequence involves measuring deformation gradients rather than displacements of the tissue, which requires adapting the NLI scheme to account for deformation measurements. In this work, we see potential shortcomings when modeling the brain as a viscoelastic material under low frequencies in mainly two ways: the recovery of non-unique solutions and the relatively inconsistent characterization of the damping ratio distribution. As mentioned before, implementing a poroelastic model could potentially help alleviate both problems, while introducing different challenges. For instance, poroelastography methods are highly sensitive to the prescribed fluid permeability values at low frequencies (McGarry et al., 2019), which necessitates accurate measurements or estimations of these values. Future work aims to implement both an improved DENSE sequence in the acquisition and the poroelastic model in the NLI scheme to further explore the potential of intrinsic actuation MRE.

5 Conclusion

In this study, 7T MR displacement measurements of cardiac-induced brain tissue deformation were used to successfully reconstruct the viscoelastic properties of the brain in eight healthy subjects. The sensitivity of the method for detecting differences in stiffness was also explored by performing a region-wise analysis where the viscoelastic properties could consistently be distinguished between various brain regions. The repeatability was investigated using repeated scans and was found to be generally consistent. The major challenges of the current implementation include hotspot-like artifacts due to fluid flow and the recovery of non-unique viscoelastic solutions at low frequencies. Future work thus aims to investigate the performance of adapting the NLI scheme for deformation measurements and poroelastic reconstruction to deal with such challenges.

Acknowledgements

This work was supported by a Vici Grant from the Netherlands Organization for Scientific Research (NWO) awarded to Jaco J.M. Zwanenburg under grant agreement no. 18674.

References

Adams, A. L., Kuijf, H. J., Viergever, M. A., Luijten, P. R., & Zwanenburg, J. J. M. (2019). Quantifying cardiac-induced brain tissue expansion using DENSE. *NMR in Biomedicine*, *32*(2), e4050. https://doi.org/10.1002/nbm.4050

Adams, A. L., Viergever, M. A., Luijten, P. R., & Zwanenburg, J. J. M. (2020). Validating faster DENSE measurements of cardiac-induced brain tissue expansion as a potential tool for investigating cerebral microvascular pulsations. *NeuroImage*, *208*, 116466. https://doi.org/10.1016/j.neuroimage.2019.116466

Aletras, A. H., Ding, S., Balaban, R. S., & Wen, H. (1999). DENSE: displacement encoding with stimulated echoes in cardiac functional MRI. *Journal of Magnetic Resonance (San Diego, Calif. : 1997)*, *137*(1), 247–252. https://doi.org/10.1006/jmre.1998.1676

Barnes, J. M., Przybyla, L., & Weaver, V. M. (2017). Tissue mechanics regulate brain development, homeostasis and disease. *Journal of Cell Science*, *130*(1), 71–82. https://doi.org/10.1242/jcs.191742

Bland, J. M., & Altman, D. G. (1986). Statistical methods for assessing agreement between two methods of clinical measurement. *Lancet (London, England)*, *1*(8476), 307–310.

Braun, J., Guo, J., Lützkendorf, R., Stadler, J., Papazoglou, S., Hirsch, S., Sack, I., & Bernarding, J. (2014). High-resolution mechanical imaging of the human brain by three-dimensional multifrequency magnetic resonance elastography at 7T. *NeuroImage*, *90*, 308–314. https://doi.org/10.1016/j.neuroimage.2013.12.032

Budday, S., Ovaert, T. C., Holzapfel, G. A., Steinmann, P., & Kuhl, E. (2020). Fifty Shades of Brain: A Review on the Mechanical Testing and Modeling of Brain Tissue. *Archives of Computational Methods in Engineering*, *27*(4), 1187–1230. https://doi.org/10.1007/s11831-019-09352-w

Budday, S., Sommer, G., Birkl, C., Langkammer, C., Haybaeck, J., Kohnert, J., Bauer, M., Paulsen, F., Steinmann, P., Kuhl, E., & Holzapfel, G. A. (2017). Mechanical characterization of human brain tissue. *Acta Biomaterialia*, *48*, 319–340. https://doi.org/10.1016/j.actbio.2016.10.036

Forouhandehpour, R., Bernier, M., Gilbert, G., Butler, R., Whittingstall, K., & Van Houten, E. (2021). Cerebral stiffness changes during visual stimulation: Differential physiological mechanisms characterized by opposing mechanical effects. *Neuroimage: Reports*, *1*(2), 100014. https://doi.org/10.1016/j.ynirp.2021.100014

Glaser, K. J., Manduca, A., & Ehman, R. L. (2012). Review of MR elastography applications and recent developments. *Journal of Magnetic Resonance Imaging : JMRI*, *36*(4), 757–774. https://doi.org/10.1002/jmri.23597

Goriely, A., Geers, M. G. D., Holzapfel, G. A., Jayamohan, J., Jérusalem, A., Sivaloganathan, S., Squier, W., van Dommelen, J. A. W., Waters, S., & Kuhl, E. (2015). Mechanics of the brain: perspectives, challenges, and opportunities. *Biomechanics and Modeling in Mechanobiology*, *14*(5), 931–965. https://doi.org/10.1007/s10237-015-0662-4

Herthum, H., Dempsey, S. C. H., Samani, A., Schrank, F., Shahryari, M., Warmuth, C., Tzschätzsch, H., Braun, J., & Sack, I. (2021). Superviscous properties of the in vivo brain at large scales. *Acta Biomaterialia*, *121*, 393–404. https://doi.org/10.1016/j.actbio.2020.12.027

Herthum, H., Hetzer, S., Kreft, B., Tzschätzsch, H., Shahryari, M., Meyer, T., Görner, S., Neubauer, H., Guo, J., Braun, J., & Sack, I. (2022). Cerebral tomoelastography based on multifrequency MR elastography in two and three dimensions. *Frontiers in Bioengineering and Biotechnology*, *10*. https://doi.org/10.3389/fbioe.2022.1056131

Hetzer, S., Birr, P., Fehlner, A., Hirsch, S., Dittmann, F., Barnhill, E., Braun, J., & Sack, I. (2018). Perfusion alters stiffness of deep gray matter. *Journal of Cerebral Blood Flow and Metabolism : Official*

Journal of the International Society of Cerebral Blood Flow and Metabolism, *38*(1), 116–125. https://doi.org/10.1177/0271678X17691530

Hirsch, S., Klatt, D., Freimann, F., Scheel, M., Braun, J., & Sack, I. (2013). In vivo measurement of volumetric strain in the human brain induced by arterial pulsation and harmonic waves. *Magnetic Resonance in Medicine*, *70*(3), 671–683. https://doi.org/10.1002/mrm.24499

Hiscox, L. V, Johnson, C. L., Barnhill, E., McGarry, M. D. J., Huston, J., van Beek, E. J. R., Starr, J. M., & Roberts, N. (2016). Magnetic resonance elastography (MRE) of the human brain: technique, findings and clinical applications. *Physics in Medicine and Biology*, *61*(24), R401–R437. https://doi.org/10.1088/0031-9155/61/24/R401

Hiscox, L. V., McGarry, M. D. J., Schwarb, H., Van Houten, E. E. W., Pohlig, R. T., Roberts, N., Huesmann, G. R., Burzynska, A. Z., Sutton, B. P., Hillman, C. H., Kramer, A. F., Cohen, N. J., Barbey, A. K., Paulsen, K. D., & Johnson, C. L. (2020). Standard-space atlas of the viscoelastic properties of the human brain. *Human Brain Mapping*, *41*(18), 5282–5300. https://doi.org/10.1002/hbm.25192

Huang, X., Chafi, H., Matthews, K. L., Carmichael, O., Li, T., Miao, Q., Wang, S., & Jia, G. (2019). Magnetic resonance elastography of the brain: A study of feasibility and reproducibility using an ergonomic pillow-like passive driver. *Magnetic Resonance Imaging*, *59*, 68–76. https://doi.org/10.1016/j.mri.2019.03.009

Johnson, C. L., McGarry, M. D. J., Gharibans, A. A., Weaver, J. B., Paulsen, K. D., Wang, H., Olivero, W. C., Sutton, B. P., & Georgiadis, J. G. (2013). Local mechanical properties of white matter structures in the human brain. *NeuroImage*, *79*, 145–152. https://doi.org/10.1016/j.neuroimage.2013.04.089

Johnson, C. L., Schwarb, H., D J McGarry, M., Anderson, A. T., Huesmann, G. R., Sutton, B. P., & Cohen, N. J. (2016). Viscoelasticity of subcortical gray matter structures. *Human Brain Mapping*, *37*(12), 4221–4233. https://doi.org/10.1002/hbm.23314

Klein, S., Staring, M., Murphy, K., Viergever, M. A., & Pluim, J. P. W. (2010). elastix: a toolbox for intensity-based medical image registration. *IEEE Transactions on Medical Imaging*, *29*(1), 196–205. https://doi.org/10.1109/TMI.2009.2035616

Lan, P. S., Glaser, K. J., Ehman, R. L., & Glover, G. H. (2020). Imaging brain function with simultaneous BOLD and viscoelasticity contrast: fMRI/fMRE. *NeuroImage*, *211*, 116592. https://doi.org/10.1016/j.neuroimage.2020.116592

Manera, A. L., Dadar, M., Fonov, V., & Collins, D. L. (2020). CerebrA, registration and manual label correction of Mindboggle-101 atlas for MNI-ICBM152 template. *Scientific Data*, *7*(1), 237. https://doi.org/10.1038/s41597-020-0557-9

McGarry, M. D. J., Johnson, C. L., Sutton, B. P., Georgiadis, J. G., Van Houten, E. E. W., Pattison, A. J., Weaver, J. B., & Paulsen, K. D. (2015). Suitability of poroelastic and viscoelastic mechanical models for high and low frequency MR elastography. *Medical Physics*, *42*(2), 947–957. https://doi.org/10.1118/1.4905048

McGarry, M. D. J., Van Houten, E. E. W., Johnson, C. L., Georgiadis, J. G., Sutton, B. P., Weaver, J. B., & Paulsen, K. D. (2012). Multiresolution MR elastography using nonlinear inversion. *Medical Physics*, *39*(10), 6388–6396. https://doi.org/10.1118/1.4754649

McGarry, M., Van Houten, E., Solamen, L., Gordon-Wylie, S., Weaver, J., & Paulsen, K. (2019). Uniqueness of poroelastic and viscoelastic nonlinear inversion MR elastography at low frequencies. *Physics in Medicine and Biology*, *64*(7), 075006. https://doi.org/10.1088/1361-6560/ab0a7d

Murphy, M. C., Huston, J., Jack, C. R., Glaser, K. J., Senjem, M. L., Chen, J., Manduca, A., Felmlee, J. P., & Ehman, R. L. (2013). Measuring the Characteristic Topography of Brain Stiffness with

Magnetic Resonance Elastography. *PLoS ONE*, *8*(12), e81668. https://doi.org/10.1371/journal.pone.0081668

Muthupillai, R., Lomas, D. J., Rossman, P. J., Greenleaf, J. F., Manduca, A., & Ehman, R. L. (1995). Magnetic resonance elastography by direct visualization of propagating acoustic strain waves. *Science (New York, N.Y.)*, *269*(5232), 1854–1857. https://doi.org/10.1126/science.7569924

Perriñez, P. R., Kennedy, F. E., Van Houten, E. E. W., Weaver, J. B., & Paulsen, K. D. (2010). Magnetic resonance poroelastography: an algorithm for estimating the mechanical properties of fluid-saturated soft tissues. *IEEE Transactions on Medical Imaging*, *29*(3), 746–755. https://doi.org/10.1109/TMI.2009.2035309

Reese, T. G., Feinberg, D. A., Dou, J., & Wedeen, V. J. (2002). Phase contrast MRI of myocardial 3D strain by encoding contiguous slices in a single shot. *Magnetic Resonance in Medicine*, *47*(4), 665–676. https://doi.org/10.1002/mrm.10111

Rouvière, O., Yin, M., Dresner, M. A., Rossman, P. J., Burgart, L. J., Fidler, J. L., & Ehman, R. L. (2006). MR elastography of the liver: preliminary results. *Radiology*, *240*(2), 440–448. https://doi.org/10.1148/radiol.2402050606

Schwarb, H., Johnson, C. L., McGarry, M. D. J., & Cohen, N. J. (2016). Medial temporal lobe viscoelasticity and relational memory performance. *NeuroImage*, *132*, 534–541. https://doi.org/10.1016/j.neuroimage.2016.02.059

Sloots, J. J., Biessels, G. J., de Luca, A., & Zwanenburg, J. J. M. (2021). Strain Tensor Imaging: Cardiac-induced brain tissue deformation in humans quantified with high-field MRI. *NeuroImage*, *236*, 118078. https://doi.org/10.1016/j.neuroimage.2021.118078

Sloots, J. J., Biessels, G. J., & Zwanenburg, J. J. M. (2020). Cardiac and respiration-induced brain deformations in humans quantified with high-field MRI. *NeuroImage*, *210*, 116581. https://doi.org/10.1016/j.neuroimage.2020.116581

Soellinger, M., Rutz, A. K., Kozerke, S., & Boesiger, P. (2009). 3D cine displacement-encoded MRI of pulsatile brain motion. *Magnetic Resonance in Medicine*, *61*(1), 153–162. https://doi.org/10.1002/mrm.21802

Sowinski, D. R., McGarry, M. D. J., Van Houten, E. E. W., Gordon-Wylie, S., Weaver, J. B., & Paulsen, K. D. (2021). Poroelasticity as a Model of Soft Tissue Structure: Hydraulic Permeability Reconstruction for Magnetic Resonance Elastography in Silico. *Frontiers in Physics*, *8*. https://doi.org/10.3389/fphy.2020.617582

Svensson, S. F., De Arcos, J., Darwish, O. I., Fraser-Green, J., Storås, T. H., Holm, S., Vik-Mo, E. O., Sinkus, R., & Emblem, K. E. (2021). Robustness of MR Elastography in the Healthy Brain: Repeatability, Reliability, and Effect of Different Reconstruction Methods. *Journal of Magnetic Resonance Imaging : JMRI*, *53*(5), 1510–1521. https://doi.org/10.1002/jmri.27475

Van Houten, E. E., Miga, M. I., Weaver, J. B., Kennedy, F. E., & Paulsen, K. D. (2001). Three-dimensional subzone-based reconstruction algorithm for MR elastography. *Magnetic Resonance in Medicine*, *45*(5), 827–837. https://doi.org/10.1002/mrm.1111

Van Houten, E. E., Paulsen, K. D., Miga, M. I., Kennedy, F. E., & Weaver, J. B. (1999). An overlapping subzone technique for MR-based elastic property reconstruction. *Magnetic Resonance in Medicine*, *42*(4), 779–786. https://doi.org/10.1002/(sici)1522-2594(199910)42:4<779::aid-mrm21>3.0.co;2-z

Weaver, J. B., Pattison, A. J., McGarry, M. D., Perreard, I. M., Swienckowski, J. G., Eskey, C. J., Lollis, S. S., & Paulsen, K. D. (2012). Brain mechanical property measurement using MRE with intrinsic activation. *Physics in Medicine and Biology*, *57*(22), 7275–7287. https://doi.org/10.1088/0031-9155/57/22/7275

Weickenmeier, J., de Rooij, R., Budday, S., Steinmann, P., Ovaert, T. C., & Kuhl, E. (2016). Brain stiffness increases with myelin content. *Acta Biomaterialia*, *42*, 265–272. https://doi.org/10.1016/j.actbio.2016.07.040

Yin, M., Woollard, J., Wang, X., Torres, V. E., Harris, P. C., Ward, C. J., Glaser, K. J., Manduca, A., & Ehman, R. L. (2007). Quantitative assessment of hepatic fibrosis in an animal model with magnetic resonance elastography. *Magnetic Resonance in Medicine*, *58*(2), 346–353. https://doi.org/10.1002/mrm.21286

Zorgani, A., Souchon, R., Dinh, A.-H., Chapelon, J.-Y., Ménager, J.-M., Lounis, S., Rouvière, O., & Catheline, S. (2015). Brain palpation from physiological vibrations using MRI. *Proceedings of the National Academy of Sciences of the United States of America*, *112*(42), 12917–12921. https://doi.org/10.1073/pnas.1509895112

Supplementary material

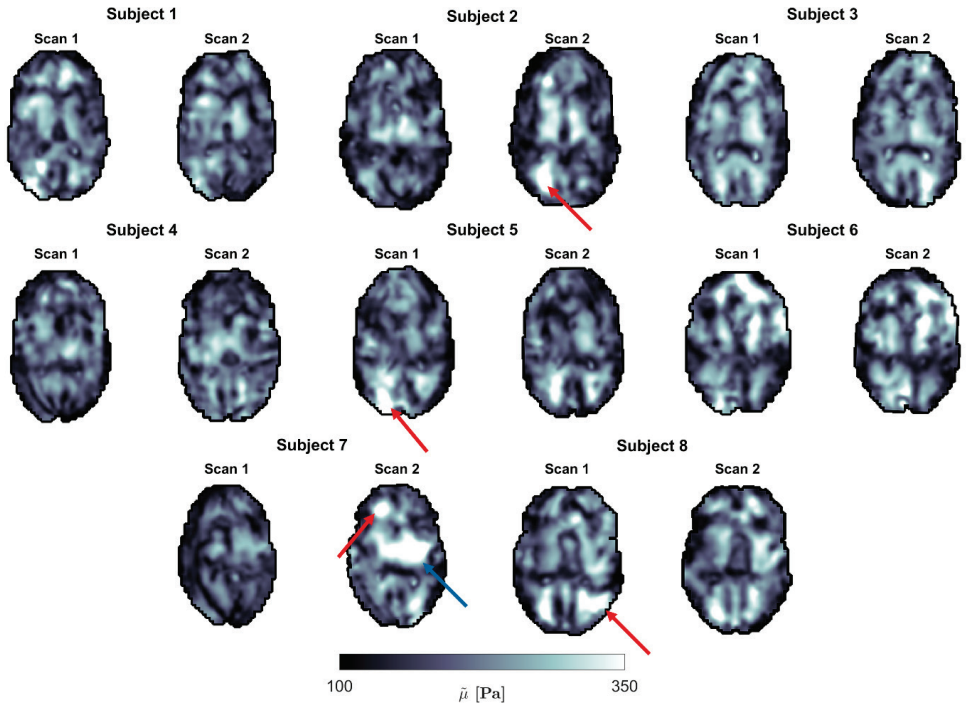


Figure S1: Representative axial slices of the shear stiffness, μ̃, for all subjects alongside the repeated scans which have been rigidly registered to the original scans. Each repeated scan shows considerable structural similarity to the original scan, with the exception of large-valued hotspots that likely arise due to fluid flow (exampled are indicated with red arrow). A more significant hotspot (indicated with blue arrow) can be seen in scan 2 of Subject 7, likely due to subject motion in the scanner.

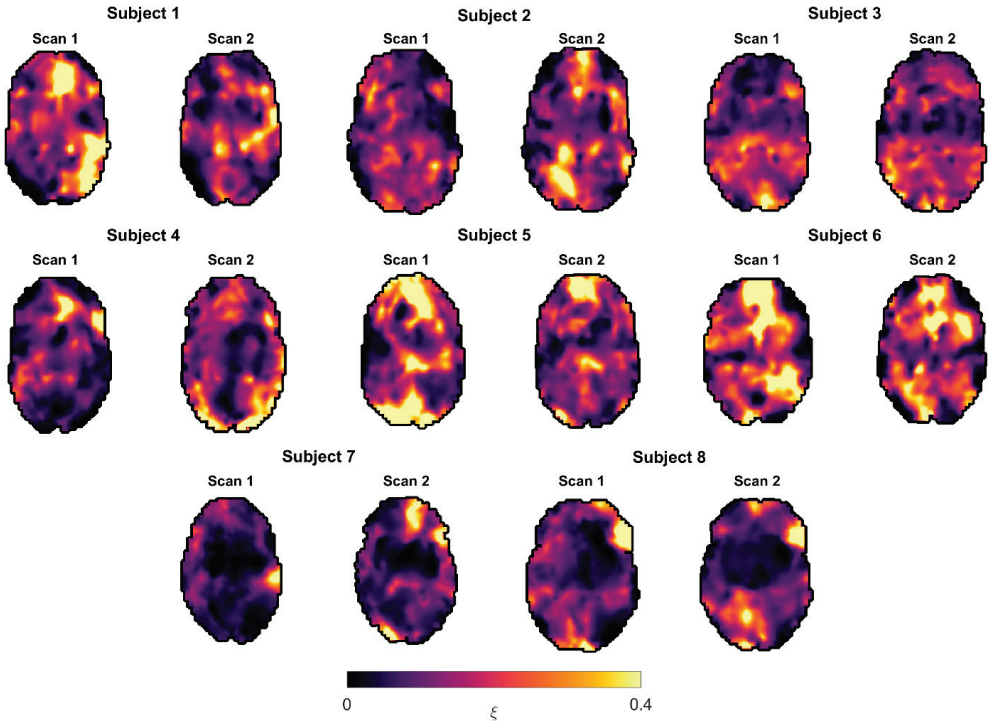


Figure S2: Representative axial slices of the damping ratio, ξ, for all subjects alongside the repeated scans which have been rigidly registered to the original scans.

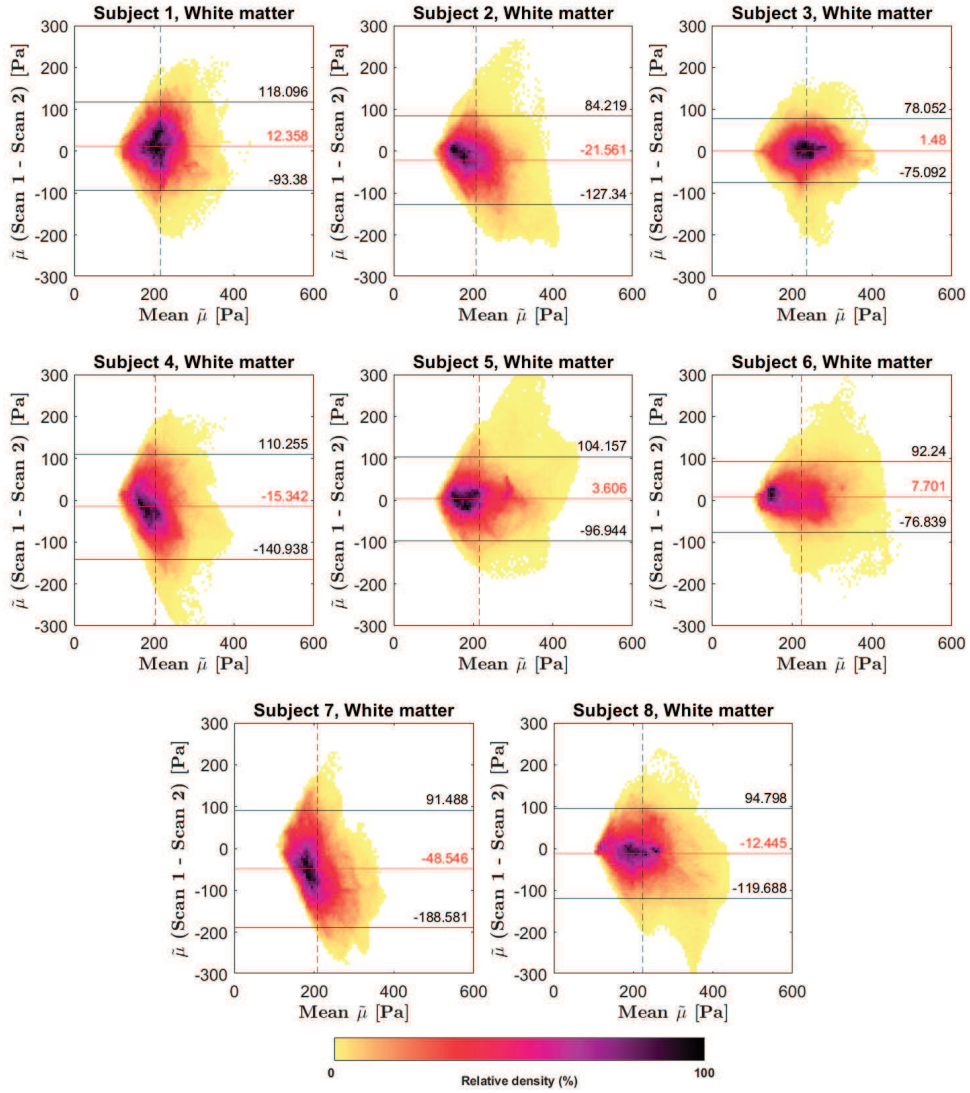


Figure S3: Bland-Altman plots for the WM shear stiffness in all subjects. The horizontal red line represents the bias *b* which is the mean of the voxel-wise differences between the two measurements. The upper and lower horizontal black lines represent the upper and lower limits of agreement respectively, defined as b ± 1.96·std. The vertical dashed line indicates the mean over all voxels for the two measurements.

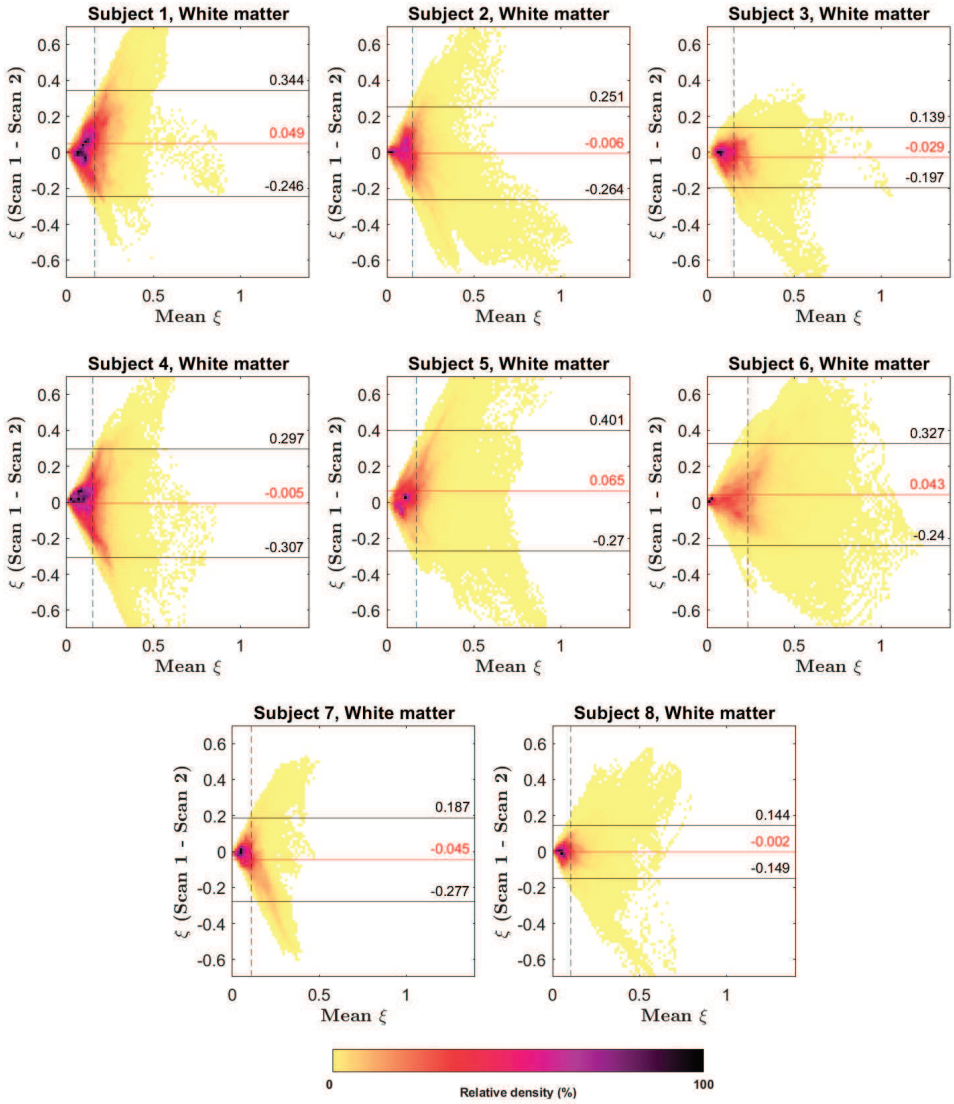


Figure S4: Bland-Altman plots for the WM damping ratio in all subjects. The horizontal red line represents the bias b which is the mean of the voxel-wise differences between the two measurements. The upper and lower horizontal black lines represent the upper and lower limits of agreement respectively, defined as b ± 1.96·std. The vertical dashed line indicates the mean over all voxels for the two measurements.

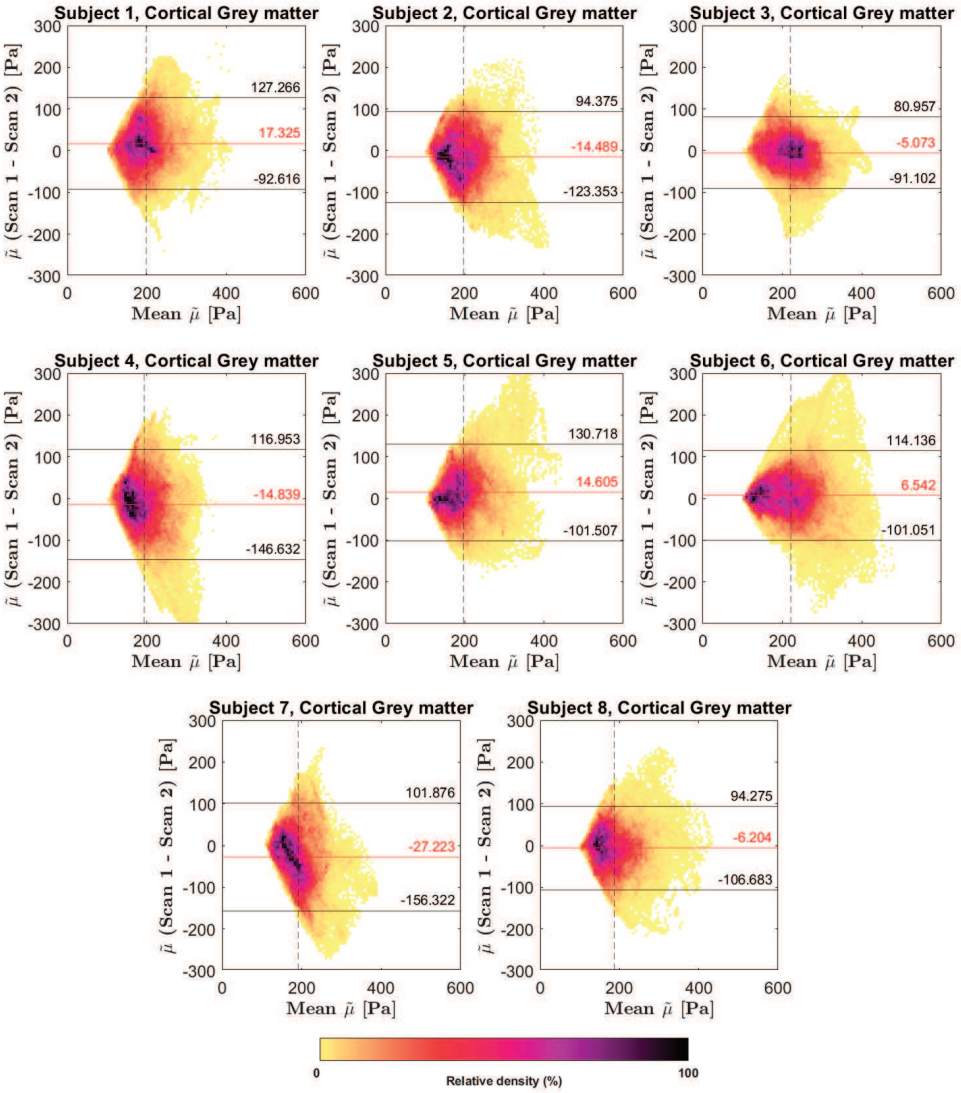


Figure S5: Bland-Altman plots for the cortical GM shear stiffness in all subjects. The horizontal red line represents the bias b which is the mean of the voxel-wise differences between the two measurements. The upper and lower horizontal black lines represent the upper and lower limits of agreement respectively, defined as b ± 1.96·std. The vertical dashed line indicates the mean over all voxels for the two measurements.

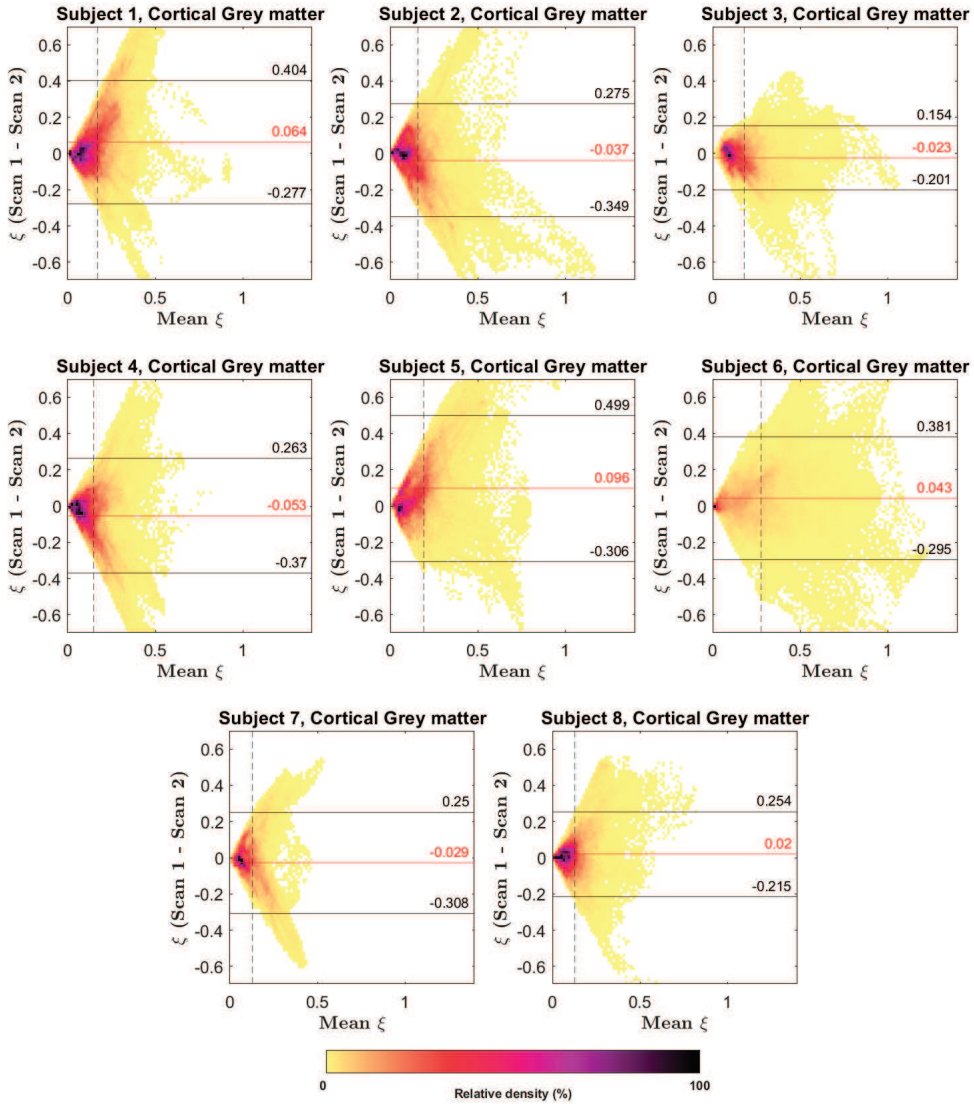


Figure S6: Bland-Altman plots for the cortical GM damping ratio in all subjects. The horizontal red line represents the bias b which is the mean of the voxel-wise differences between the two measurements. The upper and lower horizontal black lines represent the upper and lower limits of agreement respectively, defined a b ± 1.96·std. The vertical dashed line indicates the mean over all voxels for the two measurements.

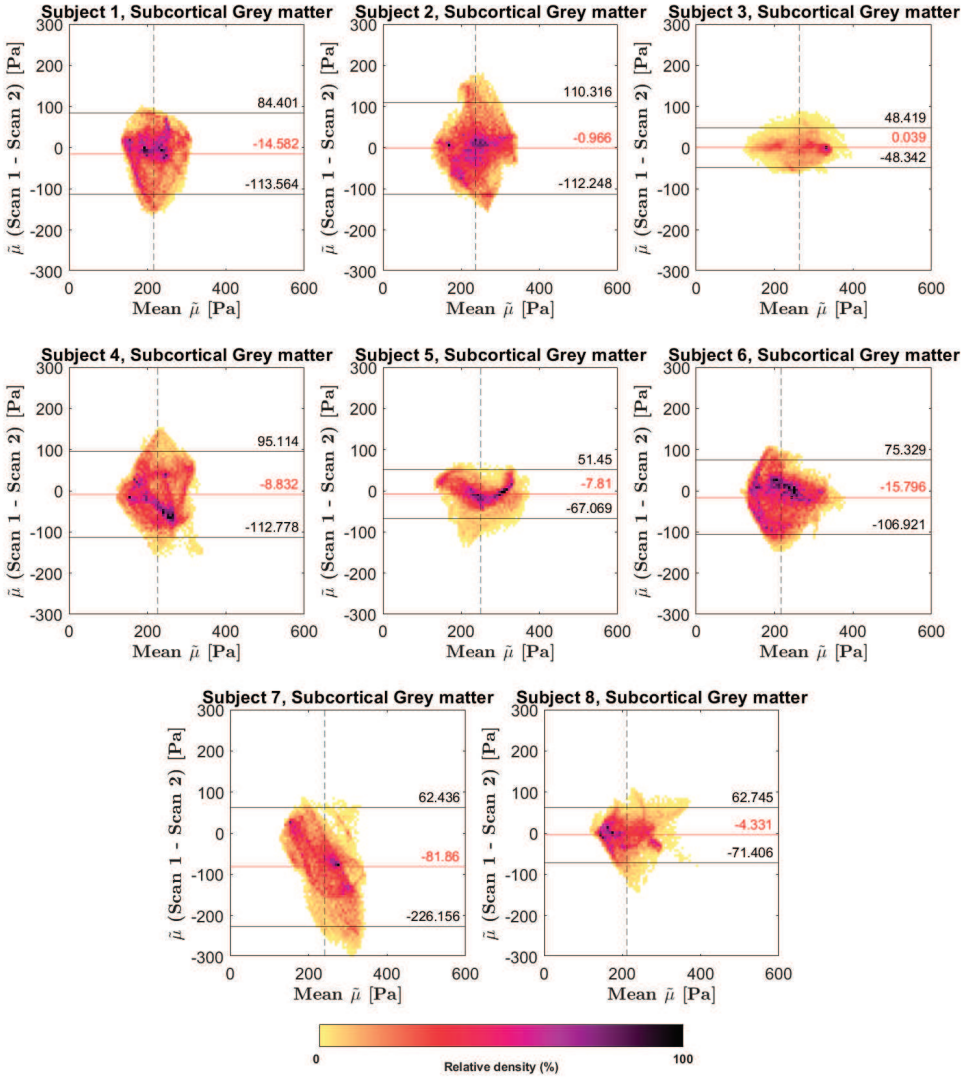


Figure S7: Bland-Altman plots for the subcortical GM shear stiffness in all subjects. The horizontal red line represents the bias b which is the mean of the voxel-wise differences between the two measurements. The upper and lower horizontal black lines represent the upper and lower limits of agreement respectively, defined as b ± 1.96·std. The vertical dashed line indicates the mean over all voxels for the two measurements.

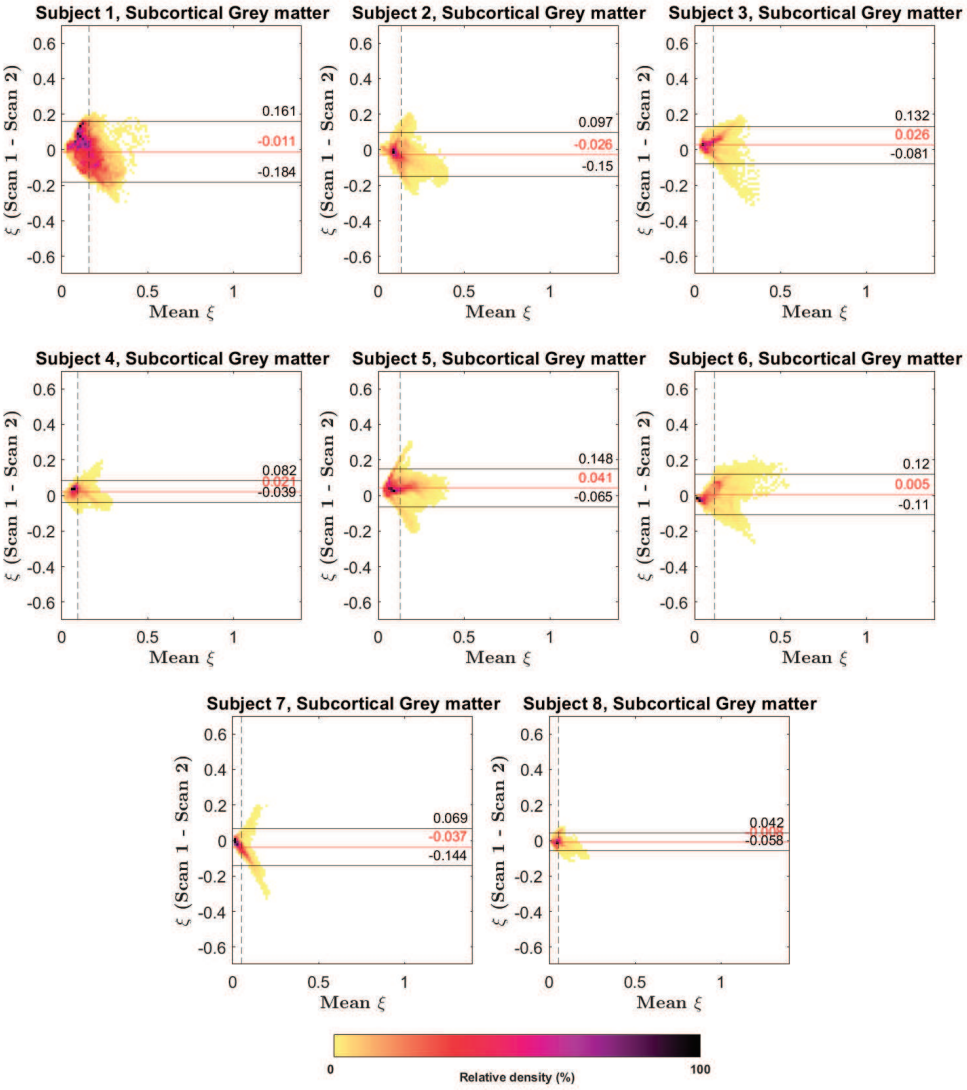


Figure S8: Bland-Altman plots for the subcortical GM damping ratio in all subjects. The horizontal red line represents the bias b which is the mean of the voxel-wise differences between the two measurements. The upper and lower horizontal black lines represent the upper and lower limits of agreement respectively, defined as b ± 1.96·std. The vertical dashed line indicates the mean over all voxels for the two measurements.



Chapter 3

Evaluating the performance and repeatability of poroelastic and poroviscoelastic models in intrinsic MR elastography

Marius Burman Ingeberg[1], Elijah Van Houten[2], Jaco J.M Zwanenburg[1]

[1]Translational Neuroimaging Group, Center for Image Sciences, University Medical Center Utrecht and Utrecht University, Utrecht, The Netherlands

[2]Université de Strasbourg, CNRS, INSERM, ICube, UMR7357, Strasbourg, France.

Original work published in NMR in Biomedicine:

Burman Ingeberg M, Van Houten E, Zwanenburg JJM. Evaluating the Performance and Repeatability of Poroelastic and Poroviscoelastic Models in Intrinsic MR Elastography. NMR Biomed. 2025 Jul;38(7):e70073. doi: 10.1002/nbm.70073. PMID: 40474828; PMCID: PMC12142453.

Author Contribution Statement:

Marius Burman Ingeberg was responsible for conceptualization, methodology, software development, investigation, formal analysis, data management, and visualization, and wrote the original draft of the manuscript. Eli van Houten contributed to conceptualization, provided supervision and resources, and reviewed and edited the manuscript. Jaco Zwanenburg contributed to conceptualization, secured funding, provided resources and supervision, and reviewed and edited the manuscript.

Abstract

Introduction

Intrinsic MR elastography (iMRE) leverages brain pulsations that arise from cerebral arterial pulsations to reconstruct mechanical properties of the brain. While iMRE has shown much potential recently, the technique was demonstrated for a viscoelastic brain model only, which suffered from data-model mismatch at the low actuation frequencies of the arterial pulsations. This work aims to address those limitations by considering the porous nature of brain tissue, where both a poroelastic and a poroviscoelastic model are assessed and compared. As a secondary goal, the influence of two driving frequencies on the material properties is investigated by looking at the 1 Hz and 2 Hz components of the motion data.

Method

The poro- and poroviscous properties of the brain were reconstructed using a subzone-based non-linear inversion scheme, using displacement measurements of 8 healthy subjects from a previous study at 7T MRI. The performance of each model was evaluated by assessing consistency of spatial distributions, repeatability through repeated scans, and left-right symmetry.

Results

The poroelastic model yielded mean storage moduli of 6.08 ± 0.87 Pa and 32.01 ± 11.92 Pa, and the poroviscoelastic model yielded 5.32 ± 0.87 Pa and 26.15 ± 8.02 Pa for the 1 Hz and 2 Hz motion components, respectively. Among the mechanical properties of interest, the storage modulus was the most consistent, with low limits of agreements of (upper/lower) 15.0% / -22.2% for the poroelastic model and 10.9% / -18.5% for the poroviscoelastic model, relative to the whole-brain mean. It was also highly symmetric, with a mean whole-brain symmetry ratio of 0.99 across subjects for both models. Mechanical properties related to fluid flow demonstrated less consistency. The 2 Hz motion component was found to contain considerable information as it reflected the frequency-related stiffening associated with porous media, highlighting its relevance for use in multifrequency mechanical characterization.

Conclusion

Both models demonstrated good performance, with the poroviscoelastic model in general showing the highest consistency in terms of test-retest repeatability. Future work aims to improve the models by addressing current assumptions on the boundary conditions of the pressure field.

1 Introduction

Magnetic Resonance Elastography (MRE) is an advanced imaging technique that enables non-invasive *in vivo* measurements of tissue mechanical properties, providing insight into how different pathologies affect tissue microstructure (Glaser et al., 2012; Hiscox et al., 2016; Rouvière et al., 2006; Yin et al., 2007). While it can in principle be applied to any tissue, there has recently been much interest in its potential for assessing brain pathology such as tumors (Bunevicius et al., 2020), neurodegenerative diseases (Feng et al., 2024), and small vessel disease (Farhat et al., 2019). Furthermore, it may also provide insight into the relationship between brain structure and function (Barnes et al., 2017a; Forouhandehpour et al., 2021; Goriely et al., 2015b; Lan et al., 2020; Schwarb et al., 2016), all while the brain is its natural environment. The standard approach uses mechanical actuators, typically pneumatic pillows positioned beneath the subject's head, to generate steady-state mechanical waves within the region of interest. These waves induce displacement fields that can be captured using phase-contrast imaging techniques, which are subsequently processed using various inversion algorithms to reconstruct the tissue's mechanical properties (Meyer et al., 2024).

Recent work has demonstrated the feasibility of a technique called intrinsic MRE (iMRE), which eliminates the need for external actuation by leveraging the naturally occurring cerebral vascular pulsations driven by the cardiac pulse (Burman Ingeberg et al., 2023; Solamen et al., 2021; Weaver et al., 2012; Zorgani et al., 2015). iMRE is particularly advantageous for a few reasons: it eliminates the requirement for external actuators, thereby simplifying the acquisition process and significantly enhancing the method's accessibility; it addresses the challenge of poor shear wave penetration through the skull (Weaver et al., 2012); and it provides insights into the brain's mechanical properties in its natural state, rather than in a state of externally generated vibration. However, despite the demonstrated feasibility of the method, a number of challenges were also highlighted, such as the occurrence of artifacts due to fluid motion present within the brain volume, the recovery of non-unique solutions when using a viscoelastic model at low actuation frequencies, and data-model mismatch. On the other hand, the adoption of a poroelastic model, which models the brain as a porous elastic matrix which is saturated by a viscous pore fluid, has been shown to mitigate many of these issues (McGarry et al., 2019, 2015; Sowinski et al., 2021). Specifically, a poroelastic model can facilitate the recovery of unique solutions and provide a more accurate representation of the brain's behavior at low actuation frequencies. Moreover, poroelastic reconstruction enables the estimation of the fluid permeability, an additional parameter that most likely reflects microvascular and/or interstitial fluid properties. This could be highly relevant for understanding cerebrovascular diseases and the impact of vascular dysfunction in neurodegenerative dis-

orders, highlighting another potential advantage of iMRE as the suitability of poroelastic models is less evident at higher actuation frequencies (McGarry et al., 2019, 2015).

While the advantages of employing a poroelastic model at low actuation frequencies has been previously shown (McGarry et al., 2019, 2015), thorough analysis of the performance of such a model has not been conducted. Furthermore, a poroelastic model can be extended to a poroviscoelastic model which additionally accounts for the viscous properties of the tissue at the cost of additional model complexity. It is currently unknown which model is best suited to recover accurate representations of the underlying tissue properties. The aim of this work is thus to investigate the performance and reliability of employing poroelastic and poroviscoelastic models using iMRE, and to directly compare results between the two models. This is assessed by investigating regional variation, repeatability (by the means of repeated scans) and right-left symmetry over different regions of interest. As a secondary goal, we investigate how the material properties are influenced by the driving frequencies by looking at the 1 Hz and 2 Hz components of the motion data in the frequency domain, for both models. This analysis serves several purposes: first, to evaluate the impact of different low-frequency driving conditions on material properties; and second, to examine how noisier data (given the lower signal to noise ratio within the 2 Hz cardiac component) affects the quality of mechanical property reconstruction. This enables us to test the robustness of the models under varying noise levels and frequency ranges, ultimately helping to determine the feasibility of incorporating higher-frequency components in multifrequency reconstructions within iMRE.

2 Method

2.1 Displacement data

This following analysis was conducted on pre-existing displacement data, acquired by Adams *et al.* (Adams et al., 2020). We only briefly summarize the method of acquisition here, as a detailed description can be found in the original publication. All subjects gave written-informed consent for participation in the study, which was approved by the ethical review board of our institution.

Eight healthy young adults (three females; mean age: 27 ± 6 years) underwent imaging using a Displacement Encoding with Stimulated Echoes (DENSE) sequence on a 7T MR scanner (Philips Healthcare) using a 3D EPI readout scheme. Repeated scans were performed with subjects briefly exiting the scanner for up to 10 minutes between sessions. Retrospective gating was used to synchronize DENSE measurements with the cardiac cycle, detected via pulse oximetry. The acquired spatial resolution was 1.95 mm × 1.95 mm × 2.2 mm (AP, RL, FH), with 20 temporal phases reconstructed per cardiac cycle. Three

separate acquisitions were performed with displacement encoding (DENC) sensitivities of 0.175 mm, 0.175 mm, and 0.35 mm in the anterior-posterior (AP), right-left (RL), and foot-head (FH) directions, respectively. The acquisition time per motion encoding direction was 144 heartbeats (which correspond to 2:24 minutes for an average heart rate of 60 beats per minute). Additionally, T1-weighted images with a resolution of 0.93 mm × 0.93 mm × 1.0 mm were acquired during both scanning sessions for segmentation and registration purposes. The Computational Anatomy Toolbox (Jena University Hospital, Departments of Psychiatry and Neurology) extension for SPM12 (Wellcome Trust Centre for Neuroimaging, University College London) was used to generate tissue probability maps from the T1-weighted images. To account for subject motion between the three DENSE acquisitions, AP and FH magnitude images were rigidly registered to the RL magnitude images. The final RL image of the cardiac cycle was then non-linearly registered to a T1-weighted image for all subjects, as those images showed minimal artifacts and had the most optimal gray and white matter contrast. All images were then transformed to the T1-weighted image using the registration parameters given by the transformation from the RL magnitude image to the T1-weighted image.

The SNR of the displacement data was assessed as described by Adams et al. (2020), and was used to identify voxels with motion artifacts. The number of voxels with motion artifacts was used as a metric to evaluate the quality of each data set. One repeated scan of Subject 7 was omitted due to containing more than twice as many voxels with motion artifacts in the displacement measurements as compared to the mean of all other scans.

2.2 Preparation of displacement data

The displacement data were transformed into frequency space by applying the Fast Fourier Transform (FFT) to the temporal phases for each voxel. The motion at the first two harmonic frequencies, which roughly correspond to 1 Hz and 2 Hz, were selected for further analysis. While there were some variations in the exact frequency across subjects due to varying heart rates, we use the names “1 Hz” and “2 Hz” for simplicity and clarity throughout the analysis. Figure 1 presents axial slices of the displacement amplitude fields for each motion encoding direction and frequency component along with the mean displacement amplitude for the first five frequency components. To address fluid motion artifacts from cerebrospinal fluid (CSF) and larger blood vessels, a fluid motion mask was generated for each subject, as reported in our previous iMRE study (Burman Ingeberg et al., 2023). These masks were constructed by combining CSF masks derived from tissue probability maps - where regions with less than 95% probability of being gray or white matter were classified as CSF - and masks taking extreme displacements likely due to fluid motion. The threshold for extreme displacements was set at five times the standard deviation of the displacement distribution within the brain, determined em-

pirically through trial runs across multiple subjects. To ensure minimal contribution from fluid motion in the displacement data, these masks were further dilated by one voxel.

Because mechanical property reconstruction relies on finite element meshes, gaps in the displacement data caused by fluid motion masking create large holes in the meshes, leading to significant issues. To address this, the gaps were interpolated using a publicly available MATLAB extension (John D'Errico, 2024) to ensure that displacements in these regions were continuous and differentiable. Following reconstruction, the fluid motion masks were reapplied to exclude all voxels where interpolated displacements were used, ensuring that the final parameter maps contained only values derived from actual measurements.

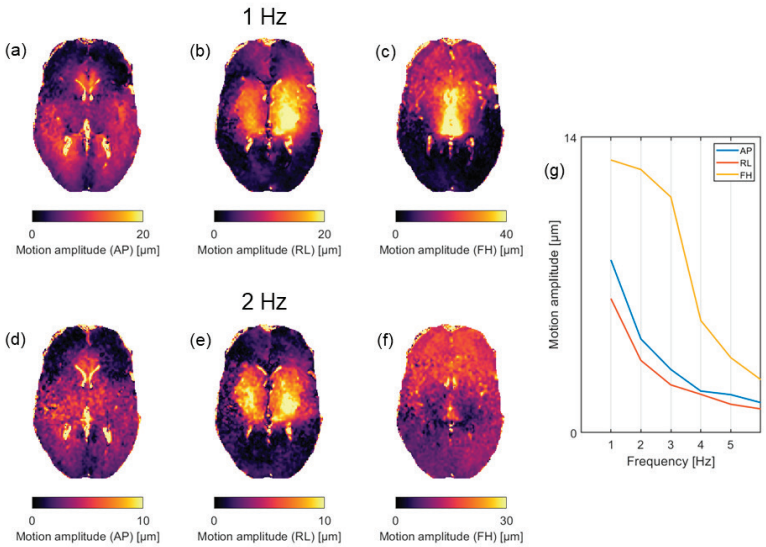


Figure 1: Representative axial slices of motion amplitude fields for each motion encoding direction at 1 Hz (a-c) and 2 Hz (d-f) for a single subject. The mean motion amplitude across motion encoding directions is shown in (g) for the first five frequencies.

2.3 Mechanical property estimation

Tetrahedral finite element models of each subject's brain were created from the corresponding displacement maps. The meshes were constructed to have an average edge length of approximately 2 mm. These finite element models were then utilized in a subzone-based nonlinear inversion scheme (McGarry et al., 2012; Van Houten et al., 2001) to estimate mechanical properties, using two brain models: a poroelastic model and a poroviscoelastic model. In a poroelastic model, the brain is modeled as a biphasic material consisting of a porous elastic matrix which is saturated by a viscous pore fluid. The mathematical details of such models have been extensively described in previous

work (McGarry et al., 2019; Perriñez et al., 2010; Sowinski et al., 2021; Tan et al., 2017), and only the main features will be highlighted here. The equation of motion in the frequency domain is given by

$$\begin{aligned} \nabla \cdot \mu \nabla u + \nabla(\lambda + \mu)(\nabla \cdot u) - (1 - \beta)\nabla P &= -(\rho - \beta\rho_f)\omega^2 u \\ \rho_f \omega^2 \nabla \cdot \left((1 - \beta)u\right) + \nabla \cdot \left(\beta \nabla P\right) &= 0 \\ \beta = \frac{\omega\phi^2\rho_f\kappa}{\omega\kappa(\rho_a + \phi\rho_f) + i\phi^2}, & \end{aligned} \quad (1)$$

where ***u*** is the 3D complex-valued motion amplitude, *G′* and v_p are the storage modulus and Poisson ratio of the drained porous solid, κ is the fluid permeability, *P* is the pore fluid pressure, ρ_f is the pore fluid density, ρ_a is the apparent mass density, and φ is the relative porosity. Lamé's first constant (here referred to as the lambda modulus) is defined by

$$\lambda = \frac{2G'\nu_p}{1-2\nu_p},$$

and describes the compressive resistance of the drained porous solid. While the model assumes the individual material constituents (i.e. the solid and fluid components) to be incompressible, the mechanical properties of the drained solid matrix must be compressible to allow for fluid motion in response to volumetric strain (Perriñez et al., 2010). Thus, instead of setting λ to a large value to model incompressibility, as is typically done in viscoelastic elastography, it becomes a property of interest as it describes the resistance of the tissue matrix to volumetric changes in the absence of vascular and/or extracellular fluids.

The formulation shown in Eq. (1) is based on several assumptions, including time-harmonic displacements, the absence of fluid sources, and the incompressibility of the constituent solid and fluid components. The poroviscoelastic model is identical to the abovementioned formulation, with the exception that the storage modulus is replaced by the complex valued shear modulus $G^* = G' + iG''$, where the real part is the storage modulus and the imaginary part is the loss modulus, representing the viscosity of the drained solid matrix. Using a poroelastic model, three properties of interest are recovered: The storage modulus *G′*, Lamé's first constant λ, and the fluid permeability κ. The poroviscoelastic model recovers the same properties, with the addition of the loss modulus *G′*, which can be used to calculate the damping ratio, $\xi = G''/2G'$.

Poroelastic and poroviscoelastic property maps were reconstructed for the 1 Hz and 2 Hz displacement components for all subjects and repeated scans. A total of 600 global iterations were allowed for each subject, and a subzone size of 20 mm^3 with 15% overlap between zones was used.

2.4 Regional analysis

Differences in regional variation in the property maps between models and driving frequencies were assessed by performing a regional analysis. To enable direct comparison with existing literature, we analyzed the same regions as those used in the publicly available atlas (in standard-space) of viscoelastic properties obtained with extrinsic actuation (Hiscox et al., 2020), as well those investigated in previously with iMRE using a viscoelastic brain model (Burman Ingeberg et al., 2023). A total of 30 regions were investigated, categorized as cortical gray matter (CGM), subcortical gray matter (SGM), and white matter tracts (WMT). The CGM and SGM regions were identified using the MNI-ICBM2009c nonlinear symmetric 1mm atlas (Manera et al., 2020) while the WMT regions were identified using the JHU-ICBM-tracts and JHU-ICBM-labels 1 mm atlases (Mori et al., 2008; Mori S et al., 2006). Each region mask was individually eroded by 1 voxel to minimize partial volume effects. Regions with less than 500 voxels after erosion were removed from the analysis. All included regions are presented in Table 1 with the corresponding major region categorization, abbreviation and region size.

To determine the regional values of each property, all property maps were registered to MNI space using the MNI-ICBM2009c non-linear average template. To achieve this, the T1-weighted images (which are in the same space as the property maps) of each subject were non-linearly registered to the MNI template for two levels of resolutions with 250 iterations per resolution. This was done following an initial alignment using rigid registration for 100 iterations for 4 levels of resolution and affine registration for 100 iterations for two levels of resolution. The corresponding transformations were then applied to all property maps using nearest neighbor interpolation. The JHU-ICBM atlases were additionally interpolated (nearest neighbor) to the resolution of the MNI-ICBM2009c template to assure equivalent resolution of all atlases. Repeated measurements were averaged for all properties.

Table 1: Regions of interests with their corresponding major region categorization, abbreviation and region size in number of voxels.

Major region	Minor region	Abbreviation	Region size
CGM	Cuneus	CN	2769
	Fusiform gyrus	FSG	5731
	Inferior temporal cortex	ITC	6444
	Lateral occipital cortex	LaO	10660
	Lingual occipital cortex	LiO	5497
	Precuneus	PCN	9513
	Postcentral cortex	POST	2545
	Superior frontal cortex	SFC	24885
	Superior parietal cortex	SPC	3298

Table 1: Regions of interests with their corresponding major region categorization, abbreviation and region size in number of voxels. (*continued*)

Major region	Minor region	Abbreviation	Region size
	Superior temporal cortex	STC	9251
	Rostral middle frontal cortex	RMF	9037
	Precentral cortex	PRE	5682
SGM	Amygdala	AM	858
	Caudate	CA	3533
	Hippocampus	HC	2446
	Pallidum	PA	1067
	Putamen	PU	6240
	Thalamus	TH	10112
WMT	Forceps major	FMa	1283
	Forceps minor	FMi	10048
	Corpus callosum	CC	16116
	Anterior thalamic radiation	ATR	6119
	Corticospinal tract	CST	2853
	Inferior frontal occipital fasciculus	IFOF	1656
	Inferior longitudinal fasciculus	ILF	1678
	Superior longitudinal fasciculus	SLF	3605
	Posterior thalamic radiation	PTR	19957
	Corona radiata	CRa	5731

2.4 Repeatability analysis

The repeatability of the poroelastic and poroviscoelastic brain models was assessed for the 1 Hz and 2 Hz displacement components across all subjects by performing a subject-wise Bland-Altman analysis on the mean whole-brain material properties. Considering the dependence of material properties on actuation frequency (Herthum et al., 2021), the reported limits of agreement (LoA) were normalized to the mean global value to facilitate comparison with literature.

2.6 Influence of fluid permeability

The influence of varying levels of fluid permeability on the storage modulus was investigated for one subject. This investigation was conducted for the purely poroelastic model and the 1 Hz motion component. The estimation of mechanical properties followed the procedure outlined in Section 2.3, with the exception that fluid permeability was set to a fixed, homogeneous value across the brain. The permeability values investigated ranged from $\kappa = 10^{-8}$ $m^3 s\ kg^{-1}$ to $\kappa = 10^{-3}$ $m^3 s\ kg^{-1}$, evaluated at each order of magnitude.

3 Results

2.5 Symmetry analysis

The left-right symmetry of the material property maps was investigated for the poroelastic and poroviscoelastic models for the 1 Hz and 2 Hz displacement components. This was done by computing the symmetry ratio *s*, that we define as

$$s = \frac{p_{mean,right}}{p_{mean,left}},$$

where $p_{mean,right}$ is the mean property value in the right hemisphere and $p_{mean,left}$ is the mean property value of the left hemisphere. The material properties were averaged across repeated scans. The symmetry ratio was computed across all major brain regions and material properties.

3.1 Representative parameter maps

The poroelastic and poroviscoelastic property maps were successfully reconstructed for all subjects, for both the 1 Hz and 2 Hz motion components. The tetrahedral finite element meshes consisted of (mean ± std) 156220 ± 8276 nodes. All property maps reached convergence, as expressed by a low total change in property values between the final iterations of the non-linear inversion, which was less than 0.02% for all scans. Figure 2 displays representative axial slices for one subject of all property maps for both the poroelastic and poroviscoelastic models. The repeated scans are additionally placed alongside the original scans, where they have been co-registered to the original scan using non-linear registration of their respective T1-weighted images. Similarity in spatial patterns can be seen between both repeated scans and material models across all properties. The largest differences between the models were observed in the fluid permeability maps, where the viscous attenuation in the poroviscoelastic model, expressed in terms of the damping ratio seemed to be partly represented in the fluid permeability maps of the poroelastic model. No fluid motion-induced artifacts were observed in the parameter maps. The storage modulus maps exhibited good left-right symmetry, while asymmetric low-valued regions were observed in the fluid permeability maps. Figure S1 in the supplementary materials shows the equivalent figure for the 2 Hz motion component property maps.

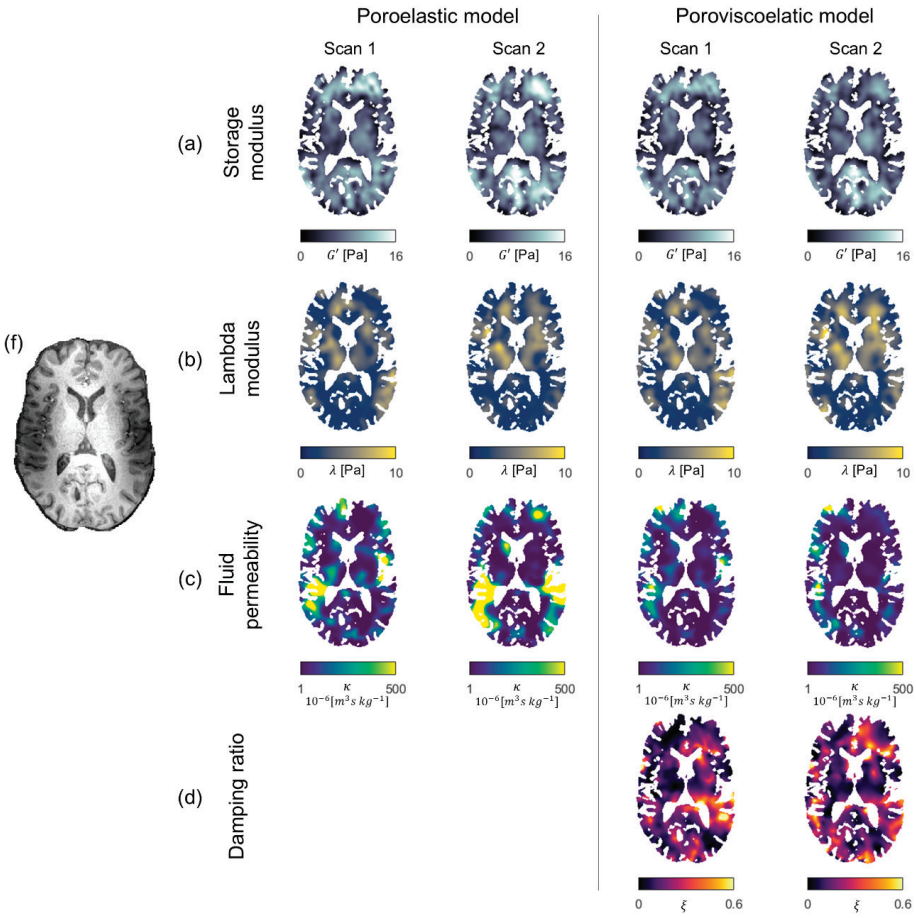


Figure 2: Representative axial slices of the storage modulus (a), lambda modulus (b), fluid permeability (c), and damping ratio (d) obtained from the 1 Hz motion component for one subject along with a repeated scan which has been co-registered to the first scan. The equivalent slice of the T1-weighted image is shown in (f) for anatomical reference. All property maps show consistent spatial patterns across both repeated scans and material models.

3.2 Group-wise mean maps

Figure 3 displays axial slices of maps containing the mean over all scans for all material properties of the poroelastic and poroviscoelastic brain models for both the 1 Hz and 2 Hz motion components. The spatial patterns of the storage and lambda modulus were substantially similar across brain models but varied slightly across motion components. Similar spatial patterns were observed in the poroelastic fluid permeability map as in the poroviscoelastic damping ratio map. The fluid permeability generally demonstrated lower values when using the poroviscoelastic model compared to the poroelastic model. The storage modulus maps exhibited excellent left-right symmetry in comparison to the

other maps. The lambda modulus and fluid permeability maps showed less consistent symmetry.

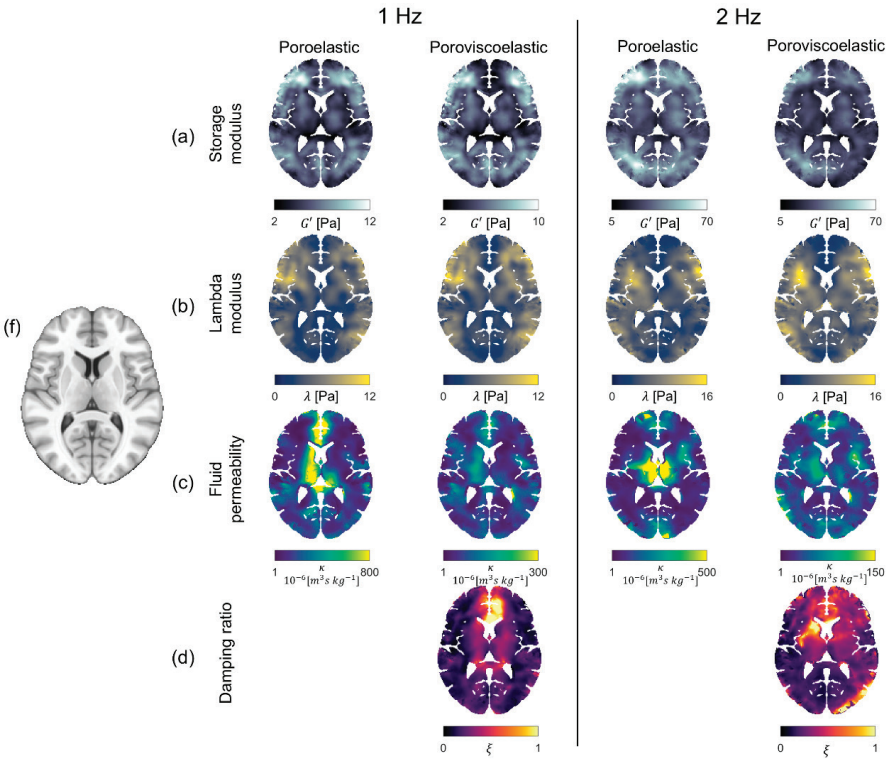


Figure 3: Axial slices of the mean storage modulus (a), lambda modulus (b), fluid permeability (c), and damping ratio (d) across all scans, where each property map has been registered to the MNI-ICBM2009c non-linear average template. The equivalent slice of the T1-weighted template is shown in (f) for anatomical reference. The spatial patterns of the storage and lambda moduli are largely consistent across brain models, with slight variations observed between different motion components. The storage modulus and damping ratio exhibit good left-right symmetry, while the lambda modulus and fluid permeability exhibit poorer symmetry.

3.3 Regional analysis

All regions were successfully identified within the property maps for each scan. Figure 4a presents boxplots illustrating the material property values across major regions for all subjects for the 1 Hz motion component, while Figure 4b shows the corresponding boxplots for the 2 Hz motion component. Table S1 in the supplementary material contains the corresponding mean and standard deviation for each boxplot. Similar regional trends were observed for the majority of the properties for both motion components. The poroviscoelastic model generally yielded lower storage modulus and fluid perme-

ability values compared to the poroelastic model, though it produced slightly higher lambda modulus values. Large differences in storage modulus were observed between the two motion components, with the 2 Hz component demonstrating approximately 5 times higher values for both models. Boxplots displaying the storage modulus values across all minor regions for all subjects are presented in Figure 5 for both motion components. Similar regional trends were observed across both material models and motion components, with the CGM generally being the stiffest region and the SGM the softest. In accordance with what was found for the major regions, the poroviscoelastic model consistently yielded lower storage modulus values for all minor regions. The mean and standard deviation across material properties for all brain regions are presented in Table S2-S4 in supplementary material.

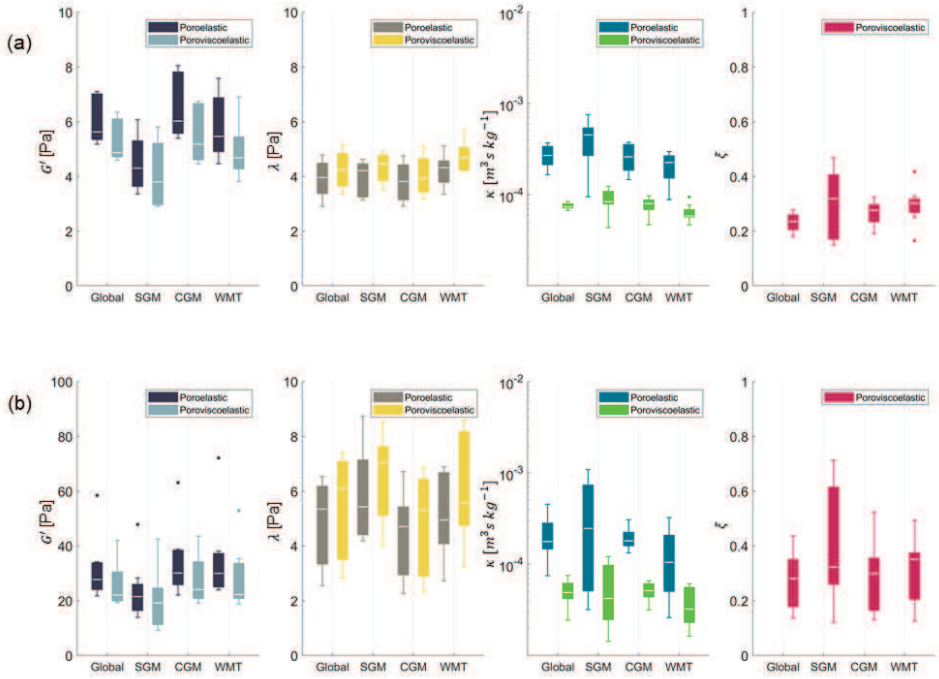


Figure 4: Boxplots illustrating the mean regional material properties across major regions for all subjects for the 1 Hz motion component in (a) and 2 Hz motion component in (b). The white line inside the boxplots represents the median value, while the upper and lower ends of the boxplots correspond to the 25th and 75th quartiles. The whiskers represent the maximum and minimum values which are not outliers (presented as dots and are defined as values that lie more than 1.5·IQR away from the upper or lower quartiles).

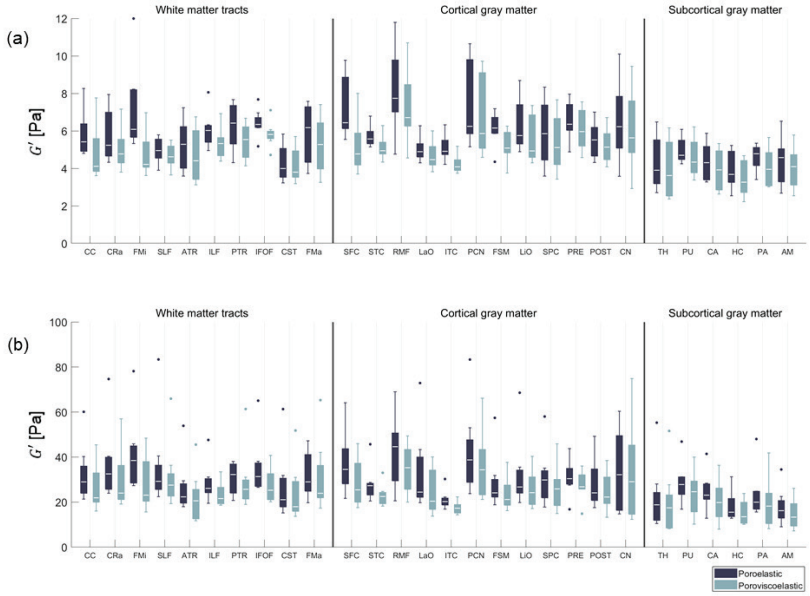


Figure 5: Boxplots illustrating the mean regional storage modulus across minor regions for all subjects for the 1 Hz motion component in (a) and 2 Hz motion component in (b). The white line inside the boxplots represents the median value, while the upper and lower ends of the boxplots correspond to the 25th and 75th quartiles. The whiskers represent the maximum and minimum values which are not outliers (presented as dots and are defined as values that lie more than 1.5·IQR away from the upper or lower quartiles).

3.4 Repeatability analysis

Figure 6 presents subject-wise Bland-Altman plots for the whole-brain mean material properties, spanning both material models and driving frequencies. Black horizontal lines indicate the limits of agreement in each plot. These limits are further detailed in Table 2 for the 1 Hz motion component and Table 3 for the 2 Hz motion component, both expressed relative to the mean whole-brain values. Additionally, the limits of agreements across major regions are also included in both tables.

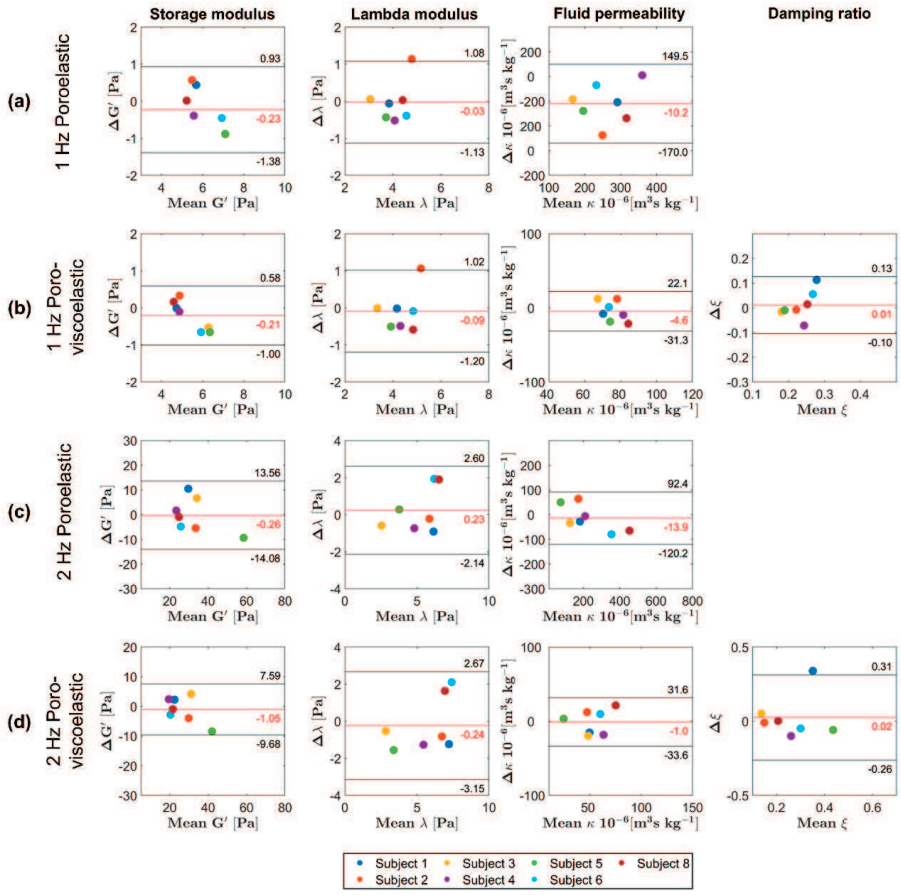


Figure 6: Subject-wise Bland-Altman plots for the whole-brain mean material properties for 1 Hz poroelastic reconstruction (a), 1 Hz poroviscoelastic reconstruction (b), 2 Hz poroelastic reconstruction (c), and 2 Hz poroviscoelastic reconstruction (d). The horizontal red line demonstrates the bias *b* which is the mean of the differences between two repeated measurements, and the upper and lower horizontal black lines illustrate the upper and lower limits of agreement respectively, defined as $b \pm 1.96 \cdot \text{std}$.

Table 2: Table containing the limits of agreement (upper / lower) for all material properties across the major regions for the 1 Hz motion component, expressed relative to the mean whole-brain values.

	Region	***Poroelastic***	***Poroviscoelastic***
Storage modulus	Global	0.151 / -0.225	0.109 / -0.187
	SGM	0.173 / -0.262	0.190 / -0.327
	CGM	0.236 / -0.292	0.157 / -0.209
	WMT	0.138 / -0.200	0.125 / -0.242
Lambda modulus	Global	0.266 / -0.279	0.233 / -0.275
	SGM	0.454 / -0.410	0.313 / -0.293
	CGM	0.277 / -0.285	0.252 / -0.279
	WMT	0.238 / -0.326	0.157 / -0.243
Fluid permeability	Global	0.578 / -0.657	0.292 / -0.415
	SGM	1.612 / -1.545	0.496 / -0.930
	CGM	0.532 / -0.710	0.723 / -0.895
	WMT	0.992 / -0.754	0.204 / -0.181
Damping ratio	Global	N/A	0.541 / -0.447
	SGM	N/A	0.805 / -0.579
	CGM	N/A	0.707 / -0.710
	WMT	N/A	0.821 / -0.473

Table 3: Table containing the limits of agreement (upper / lower) for all material properties across the major regions for the 2 Hz motion component, expressed relative to the mean whole-brain values.

	Region	***Poroelastic***	***Poroviscoelastic***
Storage modulus	Global	0.413 / -0.429	0.284 / -0.362
	SGM	0.690 / -0.785	0.711 / -0.864
	CGM	0.514 / -0.557	0.406 / -0.526
	WMT	0.579 / -0.580	0.496 / -0.723
Lambda modulus	Global	0.508 / -0.417	0.467 / -0.551
	SGM	0.506 / -0.513	0.498 / -0.927
	CGM	0.815 / -0.560	0.653 / -0.574
	WMT	0.493 / -0.387	0.465 / -0.542
Fluid permeability	Global	0.411 / -0.535	0.602 / -0.638
	SGM	1.423 / -1.526	0.631 / -1.086
	CGM	0.956 / -0.812	0.709 / -0.894
	WMT	1.219 / -1.030	0.977 / -0.571
Damping ratio	Global	N/A	1.189 / -1.000
	SGM	N/A	3.371 / -2.376
	CGM	N/A	0.841 / -0.853
	WMT	N/A	1.898 / -1.190

3.5 Symmetry analysis

The symmetry ratio was computed for all material properties and is presented in Figure 7 as boxplots, showing the symmetry ratio distribution across all subjects for different major regions, material models, and motion components. Table S5 and S6 in the supplementary material contain the corresponding mean and standard deviation for each boxplot. Overall, the storage modulus demonstrated good symmetry in both CGM and WMT, with median values near zero and minimal inter-subject variability. In contrast, greater asymmetry was observed in the SGM, with shifted medians and higher inter-subject variability, a trend consistently seen across all other properties. The lambda and loss moduli demonstrated less symmetry than the storage modulus in all regions, and the fluid permeability exhibited the highest asymmetry of all material properties. The storage modulus displayed similar symmetry ratio across models, though the poroviscoelastic model yielded slightly better symmetry for both motion components. For the lambda modulus and fluid permeability, the poroviscoelastic model yielded generally less symmetry for both motion components.

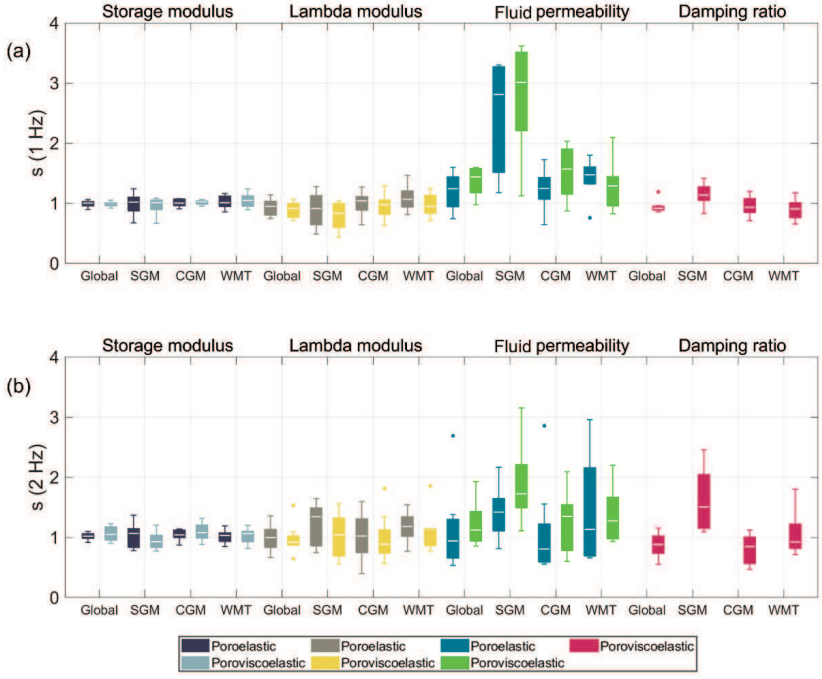


Figure 7: Boxplots displaying the mean regional symmetry ratio distributions across major regions for all subjects for the 1 Hz motion component (top) and 2 Hz motion component (bottom). Higher symmetry ratios correspond to the right-hand side of the brain containing higher values of the material property. The white line inside the boxplots represents the median value, while the upper and lower ends of the boxplots correspond to the 25th and 75th quartiles. The whiskers represent the maximum and minimum values which are not outliers (presented as dots and are defined as values that lie more than 1.5·IQR away from the upper or lower quartiles).

3.6 Influence of fluid permeability

Figure 8a displays representative axial slices of storage modulus maps for varying mean global values of fluid permeability in a single subject. The maps show increasing spatial heterogeneity as the fluid permeability is increased, particularly for $\kappa = 10^{-5}$ $m^3 s\ kg^{-1}$ and $\kappa = 10^{-4}$ $m^3 s\ kg^{-1}$. Figure 8b shows the corresponding global mean storage modulus, where the whiskers represent the standard deviation. The storage modulus demonstrates high sensitivity to varying levels of fluid permeability.

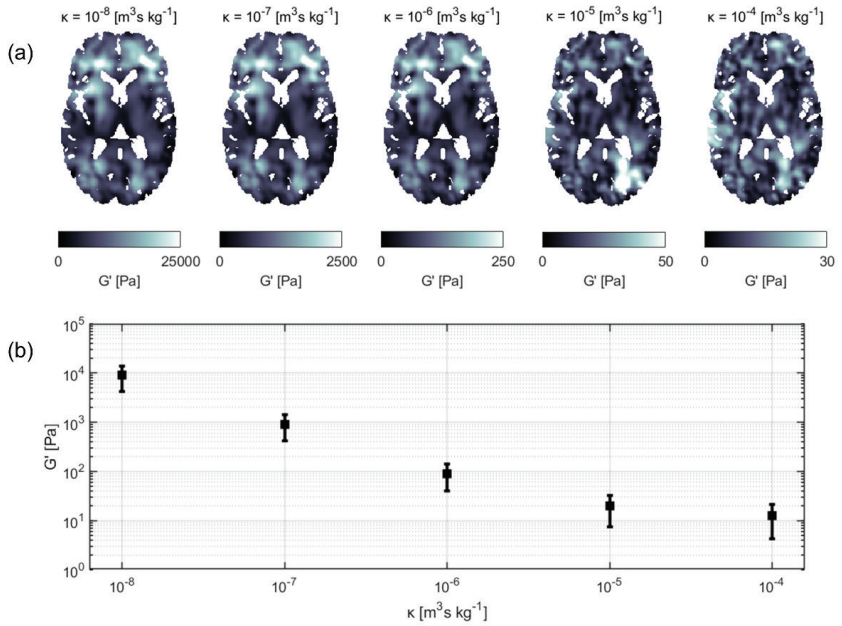


Figure 8: Representative axial slices of storage modulus maps for varying mean global values of fluid permeability in a single subject (a). The corresponding global mean storage modulus are shown in (b), where the whiskers represent the standard deviation.

4 Discussion

This study evaluated the performance and reliability of poroelastic and poroviscoelastic brain models for 7T iMRE with test-retest repeatability analysis, while also assessing how the reconstructed material properties are affected by different driving frequencies and noise levels. The material properties were successfully reconstructed for both brain models and driving frequencies for all subjects. The results demonstrated good consistency in material properties across repeated scan sessions, as evidenced by the relatively low LoA particularly for the storage modulus. Additionally, the storage modulus exhibited good left-right symmetry across models and driving frequencies, while other properties showed greater asymmetry. The poroelastic and poroviscoelastic models produced

generally similar results, with the largest differences observed in fluid permeability. On average, the poroviscoelastic model yielded lower values for the storage modulus and fluid permeability across all regions, while slightly higher values were observed for the lambda modulus. It also demonstrated slightly better repeatability across material properties compared to the poroelastic model, though symmetry was comparable or slightly worse. The material properties derived from the 2 Hz motion component showed higher storage modulus and lower fluid permeability, consistent with the frequency-related stiffening associated with porous media (Herthum et al., 2021). Their spatial distributions were similar to those from the 1 Hz component across both models, albeit at reduced repeatability and symmetry. This suggests that a significant portion of the cardiac signal is still captured in the 2 Hz motion component, which highlights its potential for use in multifrequency reconstruction (Papazoglou et al., 2012).

In contrast to previous attempts at iMRE using a viscoelastic model (Burman Ingeberg et al., 2023), the porous models recover unique solutions with consistent property convergence across all subjects. This is because the elastic forces can be balanced by fluid-solid interaction forces even at low actuation frequencies, a mechanism absent in the viscoelastic model. An interesting consequence is that this may shed some more light on the stiffness of the brain within its natural environment, as brain stiffness is characterized at a physiologically relevant frequency. This contrasts with extrinsic MRE, which typically recovers brain stiffness on the order of kPa (Hiscox et al., 2020; Johnson, McGarry, Van Houten, et al., 2013; Zhang et al., 2011) due to the complex shear modulus increasing strongly with actuation frequency (Herthum et al., 2021). Furthermore, previous studies on poroelastic iMRE fixed a global value for the fluid permeability of $\kappa = 10^{-7}$ m^3 s kg^{-1} rather than performing a voxel-wise reconstruction during the inversion process (McGarry et al., 2019). This approach resulted in higher recovered stiffness values, within the kilopascal range, which scaled with the chosen fluid permeability. A similar relationship was observed between stiffness and the assigned fluid permeability for our data, as highlighted in Figure 8. Instead, by allowing fluid permeability to be determined with the other mechanical properties, we find very low values for the complex shear modulus, with a mean storage modulus of around 5-6 Pa for the whole brain at an estimated fluid permeability in the order of 10^{-4} m^3 s kg^{-1}. Although very low, these values show some similarity with values reported by Herthum et al., who reported ultra-soft stiffness obtained by performing a wavelength analysis in intrinsic activation using steady-state MRE (Herthum et al., 2021). Using viscoelastic model-fitting, they found a shear modulus of 42 ± 13 Pa. While this is higher than what we report, they noted that they may have overestimated their values due to misplacement of the image plane. Furthermore, we reconstructed the complex shear modulus of the drained porous solid rather than the saturated matrix, which could also play a role in the observed differences. In both cases,

the measured stiffness points towards the brain exhibiting ultra-soft properties when unperturbed by external vibrations with relatively high frequencies.

For both porous models, the CGM region exhibited higher storage modulus values than the SGM region. This contrasts with what was found in viscoelastic reconstruction, where the SGM region showed higher stiffnesses. Despite this discrepancy, the relative storage modulus across SGM subregions with respect to each other aligns well with findings from both intrinsic and standard MRE (Burman Ingeberg et al., 2023; Hiscox et al., 2020). The agreement between porous and viscoelastic models is generally less consistent across CGM regions, likely due to differences in how the models interpret the complex geometry of gyri and sulci in the CGM. Thus, while the relative stiffness of subregions within the SGM and CGM shows good agreement with viscoelastic reconstruction, the overall stiffness across the entire SGM and CGM regions differs between porous and viscoelastic models. This suggests that these discrepancies may arise from differences in fluid motion dynamics between tissue types, and how the different material models treat these fluid-solid interactions differently. Using the porous models, the shear modulus is reconstructed for the drained porous solid, while for the viscoelastic model, the storage modulus is reconstructed for the fully saturated matrix. Consequently, some amount of discrepancy between poroelastic and viscoelastic reconstruction is expected.

Given the visual similarity in the spatial patterns of the damping ratio maps in the poroviscoelastic model and the fluid permeability maps in the poroelastic model, it seems that a portion of the effective mechanical attenuation depicted in the fluid permeability maps of the poroelastic model are accounted for by increased damping in the poroviscoelastic model. This effect is clearly expressed in the anterior region of the brain and surrounding the ventricles (Figure 3), where there are high-valued regions along with considerable inter-subject variability, causing artifact-like structures in the mean maps for the poroelastic model. In the poroviscoelastic model, where the damping ratio expresses part of the mechanical attenuation, such artifacts disappear and the inter-subject variability decreases. Subsequently, regions with very high fluid permeability for the poroelastic model instead become apparent in the mean damping ratio maps for the poroviscoelastic model. This is particularly the case surrounding the frontal lobe, where the damping ratio reaches exceedingly high values in the anterior side of the ventricles, and on either side of the hemispheric fissure. This region of high damping ratio is also observed using a viscoelastic model in intrinsic MRE (Burman Ingeberg et al., 2023), and likely arises for two main reasons. First, in and around the corpus callosum, high damping ratio is likely exhibited due to destructive interference between the displacement waves propagating inwards from the right- and left-hand side of the brain. Secondly, as the Falx Cerebri is very stiff in comparison to the surrounding brain tissue, right-left motions in this region rapidly decrease to zero which gets interpreted as a viscous effect during property re-

construction. These effects are much less prominent in the posterior region of the brain, where right-left motion amplitudes are relatively smaller.

The storage modulus demonstrates relatively good repeatability for the poroviscoelastic model, as indicated by relatively low whole-brain LoA (upper / lower): 10.9% / -18.5%, and slightly worse repeatability for the poroelastic model with a whole-brain LoA of 15.7 % / 22.2%, both relative to the mean whole brain storage modulus. In comparison, a recent study on the repeatability of extrinsic MRE using a viscoelastic model reported whole-brain LoA of 9.6% / 6.2% relative to the whole-brain mean for the storage modulus, using a 3T scanner and a 50 Hz actuation frequency in 15 healthy subjects (Svensson et al., 2021). The fluid permeability showed the worst repeatability out of all properties for the poroelastic model but was substantially more repeatable using the poroviscoelastic model. This is likely because in the poroelastic model, the fluid permeability seems to account for the mechanical attenuation effects, whereas in the poroviscoelastic model, these attenuation effects are separated into distinct viscoelastic and poroelastic components, allowing the fluid permeability to primarily reflect fluid motion rather than the combined influence of both fluid movement and tissue viscosity. This separation reduces the complexity and variability of the fluid permeability measurements, improving repeatability. The whole-brain damping ratio using the poroviscoelastic model demonstrates comparatively poor repeatability (LoA: 54.0% / -44.7%), comparable to what was found using a viscoelastic model (LoA: 51.2% / -47.0%) (Burman Ingeberg et al., 2023). This issue arises partly because the damping ratio is derived from two reconstructed parameters, the storage and loss moduli, causing noise to propagate from both sources. In addition, the low wave speed of cerebral arterial pulsations should be considered, which are substantially lower than the mechanical waves applied in standard MRE. Since the loss modulus is linked to the velocity of the propagating wave, extremely low velocities introduce greater uncertainty in the loss modulus measurements, leading to higher inconsistency in the damping ratio. This is a fundamental limitation of iMRE and explains in part the interest in poroelastic material models at these low frequencies (Burman Ingeberg et al., 2023; McGarry et al., 2019; Sowinski et al., 2021; Tan et al., 2017).

The symmetry analysis revealed patterns consistent with those observed in the repeatability analysis. Among the material properties, the storage modulus exhibited the highest level of symmetry, and the fluid permeability showed the least symmetry. This is likely related to differences in the relative timing between the right and left hemispheres when the cardiac-induced arterial pulse enters the brain. Because the heart is situated on the left-hand side of the body, the distance from the aortic arch to the skull base is slightly larger for the right side than for the left (22.2 ± 2.2 cm and 20.8 ± 1.9 cm respectively) (Choudhry et al., 2016), resulting in a delay in the pulse pressure wave in the right hemisphere. Furthermore, there is also a difference in early systolic pulse wave velocity

between the right and left carotid artery of 5.29 m/s and 5.63 m/s respectively (Yin et al., 2021), which further adds to the asymmetry. For this reason, some degree of hemispheric asymmetry may be expected in the fluid-related properties. Still, the pronounced asymmetry observed in the fluid permeability and lambda modulus is likely amplified by the pressure boundary conditions, as both properties are related to fluid motion. In the current implementation, as the pressure on the boundaries is unknown, they are assumed to be 0 across all subzones thus assuming symmetrical pressures despite asymmetrical motions. This simplification overlooks the physiological differences in local pressure and potentially leads to inaccuracies in the reconstructed properties related to fluid flow, such as the fluid permeability and the lambda modulus. Alternative pressure boundary condition formulations have been proposed in the past by Tan *et al*. (Tan et al., 2017), however this approach, based on direct use of differentiated data within the inversion formulation led to instabilities when treating the data presented here. Recent development of coupled adjoint-field formulations for the subzone gradient-based inversion scheme removes the requirement for boundary conditions on the displacement field in the gradient calculation for nonlinear inversion (Kurtz et al., 2024). Similar formulations for the governing poroelastic equations, coupled with the pressure-forward-problem described by Tan et al. in 2017, would similarly remove the requirement for boundary conditions on the pressure field for the poroelastic system, and provide a robust approach to the reconstruction of physiologically relevant internal pressure measurements via MRE. This may prove to be a key step in reconstructing robust and accurate material property maps using poroelastic models.

The property maps recovered from the 2 Hz motion component generally exhibited spatial distributions similar to those observed with the 1 Hz component, though with reduced detail. This difference was particularly evident in the regional analysis, where the relative mean storage modulus across major regions appears more homogenous compared to the 1 Hz case. At the same time, very similar regional trends were recovered across motion components, both in the major regions across all material properties, and for the minor regions for the storage modulus. Remarkably, the storage modulus recovered using the 2 Hz component exhibited approximately five times higher values than for the 1 Hz component for both material models. This is consistent with the frequency-related stiffening that is associated with porous media, as reported by Herthum et al. (Herthum et al., 2021). Although the underlying mechanism probably is multifactorial, a large contributing factor is likely the impact of higher actuation frequencies on fluid-matrix interactions. At higher frequencies, the reduced time available for fluid redistribution within the porous network leads to greater confinement of the fluid within the solid matrix. This confinement enhances the coupling between the fluid and solid phases, resulting in increased effective stiffness and decreased fluid permeability. These effects are consistent with our findings, where the fluid permeability is lower for the 2 Hz

motion component in both material models. Notably, the lambda modulus of the solid matrix does not change significantly with frequency, which may be due to the fluid-solid coupling effect being primarily felt in the shear resistance, or due to the poorer quality of the divergence field measurements compared to the strain deformation field. Overall, although the 2 Hz component is expected to generate considerably noisier property maps than the 1 Hz component, many of the prominent features are preserved across motion components. Therefore, as much of the information is preserved in the 2 Hz motion component, it is likely beneficial to include this frequency component for future implementation of multifrequency reconstruction (Papazoglou et al., 2012).

Both the poroelastic model and the poroviscoelastic model exhibited good performance on several fronts. Two of the main limitations encountered using a viscoelastic model were resolved, namely the problem of non-unique solutions and the existence of high-valued artifact-like *hotspots* in the stiffness maps (Burman Ingeberg et al., 2023). Overall, the poroviscoelastic model outperformed the poroelastic model in the current implementation in terms of consistency of spatial distribution, repeatability, and symmetry of the storage modulus. Thus, despite being more complex, the poroviscoelastic model seemingly exhibits more consistency while also providing added details about the mechanical properties of the brain. Similar conclusions were reached by Greiner et al. (2024), who found that a poroviscoelastic model better captured time-dependent material behavior compared to a purely poroelastic model. At the same time, both models exhibited limitations in their current implementation. More specifically, the assumption of having the pressure field boundary conditions as $p = 0$ has large effects during non-linear inversion, affecting the reconstructed material property maps with the flow related properties being the most influenced. The effects of this assumption are likely reflected in the quality of the lambda modulus and fluid permeability maps, where the repeatability and symmetry were considerably worse than for the storage modulus. Therefore, the natural step forward is to, as previously discussed, develop a coupled adjoint-field formulation (Kurtz et al., 2024) for the non-linear inversion scheme in combination with the pressure forward problem (Tan et al., 2017). This approach would remove the necessity for pressure boundary conditions for both the poroelastic and poroviscoelastic models and rectify certain inconsistencies encountered in this work. Furthermore, the results presented here have not been validated using phantom or simulation studies, which would be essential for further assessing the accuracy and robustness of both models and are to be addressed in future studies.

5 Conclusion

In this work, the mechanical properties of the brain were successfully reconstructed using poroelastic and poroviscoelastic models and intrinsic MRE at 7 T. Notably, this is the first application of a poroviscoelastic model in brain MRE, in addition to the first time that the fluid permeability has been reconstructed on a voxel-wise basis. The performance and reliability of the poroelastic and poroviscoelastic models were compared, with the poroviscoelastic model generally found to be more suitable for iMRE in the current implementation. Additionally, the use of the 2 Hz motion component in the non-linear inversion algorithm was explored and found to provide reasonable mechanical property maps, suggesting that it could be advantageous for future multifrequency reconstruction approaches. The main limitation of this work includes the assumption on the boundary conditions of the pressure field. Future work thus aims to develop a coupled adjoint-field formulation in combination with the pressure forward problem for the non-linear inversion scheme, as well as investigating multifrequency inversion approaches.

6 References

Adams, A. L., Viergever, M. A., Luijten, P. R., & Zwanenburg, J. J. M. (2020). Validating faster DENSE measurements of cardiac-induced brain tissue expansion as a potential tool for investigating cerebral microvascular pulsations. *NeuroImage*, *208*, 116466. https://doi.org/10.1016/j.neuroimage.2019.116466

Barnes, J. M., Przybyla, L., & Weaver, V. M. (2017). Tissue mechanics regulate brain development, homeostasis and disease. *Journal of Cell Science*, *130*(1), 71–82. https://doi.org/10.1242/jcs.191742

Bunevicius, A., Schregel, K., Sinkus, R., Golby, A., & Patz, S. (2020). REVIEW: MR elastography of brain tumors. *NeuroImage. Clinical*, *25*, 102109. https://doi.org/10.1016/j.nicl.2019.102109

Burman Ingeberg, M., Van Houten, E., & Zwanenburg, J. J. M. (2023). Estimating the viscoelastic properties of the human brain at 7T MRI using intrinsic MRE and nonlinear inversion. *Human Brain Mapping*, *44*(18), 6575–6591. https://doi.org/10.1002/hbm.26524

Choudhry, F. A., Grantham, J. T., Rai, A. T., & Hogg, J. P. (2016). Vascular geometry of the extracranial carotid arteries: an analysis of length, diameter, and tortuosity. *Journal of Neurointerventional Surgery*, *8*(5), 536–540. https://doi.org/10.1136/neurintsurg-2015-011671

Farhat, N. S., Theiss, R., Santini, T., Ibrahim, T. S., & Aizenstein, H. J. (2019). Neuroimaging of Small Vessel Disease in Late-Life Depression. *Advances in Experimental Medicine and Biology*, *1192*, 95–115. https://doi.org/10.1007/978-981-32-9721-0_5

Feng, Y., Murphy, M. C., Hojo, E., Li, F., & Roberts, N. (2024). Magnetic Resonance Elastography in the Study of Neurodegenerative Diseases. *Journal of Magnetic Resonance Imaging : JMRI*, *59*(1), 82–96. https://doi.org/10.1002/jmri.28747

Forouhandehpour, R., Bernier, M., Gilbert, G., Butler, R., Whittingstall, K., & Van Houten, E. (2021). Cerebral stiffness changes during visual stimulation: Differential physiological mechanisms characterized by opposing mechanical effects. *Neuroimage: Reports*, *1*(2), 100014. https://doi.org/10.1016/j.ynirp.2021.100014

Glaser, K. J., Manduca, A., & Ehman, R. L. (2012). Review of MR elastography applications and recent developments. *Journal of Magnetic Resonance Imaging : JMRI*, *36*(4), 757–774. https://doi.org/10.1002/jmri.23597

Goriely, A., Geers, M. G. D., Holzapfel, G. A., Jayamohan, J., Jérusalem, A., Sivaloganathan, S., Squier, W., van Dommelen, J. A. W., Waters, S., & Kuhl, E. (2015). Mechanics of the brain: perspectives, challenges, and opportunities. *Biomechanics and Modeling in Mechanobiology*, *14*(5), 931–965. https://doi.org/10.1007/s10237-015-0662-4

Greiner, A., Reiter, N., Hinrichsen, J., Kainz, M. P., Sommer, G., Holzapfel, G. A., Steinmann, P., Comellas, E., & Budday, S. (2024). Model-driven exploration of poro-viscoelasticity in human brain tissue: be careful with the parameters! *Interface Focus*, *14*(6). https://doi.org/10.1098/rsfs.2024.0026

Herthum, H., Dempsey, S. C. H., Samani, A., Schrank, F., Shahryari, M., Warmuth, C., Tzschätzsch, H., Braun, J., & Sack, I. (2021). Superviscous properties of the in vivo brain at large scales. *Acta Biomaterialia*, *121*, 393–404. https://doi.org/10.1016/j.actbio.2020.12.027

Hiscox, L. V, Johnson, C. L., Barnhill, E., McGarry, M. D. J., Huston, J., van Beek, E. J. R., Starr, J. M., & Roberts, N. (2016). Magnetic resonance elastography (MRE) of the human brain: technique, findings and clinical applications. *Physics in Medicine and Biology*, *61*(24), R401–R437. https://doi.org/10.1088/0031-9155/61/24/R401

Hiscox, L. V., McGarry, M. D. J., Schwarb, H., Van Houten, E. E. W., Pohlig, R. T., Roberts, N., Huesmann, G. R., Burzynska, A. Z., Sutton, B. P., Hillman, C. H., Kramer, A. F., Cohen, N. J., Barbey, A. K.,

Paulsen, K. D., & Johnson, C. L. (2020). Standard-space atlas of the viscoelastic properties of the human brain. *Human Brain Mapping*, *41*(18), 5282–5300. https://doi.org/10.1002/hbm.25192

John D'Errico. (2024). *Inpainting nan elements in 3-d (https://www.mathworks.com/matlabcentral/fileexchange/21214-inpainting-nan-elements-in-3-d), MATLAB Central File Exchange.* (Retrieved November 27, 2024.).

Johnson, C. L., McGarry, M. D. J., Van Houten, E. E. W., Weaver, J. B., Paulsen, K. D., Sutton, B. P., & Georgiadis, J. G. (2013). Magnetic resonance elastography of the brain using multishot spiral readouts with self-navigated motion correction. *Magnetic Resonance in Medicine*, *70*(2), 404–412. https://doi.org/10.1002/mrm.24473

Kurtz, S., Wattrisse, B., & Van Houten, E. E. W. (2024). Minimizing Measurement-Induced Errors in Viscoelastic MR Elastography. *IEEE Transactions on Medical Imaging*, *43*(3), 1138–1148. https://doi.org/10.1109/TMI.2023.3329293

Lan, P. S., Glaser, K. J., Ehman, R. L., & Glover, G. H. (2020). Imaging brain function with simultaneous BOLD and viscoelasticity contrast: fMRI/fMRE. *NeuroImage*, *211*, 116592. https://doi.org/10.1016/j.neuroimage.2020.116592

Manera, A. L., Dadar, M., Fonov, V., & Collins, D. L. (2020). CerebrA, registration and manual label correction of Mindboggle-101 atlas for MNI-ICBM152 template. *Scientific Data*, *7*(1), 237. https://doi.org/10.1038/s41597-020-0557-9

McGarry, M. D. J., Johnson, C. L., Sutton, B. P., Georgiadis, J. G., Van Houten, E. E. W., Pattison, A. J., Weaver, J. B., & Paulsen, K. D. (2015). Suitability of poroelastic and viscoelastic mechanical models for high and low frequency MR elastography. *Medical Physics*, *42*(2), 947–957. https://doi.org/10.1118/1.4905048

McGarry, M. D. J., Van Houten, E. E. W., Johnson, C. L., Georgiadis, J. G., Sutton, B. P., Weaver, J. B., & Paulsen, K. D. (2012). Multiresolution MR elastography using nonlinear inversion. *Medical Physics*, *39*(10), 6388–6396. https://doi.org/10.1118/1.4754649

McGarry, M., Van Houten, E., Solamen, L., Gordon-Wylie, S., Weaver, J., & Paulsen, K. (2019). Uniqueness of poroelastic and viscoelastic nonlinear inversion MR elastography at low frequencies. *Physics in Medicine and Biology*, *64*(7), 075006. https://doi.org/10.1088/1361-6560/ab0a7d

Meyer, T., Castelein, J., Schattenfroh, J., Sophie Morr, A., Vieira da Silva, R., Tzschätzsch, H., Reiter, R., Guo, J., & Sack, I. (2024). Magnetic resonance elastography in a nutshell: Tomographic imaging of soft tissue viscoelasticity for detecting and staging disease with a focus on inflammation. *Progress in Nuclear Magnetic Resonance Spectroscopy*, *144–145*, 1–14. https://doi.org/10.1016/j.pnmrs.2024.05.002

Mori, S., Oishi, K., Jiang, H., Jiang, L., Li, X., Akhter, K., Hua, K., Faria, A. V, Mahmood, A., Woods, R., Toga, A. W., Pike, G. B., Neto, P. R., Evans, A., Zhang, J., Huang, H., Miller, M. I., van Zijl, P., & Mazziotta, J. (2008). Stereotaxic white matter atlas based on diffusion tensor imaging in an ICBM template. *NeuroImage*, *40*(2), 570–582. https://doi.org/10.1016/j.neuroimage.2007.12.035

Mori S, Wakana S, Nagae-Poetscher L M, & van Zijl P C M. (2006). MRI Atlas of Human White Matter. *AJNR Am J Neuroradiol*, *27*(6), 1384–1385.

Papazoglou, S., Hirsch, S., Braun, J., & Sack, I. (2012). Multifrequency inversion in magnetic resonance elastography. *Physics in Medicine and Biology*, *57*(8), 2329–2346. https://doi.org/10.1088/0031-9155/57/8/2329

Perriñez, P. R., Kennedy, F. E., Van Houten, E. E. W., Weaver, J. B., & Paulsen, K. D. (2010). Magnetic resonance poroelastography: an algorithm for estimating the mechanical properties of fluid-saturated soft tissues. *IEEE Transactions on Medical Imaging*, *29*(3), 746–755. https://doi.org/10.1109/TMI.2009.2035309

Rouvière, O., Yin, M., Dresner, M. A., Rossman, P. J., Burgart, L. J., Fidler, J. L., & Ehman, R. L. (2006). MR elastography of the liver: preliminary results. *Radiology*, *240*(2), 440–448. https://doi.org/10.1148/radiol.2402050606

Schwarb, H., Johnson, C. L., McGarry, M. D. J., & Cohen, N. J. (2016). Medial temporal lobe viscoelasticity and relational memory performance. *NeuroImage*, *132*, 534–541. https://doi.org/10.1016/j.neuroimage.2016.02.059

Solamen, L. M., McGarry, M. D. J., Fried, J., Weaver, J. B., Lollis, S. S., & Paulsen, K. D. (2021). Poroelastic Mechanical Properties of the Brain Tissue of Normal Pressure Hydrocephalus Patients During Lumbar Drain Treatment Using Intrinsic Actuation MR Elastography. *Academic Radiology*, *28*(4), 457–466. https://doi.org/10.1016/j.acra.2020.03.009

Sowinski, D. R., McGarry, M. D. J., Van Houten, E. E. W., Gordon-Wylie, S., Weaver, J. B., & Paulsen, K. D. (2021). Poroelasticity as a Model of Soft Tissue Structure: Hydraulic Permeability Reconstruction for Magnetic Resonance Elastography in Silico. *Frontiers in Physics*, *8*. https://doi.org/10.3389/fphy.2020.617582

Svensson, S. F., De Arcos, J., Darwish, O. I., Fraser-Green, J., Storås, T. H., Holm, S., Vik-Mo, E. O., Sinkus, R., & Emblem, K. E. (2021). Robustness of MR Elastography in the Healthy Brain: Repeatability, Reliability, and Effect of Different Reconstruction Methods. *Journal of Magnetic Resonance Imaging : JMRI*, *53*(5), 1510–1521. https://doi.org/10.1002/jmri.27475

Tan, L., McGarry, M. D. J., Van Houten, E. E. W., Ji, M., Solamen, L., Zeng, W., Weaver, J. B., & Paulsen, K. D. (2017). A numerical framework for interstitial fluid pressure imaging in poroelastic MRE. *PloS One*, *12*(6), e0178521. https://doi.org/10.1371/journal.pone.0178521

Van Houten, E. E., Miga, M. I., Weaver, J. B., Kennedy, F. E., & Paulsen, K. D. (2001). Three-dimensional subzone-based reconstruction algorithm for MR elastography. *Magnetic Resonance in Medicine*, *45*(5), 827–837. https://doi.org/10.1002/mrm.1111

Weaver, J. B., Pattison, A. J., McGarry, M. D., Perreard, I. M., Swienckowski, J. G., Eskey, C. J., Lollis, S. S., & Paulsen, K. D. (2012). Brain mechanical property measurement using MRE with intrinsic activation. *Physics in Medicine and Biology*, *57*(22), 7275–7287. https://doi.org/10.1088/0031-9155/57/22/7275

Yin, L.-X., Ma, C.-Y., Wang, S., Wang, Y.-H., Meng, P.-P., Pan, X.-F., Yang, J., Zhang, Y.-H., Liu, M.-H., Li, M.-X., Gao, J., Wu, Q., Feng, N.-N., Wu, Y.-Y., Zhang, J.-X., Xue, L., Chang, F.-L., Chen, L., Sun, Y.-X., … Li, Y.-H. (2021). Reference Values of Carotid Ultrafast Pulse-Wave Velocity: A Prospective, Multicenter, Population-Based Study. *Journal of the American Society of Echocardiography*, *34*(6), 629–641. https://doi.org/10.1016/j.echo.2021.01.003

Yin, M., Woollard, J., Wang, X., Torres, V. E., Harris, P. C., Ward, C. J., Glaser, K. J., Manduca, A., & Ehman, R. L. (2007). Quantitative assessment of hepatic fibrosis in an animal model with magnetic resonance elastography. *Magnetic Resonance in Medicine*, *58*(2), 346–353. https://doi.org/10.1002/mrm.21286

Zhang, J., Green, M. A., Sinkus, R., & Bilston, L. E. (2011). Viscoelastic properties of human cerebellum using magnetic resonance elastography. *Journal of Biomechanics*, *44*(10), 1909–1913. https://doi.org/10.1016/j.jbiomech.2011.04.034

Zorgani, A., Souchon, R., Dinh, A.-H., Chapelon, J.-Y., Ménager, J.-M., Lounis, S., Rouvière, O., & Catheline, S. (2015). Brain palpation from physiological vibrations using MRI. *Proceedings of the National Academy of Sciences of the United States of America*, *112*(42), 12917–12921. https://doi.org/10.1073/pnas.1509895112

Supplementary material

1 Representative parameter maps

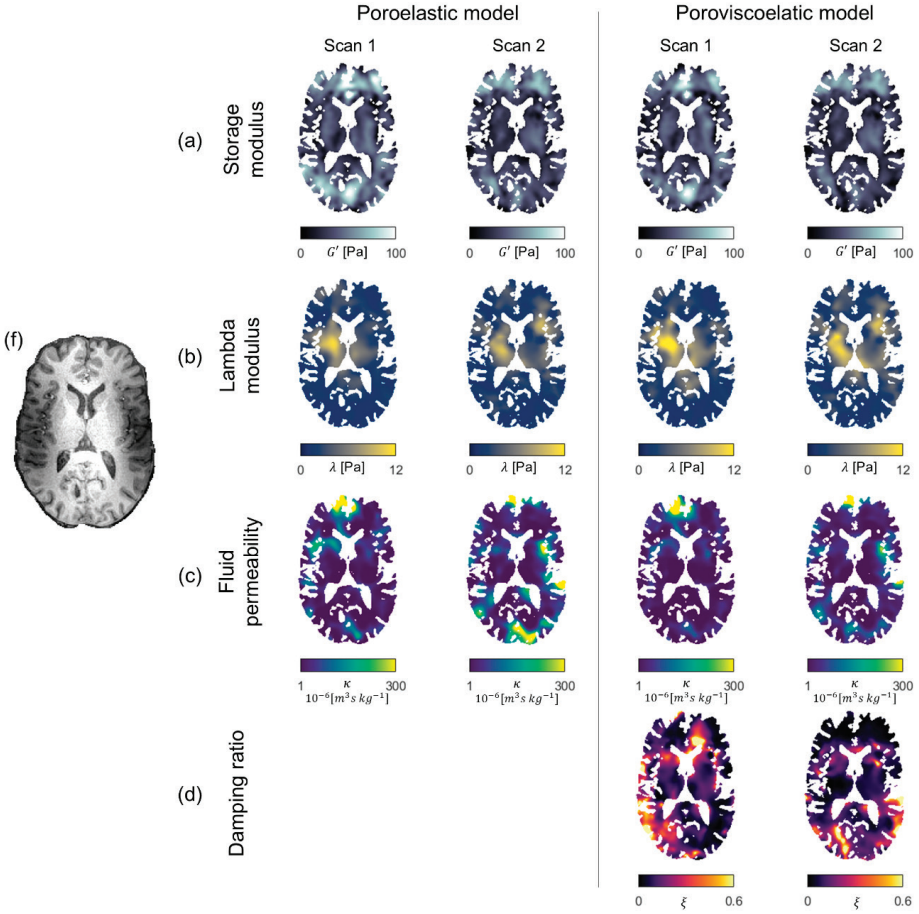


Figure S1: Representative axial slices of the storage modulus (a), lambda modulus (b), fluid permeability (c), and damping ratio (d) obtained from the 2 Hz motion component for one subject along with a repeated scan which has been co-registered to the first scan. The equivalent slice of the T1-weighted image is shown in (f) for anatomical reference.

2 Regional analysis

Table S1: The mean material properties and corresponding standard deviation across major brain regions for both material models and motion frequency components.

		1 Hz		2 Hz	
Region	**Quantity**	**Poroelastic**	**Poroviscoelastic**	**Poroelastic**	**Poroviscoelastic**
Global	G' [Pa]	6.09 (0.87)	5.33 (0.77)	32.08 (11.98)	26.22 (8.06)
	λ [Pa]	3.99 (0.67)	4.31 (0.69)	4.98 (1.60)	5.58 (1.96)
	$\kappa\ 10^{-6}$ [$m^3\ s\ kg^{-1}$]	266 (79)	75 (9)	221 (127)	52 (17)
	ξ	N/A	0.23 (0.04)	N/A	0.27 (0.12)
Subcortical GM	G' [Pa]	4.46 (1.03)	4.03 (1.23)	23.88 (11.56)	20.20 (11.61)
	λ [Pa]	4.00 (0.73)	4.35 (0.62)	5.94 (1.82)	6.49 (2.04)
	$\kappa\ 10^{-6}$ [$m^3\ s\ kg^{-1}$]	419 (260)	89 (31)	421 (460)	60 (43)
	ξ	N/A	0.31 (0.13)	N/A	0.48 (0.50)
Cortical GM	G' [Pa]	6.61 (1.18)	5.58 (1.00)	35.04 (13.45)	28.16 (9.01)
	λ [Pa]	3.87 (0.71)	4.09 (0.72)	4.49 (1.69)	4.91 (1.96)
	$\kappa\ 10^{-6}$ [$m^3\ s\ kg^{-1}$]	265 (99)	78 (22)	196 (71)	52 (15)
	ξ	N/A	0.26 (0.06)	N/A	0.28 (0.14)
WMT	G' [Pa]	5.84 (1.16)	4.95 (1.03)	35.79 (16.39)	28.57 (12.31)
	λ [Pa]	4.29 (0.60)	4.76 (0.58)	5.22 (1.58)	6.14 (2.13)
	$\kappa\ 10^{-6}$ [$m^3\ s\ kg^{-1}$]	207 (86)	64 (15)	140 (111)	39 (19)
	ξ	N/A	0.29 (0.09)	N/A	0.30 (0.17)

Table S2: The mean material properties and corresponding standard deviation across brain regions in subcortical gray matter for both material models and motion frequency components.

		1 Hz		2 Hz	
Region	**Quantity**	**Poroelastic**	**Poroviscoelastic**	**Poroelastic**	**Poroviscoelastic**
AM	G' [Pa]	4.38 (1.26)	4.03 (1.09)	17.86 (7.91)	14.66 (6.76)
AM	λ [Pa]	2.94 (0.39)	3.18 (0.54)	4.05 (1.88)	4.42 (2.14)
AM	κ 10^{-6} [m^3 s kg^{-1}]	141 (67)	67 (35)	332 (262)	55 (22)
AM	ξ	N/A	0.17 (0.04)	N/A	0.26 (0.10)
CA	G' [Pa]	4.36 (1.00)	3.92 (1.13)	24.88 (8.24)	20.42 (9.14)
CA	λ [Pa]	3.46 (0.75)	3.70 (0.65)	4.50 (1.18)	4.51 (0.84)
CA	κ 10^{-6} [m^3 s kg^{-1}]	458 (294)	72 (27)	194 (254)	36 (22)
CA	ξ	N/A	0.34 (0.14)	N/A	0.68 (0.49)
HC	G' [Pa]	3.94 (0.99)	3.47 (0.94)	18.21 (6.70)	15.24 (5.65)
HC	λ [Pa]	3.00 (1.03)	3.27 (1.14)	4.82 (2.39)	5.47 (2.59)
HC	κ 10^{-6} [m^3 s kg^{-1}]	249 (91)	88 (72)	238 (202)	71 (48)
HC	ξ	N/A	0.23 (0.07)	N/A	0.25 (0.10)
PA	G' [Pa]	4.61 (0.68)	4.05 (1.06)	23.35 (10.63)	19.41 (11.06)
PA	λ [Pa]	4.58 (0.73)	4.87 (0.81)	5.32 (1.45)	5.65 (1.62)
PA	κ 10^{-6} [m^3 s kg^{-1}]	451 (219)	136 (55)	534 (710)	64 (64)
PA	ξ	N/A	0.37 (0.24)	N/A	0.58 (0.48)
PU	G' [Pa]	4.96 (0.66)	4.58 (1.02)	28.56 (8.82)	23.70 (9.73)
PU	λ [Pa]	5.34 (0.82)	5.73 (0.78)	6.93 (2.69)	7.09 (2.36)
PU	κ 10^{-6} [m^3 s kg^{-1}]	257 (187)	85 (47)	212 (284)	53 (36)
PU	ξ	N/A	0.33 (0.17)	N/A	0.68 (0.73)
TH	G' [Pa]	4.30 (1.45)	3.96 (1.59)	21.94 (14.67)	19.75 (14.54)
TH	λ [Pa]	3.40 (1.00)	3.84 (1.01)	5.93 (2.25)	7.17 (2.32)
TH	κ 10^{-6} [m^3 s kg^{-1}]	567 (307)	89 (33)	653 (753)	64 (55)
TH	ξ	N/A	0.27 (0.14)	N/A	0.31 (0.19)

Table S3: The mean material properties and corresponding standard deviation across brain regions in cortical gray matter for both material models and motion frequency components.

		1 Hz		2 Hz	
Region	**Quantity**	**Poroelastic**	**Poroviscoelastic**	**Poroelastic**	**Poroviscoelastic**
CN	G' [Pa]	6.50 (2.11)	6.07 (2.12)	39.64 (30.91)	33.16 (22.02)
CN	λ [Pa]	2.31 (1.02)	2.34 (0.91)	3.84 (2.93)	4.08 (3.07)
CN	κ 10^{-6} [m^3 s kg^{-1}]	340 (211)	91 (55)	176 (136)	66 (25)
CN	ξ	N/A	0.18 (0.11)	N/A	0.15 (0.07)
FSG	G' [Pa]	6.13 (0.88)	5.21 (0.81)	28.64 (12.30)	23.53 (7.19)
FSG	λ [Pa]	3.34 (0.73)	3.67 (0.89)	4.12 (1.64)	4.81 (1.45)
FSG	κ 10^{-6} [m^3 s kg^{-1}]	183 (54)	93 (26)	194 (143)	57 (31)
FSG	ξ	N/A	0.21 (0.07)	N/A	0.23 (0.10)
ITC	G' [Pa]	5.11 (0.68)	4.23 (0.49)	21.05 (4.10)	17.43 (2.70)
ITC	λ [Pa]	2.18 (0.45)	2.40 (0.52)	2.29 (0.77)	2.78 (1.00)
ITC	κ 10^{-6} [m^3 s kg^{-1}]	474 (363)	151 (119)	376 (169)	60 (25)
ITC	ξ	N/A	0.24 (0.02)	N/A	0.30 (0.11)
LaO	G' [Pa]	5.03 (0.65)	4.68 (0.72)	33.24 (18.02)	24.58 (10.17)
LaO	λ [Pa]	3.64 (1.48)	4.00 (1.57)	5.75 (3.74)	6.40 (4.04)
LaO	κ 10^{-6} [m^3 s kg^{-1}]	195 (118)	59 (28)	152 (173)	54 (36)
LaO	ξ	N/A	0.18 (0.03)	N/A	0.45 (0.51)
LiO	G' [Pa]	6.31 (1.36)	5.55 (1.27)	32.28 (15.51)	25.74 (8.04)
LiO	λ [Pa]	3.14 (0.99)	3.19 (0.79)	4.35 (2.34)	5.07 (2.49)
LiO	κ 10^{-6} [m^3 s kg^{-1}]	244 (230)	58 (43)	143 (133)	41 (16)
LiO	ξ	N/A	0.24 (0.08)	N/A	0.20 (0.07)
PCN	G' [Pa]	7.45 (2.23)	6.80 (2.15)	42.17 (19.05)	36.13 (15.33)
PCN	λ [Pa]	2.44 (0.82)	2.69 (0.82)	3.35 (1.57)	3.77 (1.91)
PCN	κ 10^{-6} [m^3 s kg^{-1}]	281 (228)	67 (23)	151 (81)	63 (27)
PCN	ξ	N/A	0.24 (0.17)	N/A	0.16 (0.06)
POST	G' [Pa]	5.51 (0.96)	5.22 (0.92)	28.25 (10.68)	24.63 (8.27)
POST	λ [Pa]	4.41 (1.07)	4.64 (1.10)	5.42 (2.61)	6.39 (2.88)
POST	κ 10^{-6} [m^3 s kg^{-1}]	234 (140)	64 (19)	154 (72)	40 (13)
POST	ξ	N/A	0.14 (0.03)	N/A	0.17 (0.08)
PRE	G' [Pa]	6.56 (1.01)	6.08 (1.10)	30.89 (7.88)	27.52 (6.54)
PRE	λ [Pa]	6.19 (1.79)	6.56 (1.79)	6.32 (2.18)	7.28 (2.94)
PRE	κ 10^{-6} [m^3 s kg^{-1}]	160 (107)	60 (24)	144 (141)	40 (14)
PRE	ξ	N/A	0.14 (0.04)	N/A	0.16 (0.06)
RMF	G' [Pa]	8.20 (2.24)	7.27 (1.89)	42.39 (15.53)	34.76 (10.58)
RMF	λ [Pa]	5.97 (0.95)	6.88 (1.15)	6.30 (2.54)	6.46 (2.61)
RMF	κ 10^{-6} [m^3 s kg^{-1}]	94 (51)	62 (45)	77 (46)	34 (13)
RMF	ξ	N/A	0.17 (0.07)	N/A	0.33 (0.23)

Table S3: The mean material properties and corresponding standard deviation across brain regions in cortical gray matter for both material models and motion frequency components. (*continued*)

		1 Hz		2 Hz	
SFC	G' [Pa]	7.27 (1.63)	5.18 (1.40)	37.30 (13.48)	28.58 (10.39)
SFC	λ [Pa]	4.05 (1.07)	3.94 (1.05)	3.68 (1.59)	3.69 (1.52)
SFC	κ 10^{-6} [m^3 s kg^{-1}]	351 (174)	82 (34)	276 (214)	58 (34)
SFC	ξ	N/A	0.46 (0.17)	N/A	0.36 (0.19)
SPC	G' [Pa]	5.91 (1.77)	5.38 (1.56)	30.89 (12.62)	26.20 (9.92)
SPC	λ [Pa]	3.21 (0.93)	3.48 (1.01)	3.51 (2.05)	3.90 (2.34)
SPC	κ 10^{-6} [m^3 s kg^{-1}]	355 (232)	61 (25)	290 (394)	45 (20)
SPC	ξ	N/A	0.20 (0.07)	N/A	0.20 (0.09)
STC	G' [Pa]	5.71 (0.54)	5.11 (0.59)	27.96 (7.75)	22.91 (4.74)
STC	λ [Pa]	3.60 (0.86)	3.98 (0.88)	4.48 (1.60)	5.17 (2.13)
STC	κ 10^{-6} [m^3 s kg^{-1}]	223 (132)	79 (28)	130 (73)	43 (17)
STC	ξ	N/A	0.18 (0.04)	N/A	0.24 (0.08)

Table S4: The mean material properties and corresponding standard deviation across brain regions in white matter tracts for both material models and motion frequency components.

		1 Hz		2Hz	
Region	**Field**	**Poroelastic**	**Poroviscoelastic**	**Poroelastic**	**Poroviscoelastic**
ATR	G' [Pa]	5.24 (1.30)	4.70 (1.41)	26.48 (11.74)	21.85 (11.29)
ATR	λ [Pa]	4.19 (0.80)	4.81 (0.81)	5.89 (1.80)	6.90 (1.97)
ATR	κ 10^{-6} [m^3 s kg^{-1}]	338 (205)	73 (19)	537 (599)	50 (36)
ATR	ξ	N/A	0.27 (0.09)	N/A	0.44 (0.29)
CC	G' [Pa]	5.81 (1.26)	4.81 (1.46)	32.39 (12.66)	26.39 (10.32)
CC	λ [Pa]	3.11 (0.38)	3.29 (0.34)	3.92 (0.94)	4.57 (1.14)
CC	κ 10^{-6} [m^3 s kg^{-1}]	318 (159)	76 (34)	87 (63)	34 (22)
CC	ξ	N/A	0.45 (0.15)	N/A	0.34 (0.13)
CRa	G' [Pa]	5.75 (1.36)	5.03 (1.06)	36.86 (16.60)	29.88 (12.88)
CRa	λ [Pa]	5.12 (0.64)	6.00 (0.71)	6.10 (2.45)	7.62 (3.39)
CRa	κ 10^{-6} [m^3 s kg^{-1}]	110 (29)	40 (7)	69 (61)	29 (18)
CRa	ξ	N/A	0.24 (0.04)	N/A	0.28 (0.12)
CST	G' [Pa]	4.28 (0.97)	4.18 (0.93)	26.94 (15.03)	23.95 (12.78)
CST	λ [Pa]	4.18 (1.02)	4.78 (1.05)	6.89 (3.17)	7.91 (3.30)
CST	κ 10^{-6} [m^3 s kg^{-1}]	234 (125)	59 (22)	382 (470)	60 (48)
CST	ξ	N/A	0.18 (0.06)	N/A	0.21 (0.10)
FMa	G' [Pa]	5.86 (1.54)	5.25 (1.52)	39.07 (27.14)	30.84 (15.85)
FMa	λ [Pa]	2.67 (0.77)	3.16 (0.89)	4.30 (1.97)	5.63 (2.23)
FMa	κ 10^{-6} [m^3 s kg^{-1}]	171 (107)	44 (27)	47 (30)	26 (15)
FMa	ξ	N/A	0.24 (0.11)	N/A	0.18 (0.08)

Table S4: The mean material properties and corresponding standard deviation across brain regions in white matter tracts for both material models and motion frequency components. (*continued*)

		1 Hz		2Hz	
FMi	G' [Pa]	7.15 (2.26)	4.75 (1.13)	41.16 (16.73)	28.34 (11.58)
FMi	λ [Pa]	4.29 (0.88)	4.49 (0.92)	4.03 (1.60)	3.98 (1.76)
FMi	κ 10^{-6} [m^3 s kg^{-1}]	252 (154)	63 (11)	122 (51)	48 (26)
FMi	ξ	N/A	0.50 (0.25)	N/A	0.49 (0.27)
IFOF	G' [Pa]	6.42 (0.71)	5.83 (0.66)	35.38 (12.77)	27.32 (7.34)
IFOF	λ [Pa]	4.48 (1.21)	5.04 (1.21)	5.48 (1.70)	6.29 (2.43)
IFOF	κ 10^{-6} [m^3 s kg^{-1}]	119 (26)	60 (15)	80 (58)	41 (19)
IFOF	ξ	N/A	0.20 (0.07)	N/A	0.34 (0.18)
ILF	G' [Pa]	6.05 (0.97)	5.33 (0.81)	28.54 (8.52)	23.37 (5.22)
ILF	λ [Pa]	3.32 (0.98)	3.57 (0.99)	3.45 (1.38)	4.13 (1.61)
ILF	κ 10^{-6} [m^3 s kg^{-1}]	152 (102)	71 (36)	103 (76)	41 (17)
ILF	ξ	N/A	0.18 (0.05)	N/A	0.21 (0.07)
PTR	G' [Pa]	6.27 (1.22)	5.44 (0.96)	39.08 (27.55)	29.25 (13.66)
PTR	λ [Pa]	3.28 (1.35)	3.80 (1.43)	4.15 (2.48)	5.13 (3.14)
PTR	κ 10^{-6} [m^3 s kg^{-1}]	146 (64)	73 (44)	45 (25)	34 (21)
PTR	ξ	N/A	0.18 (0.04)	N/A	0.22 (0.11)
SLF	G' [Pa]	4.98 (0.65)	4.67 (0.62)	36.00 (19.91)	31.34 (14.96)
SLF	λ [Pa]	5.21 (1.15)	5.70 (1.08)	6.01 (2.81)	7.29 (3.56)
SLF	κ 10^{-6} [m^3 s kg^{-1}]	145 (96)	74 (54)	53 (39)	28 (16)
SLF	ξ	N/A	0.16 (0.04)	N/A	0.18 (0.08)

3 Symmetry analysis

Table S5: The mean and standard deviation of the symmetry ratio for all material properties across the major regions for the 1 Hz motion component.

	Region	Poroelastic	Poroviscoelastic
Storage modulus	Global	0.99 (0.05)	0.99 (0.04)
	SGM	0.99 (0.18)	0.96 (0.14)
	CGM	1.01 (0.06)	1.01 (0.04)
	WMT	1.02 (0.11)	1.05 (0.12)
Lambda modulus	Global	0.93 (0.14)	0.89 (0.13)
	SGM	0.89 (0.29)	0.79 (0.24)
	CGM	1.00 (0.20)	0.95 (0.20)
	WMT	1.09 (0.21)	0.97 (0.19)
Fluid permeability	Global	1.20 (0.30)	1.37 (0.25)
	SGM	3.34 (2.97)	3.59 (2.78)
	CGM	1.23 (0.33)	1.52 (0.44)
	WMT	1.42 (0.31)	1.29 (0.41)
Damping ratio	Global	N/A	0.94 (0.10)
	SGM	N/A	1.14 (0.19)
	CGM	N/A	0.95 (0.16)
	WMT	N/A	0.90 (0.17)

Table S6: The mean and standard deviation of the symmetry ratio for all material properties across the major regions for the 2 Hz motion component.

	Region	Poroelastic	Poroviscoelastic
Storage modulus	Global	1.02 (0.06)	1.06 (0.13)
	SGM	1.03 (0.21)	0.95 (0.15)
	CGM	1.04 (0.09)	1.09 (0.15)
	WMT	1.02 (0.11)	1.03 (0.14)
Lambda modulus	Global	0.99 (0.23)	0.98 (0.26)
	SGM	1.22 (0.35)	1.03 (0.37)
	CGM	1.02 (0.41)	0.99 (0.41)
	WMT	1.18 (0.25)	1.12 (0.34)
Fluid permeability	Global	1.13 (0.70)	1.22 (0.37)
	SGM	1.42 (0.43)	1.89 (0.66)
	CGM	1.08 (0.79)	1.25 (0.51)
	WMT	1.45 (0.87)	1.37 (0.45)
Damping ratio	Global	N/A	0.87 (0.20)
	SGM	N/A	1.62 (0.52)
	CGM	N/A	0.80 (0.24)
	WMT	N/A	1.06 (0.36)



Chapter 4

Evidence for the ultra-soft brain provided by uniqueness in intrinsic MR elastography

Marius Burman Ingeberg[1], Elijah Van Houten[2], Jaco J.M Zwanenburg[1]

[1]Translational Neuroimaging Group, Center for Image Sciences, University Medical Center Utrecht and Utrecht University, Utrecht, The Netherlands

[2]Université de Strasbourg, CNRS, INSERM, ICube, UMR7357, Strasbourg, France.

Original work currently under submission.

Author Contribution Statement:

Marius Burman Ingeberg was responsible for conceptualization, methodology, software development, investigation, formal analysis, data management, and visualization, and wrote the original draft of the manuscript. Eli van Houten contributed to conceptualization, provided supervision and resources, and reviewed and edited the manuscript. Jaco Zwanenburg contributed to conceptualization, secured funding, provided resources and supervision, and reviewed and edited the manuscript.

Abstract

Introduction

Brain tissue is exceptionally soft. Recent *in vivo* work, including intrinsic MRE using naturally occurring cardiac pulsations, has shown stiffness values far below those obtained from post-mortem testing or externally actuated MRE. Such extreme softness allows a balance of elastic and inertial forces at even low frequencies, restoring uniqueness in viscoelastic iMRE inversion. Here, we demonstrate that viscoelastic iMRE can provide unique and stable stiffness estimates across frequencies, enabled by the brain's ultra-soft nature.

Method

iMRE data was obtained for 8 healthy subjects from a previous 7T MRI study, and MRE data was obtained at 50 Hz for 38 healthy subjects from two prior studies. The elastic-to-inertial force ratio was calculated for all subjects and compared between intrinsic and extrinsic datasets. The convergence of the viscoelastic iMRE was evaluated across a range of initial conditions and was examined at approximately 1, 2, and 3 Hz.

Results

At a brain stiffness of 2600 Pa, the iMRE force ratio exceeded the MRE value by nearly four orders of magnitude, whereas at 4-35 Pa it fell to within approximately 0.5-2.5 orders of magnitude. Convergence was consistent across initial stiffness estimates. The mean storage modulus across all subjects was 5.29±0.95 Pa at 1 Hz, 34±17 Pa at 2 Hz, and 160±98 Pa at 3 Hz, consistent with previously reported frequency dependency.

Conclusion

Balanced force ratios, consistent convergence, and physiologically plausible results support uniqueness of the viscoelastic inversion. These findings resolve a key limitation in iMRE modeling and provide further evidence for the brain's ultra-soft nature at low frequencies.

1 Introduction

Brain tissue is among the most complex tissues in the human body and is notoriously difficult to characterize. Emerging evidence suggests that the brain is exceptionally soft, and reported stiffness values have decreased progressively as measurement techniques have improved. Mechanical testing often yields values approximately in the range of 200 Pa to 1 kPa, positioning the brain as one of the softest organs in the body (Budday et al., 2020). However, such measurements are typically performed on post-mortem tissue, where the brain is removed from its natural, vascularized, and pressurized environment, potentially altering its mechanical properties. Magnetic resonance elastography (MRE) enables non-invasive *in vivo* assessment of brain stiffness, but standard externally actuated MRE often reports significantly higher values (2-3 kPa (Hiscox et al., 2020; Johnson, McGarry, Van Houten, et al., 2013)), as the measured stiffness increases strongly with actuation frequency (Herthum et al., 2021). Consequently, the natural softness of brain tissue in its normal environment and conditions remains difficult to establish using existing methodologies.

The feasibility of an adaptation of the MRE technique, called intrinsic MRE (iMRE), was recently shown, where the need for external actuation is circumvented by leveraging naturally occurring brain pulsations driven by the cardiac pulse (Burman Ingeberg et al., 2023; Solamen et al., 2021; Weaver et al., 2012; Zorgani et al., 2015). An advantage of iMRE is the ability to characterize brain tissue stiffness in a more physiologically natural state, rather than one altered by externally applied vibrations, and may thus provide more accurate measurements of the brain's natural stiffness. However, when brain tissue is modeled as a viscoelastic material, as is common in standard MRE, the inversion problem at the low frequencies of cardiac pulsation becomes non-unique (McGarry et al., 2019). Here, the term non-unique refers to the fact that any scalar multiple of the viscoelastic properties provides indistinguishable tissue displacements, making it impossible to determine the tissue's mechanical properties in an absolute sense. This ambiguity can lead to an inability for iMRE to detect clinical conditions leading to bulk stiffness changes, such as neurodegeneration or regeneration (Guo et al., 2019; McIlvain, Schneider, et al., 2022; Pavuluri et al., 2024; Takamura et al., 2020). The issue of non-uniqueness arises because, under high-stiffness and low-frequency conditions, elastic forces dominate over inertial forces, making the equilibrium conditions essentially quasi-static and valid for any constant scalar of the elasticity greater than unity (McGarry et al., 2019).

Recently, poroelastic inversion using iMRE was successfully performed. iMRE with poroelastic inversion preserves uniqueness due to fluid-matrix interaction (M. McGarry et al., 2019) and enables voxel-wise reconstruction of both fluid permeability (Burman Ingeberg et al., 2025). By contrast, iMRE implementations that impose a global fluid

permeability scale the entire stiffness distribution (Burman Ingeberg et al., 2025), making this voxel-wise approach an important development that removes dependence on assumed global parameters. Using this approach, brain tissue stiffness was estimated at 5-6 Pa. Similarly, wavelength analysis with intrinsic activation steady-state MRE yielded an absolute complex shear modulus of 21 Pa (Herthum et al., 2021). Together, these findings indicate that the brain in its natural state is considerably softer than previously believed.

This insight carries important implications for computational modeling, as accurate simulations of brain mechanics rely on accurate stiffness estimates to reliably predict deformation under physiological and pathological conditions. It also highlights the brain's vulnerability to even small mechanical stresses and the important role of fluid-structure interactions in normal brain function. Importantly, the brain's extreme softness suggests that during the low-frequency cardiac vibrations measured in iMRE, elastic forces may no longer dominate inertial forces, potentially restoring uniqueness in the viscoelastic iMRE inversion process. Previous reports of non-uniqueness in viscoelastic modeling were likely influenced by the assumption that brain tissue exhibits much higher stiffness, i.e., values around 3 kPa typically observed in MRE (McGarry et al., 2019). In these cases, lower bounds on stiffness - typically around 100 Pa - were imposed to prevent the inversion from producing values considered unrealistically low (Burman Ingeberg et al., 2023; McGarry et al., 2019). However, these bounds can constrain convergence during inversion and artificially scale the resulting stiffness estimates, masking the underlying uniqueness of the solution.

In this study, we build on the observation that the brain is ultra-soft in its natural, unperturbed state. We demonstrate that, under these conditions, the balance between inertial and elastic forces in iMRE resembles that of conventional, externally actuated MRE. We further show that viscoelastic inversion in iMRE yields unique and stable in vivo property estimates without the need to impose a lower stiffness bound. Finally, we show that the viscoelastic model produces physically meaningful solutions, consistent with the frequency dependence observed by Herthum et al. (2021) by recovering property estimates at approximately 1, 2 and 3 Hz (using the first, second and third harmonic of the cardiac waveform). This ability to obtain unique iMRE solutions at low frequencies provides additional evidence of the brain's extreme softness, with stiffness values low enough that the elastic forces of intrinsic, cardiac-driven brain deformation are balanced by inertial forces caused by the concomitant tissue motion.

2 Method

2.1 Intrinsic displacement data acquisition

The iMRE displacement data was previously obtained for a separate study by Adams et al., (2020). A brief overview of the acquisition method is provided here as full details are available in the original publication. All subjects gave written-informed consent for participation in the study, which was approved by the ethical review board of our institution.

Eight healthy young adults (three females; mean age: 27 ± 6 years) underwent imaging on a 7T MR scanner (Philips Healthcare) using a Displacement Encoding with Stimulated Echoes (DENSE) (Aletras et al., 1999) sequence with a 3D EPI readout. Cardiac synchronization was achieved through retrospective gating, using pulse oximetry to track the cardiac cycle. The spatial resolution of the acquired images was 1.95 mm × 1.95 mm × 2.2 mm (anterior-posterior, feet-head, right-left), and 20 temporal phases were reconstructed per cardiac cycle. Three separate acquisitions were conducted with displacement encoding (DENC) sensitivities of 0.175 mm, 0.175 mm, and 0.35 mm in the anterior-posterior (AP), right-left (RL), and foot-head (FH) directions, respectively. The time of acquisition per motion encoding direction was 144 heartbeats (corresponding to 2:24 minutes for an average heart rate of 60 beats per minute).

A Fast Fourier Transform (FFT) was applied to the temporal phases at each voxel to convert the displacement data into the frequency domain. Motion components at the first three harmonic frequencies, approximately 1 Hz, 2 Hz, and 3 Hz, were selected for further analysis. Although exact frequencies varied slightly depending on the subject's resting hear rate, the terms "1 Hz", "2 Hz" and "3 Hz" are used for simplicity and clarity.

2.2 Extrinsic displacement data acquisition

The externally actuated MRE displacement data (here referred to as extrinsic data) were obtained in separate, previously published studies (Caban-Rivera et al., 2024; Smith et al., 2022). A brief summary of the acquisition protocol is provided below as the full details can be found in the original publications. All participants provided informed, written consent to participate in this study approved by the Delaware Institutional Review Board.

A total of 38 subjects (19 males, 19 females; mean age: 46 ± 22 years) were scanned on a Siemens 3T Prisma MRI scanner. A pneumatic system (Resoundant, Inc., Rochester, MN) was used to introduce mechanical shear waves into the brain at 50 Hz. Two vibration sources were applied separately: a pillow driver producing AP motion, and a custom-designed LR actuator. The displacement fields from both actuations were acquired with a 3D multiband, multishot spiral sequence (McIlvain, Cerjanic, et al., 2022). Imaging param-

eters included 4 phase offsets, 2.0 mm isotropic voxel resolution, 240x240 mm^2 FOV, 64 slices, and TR/TE = 2240/76 ms.

2.3 Ratio of elastic and inertial forces

The equation of motion for a heterogeneous viscoelastic material, without internal body forces, can be written in the frequency domain as

$$\nabla \cdot G^*\left(\nabla u + \nabla u^T\right) + \nabla(\lambda \nabla \cdot u) = -\rho\omega^2 u, \qquad (1)$$

where u is the 3D complex-valued motion amplitude, λ is Lamé's first constant [Pa], ρ is the density [kg/m^3], and ω is the actuation frequency [rad/sec]. The complex-valued shear modulus G^* [Pa] consists of the storage modulus G' and the loss modulus G'', such that $G^* = G' + iG''$. The left-hand side of Equation (1) describes the elastic forces while the right-hand side describes the inertial forces.

Using this formulation, the ratio of elastic to inertial forces - capturing their balance - was calculated for three specific cases:

1. Extrinsic data at 2600 Pa: Extrinsic motion fields were evaluated at a global brain stiffness of 2600 Pa with an actuation frequency of 50 Hz. This value corresponds approximately to the average brain stiffness measured by standard MRE at 50 Hz (Hiscox et al., 2020)
2. Intrinsic data at 4 - 35 Pa: Intrinsic motion fields were evaluated across a range of global brain stiffnesses from 4 Pa to 35 Pa, representing the approximate lower and upper bounds obtained using intrinsic-actuation based methods at approximately 1 Hz (Burman Ingeberg et al., 2025; Herthum et al., 2021).
3. Intrinsic data at 2600 Pa: Intrinsic motion fields were also evaluated at a global brain stiffness of 2600 Pa with an actuation frequency of 1 Hz, reflecting previous assumptions on brain stiffness and allowing direct comparison to the extrinsic case.

For all cases, the density was set to ρ = 1000 kg m^{-3} and Lamé's first constant was set to $\lambda = 10G'$ to model near-incompressibility of soft tissue. The damping ratio $\xi = G''/2G'$ was set to 0.2, consistent with reported values for both extrinsic and intrinsic MRE (Burman Ingeberg et al., 2023; Hiscox et al., 2020).

2.4 Viscoelastic property estimation

For all following iMRE experiments, viscoelastic property values were estimated using a subzone-based non-linear inversion (NLI) scheme (McGarry et al., 2012; Van Houten et al., 2001), which incorporated quadratic hexahedral finite element models generated from each subject's displacement data. A mesh size of 2.0 mm^3 was used, along with a subzone size of 20 mm^3 and 800 global iterations. A more detailed description of this methodology

is provided by Burman Ingeberg et al., (2023). Viscoelastic inversion recovers the complex shear modulus $G^* = G' + iG''$.

2.5 Initial condition assessment

To assess convergence of the viscoelastic iMRE inversion at 1 Hz, five separate inversions were performed for each subject using different initial conditions for the storage and loss moduli (G', G''): [1, 0.2], [5, 1], [10, 2], [20, 4], and [50, 10]. Under conditions where the inverse problem is well-posed and the solution is unique; converged property estimates should be independent of the initial condition. No lower bounds were imposed on the storage and loss moduli in order to avoid artificially constraining the inversion or biasing the solution toward a predefined minimum.

2.6 Viscoelastic frequency dependence

The frequency dependence of the viscoelastic model was assessed by performing viscoelastic inversion on the 1 Hz, 2 Hz and 3 Hz motion components for each subject. If the model yields unique and physically meaningful solutions, the recovered property values are expected to increase with frequency (Herthum et al., 2021). Analysis was limited to the first three harmonic components due to a substantial decline in signal-to-noise ratio (SNR) at higher frequencies. For all inversions, the initial conditions for G' and G'' were set to 30 Pa and 6 Pa, respectively. Lamé's first constant was set 10 times the initial guess for G'.

The resulting mean global property estimates were directly compared to a dispersion curve measured by Herthum et al., (2021) by converting the estimated complex shear modulus to shear wave speed (SWS) using

$$SWS = \sqrt{\frac{2(G'^2+G''^2)}{\rho\left(G'+\sqrt{G'^2+G''^2}\right)}}. \qquad (2)$$

Here, ρ represents the tissue density and was set to ρ = 1000 kg m^{-3}. Following the approach of Herthum et al., (2021) both viscous- and Kelvin-Voigt models were fitted to our data and to Herthum's data using a nonlinear least-squares algorithm. The viscous model can be expressed as

$$G^* = i\omega\eta, \qquad (3)$$

and the Kelvin-Voigt model by

$$G^* = G' + i\omega\eta, \qquad (4)$$

where η is the viscosity. For the least-squares fitting, data above 3 Hz were obtained from Herthum et al. (2021), data in the 2-3 Hz range were taken from the iMRE in the present study, and the 1 Hz data was calculated as the mean of both datasets.

3 Results

3.1 Balance of inertial and elastic forces

The ratio between the inertial and elastic forces was successfully calculated using Equation 1 for all subjects for both intrinsic and extrinsic displacement data. The mean ratio (inertial/elastic) across all subjects was 107 ± 34 for extrinsic actuation at 2600 Pa, spanned from 627 to 5490 for intrinsic actuation at 4 - 35 Pa, and $4.1 \times 10^5 \pm 4.7 \times 10^4$ for intrinsic actuation at 2600 Pa. Figure 1 presents boxplots displaying the distribution of force ratios across subjects for each respective situation. Intrinsic actuation within the 4-35 Pa stiffness range yielded force ratios at the lowest stiffness that were within half an order of magnitude of those observed for extrinsic actuation at 2600 Pa. At the upper end of the range, the force ratios increased to approximately 2.5 orders of magnitude. In contrast, intrinsic actuation at 2600 Pa produced ratios nearly four orders of magnitude higher than extrinsic actuation at the same stiffness.

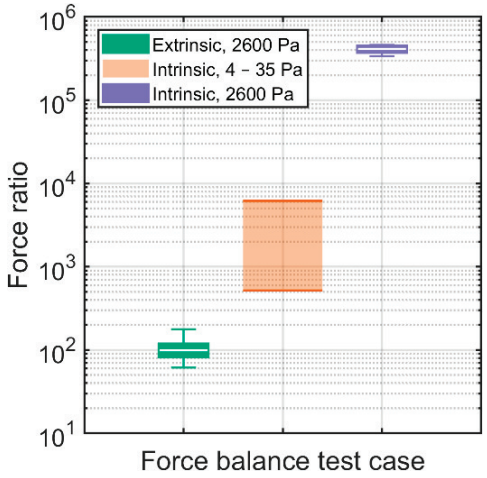


Figure 1: Boxplots of the distribution of force ratios across subjects for three cases: extrinsic actuation at 2600 Pa and 50 Hz, intrinsic actuation at 1 Hz with global brain stiffness spanning 4-35 Pa (visualized as a shaded range in the figure), and intrinsic actuation at 1 Hz at a brain stiffness of 2600 Pa. In each boxplot, the edges represent the 25th and 75th percentiles, the whiskers show the minimum and maximum values within 1.5x the interquartile range, and the white line indicates the mean.

3.2 Initial condition assessment

The iMRE viscoelastic properties were successfully reconstructed for all subjects and across all initial conditions. The mean global storage and loss moduli across subjects are presented in Table 1. Figure 1a shows storage modulus maps, and Figure 1b shows loss modulus maps for a representative subject under different initial conditions. Conver-

gence plots for both moduli are presented in Figures 1c and 1d, while Figures 1e and 1f display violin plots summarizing the mean values across subjects for the storage and loss moduli, respectively. Regardless of the initial conditions, all subjects converged toward similar mean property values. However, the loss modulus converged considerably slower than the storage modulus, failing to fully stabilize after 800 iterations when initialized at particularly low values (e.g., 0.2 Pa). These effects are evident in both the loss modulus maps and the decreased values observed at the 800th iteration for the 0.2 Pa initialization. Consequently, the storage modulus exhibited slightly higher final values for the 1 Pa initial condition. Despite these differences, the storage modulus retained a consistent spatial distribution across different initial conditions.

Table 1: Global storage and loss moduli (mean ± standard deviation across subjects) for different initial conditions.

Initial conditions [G′, G″] [Pa]	**[1, 0.2]**	**[5, 1]**	**[10, 2]**	**[20, 4]**	**[50, 10]**
G′ [Pa]	5.48 ± 0.94	5.33 ± 0.94	5.29 ± 0.92	5.28 ± 0.91	5.33 ± 0.86
G″ [Pa]	0.57 ± 0.34	0.78 ± 0.33	0.82 ± 0.34	0.85 ± 0.35	0.84 ± 0.35

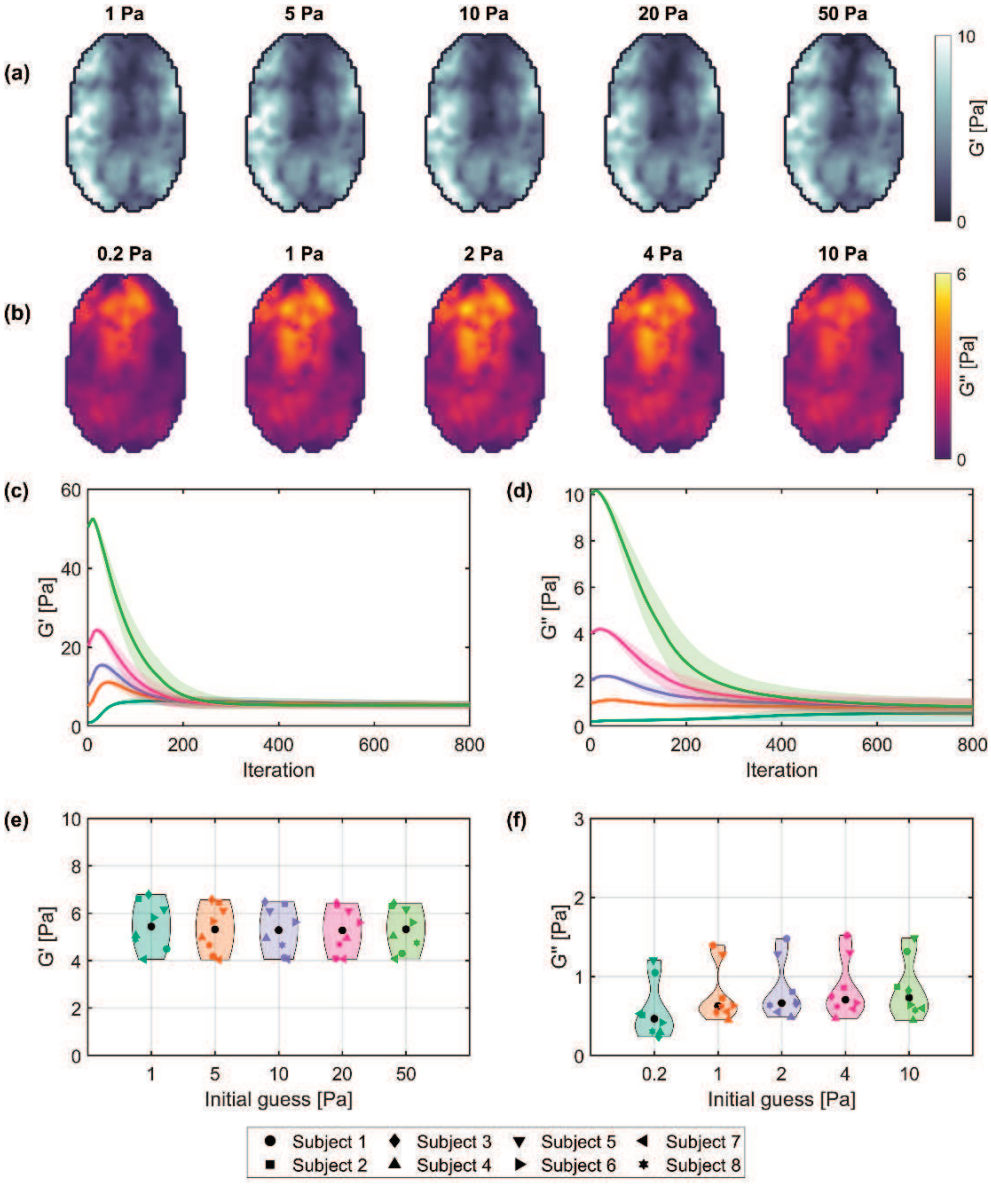


Figure 2: Property maps for Subject 1 at different initial conditions: (a) storage modulus and (b) loss modulus. The loss modulus failed to fully stabilize when initialized at 0.2 Pa due to slower convergence. Convergence plots across all subjects for the storage modulus (c) and loss modulus (d) across initial conditions. Solid lines indicate mean values across subjects, and shaded areas represent the standard deviation. Violin plots in (e) and (f) show the distribution of mean storage and loss moduli, respectively, at the final iteration.

3.3 Viscoelastic frequency dependence

The storage and loss moduli were successfully reconstructed for the 1 Hz, 2 Hz, and 3 Hz motion components for all subjects. Representative axial slices of the corresponding storage and loss modulus maps are provided in Figures S1 and S2 of the supplementary material. The mean storage modulus across all subjects after 800 iterations was 5.29 ± 0.95 Pa at 1 Hz, 34 ± 17 Pa at 2 Hz, and 160 ± 98 Pa at 3 Hz. Similarly, the mean loss modulus across all subjects was 0.85 ± 0.38 Pa at 1 Hz, 6.8 ± 3.8 Pa at 2 Hz, and 12.8 ± 7.6 Pa at 3 Hz. Figure 3 shows the corresponding mean convergence plots. Both the storage and loss moduli exhibited an increase with rising frequency, consistent with frequency dependent behavior of viscoelastic material. The variability, as reflected by the standard deviation across subjects, increased considerably at higher frequencies, which can be attributed to the progressive reduction in signal-to-noise ratio (SNR) with each incremental frequency.

Both the viscous and Kelvin-Voigt models were fitted successfully, resulting in η = 6.1 Pa·s for the viscous model and G' = 40 Pa, η = 6.5 Pa·s for the Kelvin-Voigt model. The corresponding model fits are presented in Figure 4, together with shear wave speeds calculated from the storage and loss moduli using Equation 2, and higher-frequency measurements reported by Herthum et al., (2021).

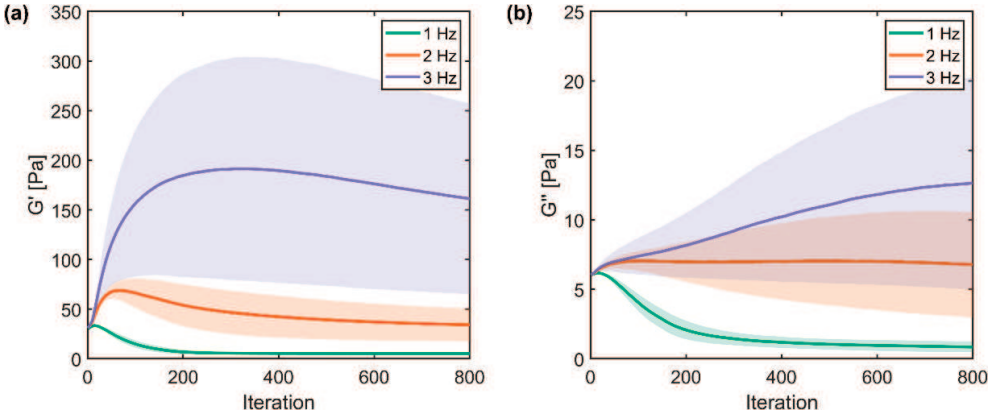


Figure 3: Convergence plots across for the storage modulus (a) and loss modulus (b) for the 1 Hz, 2 Hz, and 3 Hz motion components. The solid line represents the mean across all subjects, with the shaded area representing the corresponding standard deviation.

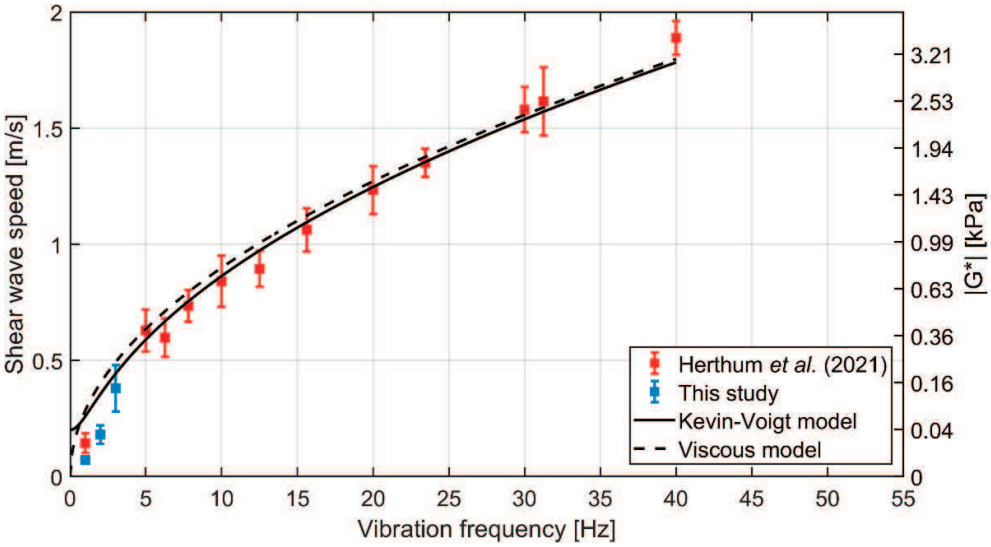


Figure 4: Dispersion curve showing the frequency dependence of shear wave speed (left y-axis) or absolute complex shear modulus |*G**| (right y-axis) for the present study and for the data reported by Herthum et al., (2021). The dots indicate mean values while whiskers indicate standard deviation. Solid and dashed lines show model fits using a Kelvin–Voigt and a viscous model, respectively. The right y-axis was calculated using $SWS = \sqrt{(2\,|G^*|)/(\rho(1+cos(\phi)))}$ with $\varphi = 0$ to provide an approximate conversion to the magnitude of the complex shear modulus.

4 Discussion

Viscoelastic inversion in low-frequency settings such as iMRE has been considered ill-posed due to an assumed imbalance between elastic and inertial forces, leading to non-unique solutions. To address this, inversion pipelines commonly impose lower-bound stiffness constraints to enforce convergence. However, recent hints of the ultra-soft nature of the brain in its natural state, and the findings of our current study challenge the necessity of this assumption. We present multiple lines of evidence demonstrating that viscoelastic inversion at 1 Hz yields unique and physiologically meaningful stiffness estimates, without the need for artificial regularization via stiffness floors.

The uniqueness of viscoelastic solutions in iMRE depends on the balance between elastic and inertial forces, which in turn is influenced by tissue stiffness and actuation frequency. In this analysis, global stiffness values spanning 4 - 35 Pa were used to compute the elastic-inertial force balance, representing literature-based estimates for brain stiffness under intrinsic actuation without imposing arbitrary lower boundaries (Burman Ingeberg et al., 2025; Herthum et al., 2021). The resulting ratios ranged from values within approximately half an order of magnitude of those observed for extrinsic actuation at the lowest stiffness, to up to 2.5 orders of magnitude higher at the upper end of the range. In contrast,

assuming a stiffness of 2600 Pa for intrinsic actuation yielded a force ratio more than three orders of magnitude greater than in the extrinsic case, placing the system deep within an elastic-dominated regime where non-uniqueness is expected. These results suggest that intrinsic actuation at low stiffnesses produces force balances more comparable to extrinsic conditions, whereas increasing stiffness markedly amplifies the imbalance and likely contributes to non-unique viscoelastic reconstructions. This may help explain why previous studies have reported non-uniqueness in viscoelastic inversions at 1 Hz, where assumed stiffness values were as high as 3.3 kPa (McGarry et al., 2019).

If the viscoelastic model yields unique solutions, the inversion process should converge to similar property maps regardless of the initial conditions, provided sufficient time for convergence. In this study we observed that both the storage and loss moduli reached nearly identical global mean values across a range of different initializations. This led to nearly identical global means and spatial distributions of the storage and loss moduli, regardless of initial conditions, even without stiffness lower bounds that could artificially enforce consistency. Furthermore, very similar mean stiffness values were obtained across subjects, with the viscoelastic inversion yielding a mean of 5.29 Pa, closely matching previously obtained poroelastic (6.09 Pa) and poroviscoelastic (5.33 Pa) inversions (Burman Ingeberg et al., 2025). This also highlights the tendency for slightly higher stiffness estimates when the loss modulus is not modeled, as in the purely poroelastic inversion.

However, when the loss modulus was initialized at 0.2 Pa, the inversion did not have sufficient time to fully converge, leading to noticeable differences in the final results. In general, the loss modulus converged considerably more slowly than the storage modulus, contributing to larger discrepancies in the property maps at the final iteration. This behavior is likely related to the use of a purely viscoelastic model at low actuation frequencies, where poroelastic effects become more prominent (McGarry et al., 2019). In such conditions, poroelastic damping in the brain is inadequately captured by a viscous model, causing the loss modulus to poorly represent the observed attenuation and consequently to converge more slowly. This also likely explains the slight increase observed in the global mean storage modulus for the 1 Pa initial condition, highlighting the importance of appropriate initial conditions for effective convergence, particularly for the loss modulus.

The viscoelastic properties of brain tissue generally show a strong frequency dependence. If the viscoelastic model yields unique, physically meaningful solutions, an increase in property values with increasing frequency would be expected. This trend was consistently observed across all subjects, providing additional support for uniqueness. However, the relative amplitude of the motion decreases for higher harmonics, leading to a corresponding reduction in the signal-to-noise ratio (SNR) which considerably af-

fects the quality of the property estimates. This, in turn, can make convergence difficult and was reflected in the larger inter-subject variability observed in the storage and loss moduli at 2 Hz and 3 Hz. This effect was most pronounced at 3 Hz, where the final property estimates should be interpreted with caution.

The observed frequency dependence closely resembled the dispersion behavior reported by Herthum et al., (2021), as shown in Figure 4, with a steep increase in stiffness at low frequencies. The measured values at the lowest frequencies were, however, consistently lower than predicted by the both the viscous- and Kelvin-Voigt models. This deviation is expected, as the viscoelastic model provides an incomplete description of brain mechanics at low actuation frequencies, where poroelastic effects start to dominate. When the fluid equilibration timescale approaches the motion period, as at 1 Hz, poroelastic modeling is required for accurate reconstruction. At higher frequencies, the equilibration time becomes much longer than the oscillation period, and the viscoelastic model serves as an adequate and simpler approximation of poroelastic behavior (McGarry et al., 2019, 2015).

The evidence presented above strongly supports the ability of viscoelastic inversion to yield unique solutions in iMRE. Notably, the very existence of such unique solutions at low frequencies can itself be interpreted as indirect evidence of the brain's ultra-soft nature, as only in this regime do elastic and inertial forces remain sufficiently balanced to prevent non-uniqueness. To better understand this regime, it is useful to compare iMRE-derived stiffness values with those obtained from mechanical testing, which are typically much higher (0.4–1.4 kPa (Budday et al., 2017b)). Several factors likely contribute to this discrepancy. First, mechanical testing is generally performed on post-mortem brain tissue. While stiffness has been reported to remain relatively stable for hours to days post-mortem under appropriate preservation (Budday et al., 2017b, 2020), other studies using nanoindentation in bovine tissue observed substantial early stiffening, with increases of 26 % in the cerebrum and 58 % in the corpus callosum after only 3 minutes, rising to 41 % and 142 % after 45 minutes, respectively (Weickenmeier et al., 2018). Second, mechanical testing and iMRE probably probe different stress regimes. Whereas mechanical testing typically applies stresses on the order of 0.1 – 2 kPa (Budday et al., 2020; Chatelin et al., 2010; Hou et al., 2025), iMRE relies on subtle cardiac-induced brain pulsations. Although precise estimates of such stresses have yet to be determined, they are likely considerably smaller than that of mechanical testing, producing strains of 10^{-4} - 10^{-2} (Adams et al., 2020; Hirsch et al., 2013; Sloots et al., 2021), compared to up to 10% used in mechanical testing (Budday et al., 2020). Because biological tissue generally does not exhibit a linear stress-strain relationship over wider stress ranges, lower applied stresses may correspond to lower apparent stiffnesses. Third, the brain is a highly porous solid matrix saturated with interstitial and vascular fluids. At the low actuation frequencies used in iMRE, these fluids have sufficient time to redistribute in response to deformation, effectively reducing

the tissue's mechanical resistance. Indeed, recent work has shown that recovery of brain tissue after indentation occurs on the order of seconds (Liu et al., 2025) supporting the view that lower actuation frequencies naturally capture this redistribution and explaining why porous models are most appropriate for interpreting measurements in this regime (McGarry et al., 2019).

While the points discussed above may account for some of the discrepancies in stiffness estimates between iMRE and mechanical testing, they are unlikely to provide a complete explanation. Rather, iMRE appears to capture a distinct aspect of brain tissue mechanics, where the brain's suspension and perfusion by fluid in a living, dynamic system play a major role, producing consistently low stiffness values that suggest an almost fluid-like response at low frequencies. Recent work on poroviscoelastic modeling highlights the importance of Lamé's first constant, representing resistance to volumetric deformation, in governing fluid flow (Greiner et al., 2024). Higher values, corresponding to a stiffer brain, restrict fluid movement and lead to physically unrealistic behavior. This suggests that low stiffness may be key in maintaining healthy fluid dynamics, both in waste clearance and in vascular perfusion. In this line, one could speculate that lower brain stiffness is a means of optimizing fluid regulation. Taken together, these observations indicate that the brain's mechanical and structural integrity depends on both the surrounding fluid and the protective enclosure provided by the skull. Unlike organs such as the liver, which lack rigid external protection, the skull allows the brain to maintain its exceptionally low stiffness without compromising structural stability.

An intriguing consequence of this perspective is that systemic factors, such as cardiovascular dynamics, could modulate effective brain stiffness. For instance, lower resting heart rates - particularly during sleep - may effectively soften the brain. This, in turn, could further facilitate fluid movement and waste clearance, consistent with observations that metabolic waste removal in the brain is enhanced during sleep (Xie et al., 2013). Recent studies further support this link, demonstrating that lower heart rates are associated with enhanced clearance (Dagum et al., 2025; Hablitz et al., 2019). However, these notions remain speculative, and further work is needed to clarify the precise relationships between brain stiffness, cardiovascular dynamics, and fluid clearance.

While currently viscoelastic, poroelastic and poroviscoelastic inversions all converge towards similar stiffness estimates of approximately 5-6 Pa, they differ considerably to the 21 Pa measured by Herthum et al., (2021). However, their estimation is based on a purely elastic model, which ignores viscous effects and may produce higher apparent stiffnesses. This phenomenon would be consistent with our earlier observation that the purely poroelastic model estimates higher stiffness than the viscoelastic and poroviscoelastic model. That said, it is also possible that our own estimates slightly underestimate the true values.

Therefore, a limitation of this study is that our current iMRE framework has not yet been validated in phantom experiments. Therefore, future work aims to perform validation studies in sufficiently soft, well-characterized phantoms where the elastic-inertial force balance permits unique viscoelastic reconstructions.

5 Conclusion

This study demonstrates that viscoelastic inversion in intrinsic MR elastography can yield unique and physiologically meaningful property estimates. Due to the ultra-soft nature of the brain under low actuation frequencies, we show that the balance between elastic and inertial forces more closely resembles that of conventional MRE, thereby restoring uniqueness in the inversion process. The resulting viscoelastic properties converge consistently across varying initial conditions, display frequency dependence consistent with prior literature, and provide similar stiffness estimates as poroelastic and poroviscoelastic models - all without imposing artificial stiffness bounds. This work further establishes the brain as ultra-soft in its intact state under low actuation frequencies and addresses a major limitation of the viscoelastic model in intrinsic MR elastography.

6 Acknowledgements

We would like to thank Dr. Curtis Johnson for kindly providing the dataset that supported this research, and to Dr. Helge Herthum for contributing the data used in Figure 4.

7 References

Adams, A. L., Viergever, M. A., Luijten, P. R., & Zwanenburg, J. J. M. (2020). Validating faster DENSE measurements of cardiac-induced brain tissue expansion as a potential tool for investigating cerebral microvascular pulsations. *NeuroImage*, *208*, 116466. https://doi.org/10.1016/j.neuroimage.2019.116466

Aletras, A. H., Ding, S., Balaban, R. S., & Wen, H. (1999). DENSE: displacement encoding with stimulated echoes in cardiac functional MRI. *Journal of Magnetic Resonance (San Diego, Calif. : 1997)*, *137*(1), 247–252. https://doi.org/10.1006/jmre.1998.1676

Budday, S., Ovaert, T. C., Holzapfel, G. A., Steinmann, P., & Kuhl, E. (2020). Fifty Shades of Brain: A Review on the Mechanical Testing and Modeling of Brain Tissue. *Archives of Computational Methods in Engineering*, *27*(4), 1187–1230. https://doi.org/10.1007/s11831-019-09352-w

Budday, S., Sommer, G., Birkl, C., Langkammer, C., Haybaeck, J., Kohnert, J., Bauer, M., Paulsen, F., Steinmann, P., Kuhl, E., & Holzapfel, G. A. (2017). Mechanical characterization of human brain tissue. *Acta Biomaterialia*, *48*, 319–340. https://doi.org/10.1016/j.actbio.2016.10.036

Burman Ingeberg, M., Van Houten, E., & Zwanenburg, J. J. M. (2023). Estimating the viscoelastic properties of the human brain at 7T MRI using intrinsic MRE and nonlinear inversion. *Human Brain Mapping*, *44*(18), 6575–6591. https://doi.org/10.1002/hbm.26524

Burman Ingeberg, M., Van Houten, E., & Zwanenburg, J. J. M. (2025). Evaluating the Performance and Repeatability of Poroelastic and Poroviscoelastic Models in Intrinsic MR Elastography. *NMR in Biomedicine*, *38*(7), e70073. https://doi.org/10.1002/nbm.70073

Caban-Rivera, D. A., Williams, L. T., McGarry, M. D. J., Smith, D. R., Van Houten, E. E. W., Paulsen, K. D., Bayly, P. V., & Johnson, C. L. (2024). *Mechanical Properties of White Matter Tracts in Aging Assessed via Anisotropic MR Elastography*. https://doi.org/10.1101/2024.05.08.593260

Chatelin, S., Constantinesco, A., & Willinger, R. (2010). Fifty years of brain tissue mechanical testing: From in vitro to in vivo investigations. *Biorheology: The Official Journal of the International Society of Biorheology*, *47*(5–6), 255–276. https://doi.org/10.3233/BIR-2010-0576

Dagum, P., Giovangrandi, L., Levendovszky, S. R., Winebaum, J. J., Singh, T., Cho, Y., Kaplan, R. M., Jaffee, M. S., Lim, M. M., Vandeweerd, C., & Iliff, J. J. (2025). A wireless device for continuous measurement of brain parenchymal resistance tracks glymphatic function in humans. *Nature Biomedical Engineering*. https://doi.org/10.1038/s41551-025-01394-9

Greiner, A., Reiter, N., Hinrichsen, J., Kainz, M. P., Sommer, G., Holzapfel, G. A., Steinmann, P., Comellas, E., & Budday, S. (2024). Model-driven exploration of poro-viscoelasticity in human brain tissue: be careful with the parameters! *Interface Focus*, *14*(6). https://doi.org/10.1098/rsfs.2024.0026

Guo, J., Bertalan, G., Meierhofer, D., Klein, C., Schreyer, S., Steiner, B., Wang, S., Vieira da Silva, R., Infante-Duarte, C., Koch, S., Boehm-Sturm, P., Braun, J., & Sack, I. (2019). Brain maturation is associated with increasing tissue stiffness and decreasing tissue fluidity. *Acta Biomaterialia*, *99*, 433–442. https://doi.org/10.1016/j.actbio.2019.08.036

Hablitz, L. M., Vinitsky, H. S., Sun, Q., Stæger, F. F., Sigurdsson, B., Mortensen, K. N., Lilius, T. O., & Nedergaard, M. (2019). Increased glymphatic influx is correlated with high EEG delta power and low heart rate in mice under anesthesia. *Science Advances*, *5*(2), eaav5447. https://doi.org/10.1126/sciadv.aav5447

Herthum, H., Dempsey, S. C. H., Samani, A., Schrank, F., Shahryari, M., Warmuth, C., Tzschätzsch, H., Braun, J., & Sack, I. (2021). Superviscous properties of the in vivo brain at large scales. *Acta Biomaterialia*, *121*, 393–404. https://doi.org/10.1016/j.actbio.2020.12.027

Hirsch, S., Klatt, D., Freimann, F., Scheel, M., Braun, J., & Sack, I. (2013). In vivo measurement of volumetric strain in the human brain induced by arterial pulsation and harmonic waves. *Magnetic Resonance in Medicine*, *70*(3), 671–683. https://doi.org/10.1002/mrm.24499

Hiscox, L. V., McGarry, M. D. J., Schwarb, H., Van Houten, E. E. W., Pohlig, R. T., Roberts, N., Huesmann, G. R., Burzynska, A. Z., Sutton, B. P., Hillman, C. H., Kramer, A. F., Cohen, N. J., Barbey, A. K., Paulsen, K. D., & Johnson, C. L. (2020). Standard-space atlas of the viscoelastic properties of the human brain. *Human Brain Mapping*, *41*(18), 5282–5300. https://doi.org/10.1002/hbm.25192

Hou, J., Jiang, K., Ramanathan, A., Kumar, A. S., Zhang, W., Zhao, L., Wu, T., Pidaparti, R., Zhu, D., Li, G., Song, K., Liu, T., Razavi, M. J., Kuhl, E., & Wang, X. (2025). Mechanical Characterization of Brain Tissue: Experimental Techniques, Human Testing Considerations, and Perspectives. *ArXiv*.

Johnson, C. L., McGarry, M. D. J., Van Houten, E. E. W., Weaver, J. B., Paulsen, K. D., Sutton, B. P., & Georgiadis, J. G. (2013). Magnetic resonance elastography of the brain using multishot spiral readouts with self-navigated motion correction. *Magnetic Resonance in Medicine*, *70*(2), 404–412. https://doi.org/10.1002/mrm.24473

Liu, F., Gao, B., Lei, L., Liu, S., Li, H., & Guo, M. (2025). Intercellular flow dominates the poroelasticity of multicellular tissues. *Nature Physics*, *21*(8), 1311–1318. https://doi.org/10.1038/s41567-025-02947-0

McGarry, M. D. J., Johnson, C. L., Sutton, B. P., Georgiadis, J. G., Van Houten, E. E. W., Pattison, A. J., Weaver, J. B., & Paulsen, K. D. (2015). Suitability of poroelastic and viscoelastic mechanical models for high and low frequency MR elastography. *Medical Physics*, *42*(2), 947–957. https://doi.org/10.1118/1.4905048

McGarry, M. D. J., Van Houten, E. E. W., Johnson, C. L., Georgiadis, J. G., Sutton, B. P., Weaver, J. B., & Paulsen, K. D. (2012). Multiresolution MR elastography using nonlinear inversion. *Medical Physics*, *39*(10), 6388–6396. https://doi.org/10.1118/1.4754649

McGarry, M., Van Houten, E., Solamen, L., Gordon-Wylie, S., Weaver, J., & Paulsen, K. (2019). Uniqueness of poroelastic and viscoelastic nonlinear inversion MR elastography at low frequencies. *Physics in Medicine and Biology*, *64*(7), 075006. https://doi.org/10.1088/1361-6560/ab0a7d

McIlvain, G., Cerjanic, A. M., Christodoulou, A. G., McGarry, M. D. J., & Johnson, C. L. (2022). OSCILLATE: A low-rank approach for accelerated magnetic resonance elastography. *Magnetic Resonance in Medicine*, *88*(4), 1659–1672. https://doi.org/10.1002/mrm.29308

McIlvain, G., Schneider, J. M., Matyi, M. A., McGarry, M. D., Qi, Z., Spielberg, J. M., & Johnson, C. L. (2022). Mapping brain mechanical property maturation from childhood to adulthood. *NeuroImage*, *263*, 119590. https://doi.org/10.1016/j.neuroimage.2022.119590

Pavuluri, K., Huston, J., Ehman, R. L., Manduca, A., Jack, C. R., Senjem, M. L., Vemuri, P., & Murphy, M. C. (2024). Associations between vascular health, brain stiffness and global cognitive function. *Brain Communications*, *6*(2). https://doi.org/10.1093/braincomms/fcae073

Sloots, J. J., Biessels, G. J., de Luca, A., & Zwanenburg, J. J. M. (2021). Strain Tensor Imaging: Cardiac-induced brain tissue deformation in humans quantified with high-field MRI. *NeuroImage*, *236*, 118078. https://doi.org/10.1016/j.neuroimage.2021.118078

Smith, D. R., Caban-Rivera, D. A., McGarry, M. D. J., Williams, L. T., McIlvain, G., Okamoto, R. J., Van Houten, E. E. W., Bayly, P. V., Paulsen, K. D., & Johnson, C. L. (2022). Anisotropic mechanical properties in the healthy human brain estimated with multi-excitation transversely isotropic MR elastography. *Brain Multiphysics*, *3*, 100051. https://doi.org/10.1016/j.brain.2022.100051

Solamen, L. M., McGarry, M. D. J., Fried, J., Weaver, J. B., Lollis, S. S., & Paulsen, K. D. (2021). Poroelastic Mechanical Properties of the Brain Tissue of Normal Pressure Hydrocephalus Patients During

Lumbar Drain Treatment Using Intrinsic Actuation MR Elastography. *Academic Radiology*, *28*(4), 457–466. https://doi.org/10.1016/j.acra.2020.03.009

Takamura, T., Motosugi, U., Sasaki, Y., Kakegawa, T., Sato, K., Glaser, K. J., Ehman, R. L., & Onishi, H. (2020). Influence of Age on Global and Regional Brain Stiffness in Young and Middle-Aged Adults. *Journal of Magnetic Resonance Imaging*, *51*(3), 727–733. https://doi.org/10.1002/jmri.26881

Van Houten, E. E., Miga, M. I., Weaver, J. B., Kennedy, F. E., & Paulsen, K. D. (2001). Three-dimensional subzone-based reconstruction algorithm for MR elastography. *Magnetic Resonance in Medicine*, *45*(5), 827–837. https://doi.org/10.1002/mrm.1111

Weaver, J. B., Pattison, A. J., McGarry, M. D., Perreard, I. M., Swienckowski, J. G., Eskey, C. J., Lollis, S. S., & Paulsen, K. D. (2012). Brain mechanical property measurement using MRE with intrinsic activation. *Physics in Medicine and Biology*, *57*(22), 7275–7287. https://doi.org/10.1088/0031-9155/57/22/7275

Weickenmeier, J., Kurt, M., Ozkaya, E., de Rooij, R., Ovaert, T. C., Ehman, R. L., Butts Pauly, K., & Kuhl, E. (2018). Brain stiffens post mortem. *Journal of the Mechanical Behavior of Biomedical Materials*, *84*, 88–98. https://doi.org/10.1016/j.jmbbm.2018.04.009

Xie, L., Kang, H., Xu, Q., Chen, M. J., Liao, Y., Thiyagarajan, M., O'Donnell, J., Christensen, D. J., Nicholson, C., Iliff, J. J., Takano, T., Deane, R., & Nedergaard, M. (2013). Sleep drives metabolite clearance from the adult brain. *Science (New York, N.Y.)*, *342*(6156), 373–377. https://doi.org/10.1126/science.1241224

Zorgani, A., Souchon, R., Dinh, A.-H., Chapelon, J.-Y., Ménager, J.-M., Lounis, S., Rouvière, O., & Catheline, S. (2015). Brain palpation from physiological vibrations using MRI. *Proceedings of the National Academy of Sciences of the United States of America*, *112*(42), 12917–12921. https://doi.org/10.1073/pnas.1509895112

Supplementary files

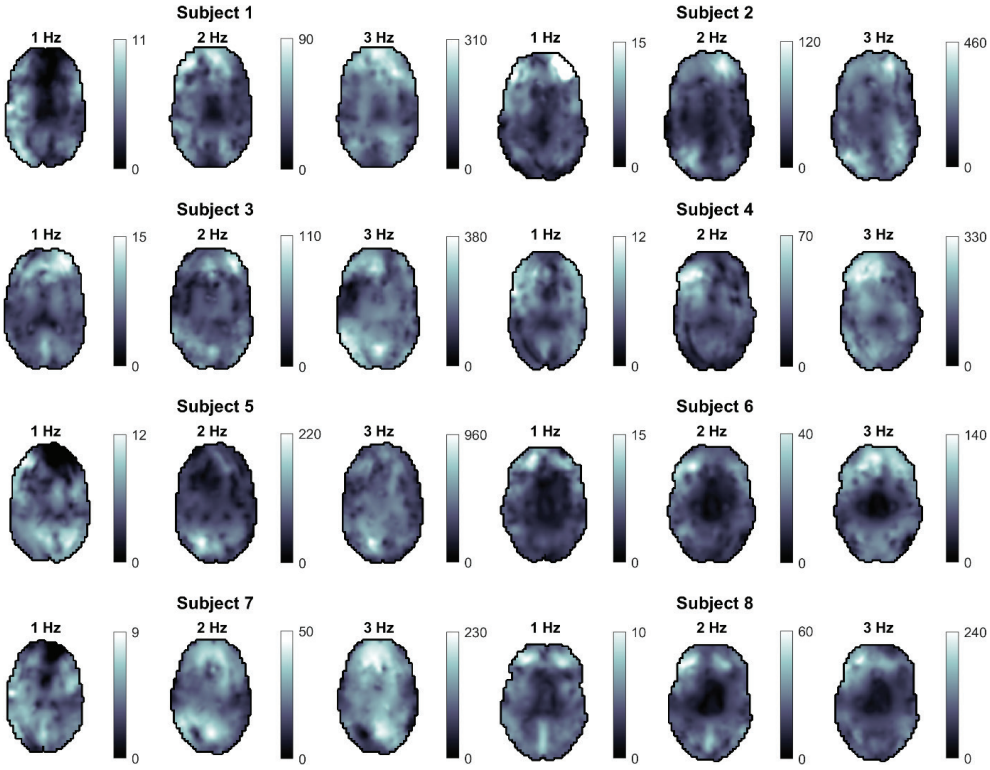


Figure S1: Representative axial slices of storage modulus maps at approximately 1, 2, and 3 Hz for all 8 subjects.

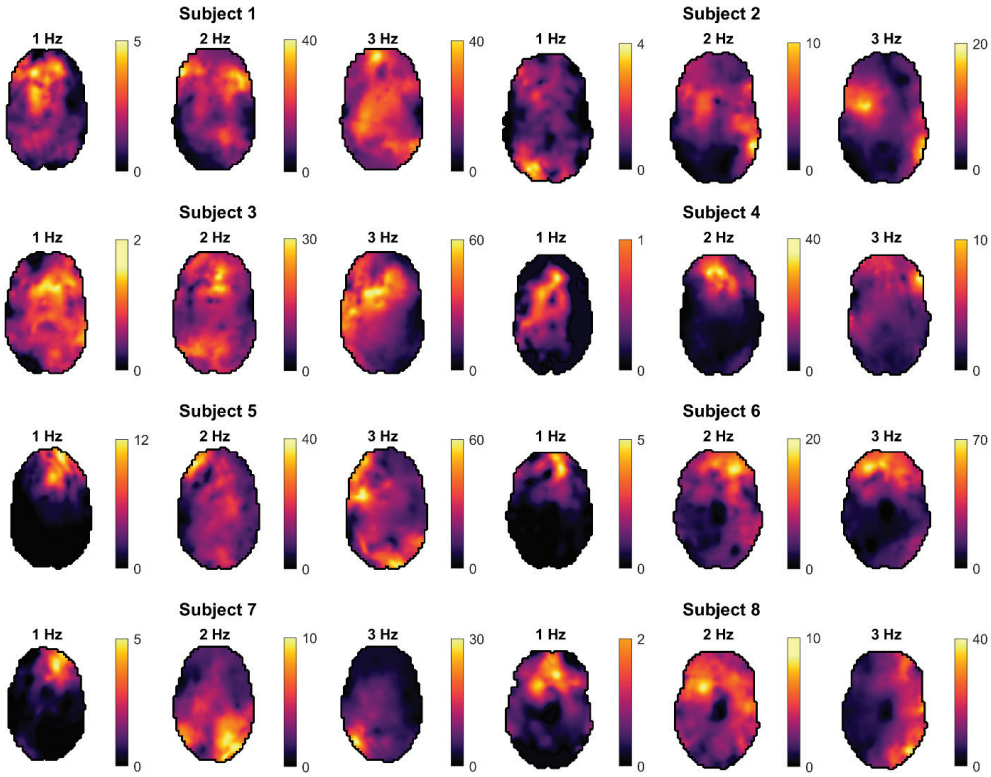


Figure S2: Representative axial slices of loss modulus maps at approximately 1, 2, and 3 Hz for all 8 subjects.



Chapter 5

Exploring the role of vascular factors and tissue properties in pulsatile brain deformation

Marius Burman Ingeberg[1], Elijah Van Houten[2], Andrej Shoykhet[1], Jaco J.M Zwanenburg[1]

[1]Translational Neuroimaging Group, Center for Image Sciences, University Medical Center Utrecht and Utrecht University, Utrecht, The Netherlands

[2]Université de Strasbourg, CNRS, INSERM, ICube, UMR7357, Strasbourg, France.

Original work accepted for publication in NMR in Biomedicine.

Author Contribution Statement:

Marius Burman Ingeberg was responsible for conceptualization, methodology, software development, investigation, formal analysis, data management, and visualization, and wrote the original draft of the manuscript. Eli van Houten contributed to conceptualization, provided supervision and resources, and reviewed and edited the manuscript. Andrej Shoykhet contributed to methodology and software related to data analysis. Jaco Zwanenburg contributed to conceptualization, secured funding, provided resources and supervision, and reviewed and edited the manuscript.

Abstract

Introduction

Strain tensor imaging (STI) provides precise measurements of brain tissue deformation caused by cerebral arterial pulsations (CAP). This CAP-related brain tissue deformation is expressed in rotation-invariant strain metrics, such as volumetric strain and octahedral shear strain, which hold promise as quantitative markers of the (mechanical) properties of both the intracerebral vasculature and the intervascular tissue components. However, the extent to which these strain metrics can be specifically linked to the underlying anatomical vascular and tissue properties remains largely unknown. This study aims to explore the relationship between STI metrics and independent markers of pulse pressure (arterial transit time, ATT), vascular function (cerebral blood volume, CBV; cerebral blood flow, CBF; mean transit time, MTT), and tissue properties (shear stiffness).

Method

Volumetric and octahedral shear strain were computed from previously obtained 7T displacement data (approximately 2 mm isotropic resolution) of eight healthy subjects (27±7 years). Shear stiffness maps were generated from the same displacement data set using poroviscoelastic intrinsic MR elastography. Regional values of CBV, CBF, MTT, and ATT were obtained from standard-space atlases. Linear mixed-effects models were used to investigate potential regional relationships between specific strain metrics and the corresponding tissue, pulse pressure, or vascular markers.

Results

Volumetric strain showed significant positive correlations with CBV (globally, and in cortical gray and white matter) and significant negative correlations with ATT (globally, and in cortical gray and white matter), but not with shear stiffness. Octahedral shear strain showed a significant negative correlation with shear stiffness (globally, and in subcortical gray and white matter) and also with ATT (globally, and in cortical gray matter).

Conclusion

Volumetric strain reflects mainly vascular properties (pulse pressure, blood volume), while octahedral shear strain is more sensitive to tissue properties. These findings provide a foundation for future studies that investigate the physiological characteristics reflected by these strain metrics and their intricate interplay.

1 Introduction

Cerebral arterial pulsations (CAP) driven by the cardiac cycle, generate blood volume changes and subtle tissue deformations throughout the brain. These deformations subsequently drive the movement of cerebrospinal fluid (CSF) (Mestre et al., 2018; Spector et al., 2015; van der Voort et al., 2024) and interstitial fluids (Asgari et al., 2016; Bakker et al., 2016) which are believed to be essential in the clearance of cerebral waste (Iliff et al., 2012; Tarasoff-Conway et al., 2015). As these pulsatile pressure waves are transmitted through the arterial tree to the level of the microvasculature (Hahn et al., 1996), direct or indirect measurements of pulsatility could probe the microvascular condition, such as in small vessel disease. Additionally, tissue perfusion and viscoelastic metrics have been shown to be highly sensitive to physiological effects, ageing and disease (Hetzer et al., 2018).Thus, methods such as *strain tensor imaging* (STI) (Adams et al., 2020; Sloots et al., 2021), that quantify strain resulting from such brain tissue deformations using MRI, have the potential to become valuable tools to assess both the vascular and biomechanical state of the human brain.

STI provides, among others, two metrics that may be of high interest in a clinical setting. The first metric is volumetric strain, which describes the relative expansion or compression of a voxel during CAPs. The second metric is octahedral shear strain, which reflects the deformation of a voxel independent of expansion or compression. Both volumetric strain and octahedral shear strain are rotationally-invariant quantities derived from the strain tensor, meaning that their values are independent of the chosen coordinate system. These metrics are of particular interest as they reflect the state of- and interaction between- vascular and intervascular tissue components of the brain. Meanwhile, the measurement of these strain metrics remains a relatively recent technical achievement, and their specificity to the underlying biological and physiological drivers are still largely unknown. Given the brain's highly dynamic and complex nature, these drivers are likely multifactorial and interdependent. Several factors may contribute to the strain observed in a given voxel, including blood pressure gradients, blood volume fraction, brain tissue stiffness, and vascular wall compliance, among others. Better understanding of the relationship between the strain metrics and the underlying drivers is important for advancing our knowledge of both normal brain function and pathophysiology, particularly in relation to diseases that affect the microvasculature. This, in turn, is an essential first step towards utilizing these metrics in clinical research.

Recent work has achieved high-quality brain tissue strain measurements by leveraging 7T imaging with Displacement Encoding with Stimulated Echoes (DENSE) (Aletras et al., 1999). This sequence achieves high signal-to-noise ratio (SNR) (Adams et al., 2020) because its displacement encoding is optimized for submillimeter motions - the same order

of magnitude as the tissue displacements produced by brain pulsations. Its sensitivity to displacements of the same magnitude as brain pulsations gives DENSE an advantage over other phase contrast techniques. With DENSE, Adams et al. (2020) observed a 2.3-fold difference in peak volumetric strain between gray and white matter, though the underlying cause remains unclear. It was speculated that the differences between tissue types likely result from variations in both blood volume and tissue viscoelasticity. Since then, intrinsic MR elastography (iMRE) has been shown to be feasible, enabling the estimation of shear stiffness from the same displacement measurements used to assess brain tissue strain (Burman Ingeberg et al., 2023, 2025). Shear stiffness has previously been shown to be a reliable indicator of the mechanical integrity of neuronal tissue (Hirsch et al., 2013; Wuerfel et al., 2010), positioning iMRE to potentially disentangle vascular contributions from tissue properties and provide deeper insight into the mechanisms underlying brain strain.

While previous works have established the technical validity of measuring cardiac-induced strain, they did not explicitly investigate how strain metrics relate to vascular and tissue properties in a combined analysis. As a result, the physiological interpretation of volumetric and octahedral shear strain remains largely uncertain. This study aims to investigate potential drivers contributing to volumetric strain and octahedral shear strain during CAPs in the human brain, with a particular focus on distinguishing vascular influences from those related to tissue stiffness. We considered three complementary categories of drivers: (1) pulse pressure effects, approximated by arterial transit time (ATT); (2) vascular and hemodynamic factors, captured by CBV, cerebral blood flow (CBF), and mean transit time (MTT); and (3) tissue properties, represented by shear stiffness. A regional analysis across gray matter (subdivided into cortical and subcortical) and white matter was performed to examine how these drivers influence strain. This study serves as a foundational exploration of drivers of strain, providing a baseline for more focused and specific future experiments.

2 Method

2.1 Acquisition

The analysis presented here is based on displacement data previously collected by Adams et al. (Adams et al., 2020). A detailed description of the data acquisition method is available in the original publication; only a brief summary is provided here. All participants provided written informed consent, and the study was approved by the institution's ethical review board.

Displacement data were acquired from eight healthy young adults (three females; mean age: 27 ± 6 years) using a 3D, time-resolved Displacement Encoding with Stimulated Echoes (DENSE) sequence on a 7T MR scanner (Philips Healthcare) with a segmented EPI readout scheme. Repeated scans were performed, with subjects briefly exiting the scanner for up to 10 minutes between sessions. Retrospective gating synchronized the DENSE measurements with the cardiac cycle, which was detected using pulse oximetry. The spatial resolution of the acquired images was 1.95 mm × 1.95 mm × 2.2 mm (FH x AP x RL), and 20 temporal phases were reconstructed per cardiac cycle. Three separate acquisitions were performed with displacement encoding (D_{enc}) sensitivities of 0.175 mm/π rad, 0.175 mm/π rad, and 0.35 mm/π rad in the anterior-posterior (AP), right-left (RL), and foot-head (FH) directions, respectively. TR was 35/30/35 ms (FH/AP/RL), and the TE was 8.7 ms. The acquisition of each motion encoding direction took 2:24 minutes, for an average heart rate of 60 beats per minute. Additionally, T1-weighted images with a resolution of 0.93 mm × 0.93 mm × 1.0 mm were acquired during both scanning sessions to facilitate segmentation and registration. Tissue probability maps were generated from the T1-weighted images using the Computational Anatomy Toolbox (Jena University Hospital, Departments of Psychiatry and Neurology) extension for SPM12 (Wellcome Trust Centre for Neuroimaging, University College London).

Because of the possibility of subject motion between the three DENSE acquisitions, images from the different motion encodings were registered to the same space. This was done by first rigidly registering the AP and FH magnitude images to the RL magnitude images. Then, the last RL image of the cardiac cycle was non-linearly registered to the corresponding T1-weighted image for each subject. Finally, all images were transformed to the T1-weighted space using the transformation parameters given by the transformation from the RL magnitude image to the T1-weighted image.

Motion artifacts related to physiological noise were identified following the methodology described by Adams et al. (Adams et al., 2020). In short, SNR maps were created by scaling DENSE magnitude images from the end of the cardiac cycle (containing the majority of artifacts) by the temporal standard deviation. The SNR maps were then thresholded to create artifact masks, which were applied to the DENSE measurements. The repeated scan of Subject 7 was excluded as it contained more than twice the number of voxels with motion artifacts in the displacement measurements compared to the average of all other scans.

2.2 Strain computation

The DENSE images were converted to displacement fields by scaling the phase images with the corresponding D_{enc} value for each displacement encoding direction. Displacement gradient fields were then computed by taking the spatial derivatives of the AP, RL,

and FH displacement maps along their respective directions. Phase wraps that occurred due to large numeric derivatives were unwrapped under the small-strain assumption, which assumes that displacement differences between neighboring voxels are smaller than the tag spacing. Hence, the maximum tolerated strain was

$$\varepsilon_{max} = \frac{3}{4}\frac{D_{enc}}{\Delta x},$$

with *Δx* being the distance between neighboring voxels (Sloots et al., 2021), which for the used data is 6.7%, 6.0% and 13% for AP, RL and FH directions, respectively. The deformation gradient tenor ***F*** was then computed as $\boldsymbol{F} = \nabla \boldsymbol{u} + \boldsymbol{I}$, where $\boldsymbol{u_x}$, $\boldsymbol{u_y}$, $\boldsymbol{u_z}$ are the displacement fields in the RL, AP and FH directions respectively, and ***I*** is the identity matrix. Finally, the Lagrangian strain tensor ***E*** was constructed as

$$E = \frac{1}{2}\left(F^T F - I\right) = \begin{pmatrix} \varepsilon_{xx} & \varepsilon_{xy} & \varepsilon_{xz} \\ \varepsilon_{yx} & \varepsilon_{yy} & \varepsilon_{yz} \\ \varepsilon_{zx} & \varepsilon_{zy} & \varepsilon_{zz} \end{pmatrix}.$$

Two properties of interest can be derived from the tensor ***E***, the volumetric strain and the octahedral shear strain. Volumetric strain reflects the net expansion or compression of a given voxel, and is calculated from the diagonal of ***E*** as

$$\varepsilon_V = \frac{\Delta V}{V} \approx \varepsilon_{xx} + \varepsilon_{yy} + \varepsilon_{zz}.$$

Octahedral shear strain reflects the deformation of a voxel, independent of the volumetric strain, and is calculated as (McGarry et al., 2011)

$$\varepsilon_S = \frac{2}{3}\sqrt{\left(\varepsilon_{xx} - \varepsilon_{yy}\right)^2 + \left(\varepsilon_{xx} - \varepsilon_{zz}\right)^2 + \left(\varepsilon_{yy} - \varepsilon_{zz}\right)^2 + 6\left(\varepsilon_{xy}^2 + \varepsilon_{xz}^2 + \varepsilon_{yz}^2\right)}.$$

Zero octahedral shear strain indicates isotropic expansion or compression of a voxel, while larger values indicate shear deformation. (McGarry et al., 2011)Absolute volumetric strain values exceeding 2% and octahedral shear strain values exceeding 4% were excluded from analysis (Adams et al., 2020). These thresholds were based empirically on the observations that these values are beyond the roughly 99% percentile of the strain histogram, and often occur at locations with partial-volume effects with CSF, large blood vessels, or residual artifacts. As the magnitude of these strains vary over the cardiac cycle, peak strains were chosen as the metric of interest. The full mean volumetric strain and octahedral shear strain waveforms over the cardiac cycle are presented in Figure 1.

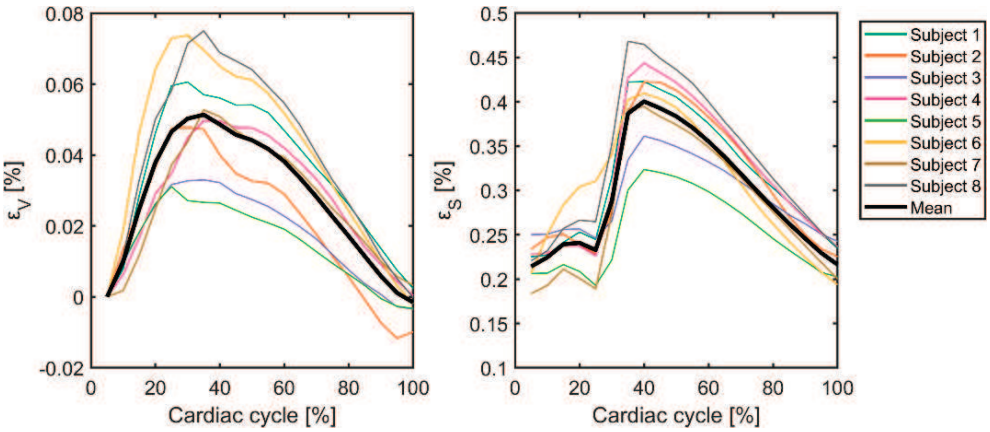


Figure 1: Whole-brain mean volumetric strain (left) and octahedral shear strain (right) across the cardiac cycle, temporally aligned to represent brain tissue volume changes relative to cardiac onset. Colored curves depict subject-averaged strain waveforms, while the thick black curve indicates the group mean. Both strain measures exhibit a characteristic systolic increase consistent with brain tissue swelling, followed by relaxation during diastole.

2.3 Tissue stiffness estimation

Brain tissue stiffness was estimated using poroviscoelastic inversion for iMRE. This method had been applied in a prior analysis, with full details provided in the original publications (Burman Ingeberg et al., 2025). A brief summary of the approach is presented here.

The displacement fields of each subject were transformed into frequency space by applying the Fast Fourier Transform to the temporal phases for each voxel. The motion at the first harmonic frequency, which roughly corresponds to 1 Hz (for a cardiac rhythm of 60 bpm), was selected for estimation of shear stiffness. Tetrahedral finite element models were created from the corresponding displacement maps for each subject. The finite element models were then used in a subzone-based nonlinear inversion scheme (McGarry et al., 2012; Van Houten et al., 2001) to estimate the underlying mechanical properties using a poroviscoelastic model. With such a model, the brain is modeled as a biphasic material that comprises a viscoelastic porous matrix which is permeated by a viscous pore fluid. A total of 600 global iterations were allowed for property map of each subject to ensure convergence. The shear stiffness was calculated from the recovered complex shear modulus, G^*, as

$$\mu = \frac{2|G^*|}{(G' + |G^*|)},$$

where G' is the real part of G^*.

2.4 Comparison with ATLAS maps

The dependence of volumetric strain and octahedral shear strain on vascular and pulse-pressure-related properties was investigated by comparison to standardized atlas maps in MNI space reported in literature. The following maps were used for analysis: a cerebral blood volume (CBV) map that was generated using 134 non-linearly registered CBV maps obtained from DSC MRI (Fuster-Garcia et al., 2021); cerebral blood flow (CBF) and arterial transit time (ATT) maps obtained using high-resolution whole brain arterial spin labeling (ASL) for 10 volunteers (Taso et al., 2021); a mean transit time (MTT) map, distributed as part of the *rapidtide* analysis package (Frederick B. Blaise, 2016). This final map was derived using the procedure described in the poster Blaise et al., 2017, updated to use the data from 4036 resting state scans from the HCP1200 release. A detailed overview of sources and subject characteristics can be found in Table S1 in supplementary files.

ATT was included as a surrogate marker of pulse pressure effects. Although ATT does not directly measure pulse pressure, it reflects the arrival time of blood which is influenced by vascular path length and resistance. Regions with shorter ATT are typically expected to receive blood with less attenuated pulsatile energy, whereas longer ATT reflects more distal propagation and greater damping. In this exploratory context, ATT was therefore used as a proxy for the spatial distribution of pulsatile drive. CBF and MTT are both convoluted metrics, relating to multiple underlying factors (such as blood volume, arterial pressure and hematocrit), which in turn hampers interpretation. In contrast, CBV corresponds to a more unambiguous representation of vascular anatomy. For this reason, we focus on CBV in the main analysis, with CBF and MTT presented in the supplementary material for completeness.

As a complementary analysis, the relationship between strain and tissue stiffness was also evaluated using a standardized atlas of shear stiffness derived from conventional MR elastography (MRE) in 134 volunteers with 50 Hz actuation frequency (Hiscox et al., 2021). This analysis was included to assess whether observed strain–stiffness associations could arise from shared data dependencies when both metrics are derived from the same displacement fields. Atlas-based stiffness maps provide an independent estimate of tissue stiffness that is not derived from the subject-specific displacement data used for strain estimation. These analyses involving the conventional MRE atlas are reported in the Supplementary Material.

Each map was registered to each respective subject using Elastix (Klein et al., 2010), with separate registrations for the repeated scans. This was done by first rigidly registering the ICBM2009c non-linear average T1-weighted template to the T1-weighted image of each respective subject, followed by an affine and non-linear registration with nearest neighbor interpolation. Figure 2 shows all properties of interest for a representative subject.

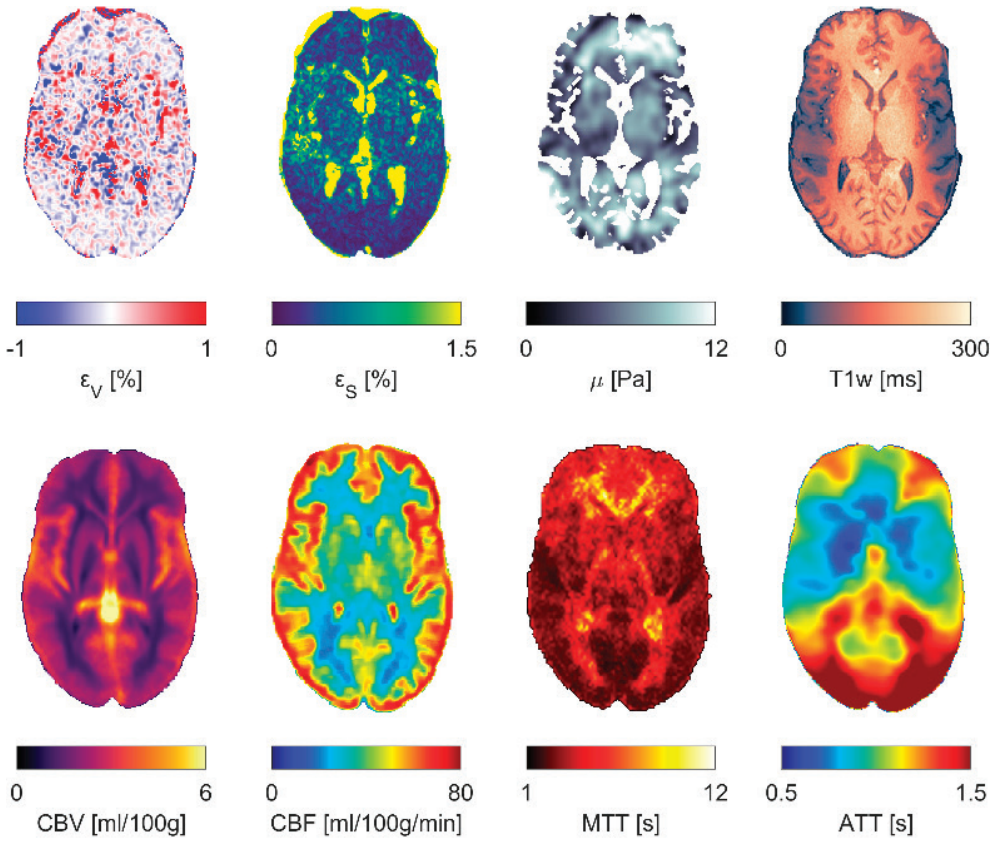


Figure 2: Representative axial slices of the properties of interest along with a T1-weighted image for anatomical reference for one subject. The top row contains subject specific measurements, while the bottom row contains standardized mean atlas maps that have been registered to subject space. Volumetric and octahedral shear strain maps are shown at a timepoint corresponding to peak strain.

2.5 Regional extraction

The potential dependence of volumetric strain and octahedral shear strain on microstructure and vascular properties was investigated by performing a regional analysis. A total of 28 regions were investigated, categorized based on the type of tissue: cortical gray matter (GM), subcortical GM, and white matter (WM). Cortical and subcortical regions were identified using the CerebrA atlas (Manera et al., 2020), and WM regions were identified using the JHU-ICBM-tracts and JHU-ICBM-labels 1 mm atlases (Mori et al., 2008; Mori S et al., 2006). Table 1 contains all regions used in this analysis, with their respective abbreviation, and tissue type. Partial volume effects were minimized by eroding each region by 1 voxel.

Voxels with less than 95% probability of being classified as either GM or WM were excluded from the analysis to avoid CSF and partial-volume effects at tissue boundaries.

To ensure mutually comparable regional correlations across the various properties, only voxels for which all parameters were available were included. Voxels corresponding to missing parameters, arising from the removal of artifactual strains in the strain maps or from problematic fluid flow in the shear stiffness map (Burman Ingeberg et al., 2023) (see Figure 2), were excluded from all property maps to maintain consistency in regional comparisons. Consequently, the number of voxels per region was considerably reduced, particularly in gray matter areas near CSF. Therefore, regions with fewer than an average of 300 voxels across subjects or those where more than 80% of voxels were removed (compared to the eroded region mask) were excluded from the analysis. The mean value of all properties of interest was computed for each region. For time-dependent properties such as volumetric strain and octahedral shear strain, the mean regional value was computed for each time point. Peak-to-peak volumetric strain $\varepsilon_{V,pp}$ and octahedral shear strain $\varepsilon_{S,pp}$ were then computed by taking the difference between the maximum and minimum value across time.

Table 1: All regions of interest and their respective abbreviations, categorized into tissue types.

Tissue type	Region	Abbreviation
Cortical GM	Frontal cortex	FC
	Occipital cortex	OC
	Cingulate cortex	CiC
	Parietal cortex	PC
	Temporal cortex	TC
	Fusiform gyrus	FSG
	Parahippocampal gyrus	PCG
	Insula	INS
	Paracentral lobule	PCe
Subcortical GM	Amygdala	AM
	Caudate	CA
	Hippocampus	HC
	Pallidum	PA
	Putamen	PU
	Thalamus	TH
WM	Anterior thalamic radiation	ATR
	Corticospinal tract	CST
	Major forceps	FMa
	Minor forceps	FMi
	Inferior frontal occipital fasciculus	IFOF
	Inferior longitudinal fasciculus	ILF
	Superior longitudinal fasciculus	SLF
	Uncinate fasciculus	UN

Table 1: All regions of interest and their respective abbreviations, categorized into tissue types. (*continued*)

Tissue type	Region	Abbreviation
	Corpus callosum	CC
	Corona radiata	CRa
	Fornix	FX
	Posterior thalamic radiation	PTR
	Cingulum Bundle	CB

2.6 Statistical analysis

The regional relationships between the measured strains and the vascular and tissue properties were investigated using linear mixed effects models. This was done separately for cortical GM, subcortical GM and WM, as well as globally (all regions). Each subject was specified as a random effect, with repeated measurements being specified as a nested random effect within each subject. The model was weighted by the size of each region, ensuring that regions with larger volumes had a greater influence on the estimation. Data points with an absolute z-score over three were considered outliers and were removed from the analysis. Bonferroni correction was used to correct for multiple comparisons such that statistically significant effects were determined at $p < 0.05/4 = 0.0125$.

3 Results

All regions except the Fornix, the Uncinate fasciculus, the Pallidum, and the Temporal cortex met the requirements to be kept for analysis for all subjects. The mean regional values for each property of interest are presented in Table 2, averaged across measurements.

Table 2: Mean and standard deviation of regional values across all measurements for all properties, along with the mean number of voxels of each region. The standard deviations of atlas properties reflect variations caused by registration differences and the variable exclusion of voxels across subjects.

		$\varepsilon_{V,pp}$ [10^{-4}]	$\varepsilon_{S,pp}$ [10^{-4}]	μ [Pa]	CBV [ml/100g]	CBF [ml/100g/min]	MTT [s]	ATT [s]	#Voxels
Cortical GM	FSG	11(3)	17(5)	5.8(0.7)	2.83(0.10)	40.0(0.5)	2.99(0.08)	1.09(0.01)	4514(956)
	PCG	15(5)	34(12)	5.0(1.2)	2.80(0.14)	34.6(0.4)	3.76(0.11)	0.85(0.02)	749(168)
	PCe	9(3)	20(6)	8.9(1.8)	2.28(0.15)	49.8(1.9)	2.93(0.08)	1.26(0.03)	2036(1098)
	INS	12(3)	21(6)	5.4(0.5)	2.52(0.09)	46.5(2.3)	3.50(0.11)	0.80(0.01)	3532(1112)
	OC	7(2)	16(4)	6.0(0.9)	2.91(0.09)	42.7(0.5)	2.57(0.03)	1.26(0.01)	15872(2389)
	FC	7(2)	21(4)	7.7(1.1)	2.16(0.01)	53.8(0.6)	3.73(0.03)	1.11(0.01)	35563(9065)
	CiC	11(4)	25(7)	7.8(2.1)	2.46(0.06)	56.1(1.6)	3.66(0.24)	0.95(0.04)	5967(2085)
	PC	6(2)	15(5)	6.9(1.1)	2.35(0.03)	48.4(0.8)	3.14(0.03)	1.34(0.02)	25117(6412)
Subcortical GM	AM	14(5)	41(12)	5.3(1.3)	1.48(0.17)	42.4(1.0)	4.18(0.04)	0.82(0.04)	544(213)
	CA	13(2)	35(9)	5.7(1.0)	2.00(0.12)	44.5(0.6)	3.84(0.09)	0.78(0.01)	2186(1063)
	HC	11(5)	37(10)	4.9(0.9)	2.31(0.10)	47.5(1.8)	3.33(0.05)	0.85(0.02)	2231(825)
	PU	9(2)	27(6)	5.7(0.6)	2.29(0.02)	42.7(0.2)	3.86(0.03)	0.71(0.01)	4763(1165)
	TH	11(3)	34(12)	5.2(1.3)	2.55(0.24)	38.5(1.5)	3.76(0.12)	1.07(0.03)	4855(2804)
WM	FMa	6(2)	19(4)	6.2(1.5)	1.45(0.14)	22.8(0.5)	4.97(0.15)	1.33(0.02)	1259(292)
	FMi	7(3)	26(5)	7.5(2.5)	1.21(0.04)	29.2(0.3)	7.07(0.09)	1.02(0.04)	6631(2978)
	CRa	5(1)	27(7)	6.3(1.0)	1.18(0.01)	28.6(0.2)	5.71(0.04)	1.24(0.02)	20249(6086)
	CC	7(2)	24(6)	7.1(1.5)	1.34(0.13)	29.4(0.7)	5.54(0.16)	1.15(0.05)	7682(4493)
	SLF	7(2)	23(6)	5.4(0.6)	1.46(0.03)	29.8(0.6)	5.04(0.08)	1.35(0.01)	7684(2004)
	CB	11(3)	26(8)	7.1(1.8)	1.87(0.14)	34.2(1.1)	4.61(0.13)	0.99(0.06)	1302(619)
	ATR	8(3)	30(7)	6.5(1.3)	1.91(0.17)	35.0(1.5)	4.89(0.12)	0.96(0.04)	3166(1558)
	CST	7(2)	27(7)	4.9(0.8)	1.48(0.13)	30.0(0.6)	5.27(0.10)	1.19(0.06)	2007(707)
	ILF	10(4)	17(6)	5.7(0.8)	1.45(0.03)	24.8(0.6)	4.38(0.07)	1.28(0.01)	911(227)
	PTR	5(1)	18(4)	6.5(1.0)	1.15(0.01)	23.1(0.2)	5.01(0.06)	1.38(0.01)	3955(558)
	IFOF	6(1)	21(5)	7.1(0.9)	1.46(0.04)	29.8(0.4)	4.87(0.15)	1.01(0.03)	2645(645)

3.1 Volumetric strain

3.1.1 Relationships with ATT (proxy for pulse pressure)

The relationships between volumetric strain and ATT are illustrated in Figure 3, with each data point representing the subject-wise mean regional values. The corresponding regression statistics for each tissue type are detailed in Table 3. Outlier analysis excluded two regional values. Volumetric strain demonstrated a significant negative trend in cortical gray matter, white matter and at the global level.

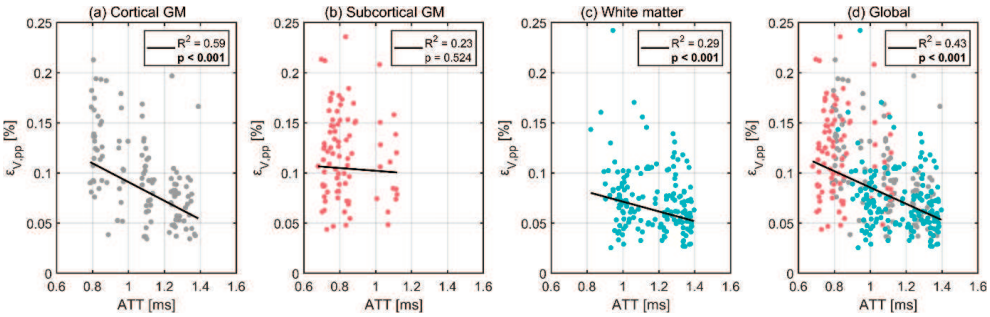


Figure 3: The dependence of volumetric strain on ATT for cortical gray matter (a), subcortical gray matter (b), white matter (c), and the global brain (d). Each dot represents the subject-wise mean value across a given region, calculated only for one repeated scan. For each tissue type, the black line shows the fixed-effect linear regression (weighted by region size) estimated from a linear mixed effects model, representing the overall population-level trend while accounting for subject- and scan-specific variability. The legend displays the corresponding *p*-values and R^2 for each regression, where significant correlations after Bonferroni correction are indicated in bold.

Table 3: The intercept and slope (both with 95% confidence intervals), p-value, and R^2 value obtained from linear regressions between volumetric strain and ATT using a linear mixed effects model for each tissue type. Significant correlations after Bonferroni correction are indicated in bold.

Region	Intercept [10^{-4}]	Slope [10^{-4}]	p-value	R^2
Global	16.7 (9.1, 14.8)	-8.1 (-7.1, -2.5)	**< 0.001**	0.43
Cortical GM	18.4 (15.3, 21.6)	-9.3 (-11.8, -6.9)	**< 0.001**	0.59
Subcortical GM	11.6 (7.7, 15.5)	-1.4 (-5.7, 2.9)	0.521	0.23
WM	12.0 (9.1, 14.8)	-4.8 (-7.1, -2.5)	**< 0.001**	0.29

3.1.2 Relationships with CBV (proxy for vascular structure)

The relationships between volumetric strain and CBV are illustrated in Figure 4, with each data point representing the subject-wise mean regional values. The corresponding regression statistics for each tissue type are detailed in Table 4. A separate outlier analysis was performed for the CBV comparison, with three regional values excluded. Linear regression analysis revealed significant positive correlations between volumetric strain and

CBV in WM, cortical GM and globally. However, a significant negative trend was observed in subcortical GM, potentially indicating distinct tissue-specific dependencies.

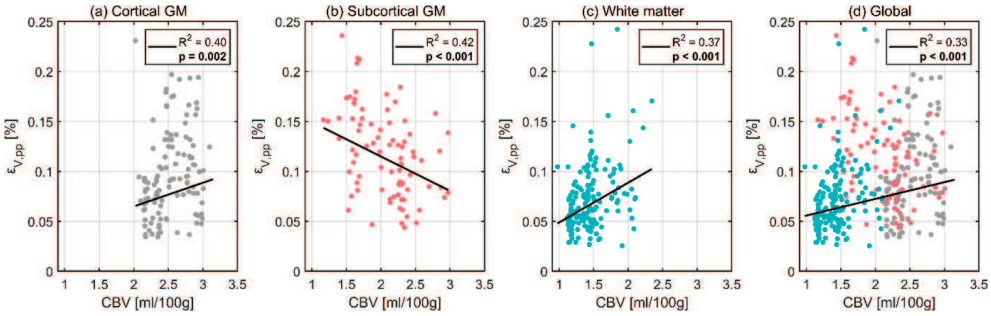


Figure 4: The dependence of volumetric strain on CBV for cortical gray matter (a), subcortical gray matter (b), white matter (c), and the global brain (d). Each dot represents the subject-wise mean value across a given region, calculated only for one repeated scan. For each tissue type, the black line shows the fixed-effect linear regression (weighted by region size) estimated from a linear mixed effects model, representing the overall population-level trend while accounting for subject- and scan-specific variability. The legend displays the corresponding *p*-values and R^2 for each regression, where significant correlations after Bonferroni correction are indicated in bold.

Table 4: The intercept and slope (both with 95% confidence intervals), *p*-value, and R^2 value obtained from linear regressions between volumetric strain and CBV using a linear mixed effects model for each tissue type. Significant correlations after Bonferroni correction are indicated in bold.

Region	Intercept [10^{-4}]	Slope [10^{-4}]	p-value	R^2
Global	3.9 (-1.0, 2.8)	1.7 (2.7, 5.3)	**< 0.001**	0.33
Cortical GM	1.8 (-2.0, 5.5)	2.4 (0.9, 3.8)	**0.002**	0.40
Subcortical GM	18.4 (14.1, 22.7)	-3.4 (-5.2, -1.7)	**< 0.001**	0.42
WM	0.9 (-1.0, 2.8)	4.0 (2.7, 5.3)	**< 0.001**	0.37

3.1.3 Relationships with tissue stiffness

The relationships between volumetric strain and shear stiffness are illustrated in Figure 5, with each data point representing the subject-wise mean regional values. The corresponding regression statistics for each tissue type are detailed in Table 5. Outlier analysis excluded two regional values. Across both tissue-specific and global analyses, only weak, non-significant associations were observed between volumetric strain and shear stiffness. Subcortical and cortical GM exhibited weak negative trends, whereas white matter displayed a weak positive trend.

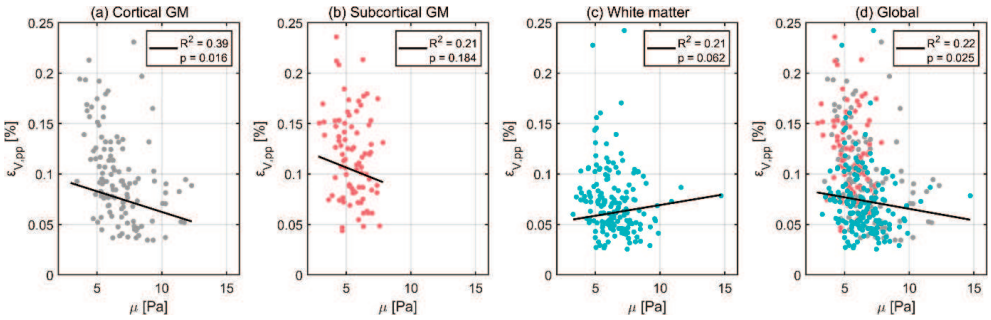


Figure 5: The dependence of volumetric strain on shear stiffness for cortical gray matter (a), subcortical gray matter (b), white matter (c), and the global brain (d). Each dot represents the subject-wise mean value across a given region, calculated only for one repeated scan. For each tissue type, the black line shows the fixed-effect linear regression (weighted by region size) estimated from a linear mixed effects model, representing the overall population-level trend while accounting for subject- and scan-specific variability. The legend displays the corresponding *p*-values and R^2 for each regression.

Table 5: The intercept and slope (both with 95% confidence intervals), *p*-value, and R^2 value obtained from linear regressions between volumetric strain and shear stiffness using a linear mixed effects model for each tissue type.

Region	Intercept [10^{-4}]	Slope [10^{-4}]	p-value	R^2
Global	8.8 (3.1, 6.5)	-0.2 (-0.0, 0.4)	0.025	0.22
Cortical GM	10.3 (7.7, 13.0)	-0.4 (-0.7, -0.1)	0.016	0.39
Subcortical GM	13.2 (8.9, 17.5)	-0.5 (-1.3, 0.2)	0.184	0.21
WM	4.8 (3.1, 6.5)	0.2 (-0.0, 0.4)	0.062	0.21

3.1 Octahedral shear strain

3.1.1 Relationships with ATT (proxy for pulse pressure)

The relationships between octahedral shear strain and ATT are illustrated in Figure 6, with each data point representing the subject-wise mean regional values. The corresponding regression statistics for each tissue type are detailed in Table 6. Outlier analysis excluded five regional values. Octahedral shear strain demonstrated significant negative correlations with ATT in cortical GM, in white matter, and at the global level. Meanwhile, a significant positive trend appeared in the subcortical GM.

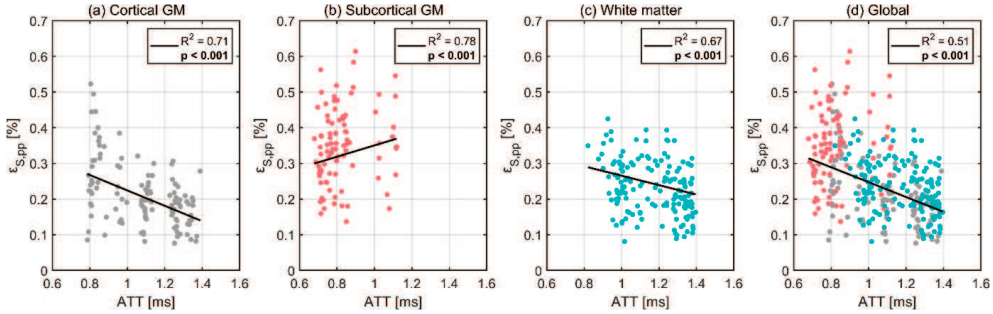


Figure 6: The dependence of octahedral shear strain on ATT for cortical gray matter (a), subcortical gray matter (b), white matter (c), and the global brain (d). Each dot represents the subject-wise mean value across a given region, calculated only for one repeated scan. For each tissue type, the black line shows the fixed-effect linear regression (weighted by region size) estimated from a linear mixed effects model, representing the overall population-level trend while accounting for subject- and scan-specific variability. The legend displays the corresponding *p*-values and R^2 for each regression, where significant correlations after Bonferroni correction are indicated in bold.

Table 6: The intercept and slope (both with 95% confidence intervals), *p*-value, and R^2 value obtained from linear regressions between octahedral shear strain and ATT using a linear mixed effects model for each tissue type. Significant correlations after Bonferroni correction are indicated in bold.

Region	Intercept [10^{-4}]	Slope [10^{-4}]	p-value	R^2
Global	45.6 (33.5, 46.0)	-20.8 (-17.6, -8.8)	**< 0.001**	0.51
Cortical GM	44.0 (38.4, 49.6)	-21.6 (-25.7, -17.4)	**< 0.001**	0.71
Subcortical GM	19.2 (11.3, 27.1)	15.9 (9.3, 22.5)	**< 0.001**	0.78
WM	39.8 (33.5, 46.0)	-13.2 (-17.6, -8.8)	**< 0.001**	0.67

3.1.2 Relationships with CBV (proxy for vascular structure)

The relationships between octahedral shear strain and CBV are illustrated in Figure 7, with each data point representing the subject-wise mean regional values. An outlier analysis was performed for the CBV comparison, with two regional values excluded. The corresponding regression statistics for each tissue type are detailed in Table 7. Linear regression analysis revealed a significant negative correlation between octahedral shear strain and CBV in cortical gray matter and globally. Both white matter and subcortical gray matter displayed minimal dependence on CBV.

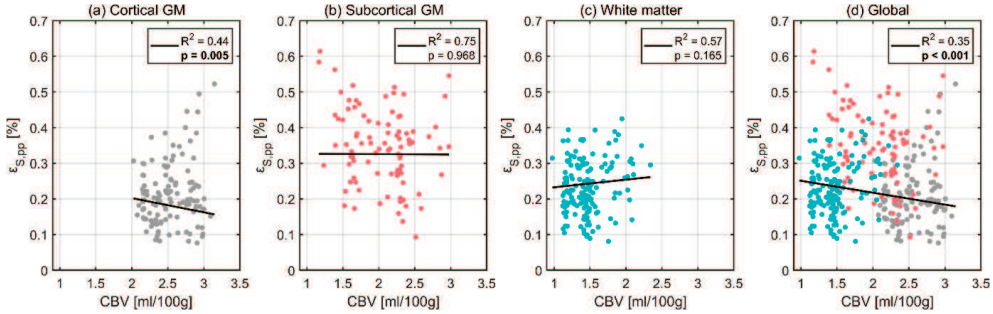


Figure 7: The dependence of octahedral shear strain on CBV for cortical gray matter (a), subcortical gray matter (b) and white matter (c), and the global brain (d). Each dot represents the subject-wise mean value across a given region, calculated only for one repeated scan. For each tissue type, the black line shows the fixed-effect linear regression (weighted by region size) estimated from a linear mixed effects model, representing the overall population-level trend while accounting for subject- and scan-specific variability. The legend displays the corresponding *p*-values and R^2 for each regression, where significant correlations after Bonferroni correction are indicated in bold.

Table 7: The intercept and slope (both with 95% confidence intervals), *p*-value, and R^2 value obtained from linear regressions between octahedral shear strain and CBV using a linear mixed effects model for each tissue type. Significant correlations after Bonferroni correction are indicated in bold.

Region	Intercept [10^{-4}]	Slope [10^{-4}]	p-value	R^2
Global	28.4 (15.9, 26.3)	-3.3 (-0.9, 5.2)	< 0.001	0.35
Cortical GM	28.2 (20.9, 35.5)	-4.0 (-6.8, -1.2)	0.005	0.44
Subcortical GM	32.7 (22.6, 42.8)	-0.1 (-3.6, 3.5)	0.968	0.75
WM	21.1 (15.9, 26.3)	2.1 (-0.9, 5.2)	0.165	0.57

3.1.3 Relationships with tissue stiffness

The relationships between octahedral shear strain and tissue stiffness are illustrated in Figure 8, with each data point representing the subject-wise mean regional values. The corresponding regression statistics for each tissue type are detailed in Table 8. Outlier analysis excluded two regional values. Octahedral shear strain showed significant negative correlations to shear stiffness across subcortical GM, WM and globally.

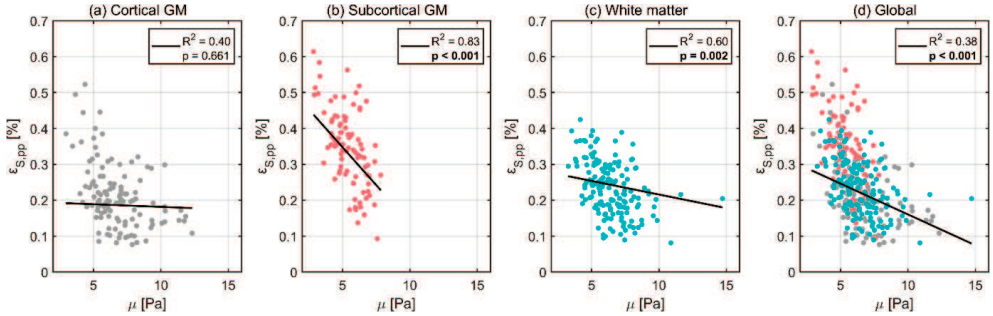


Figure 8: The dependence of octahedral shear strain on shear stiffness for cortical gray matter (a), subcortical gray matter (b), white matter (c), and the global brain (d). Each dot represents the subject-wise mean value across a given region, calculated only for one repeated scan. For each tissue type, the black line shows the fixed-effect linear regression (weighted by region size) estimated from a linear mixed effects model, representing the overall population-level trend while accounting for subject- and scan-specific variability. The legend displays the corresponding *p*-values and R^2 for each regression, where significant correlations after Bonferroni correction are indicated in bold.

Table 8: The intercept and slope (both with 95% confidence intervals), *p*-value, and R^2 value obtained from linear regressions between octahedral shear strain and shear stiffness using a linear mixed effects model for each tissue type. Significant correlations after Bonferroni correction are indicated in bold.

Region	Intercept [10^{-4}]	Slope [10^{-4}]	p-value	R^2
Global	33.2 (24.9, 33.5)	-1.7 (-1.2, -0.3)	**< 0.001**	0.38
Cortical GM	19.6 (14.2, 25.0)	-0.1 (-0.8, 0.5)	0.661	0.40
Subcortical GM	55.9 (47.8, 63.9)	-4.2 (-5.5, -3.0)	**< 0.001**	0.83
WM	29.2 (24.9, 33.5)	-0.8 (-1.2, -0.3)	**0.002**	0.60

4 Discussion

In this study, we combined strain tensor imaging (STI), intrinsic MR elastography (iMRE), and standard-space atlas maps in a regional analysis to explore potential relationships between CAP-related strain metrics and underlying drivers related to pulse pressure (ATT), vascular properties (CBV), or brain tissue (shear stiffness). While the use of regional correlations inherently limits the ability to draw causal conclusions, the results offer indications that may help to inform our understanding of potential drivers behind the measured strains. The diversity of the results underscores the complexity of the relationship between vascular or intervascular tissue properties and the resulting measured strains. In the following section, we elaborate on these observations and consider their potential implications for the understanding of CAP-related strains in the human brain.

4.1 Relationships with ATT

The pulsatile pressure gradient arising from the cardiac pulse is expected to be the highest at the moment of arrival in the brain, gradually decreasing as the pulsatile energy is absorbed by the downstream vasculature (Arts et al., 2022). While the arterial transit time (ATT) is not a direct metric for pulse pressure, it serves as a meaningful biological proxy for this explorative study. Consequently, volumetric strain is anticipated to decrease with increasing ATT, a trend observed in both cortical GM, WM, and globally. This highlights a potential relationship between the pulse pressure and volumetric strain and could partly explain why volumetric strain is higher in GM (which is perfused earlier than WM) compared to WM. A similar relationship was found in octahedral shear strain, indicating that the pulse pressure could be an important component in both strain metrics and serves as a common driver. However, this pattern was not observed in subcortical GM, where volumetric strain showed no clear dependence on ATT and octahedral shear strain exhibited the opposite trend. This can partly be explained by subcortical GM containing few regions where the cardiac pulse reaches each region at similar arrival times. This likely reduces the ability to detect clear relationships between ATT and strain metrics in this region, consequently making this region more sensitive to noise. However, it could also hint at more complex behavior arising from, for example, unique vascular architecture and/or mechanical coupling with surrounding tissues.

4.2 Relationships with vasculature

Previous studies have suggested that CBV may be a key factor in explaining the differences in volumetric strain between gray and white matter, given that similar disparities are observed in CBV (Adams et al., 2019). While our results show a modest correlation between volumetric strain and CBV, the CBV maps used in this analysis include the combined contributions of arterial, venous, and capillary blood volumes. Since most of the pulsatility in the vasculature is driven by arterial vessels (which only comprise 20-30% of the total volume (Hua et al., 2019)), with only minimal pulsations occurring in capillaries, a map that isolates arterial CBV would potentially provide a more accurate explanation of the observed volumetric strain differences. Nonetheless, it is unlikely that the blood volume alone can explain the observed 2.3 factor difference in volumetric strain between gray and white matter. In contrast, octahedral shear strain showed considerably less dependence on CBV.

4.3 Relationships with tissue stiffness

Differences in gray and white matter tissue stiffness have previously been suggested as a potential explanation for disparities in volumetric strain (Adams et al., 2019). However, our results indicate little to no correlation between shear stiffness and volumetric strain across tissue types, suggesting that tissue stiffness may contribute less to volumetric strain than vascular factors. In contrast, octahedral shear strain demonstrated a significant

negative correlation with shear stiffness in both subcortical gray matter and white matter, consistent with the expected inverse relationship between shear strain and material stiffness. Furthermore, octahedral shear strain showed considerably less overlap across tissue types when plotted against the properties of interest compared to volumetric strain. As each tissue type is expected to exhibit distinct tissue properties, this indicates that octahedral shear strain may have a stronger dependence on such tissue properties. Consistent with this interpretation, linear regressions for octahedral shear strain against stiffness yielded generally higher R^2 values when performed separately within each tissue type, emphasizing the appropriateness of this stratification for stiffness-related effects. In comparison, volumetric strain showed less improvement with tissue-specific stratification, consistent with the idea that vascular metrics play a larger role in volumetric strain, which may vary less distinctly across tissue types.

4.4 Relationships with hemodynamic properties

While mean transit time (MTT) and cerebral blood flow (CBF) capture aspects of cerebral hemodynamics, both metrics are influenced by multiple physiological factors. Specifically, MTT depends on the interplay between blood flow and blood volume, whereas CBF is affected by both pressure gradients and vascular resistance. Accordingly, these measures require cautious interpretation. In this line, we speculate that both properties to some extent reflect vascular resistance. In such case, volumetric strain is expected to increase with CBF and decrease with MTT, which is observed globally for both properties. However, in both cases, the correlations are weak with low R^2 values, tissue-specific comparisons are inconclusive, indicating that these relationships are modulated by multiple overlapping physiological factors.

4.5 Interpretation of strain metrics

Although it is known that cerebral arterial pulsations induce the measured strain in the brain, the interpretation of the observed strain metrics is still uncertain. Previous work suggested that volumetric strain reflects the swelling of the microvasculature embedded in the tissue (Adams et al., 2019), placing volumetric strain as a potential important metric to assess the state of the microvasculature. Our results suggest that volumetric strain is more strongly associated with CBV and pulse pressure, while showing minimal dependence on tissue stiffness. At the same time, octahedral shear strain showed less dependence on CBV, and stronger associations with the pulse pressure and tissue stiffness. While both metrics seem largely influenced by the pulse pressure, these results are consistent with the interpretation that volumetric strain primarily reflects vascular effects, whereas octahedral shear strain may be more related to the surrounding tissue. This interpretation is further supported by a recent case study (Sloots et al., 2023), in which STI was performed on a patient who underwent craniotomy following traumatic brain injury. In this case, the global boundary conditions of the brain were heavily influenced, which

in turn greatly affected the octahedral shear strain. In contrast, volumetric strain closely resembled that of healthy volunteers, suggesting it is predominantly influenced by the local properties of the vessel walls.

4.6 Considerations around atlas maps

We compared our values to standardized MNI atlases for certain metrics rather than direct measurements from the same subjects, which introduces a layer of potential error. While direct measurements from each subject would be preferable, the use of atlases were considered more appropriate and resource efficient for an explorative study such as this one. Nevertheless, the limited availability of atlas maps introduced variability in subject demographics. While the sex ratio and age distribution were similar for the CBF, MTT, and ATT maps, the CBV map included roughly twice as many males as females and an older overall population. Moreover, the CBV atlas was constructed from patients with grade IV glioblastoma; although tumor regions were removed from each map, it is possible that the overall CBV distribution may still be subtly affected. Finally, because of the use of group-averaged atlas maps, partial-volume effects and spatial smoothing are unavoidable and may reduce tissue specificity, particularly near CSF spaces.

4.7 Limitations

Both volumetric and octahedral shear strain are inherently noisy measurements, as they result from spatial derivative operations. While assessing peak-to-peak values over a certain region proved generally effective in handling noise, there is also information lost in such a simplification. In addition, a considerable number of voxels were excluded due to region erosion, artifact removal, and masking of problematic fluid flows. Thus, while the analysis covered most of the brain, it still represents only a subset of total brain volume.

Although the measured strain primarily reflects tissue deformation, small contributions from flowing cerebrospinal fluid, perivascular fluid or interstitial fluid cannot be fully excluded, particularly near large vessels or CSF spaces. These contributions are expected to be minor as long as these flows are incoherent (dephasing from the strong motion sensitizing gradients) but may introduce some measurement uncertainty (Sloots et al., 2022). Heartbeat-induced motion may also be modulated by respiration, which is not accounted for in the current approach (Raitamaa et al., 2021). This interaction could introduce minor bias into strain measurements. A more thorough investigation of these influences would be valuable; however, it is beyond the scope of the present study.

Given the limited sample size and the regional aggregation approach, the statistical analysis was intended to identify indicative patterns and generate hypotheses rather than to provide definitive causal inference. Importantly, the main interpretations were unchanged when analyses were performed without region-size weighting and under

alternative correction strategies, such as false discovery rate (FDR) control using the Benjamini-Hochberg procedure, indicating that the observed patterns are not driven by specific modelling choices (data not shown). Additionally, we performed a regional comparison, where each region likely contains a unique proportion of underlying contributions in the measured strains. This makes it more difficult to identify direct dependencies because regional variations in tissue composition, vascular density, or microstructural organization may independently influence both strain and the other measured properties. Such co-varying regional characteristics could either produce spurious correlations where no causal link exists or, conversely, mask genuine associations, resulting in the generally low R^2 values observed in the linear regressions.

Because the stiffness and strain metrics were derived from the same underlying displacement data, there remains a potential risk of spurious correlations arising from shared data dependencies. However, if shared data dependency were the dominant driver of the observed associations, similar correlations would be expected for both volumetric and octahedral shear strain. The fact that volumetric strain shows little to no association with shear stiffness, while octahedral shear strain exhibits a consistent relationship, indicates that this is not the case. Furthermore, we performed a complementary analysis using independently acquired stiffness maps from a standardized conventional MRE atlas (see Supplementary Material). Interestingly, correlations between volumetric strain and shear stiffness were even stronger in this analysis, suggesting that the associations observed with iMRE are not driven by shared data dependencies. At the same time, interpretation of these independent atlas comparisons is complicated by the high-frequency (50 Hz) external actuation used in conventional MRE, which induces region-specific stiffening effects (Herthum et al., 2021; Weickenmeier et al., 2018).The stiffness at 50Hz differs largely from the stiffness experienced at physiological, cardiac-driven motion, and might show different spatial variability as well (see Supplementary material for a more detailed discussion). Nonetheless, the overall pattern suggests that the observed associations reflect genuine physiological effects rather than spurious correlations arising from shared data dependencies.

4.8 Brain strain is driven by complex interplay

While our results help to shed light on possible drivers of volumetric and octahedral shear strain, they also underscore the complexity of these metrics. The observed associations suggest that both strain metrics reflect an intricate interplay of multiple physiological and structural factors, rather than being directly governed by any single metric. In particular, while CBV shows a notable relationship with volumetric strain, this likely represents only part of a broader system of influences. Not only do vascular wall compliance and pulse pressure seem to play important roles, but we further speculate that vascular architecture, such as branching patterns or hydraulic permeability (i.e., the ease with which fluid

can move through the vascular network, as described in poroelasticity), also influences strain dynamics. Recent studies have demonstrated that brain tissue permeability is deformation- and pressure-dependent, arising from strong fluid-solid interactions at the microstructural level. Such poroelastic effects introduce anisotropic flow resistance and are expected to contribute to increased mechanical dissipation within brain tissue (Yuan et al., 2023, 2024). Thus, as hydraulic permeability decreases, vascular resistance increases, potentially leading to greater energy dissipation, much like how electrical resistance in a circuit converts energy into heat. This dissipation may, in turn, modulate strain behavior in the brain. Furthermore, recent multiphysics computational models that couple pulsatile blood flow, deformable vessel walls, and viscoelastic brain tissue provide a complementary mechanistic perspective, demonstrating how vascular pulsatility and tissue mechanical properties together give rise to spatially and temporally distinct deformation components consistent with strain patterns observed using MRI (Gao et al., 2025). Given this complexity, a more comprehensive characterization of the underlying principles may require a system modeling approach, which could integrate the influences of various mechanical, vascular, and boundary condition effects to provide a more complete understanding of brain tissue deformation dynamics. Future research is needed to further unravel these interactions and their implications for brain biomechanics in both health and disease.

5 Conclusion

This study provides preliminary insights into the potential processes that may contribute to volumetric and octahedral shear strain in the human brain, suggesting that these strain metrics could reflect different physiological processes. Volumetric strain showed stronger associations with cerebral blood volume, while octahedral shear strain appeared more closely related to tissue stiffness. However, both strain metrics appear to arise from a more intricate interplay of factors than previously assumed. Within the context of a large, complex organ such as the brain, these effects underscore the need for further research to fully characterize the dynamics of brain strain. By jointly relating strain metrics to vascular and tissue-mechanical properties, this study advances prior work toward a more physiologically informed interpretation of brain strain, laying the groundwork and providing benchmarks for future computational modeling studies investigating the physiological determinants of strain metrics.

Acknowledgements

The authors would like to thank Dr. Alex A. Bhogal and Dr. Frederick B. Blaise for guidance with the atlas maps used in this study.

References

Adams, A. L., Kuijf, H. J., Viergever, M. A., Luijten, P. R., & Zwanenburg, J. J. M. (2019). Quantifying cardiac-induced brain tissue expansion using DENSE. *NMR in Biomedicine*, *32*(2), e4050. https://doi.org/10.1002/nbm.4050

Adams, A. L., Viergever, M. A., Luijten, P. R., & Zwanenburg, J. J. M. (2020). Validating faster DENSE measurements of cardiac-induced brain tissue expansion as a potential tool for investigating cerebral microvascular pulsations. *NeuroImage*, *208*, 116466. https://doi.org/10.1016/j.neuroimage.2019.116466

Aletras, A. H., Ding, S., Balaban, R. S., & Wen, H. (1999). DENSE: displacement encoding with stimulated echoes in cardiac functional MRI. *Journal of Magnetic Resonance (San Diego, Calif. : 1997)*, *137*(1), 247–252. https://doi.org/10.1006/jmre.1998.1676

Arts, T., Onkenhout, L. P., Amier, R. P., van der Geest, R., van Harten, T., Kappelle, J., Kuipers, S., van Osch, M. J. P., van Bavel, E. T., Biessels, G. J., & Zwanenburg, J. J. M. (2022). Non-Invasive Assessment of Damping of Blood Flow Velocity Pulsatility in Cerebral Arteries With <scp>MRI</scp>. *Journal of Magnetic Resonance Imaging*, *55*(6), 1785–1794. https://doi.org/10.1002/jmri.27989

Asgari, M., de Zélicourt, D., & Kurtcuoglu, V. (2016). Glymphatic solute transport does not require bulk flow. *Scientific Reports*, *6*, 38635. https://doi.org/10.1038/srep38635

Bakker, E. N. T. P., Bacskai, B. J., Arbel-Ornath, M., Aldea, R., Bedussi, B., Morris, A. W. J., Weller, R. O., & Carare, R. O. (2016). Lymphatic Clearance of the Brain: Perivascular, Paravascular and Significance for Neurodegenerative Diseases. *Cellular and Molecular Neurobiology*, *36*(2), 181–194. https://doi.org/10.1007/s10571-015-0273-8

Blaise, F. B., Lindsey, K. P., Erdogan, S. B., Hocke, L. M., & Tong, Y. (2017, June). Mapping hemodynamic delay times from Human Connectome Project Resting State Data. *23rd Annual Meeting of the Organization for Human Brain Mapping*.

Burman Ingeberg, M., Van Houten, E., & Zwanenburg, J. J. M. (2023). Estimating the viscoelastic properties of the human brain at 7T MRI using intrinsic MRE and nonlinear inversion. *Human Brain Mapping*, *44*(18), 6575–6591. https://doi.org/10.1002/hbm.26524

Burman Ingeberg, M., Van Houten, E., & Zwanenburg, J. J. M. (2025). Evaluating the Performance and Repeatability of Poroelastic and Poroviscoelastic Models in Intrinsic MR Elastography. *NMR in Biomedicine*, *38*(7), e70073. https://doi.org/10.1002/nbm.70073

Frederick B. Blaise. (2016). *rapidtide* (Version 3.0alpha5). https://doi.org/doi:10.5281/zenodo.814990

Fuster-Garcia, E., Albarracín, J. J., Hovden, I. T., del Mar Ávarez-Torres, M., Rovira, A., Oleaga, L., Revert, A. J., Filice, S., García-Gómez, J. M., & Eeg Emblem, K. (2021). *CBV-atlas*. https://www.mn.uio.no/fysikk/english/people/aca/ivarth/works/1087-abs.pdf

Gao, X., Yuan, T., Liao, Z., Yang, Y., Wu, W., Zhan, W., & Dini, D. (2025). Blood–brain mechanics: How brain tissue responds to pulsatile blood flow dynamics. *International Journal of Mechanical Sciences*, *296*, 110278. https://doi.org/10.1016/j.ijmecsci.2025.110278

Hahn, M., Klyscz, T., & Jünger, M. (1996). Synchronous measurements of blood pressure and red blood cell velocity in capillaries of human skin. *The Journal of Investigative Dermatology*, *106*(6), 1256–1259. https://doi.org/10.1111/1523-1747.ep12348955

Herthum, H., Dempsey, S. C. H., Samani, A., Schrank, F., Shahryari, M., Warmuth, C., Tzschätzsch, H., Braun, J., & Sack, I. (2021). Superviscous properties of the in vivo brain at large scales. *Acta Biomaterialia*, *121*, 393–404. https://doi.org/10.1016/j.actbio.2020.12.027

Hetzer, S., Birr, P., Fehlner, A., Hirsch, S., Dittmann, F., Barnhill, E., Braun, J., & Sack, I. (2018). Perfusion alters stiffness of deep gray matter. *Journal of Cerebral Blood Flow and Metabolism : Official*

Journal of the International Society of Cerebral Blood Flow and Metabolism, *38*(1), 116–125. https://doi.org/10.1177/0271678X17691530

Hirsch, S., Klatt, D., Freimann, F., Scheel, M., Braun, J., & Sack, I. (2013). In vivo measurement of volumetric strain in the human brain induced by arterial pulsation and harmonic waves. *Magnetic Resonance in Medicine*, *70*(3), 671–683. https://doi.org/10.1002/mrm.24499

Hiscox, L. V., Schwarb, H., McGarry, M. D. J., & Johnson, C. L. (2021). Aging brain mechanics: Progress and promise of magnetic resonance elastography. *NeuroImage*, *232*, 117889. https://doi.org/10.1016/j.neuroimage.2021.117889

Hua, J., Liu, P., Kim, T., Donahue, M., Rane, S., Chen, J. J., Qin, Q., & Kim, S.-G. (2019). MRI techniques to measure arterial and venous cerebral blood volume. *NeuroImage*, *187*, 17–31. https://doi.org/10.1016/j.neuroimage.2018.02.027

Iliff, J. J., Wang, M., Liao, Y., Plogg, B. A., Peng, W., Gundersen, G. A., Benveniste, H., Vates, G. E., Deane, R., Goldman, S. A., Nagelhus, E. A., & Nedergaard, M. (2012). A paravascular pathway facilitates CSF flow through the brain parenchyma and the clearance of interstitial solutes, including amyloid β. *Science Translational Medicine*, *4*(147), 147ra111. https://doi.org/10.1126/scitranslmed.3003748

Manera, A. L., Dadar, M., Fonov, V., & Collins, D. L. (2020). CerebrA, registration and manual label correction of Mindboggle-101 atlas for MNI-ICBM152 template. *Scientific Data*, *7*(1), 237. https://doi.org/10.1038/s41597-020-0557-9

McGarry, M. D. J., Van Houten, E. E. W., Johnson, C. L., Georgiadis, J. G., Sutton, B. P., Weaver, J. B., & Paulsen, K. D. (2012). Multiresolution MR elastography using nonlinear inversion. *Medical Physics*, *39*(10), 6388–6396. https://doi.org/10.1118/1.4754649

McGarry, M. D. J., Van Houten, E. E. W., Perriñez, P. R., Pattison, A. J., Weaver, J. B., & Paulsen, K. D. (2011). An octahedral shear strain-based measure of SNR for 3D MR elastography. *Physics in Medicine and Biology*, *56*(13), N153–N164. https://doi.org/10.1088/0031-9155/56/13/N02

Mestre, H., Tithof, J., Du, T., Song, W., Peng, W., Sweeney, A. M., Olveda, G., Thomas, J. H., Nedergaard, M., & Kelley, D. H. (2018). Flow of cerebrospinal fluid is driven by arterial pulsations and is reduced in hypertension. *Nature Communications*, *9*(1), 4878. https://doi.org/10.1038/s41467-018-07318-3

Mori, S., Oishi, K., Jiang, H., Jiang, L., Li, X., Akhter, K., Hua, K., Faria, A. V, Mahmood, A., Woods, R., Toga, A. W., Pike, G. B., Neto, P. R., Evans, A., Zhang, J., Huang, H., Miller, M. I., van Zijl, P., & Mazziotta, J. (2008). Stereotaxic white matter atlas based on diffusion tensor imaging in an ICBM template. *NeuroImage*, *40*(2), 570–582. https://doi.org/10.1016/j.neuroimage.2007.12.035

Mori S, Wakana S, Nagae-Poetscher L M, & van Zijl P C M. (2006). MRI Atlas of Human White Matter. *AJNR Am J Neuroradiol*, *27*(6), 1384–1385.

Raitamaa, L., Huotari, N., Korhonen, V., Helakari, H., Koivula, A., Kananen, J., & Kiviniemi, V. (2021). Spectral analysis of physiological brain pulsations affecting the <scp>BOLD</scp> signal. *Human Brain Mapping*, *42*(13), 4298–4313. https://doi.org/10.1002/hbm.25547

Sloots, J. J., Biessels, G. J., de Luca, A., & Zwanenburg, J. J. M. (2021). Strain Tensor Imaging: Cardiac-induced brain tissue deformation in humans quantified with high-field MRI. *NeuroImage*, *236*, 118078. https://doi.org/10.1016/j.neuroimage.2021.118078

Sloots, J.-J., Biessels, G. J., Amelink, G. J., & Zwanenburg, J. J. M. (2023). Abnormalities in cardiac-induced brain tissue deformations are now detectable with MRI: A case-report of a patient who underwent craniotomy after trauma. *Magnetic Resonance Imaging*, *98*, 62–65. https://doi.org/10.1016/j.mri.2023.01.003

Sloots, J.-J., Froeling, M., Biessels, G. J., & Zwanenburg, J. J. M. (2022). Dynamic brain ADC variations over the cardiac cycle and their relation to tissue strain assessed with DENSE at high-field MRI. *Magnetic Resonance in Medicine*, *88*(1), 266–279. https://doi.org/10.1002/mrm.29209

Spector, R., Robert Snodgrass, S., & Johanson, C. E. (2015). A balanced view of the cerebrospinal fluid composition and functions: Focus on adult humans. *Experimental Neurology*, *273*, 57–68. https://doi.org/10.1016/j.expneurol.2015.07.027

Tarasoff-Conway, J. M., Carare, R. O., Osorio, R. S., Glodzik, L., Butler, T., Fieremans, E., Axel, L., Rusinek, H., Nicholson, C., Zlokovic, B. V, Frangione, B., Blennow, K., Ménard, J., Zetterberg, H., Wisniewski, T., & de Leon, M. J. (2015). Clearance systems in the brain-implications for Alzheimer disease. *Nature Reviews. Neurology*, *11*(8), 457–470. https://doi.org/10.1038/nrneurol.2015.119

Taso, M., Munsch, F., Zhao, L., & Alsop, D. C. (2021). Regional and depth-dependence of cortical blood-flow assessed with high-resolution Arterial Spin Labeling (ASL). *Journal of Cerebral Blood Flow & Metabolism*, *41*(8), 1899–1911. https://doi.org/10.1177/0271678X20982382

van der Voort, E. C., Tong, Y., van Grinsven, E. E., Zwanenburg, J. J. M., Philippens, M. E. P., & Bhogal, A. A. (2024). CO2 as an engine for neurofluid flow: Exploring the coupling between vascular reactivity, brain clearance, and changes in tissue properties. *NMR in Biomedicine*, *37*(8), e5126. https://doi.org/10.1002/nbm.5126

Van Houten, E. E., Miga, M. I., Weaver, J. B., Kennedy, F. E., & Paulsen, K. D. (2001). Three-dimensional subzone-based reconstruction algorithm for MR elastography. *Magnetic Resonance in Medicine*, *45*(5), 827–837. https://doi.org/10.1002/mrm.1111

Weickenmeier, J., Kurt, M., Ozkaya, E., de Rooij, R., Ovaert, T. C., Ehman, R. L., Butts Pauly, K., & Kuhl, E. (2018). Brain stiffens post mortem. *Journal of the Mechanical Behavior of Biomedical Materials*, *84*, 88–98. https://doi.org/10.1016/j.jmbbm.2018.04.009

Wuerfel, J., Paul, F., Beierbach, B., Hamhaber, U., Klatt, D., Papazoglou, S., Zipp, F., Martus, P., Braun, J., & Sack, I. (2010). MR-elastography reveals degradation of tissue integrity in multiple sclerosis. *NeuroImage*, *49*(3), 2520–2525. https://doi.org/10.1016/j.neuroimage.2009.06.018

Yuan, T., Shen, L., & Dini, D. (2024). Porosity-permeability tensor relationship of closely and randomly packed fibrous biomaterials and biological tissues: Application to the brain white matter. *Acta Biomaterialia*, *173*, 123–134. https://doi.org/10.1016/j.actbio.2023.11.007

Yuan, T., Zhan, W., & Dini, D. (2023). Linking fluid-axons interactions to the macroscopic fluid transport properties of the brain. *Acta Biomaterialia*, *160*, 152–163. https://doi.org/10.1016/j.actbio.2023.02.010

Supplementary Files

ATLAS overview

Table S1: Overview of sources and subject characteristics for each atlas map used in the analysis.

Metric	Reference	Source	Number of subjects	Sex (F/M)	Age	Health status
CBV	Fuster-Garcia et al., 2021	NCT03439332 clinical study	134	66/118*	24 – 81 (mean age: 60) years*	Glioblastoma grade IV**
MTT	Frederick B. Blaise, 2016	HCP1200	1206	656/550	22 – 35 years	Healthy subjects
CBF, ATT	Taso et al., 2021	Measured in Taso et al., 2021	10	6/4	30 ± 7 years	Healthy subjects
μ	Hiscox et al., 2021	Multiple studies***	134	78/56	18 – 38 years	Healthy subjects

*A subset of 134 subjects was used to generate the final CBV map. Sex and age information were available only for the initial 184 subjects.

**Tumor regions were excluded from each subject's map.

*** Data was collected from studies conducted at the University of Edinburgh, UK; University of Illinoisat Urbana-Champaign, USA; and the Carle Foundation Hospital, USA.

Relationship between volumetric strain and hemodynamic metrics

The relationships between volumetric strain and the hemodynamic properties of interest are illustrated in Figure S1, with each data point representing the subject-wise mean regional values. The corresponding regression statistics for each tissue type and property are detailed in Table S2. A separate outlier analysis was performed for each volumetric strain comparison. Three regional values were excluded for the regressions with CBF, and two for the MTT. Linear regression analysis revealed significant positive correlations between volumetric strain and CBF in white matter and globally. Meanwhile, weak negative trends were observed in cortical and subcortical GM, potentially highlighting distinct tissue-specific dependencies. A significant negative correlation was found for MTT on the global level while a significant positive trend was observed for the subcortical GM.

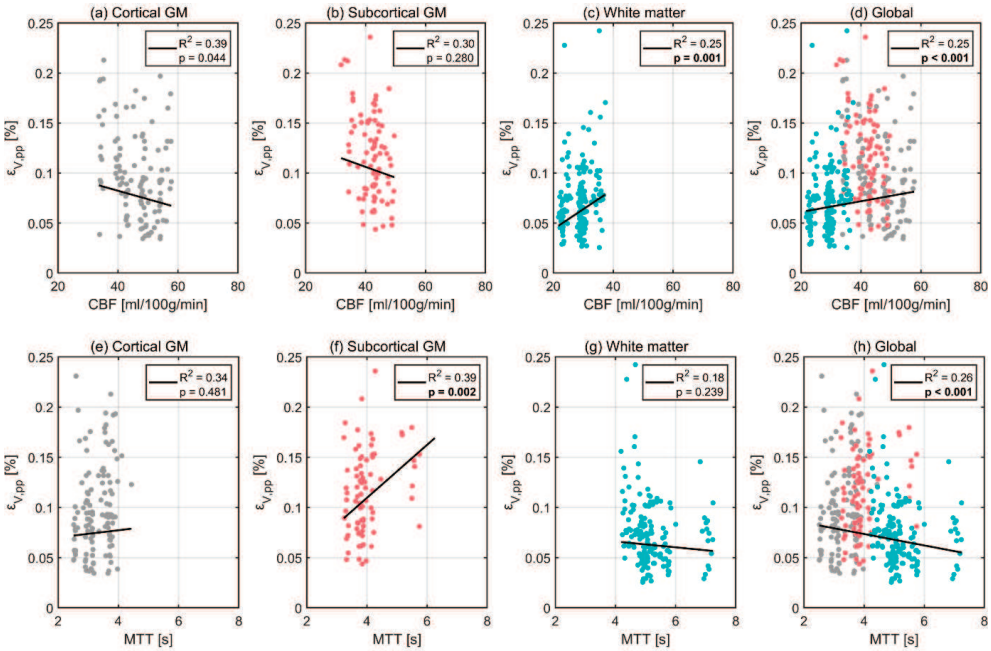


Figure S1: The dependence of volumetric strain on hemodynamic properties for cortical gray matter (a,e), subcortical gray matter (b,f), white matter (c,g), and the global brain (d,h). Each dot represents the subject-wise mean value across a given region, calculated only for one repeated scan. For each tissue type, the black line shows the fixed-effect linear regression (weighted by region size) estimated from a linear mixed effects model, representing the overall population-level trend while accounting for subject- and scan-specific variability. The legend displays the corresponding *p*-values and R^2 for each regression, where significant correlations after Bonferroni correction are indicated in bold.

Table S2: The intercept and slope (both with 95% confidence intervals), *p*-value, and R^2 value obtained from linear regressions between volumetric strain and the hemodynamic properties of interest using a linear mixed effects model for each tissue type. Significant correlations after Bonferroni correction are indicated in bold.

	Region	Intercept [10^{-4}]	Slope [10^{-4}]	p-value	R^2
CBF	Global	5.0 (-3.2, 3.9)	0.1 (0.1, 0.3)	**< 0.001**	0.25
	Cortical GM	11.6 (7.4, 15.9)	-0.1 (-0.2, -0.0)	0.044	0.39
	Subcortical GM	14.9 (6.5, 23.4)	-0.1 (-0.3, 0.1)	0.280	0.30
	WM	0.4 (-3.2, 3.9)	0.2 (0.1, 0.3)	**0.001**	0.25
MTT	Global	9.7 (5.0, 10.5)	-0.6 (-0.8, 0.2)	**< 0.001**	0.26
	Cortical GM	6.6 (3.1, 10.1)	0.3 (-0.7, 1.3)	0.598	0.34
	Subcortical GM	0.4 (-6.1, 6.9)	2.6 (1.0, 4.3)	**0.002**	0.39
	WM	7.8 (5.0, 10.5)	-0.3 (-0.8, 0.2)	0.240	0.18

Relationship between octahedral shear strain and hemodynamic metrics

The relationships between octahedral shear strain and the hemodynamic properties of interest are illustrated in Figure S2, with each data point representing the subject-wise mean regional values. An outlier analysis was performed separately for each octahedral shear strain comparison. Five regional values were excluded from the comparisons with CBF and MTT. The corresponding regression statistics for each tissue type and property are detailed in Table S3. CBF showed significant positive correlations in WM and cortical GM, while a significant negative correlation was identified at the global level. For MTT, significant positive trends were observed within cortical GM, WM, and globally. CBF exhibited markedly different behaviors across tissue types, and both metrics showed minimal overlap among data points. In general, octahedral shear strain regressions yielded considerably higher R^2 values compared to volumetric strain regressions for hemodynamic comparisons.

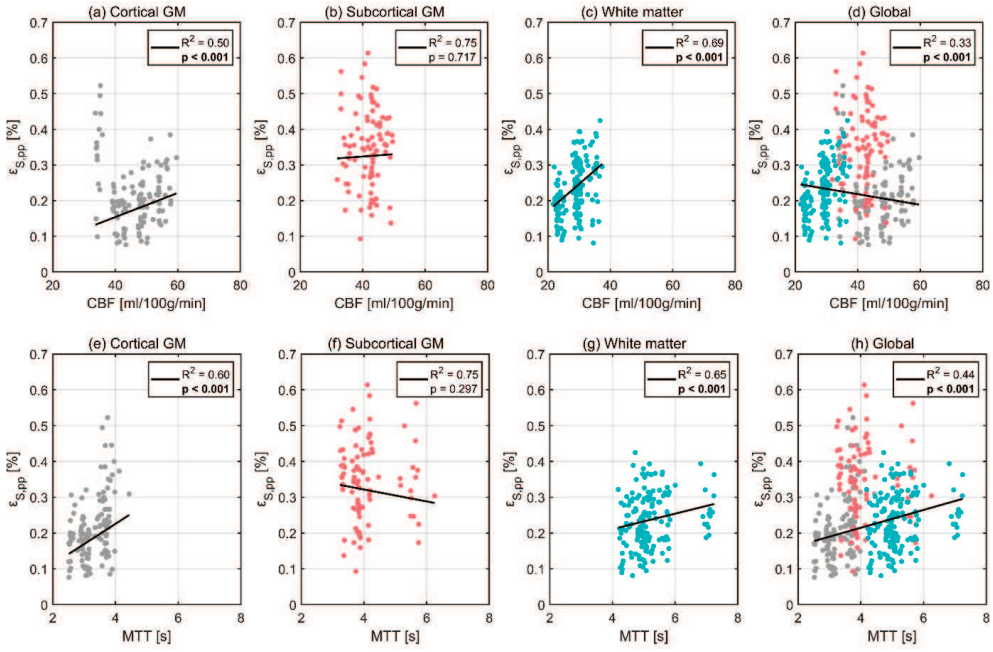


Figure S2: The dependence of octahedral shear strain on hemodynamic properties for cortical gray matter (a,e), subcortical gray matter (b,f) and white matter (d,h), and the global brain (d,h). Each dot represents the subject-wise mean value across a given region, calculated only for one repeated scan. For each tissue type, the black line shows the fixed-effect linear regression (weighted by region size) estimated from a linear mixed effects model, representing the overall population-level trend while accounting for subject- and scan-specific variability. The legend displays the corresponding *p*-values and R^2 for each regression, where significant correlations after Bonferroni correction are indicated in bold.

Table S3: The intercept and slope (both with 95% confidence intervals), *p*-value, and R^2 value obtained from linear regressions between octahedral shear strain and the hemodynamic properties of interest using a linear mixed effects model for each tissue type. Significant correlations after Bonferroni correction are indicated in bold.

	Region	Intercept [10^{-4}]	Slope [10^{-4}]	p-value	R^2
CBF	Global	27.8 (-5.2, 8.8)	-0.1 (0.5, 1.0)	**< 0.001**	0.33
	Cortical GM	1.8 (-6.0, 9.7)	0.3 (0.2, 0.5)	**< 0.001**	0.50
	Subcortical GM	29.7 (13.4, 46.1)	0.1 (-0.3, 0.4)	0.717	0.75
	WM	1.8 (-5.2, 8.8)	0.8 (0.5, 1.0)	**< 0.001**	0.69
MTT	Global	11.5 (6.0, 18.9)	2.5 (1.2, 3.2)	**< 0.001**	0.44
	Cortical GM	-0.1 (-5.9, 5.7)	5.7 (4.1, 7.2)	**< 0.001**	0.60
	Subcortical GM	38.8 (25.6, 52.1)	-1.7 (-4.8, 1.5)	0.297	0.75
	WM	12.4 (6.0, 18.9)	2.2 (1.2, 3.2)	**< 0.001**	0.65

Relationship between strain and independent tissue stiffness estimates at higher actuation frequencies

The relationships between volumetric strain, octahedral shear strain and shear stiffness obtained with conventional MR elastography (MRE) are illustrated in Figure S3, with each data point representing the subject-wise mean regional values. Outlier analysis was performed separately for each octahedral shear strain comparison as described in section 2.6. One regional value was excluded from the volumetric strain comparison, and three regional values were excluded from the octahedral shear strain comparison. The corresponding regression statistics for each tissue type and property are detailed in Table S4.

As in the comparison with intrinsic MRE (iMRE)-derived shear stiffness, no significant associations were observed between volumetric strain and shear stiffness across most regions, with the exception of cortical gray matter. In cortical gray matter, volumetric strain was significantly positively associated with shear stiffness derived from conventional MRE, in contrast to the significant negative association observed with iMRE. The relationships between octahedral shear strain and shear stiffness derived from conventional MRE were consistent with those observed using iMRE only in white matter, whereas opposite relationships were observed in cortical gray matter and globally. This disagreement may reflect, at least in part, the different physiological conditions under which conventional MRE measurements are obtained. Conventional MRE estimates stiffness under externally applied high-frequency mechanical actuation, whereas both strain and iMRE-derived stiffness reflect tissue behavior under physiological, cardiac-driven motion. As a result, frequency-dependent viscoelastic effects may confound the relationship between conventional MRE-derived stiffness and pulsation-driven strain. Additionally, recent work by (Gao et al., 2025) suggests that cortical gray matter is particularly sensitive to blood-pressure-driven tissue motion. This may partly explain why volumetric strain shows a positive

association with shear stiffness in cortical GM under high-frequency conventional MRE: frequency-dependent stiffening could be more pronounced in GM, amplifying correlations in the extrinsic actuation regime.

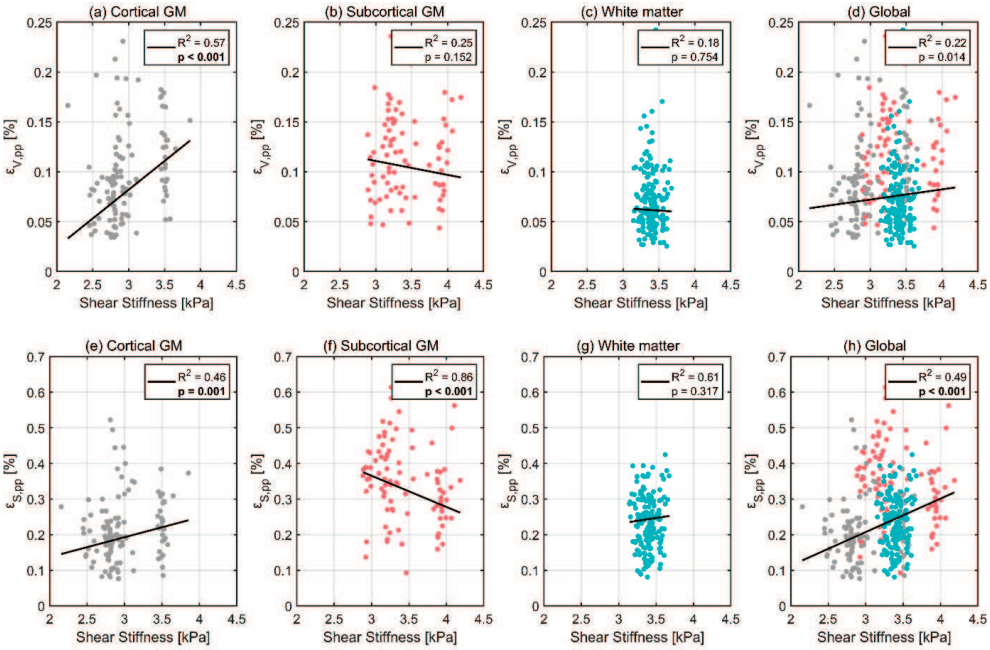


Figure S3: The dependence of volumetric strain and octahedral shear strain on shear stiffness obtained with conventional MRE (actuation frequency 50 Hz) for cortical gray matter (a,e), subcortical gray matter (b,f) and white matter (d,h), and the global brain (d,h). Each dot represents the subject-wise mean value across a given region, calculated only for one repeated scan. For each tissue type, the black line shows the fixed-effect linear regression (weighted by region size) estimated from a linear mixed effects model, representing the overall population-level trend while accounting for subject- and scan-specific variability. legend displays the corresponding *p*-values and R^2 for each regression, where significant correlations after Bonferroni correction are indicated in bold.

Table S4: The intercept and slope (both with 95% confidence intervals), *p*-value, and R^2 value obtained from linear regressions between volumetric strain, octahedral shear strain and shear stiffness obtained with conventional MRE using a linear mixed effects model for each tissue type. Significant correlations after Bonferroni correction are indicated in bold.

	Region	Intercept [10^{-4}]	Slope [10^{-4}]	p-value	R^2
$\varepsilon_{V,pp}$	Global	4.1 (-2.6, 18.3)	1.0 (-3.6, 2.6)	0.014	0.22
	Cortical GM	-9.1 (-13.7, -4.6)	5.8 (4.2, 7.3)	**< 0.001**	0.57
	Subcortical GM	15.3 (8.5, 22.1)	-1.4 (-3.3, 0.5)	0.152	0.25
	WM	7.8 (-2.6, 18.3)	-0.5 (-3.6, 2.6)	0.754	0.18
$\varepsilon_{S,pp}$	Global	-7.5 (-8.0, 35.0)	9.4 (-3.1, 9.5)	**< 0.001**	0.49

Table S4: The intercept and slope (both with 95% confidence intervals), *p*-value, and R^2 value obtained from linear regressions between volumetric strain, octahedral shear strain and shear stiffness obtained with conventional MRE using a linear mixed effects model for each tissue type. Significant correlations after Bonferroni correction are indicated in bold. (*continued*)

Region	Intercept [10^{-4}]	Slope [10^{-4}]	p-value	R^2
Cortical GM	2.5 (-7.5, 12.5)	5.6 (2.2, 8.9)	**0.001**	0.46
Subcortical GM	62.8 (52.5, 73.2)	-8.8 (-11.2, -6.3)	**< 0.001**	0.86
WM	13.5 (-8.0, 35.0)	3.2 (-3.1, 9.5)	0.317	0.61

6

Chapter 6

Alignment of cardiac-induced brain tissue strain with global boundary conditions and local microstructure: potential effects of anisotropy

Marius Burman Ingeberg[1], Elijah Van Houten[3], Martijn Froeling[2], Jaco J.M Zwanenburg[1]

[1]Translational Neuroimaging Group, Center for Image Sciences, University Medical Center Utrecht and Utrecht University, Utrecht, The Netherlands;

[2]Highfield MRI Group, UMC Utrecht, Utrecht, The Netherlands;

[3]Université de Strasbourg, CNRS, INSERM, ICube, UMR7357, Strasbourg, France.

Original work published in the Journal of the Mechanical Behavior of Biomedical Material:

Burman Ingeberg M, Van Houten E, Froeling M, Zwanenburg JJM. Alignment of cardiac-induced brain tissue strain with global boundary conditions and local microstructure: potential effects of anisotropy. J Mech Behav Biomed Mater. 2025 Oct 27;173:107252. doi: 10.1016/j.jmbbm.2025.107252.

Author Contribution Statement:

Marius Burman Ingeberg was responsible for conceptualization, methodology, software development, investigation, formal analysis, data management, and visualization, and wrote the original draft of the manuscript. Eli van Houten contributed to conceptualization, provided supervision, and reviewed and edited the manuscript. Martijn Froeling contributed to conceptualization, provided supervision, and reviewed and edited the manuscript. Jaco Zwanenburg contributed to conceptualization, secured funding, provided resources and supervision, and reviewed and edited the manuscript.

Abstract

Introduction

Strain tensor imaging allows for the construction of the full 3D strain tensor in the human brain from precise measurements of systolic cardiac-induced tissue deformation. Such tensors can be decomposed into principal strains, where the first principal strain (FPS) describes the direction of maximum stretch while the third principal strain (TPS) describes the direction of maximum shortening. This technique offers an opportunity to study the mechanical properties of brain tissue *in vivo*. It allows us to explore how strain directions are influenced by global boundary conditions and local microstructure. Additionally, it helps to determine whether human brain tissue exhibits mechanical anisotropy.

Method

We obtained strain tensor and diffusion tensor imaging (DTI) data across 8 healthy subjects from a previous 7T MRI study. The strain tensor was constructed from the DENSE displacement measurements. We compared the measured strain directions with two conceptual models to assess the impact of global boundary conditions and local brain microstructure on the measured strain.

Results

The boundary condition-based model effectively explained the measured FPS directions across all subjects (mean R^2: 0.61 ± 0.03), indicating that global boundary conditions largely dictate the direction of the stretching that occurs during cerebral arterial pulsations. The TPS demonstrated a tendency to align perpendicularly to the DTI.

Conclusion

These results highlight a potential indicator of mechanical anisotropy along white matter tracks using a novel approach, adding a new perspective to the ongoing discussion of the brain's structural characteristics.

1 Introduction

In recent decades, increasing attention has been given to understanding the mechanical behavior of the brain due to the crucial role of brain mechanics in various physiological processes, including neurodevelopment, injury response, waste clearance, and disease progression (Budday et al., 2014, 2020; El Sayed et al., 2008; Goriely et al., 2015b; Wagshul et al., 2011). Such properties are particularly difficult to measure for a multitude of reasons. A recent review by Budday et al. (2020) highlights the many challenges in characterizing brain structure, such as the ultrasoft, highly fragile, biphasic, heterogeneous nature of the brain, coupled with the fact that brain samples are very scarce. Additionally, although the ultimate goal is to characterize human brain tissue, mechanical testing is often conducted on animal brains, which may differ in scale and potentially exhibit distinct microstructures. Instead, computational modeling has emerged as a valuable tool for simulating and analyzing the mechanical behavior of the brain under various conditions, providing insight into the fundamental structure of the brain and how it is affected by disease. However, such techniques necessarily rely on accurate mechanical models which in turn require knowledge of advanced material properties describing the multi-scale mechanical response of brain tissue. It is, therefore, crucial to explain the relationship between microstructural components and macroscopic mechanical behavior to further our understanding of the mechanical properties of the brain and its role in neurological health and disease management.

One modeling characteristic of potentially high importance is mechanical anisotropy (Feng et al., 2024; Giordano et al., 2014). Despite being investigated in a large number of studies, the literature is split on whether the brain is mechanically isotropic (Budday et al., 2017a; Karimi & Navidbakhsh, 2014; Miller & Chinzei, 1997; Rashid et al., 2012), or anisotropic (Eskandari et al., 2021; Feng et al., 2013, 2017; Jin et al., 2013; Prange & Margulies, 2002; Velardi et al., 2006). The majority of such studies have been performed using mechanical testing or computational modeling, which both are limited by the factors stated above. Instead, recent work has provided a different means of investigating the mechanical behavior of the human brain in-vivo through *strain tensor imaging* (Sloots et al., 2021), where the full 3D strain tensor is calculated from precise, non-invasive displacement measurements. Such displacement measurements capture brain tissue deformation that arises due to cerebral arterial pulsations, driven by the cardiac cycle. The measured 3D strain tensor can then be decomposed into the first principal strains (FPS) and third principal strains (TPS), which correspond to the direction of maximum lengthening and maximum shortening, respectively. Figure 1 shows group-wise mean strain maps obtained with strain tensor imaging, registered to MNI space (Sloots et al., 2021). The FPS maps show global, inwardly directed strains pointing towards the foramen magnum, similar to what has been previously observed by Greitz et al. in 1992, Reese

et al. in 2002, and Hirsch et al. in 2013. Meanwhile, the TPS maps show locally heterogeneous patterns, possibly reflecting regional brain microstructure and thus offering an opportunity to further investigate the possible relationship between this microstructure and brain mechanics.

This novel approach to analyzing brain mechanics provides several interesting possibilities. First, it allows for the investigation of how local tissue strains emerge under systolic forces, and to what extent global boundary conditions as well as local microstructural effects play a role in resulting strain patterns. This may help further the understanding of mechanobiological effects in the brain, an area that remains largely unexplored despite increasing evidence of playing a critical role in the regulation of brain function (Procès et al., 2022; Tyler, 2012). Secondly, it offers an opportunity to investigate sources of mechanical anisotropy in the brain while the brain is in its natural environment. Unlike conventional mechanical testing methods that typically involve isolating brain tissue samples and subjecting them to controlled forces in laboratory settings, this approach allows for the study of mechanical properties within the intact and *in vivo* brain. This natural environment preserves the effects of vasculature, pressure dynamics, and tissue interactions, providing a true representation of real-world conditions. Finally, it also allows for direct investigation of the human brain, which provides critical insights that may not be fully captured through animal models or isolated tissue samples.

In this observational study, we employed strain tensor imaging alongside diffusion tensor imaging (DTI) and geometric modeling to quantitatively investigate the mechanical properties and behavior of the brain, building on and deepening previous qualitative observations described above. To summarize key features of the observations, and to assess whether the patterns observed in the strain maps reflect global or local (microstructural) effects, two conceptual models were used. The first model was constructed based on the global brain geometry, in particular the global boundary conditions. This geometric model was formulated using two governing principles: systolic brain tissue swelling is restricted by the surrounding cranium and brain expansion occurs primarily through the foramen magnum. The second model was based on the local microstructure, obtained from DTI measurements that were acquired during the same scan session as the strain maps. We compared both the FPS and TPS directions to each model to evaluate which model better explains the observed strain patterns.

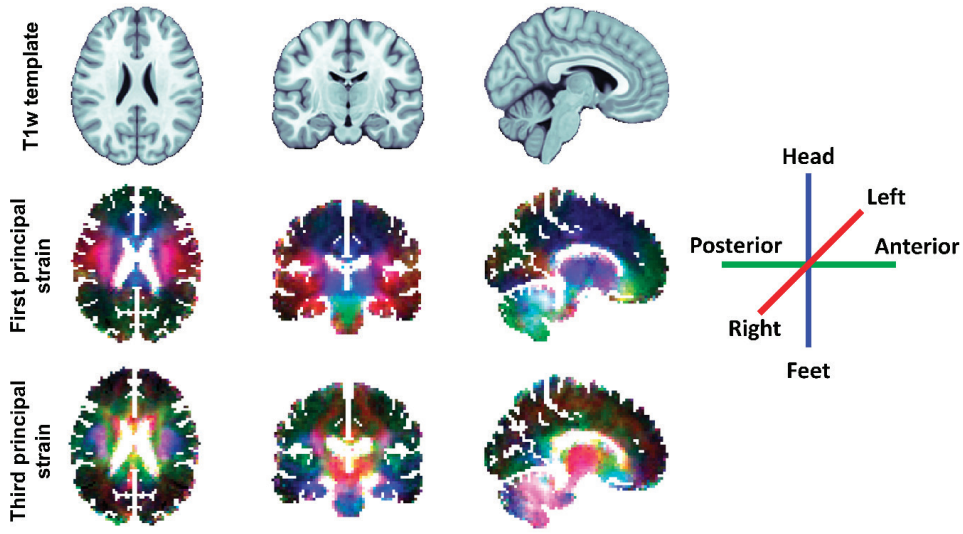


Figure 1: Axial, coronal, and sagittal views of voxel-wise mean maps of the FPS (middle) and TPS (bottom) in MNI space along with a T1 weighted template for anatomical reference (top). The direction of the strain is indicated by the color and the magnitude of the strain is indicated by the color intensity. The FPS maps display inwardly directed, funnel-like strain directions, pointed toward the foramen magnum while the TPS maps display local heterogeneous patterns that possibly reflect the brain microstructure.

2 Method

The data used in this analysis was previously obtained for a separate study by Sloots et al. (2021). The methods of data acquisition will be summarized below, but a more detailed description can be found in the original paper. All subjects gave written informed consent for participation in this study, in accordance with the study protocol that was approved by the ethical review board of our institution.

2.1 Displacement field acquisition

Nine healthy young subjects (3 females, 6 males; mean age: 30 ± 4 years) were imaged using the DENSE sequence (Aletras et al., 1999) optimized for imaging brain deformations at 7 T (Philips Healthcare) to obtain full 3D displacement fields in the Feet-Head, Anterior-Posterior, and Right-Left directions. The DENSE acquisitions were synchronized to the heartbeat, using ECG triggering. The spatial resolution was $3 \times 3 \times 3$ mm^3, with a total of 72 slices for whole brain coverage. The temporal resolution was adjusted to the heart rate, aiming for 11 time points over the first 50% of the cardiac cycle, with a minimum time step of 42 ms due to technical constraints. The motion sensitivity in each direction was such that displacement would yield a phase-shift op π. High-resolution T1-weighted

(T1w) images were also obtained for each subject, with an acquired, isotropic resolution of 1 mm^3. We refer to the original article for further details on the acquisition (Sloots et al., 2021).

2.2 DTI acquisition and processing

DTI measurements were acquired in the same scan session for eight volunteers (one subject opted out before the end of the session due to feeling uncomfortable) using a single shot multislice, pulsed gradient spin echo sequence. A total of 16 directions were obtained with a b-value of 800 s/mm^2 along with an additional b = 0 image. The DTI data was obtained with a transverse orientation and an acquired isotropic resolution of 2 mm^3. Additional parameters included a field-of-view of 224 × 224 mm^2, covering 75 slices with a slice thickness of 2 mm, and a SENSE factor of 2.4 in the anterior-posterior direction. The repetition time (TR) was set to 13.9 s, and the echo time (TE) to 71 ms. The readout bandwidth was 2.4 kHz/pixel and 35.7 Hz/pixel in the frequency and phase-encoding directions, respectively. The scan duration was 4 min and 24 s. The acquired images were corrected for subject motion, geometric distortions, and EPI distortions using ExploreDTI (Leemans et al., 2009). The DTI data were then non-linearly registered to the T1w images using ExploreDTI, which were already aligned to the DENSE space (Sloots et al., 2021), thereby bringing the DTI data into the same space and resolution as the DENSE measurements.

2.3 Strain tensor reconstruction

Full 3D gradient field maps were derived from the displacement field maps by computing the spatial derivatives along the in-plane coordinate axes. T1w scans were segmented using the Computational Anatomy Toolbox (CAT12, Jena University Hospital, Departments of Psychiatry and Neurology) of Statistical Parametric Mapping (SPM12, Wellcome Trust centre for Neuroimaging, University College London) for each subject. Voxels containing CSF were then discarded following an additional city block erosion to ensure minimal partial volume effects from CSF, as derivative calculations using neighboring voxels could affect the resulting deformation gradients. The full 3D peak systole strain tensor was then reconstructed for each volunteer from the displacement gradient field maps. These gradients were calculated relative to end-diastole (which has zero strain). Within each voxel of the strain tensor, eigenvalue decomposition was performed to determine the principal strain directions. The FPS directions correspond to the directions of the dominant stretch while the TPS directions correspond to the direction of the dominant shortening.

2.4 Tissue strain analysis

2.4.1 Global boundary condition analysis

A simple geometric model that we call the Hemodynamic Force Orientation (HFO) model was constructed to describe the general pattern of the funnel-like, inwardly directed systolic forces observed in the brain (Greitz et al., 1992; Hirsch et al., 2013; Sloots et al., 2021). This model aimed to empirically describe the observed directionality patterns based on two plain phenomenological principles:

1. The main direction of lengthening tends to be perpendicular to the inner surface of the cranium. There are two reasons for this principle: First, the manner in which the brain swells during arterial pulsation is restricted by the cranium, allowing for inwardly directed motion only. Second, the vascular anatomy yields a direction of the blood flow into the tissue (and momentum transfer to the tissue) that is mainly perpendicular to the surface of the brain.
2. The foramen magnum is the only way for incompressible brain tissue to accommodate increased volume during arterial pulsations within the confines of the cranium (Almudayni et al., 2023; Wagshul et al., 2011). Thus,
   a. lengthening near the foramen magnum should be directed downwards
   b. lengthening in the rest of the brain should be directed towards the foramen magnum.

Note that the HFO model is not a physically computed loading, but is instead constructed based on phenomenological principles outlined above. This vector field reflects the general directional patterns of the systolic forces, rather than directly representing physical forces in the traditional sense. The first principle was incorporated into the model by approximating the skull's shape with brain masks, from which 3D triangular mesh surfaces were generated using in-house MATLAB code. Inward-facing normal vectors were then defined around the skull surface (see Figure 2). For each subject, an average of 684 ± 52 normal vectors were used to envelop the skull, and vectors at the location of the foramen magnum were removed. The second principle was enforced by defining a single vector of magnitude 1 at the location of the foramen magnum, directed out of the skull. This vector was manually positioned in each subject based on anatomical T1 scans.

The HFO model directions were then defined at each voxel, yielding a vector field spanning the volume of the brain. Each vector was calculated based on its distance relative to three contributions, based on the aforementioned principles. This includes:

1. The contribution c_n of the sum over all normal vectors, normalized to 1 and inversely scaled by the distance to the model strain vector of interest.

2. The contribution c_f from the vector pointing out of the foramen magnum of magnitude 1, inversely scaled by the distance to the model strain vector of interest.
3. The contribution c_d from the unit vector directed from the position of the model strain vector towards the foramen magnum.

Each HFO model vector ε_i, where i corresponds to a given voxel, was calculated as a weighted sum of the contributions, given by

$$\varepsilon_i = w_n \boldsymbol{C}_{n,i} + w_f \boldsymbol{C}_{f,i} + \boldsymbol{C}_{d,i}. \quad (1)$$

Contributions 1 and 2 contain weight factors w_n and w_f, which balances their relative effect. Since the direction and not the magnitude of ε_i is of interest, only 2 weight factors are necessary in the calculation.

Nonlinear least square optimization was then used to obtain the optimal weights which minimize the voxel-wise angles between the HFO model directions and measured strain directions for each subject. The subsequent angle maps thus serve as a measurement of the agreement between the measured strain directions and the HFO model directions. The subject-specific angle maps were registered to MNI space using the MNI152-ICBM2009c non-linear symmetric template (Fonov et al., 2009, 2011) after which the average population angle map was calculated. Non-linear registration with nearest neighbor interpolation was performed following an initial alignment using rigid and affine registration. All registrations were performed using Elastix (Klein et al., 2010). Additionally, the goodness of fit was evaluated by computing the R-squared value for each subject.

The HFO model directions and the measured strain directions are 3D vector quantities. The probability of finding an angle between a reference vector and a randomly selected vector is related to the circumference of the circle formed around the tip of the reference vector and the set of all vectors appearing at that particular angle in question. This circumference is small for low angles and large for high angles, meaning that angles between a reference and a random distribution of vectors are skewed towards higher angles. To account for this bias, equal-solid-angle binning (He et al., 2022) is used for the histograms containing the angle distributions between the measured strain directions and the HFO model directions.

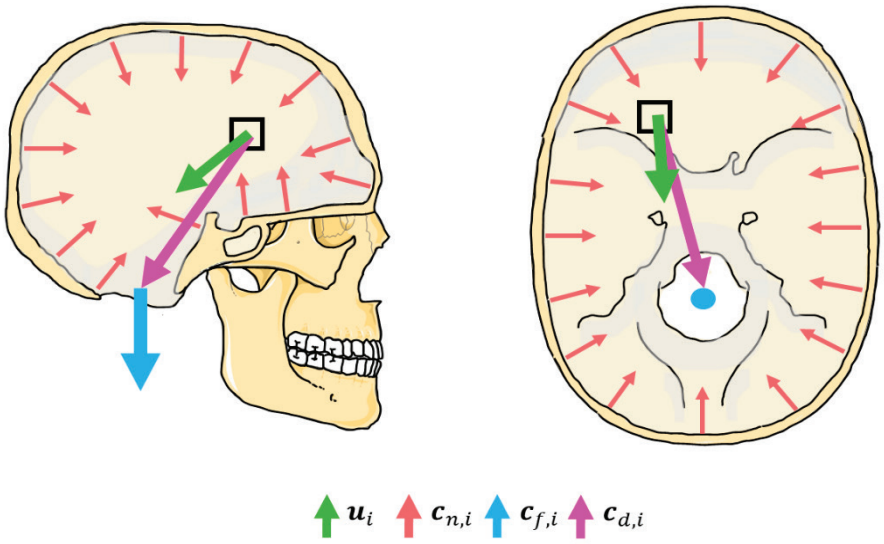


Figure 2: Schematic view of the Hemodynamic Force Orientation (HFO) model used to describe general pattern of the funnel-like, inwardly directed systolic forces observed in the brain. The red, blue, and magenta arrows represent each of the contributions used in eq. (1) to calculate the HFO model vector ε_i, represented by a green arrow.

2.4.3 Microstructure analysis

The effect of brain microstructure on the strain directions was investigated by comparing DTI measurements to strain measurements. This was done by computing the voxel-wise angles between the strain directions and the principal diffusion direction of the DTI data, which corresponds to the main direction of fiber orientations. For the remainder of the analysis, such angles will be referred to as the angle between strain directions and DTI for simplicity.

Because the FPS and TPS directions are orthogonal by definition, the orientation of one of the principal strains inherently constrains the possible orientations of the other. This interdependence could bias the relationship between the measured strain directions and the DTI orientations. For example, when we compare TPS directions with DTI for a given voxel, in the case where the FPS directions align with DTI, the TPS is constrained to the plane perpendicular to DTI. In this case, the angle between the TPS and DTI will be 90° by definition (illustrated in Figure 3a). However, in voxels where the FPS directions and DTI are perpendicular, the TPS can take any direction within the plane containing the DTI orientation, without any restrictions imposed by the FPS. This situation is illustrated in Figure 3b. This situation is reversed when comparing FPS directions with DTI. To account for this potential bias, subselections were performed to examine how the relationship

between the measured strain directions and DTI varies across different angular ranges between the FPS and its orthogonal counterpart. These ranges reflect varying levels of geometric constraint: high bias (0° - 30°, Figure 3a), medium bias (30° - 60°), and low bias (60° - 90°, Figure 3b). While low-bias regions are of primary interest in this analysis, all ranges are included for completeness and transparency.

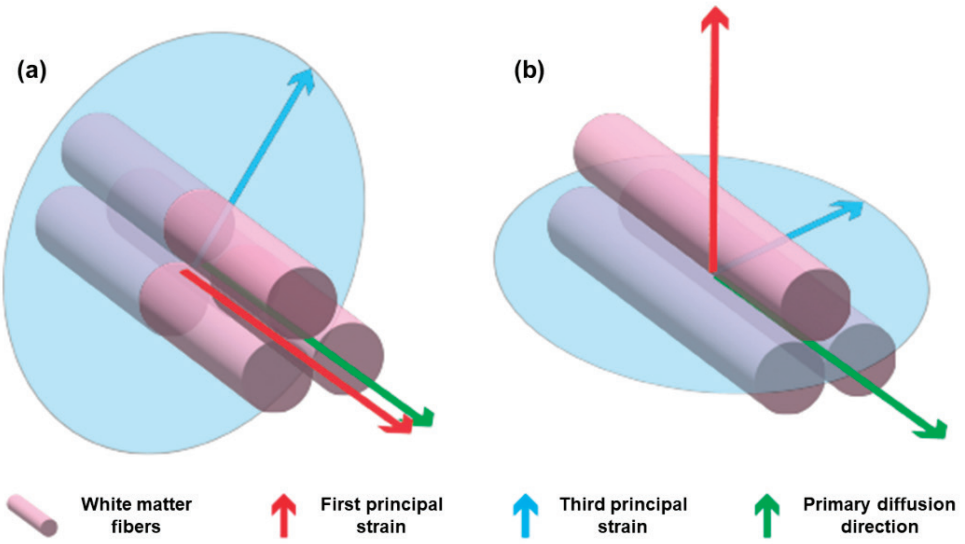


Figure 3: Schematic illustration highlighting two extreme examples of how the orientation of one principal strain direction relative to the primary diffusion direction can affect the orientation of the other, due to their inherent orthogonality. In (a), the FPS direction and primary diffusion direction are aligned, restricting the TPS direction to the plane perpendicular to the primary diffusion direction. In this case, the TPS directions can only take a 90° angle to the primary diffusion direction. In (b), the FPS direction and the primary diffusion direction are perpendicular, such that the TPS orientation lies in the plane containing the primary diffusion direction, and whose normal is the FPS direction. Here the TPS direction can take any angle relative to the primary diffusion direction, eliminating bias introduced by the FPS direction. This example highlights the case when TPS directions and DTI are compared, and FPS must be accounted for. The situation is reversed when FPS directions and DTI are compared.

While investigating only voxels where the angle between the DTI and the considered strain direction (FPS or TPS) is exactly 90° would reduce the potential bias to zero, it would also exclude nearly all voxels from the analysis. For this reason, a range of angles between 60° and 90° was used. However, this still could cause some bias when computing the angle between the considered strain direction and the DTI orientation. To account for this, the principal strain directions are first orthogonlized to the DTI orientation, effectively projecting the considered strain direction back onto the plane whose normal is perpendicular to the DTI orientation, restoring the situation depicted in Figure 3b. This strategy

is similar to what is commonly done in cardiac tractography, where projection strategies are employed to account for the complex geometry of myocardial fibers (STREETER et al., 1969; Toussaint et al., 2013). It should be noted that this technique also affects the shapes of the resulting angle distributions. However, for the low-bias subselection, the effect is nearly negligible.

To ensure that the above-mentioned subselection-projection technique did not impose any bias on the subsequent results, random principal strain directions were generated using Monte Carlo (MC) simulations, with 100 simulations conducted per subject. The corresponding angles to the DTI were subsequently calculated. The potential effects of the subselection technique on the measured angle distributions could then be evaluated by performing identical selections on the simulated random strain direction distributions. Subselections that do not introduce any angle bias for the random strains should also be valid for the measured strains, given that they do not alter the structure of the resulting distributions. Furthermore, any structure observed in the resulting angle distributions from the measured strains that deviate from those of the random strains should reflect real effects due to the relationship between TPS and DTI.

The spatial distribution of voxels following subselections was investigated by computing heatmaps displaying the number of measurements per voxel across all subjects, after registering angle maps to MNI space (MNI152-ICBM2009c). The effects of subselection technique was evaluated for simulated random strains before being used for the measured strains. Thus, we first investigated the effect of subselections on maps of angles between simulated strains with random orientations and DTI in the most general case, where all voxels within the brain were included. Here, we only looked at one MC simulation per subject for heatmaps comparable to the measured data. This was followed by an examination of the effects of regional masking on the angle distributions using the MNI152-ICBM2009c white matter mask. This is to confirm that the regional masking does not affect the shape of the distributions, as the simulated random strain direction should also have no regional dependence (as opposed to measured strains). Next, we performed the same analysis on the angles between the measured strain directions and DTI, where the angle distributions should deviate from simulated random strain distributions if there is coherent structure in the measured strain in relation to the DTI. The simulated random strain distributions were directly compared to the measured strains by computing the mean probability density function per bin along with the 95% confidence interval for 100 simulations per subject. The confidence interval was calculated as

$$CI = x \pm \left(1.96 * \frac{s}{\sqrt{n}}\right), \quad (3)$$

where $\boldsymbol{x}$ is the mean angle, s the corresponding standard deviation, and n the number of subjects.

A regional analysis was conducted to further investigate the relationship between the measured strain directions and the DTI. Here, the same conservative tissue mask as described in the strain tensor reconstruction was used to assure well-defined strains. The regions of interest include white matter, gray matter, regions where the fractional anisotropy (FA) is more than 0.8, and the brainstem. Gray and white matter masks were obtained from probability distributions computed from T1-weighted images. The brainstem was segmented with tractography using ExploreDTI (Leemans et al., 2009).

3 Results

3.1 Global boundary conditions

The weights that minimized the angles between the measured strain directions and the HFO model directions were successfully calculated for each subject using eq. (1) and are presented in Tables S1-S2 in the supplementary material. Figure 4 shows the groupwise mean distributions of angles between the measured principal strain directions and the HFO model. The model showed good agreement with the FPS directions, as indicated by angle distributions centered around zero. In contrast, it showed poor agreement with the TPS directions, with a relatively flat angle distribution that tended to increase toward higher angles . Similarly, the mean R^2 value over all subjects was (mean ± standard deviation) 0.61 ± 0.03 for the FPS directions, and only 0.18 ± 0.04 for the TPS directions. More detailed results for the FPS directions are presented in the following section, highlighting the model's performance across different regions. Due to limited agreement with the model, the corresponding results for the TPS directions are provided in the supplementary material (Figure S1).

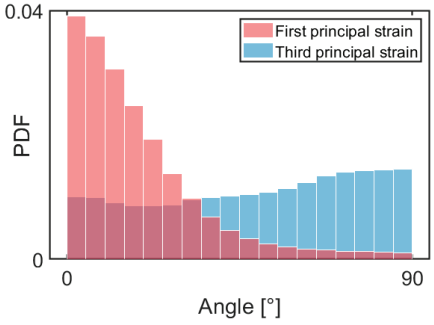


Figure 4: Groupwise mean histograms displaying the distributions of angles between the FPS and the HFO model (red) and the TPS and the HFO model (blue) across all subjects. Lower angles correspond to better agreement between the data and the model.

3.2 First principal strain

Group-wise mean FPS maps for both the data and the model are shown in Figure 5(a-b). The resulting group-wise mean voxel-wise angles between the model and data are shown in Figure 5c, along with standard deviation maps displayed in Figure 5d. The corresponding subject-wise angle maps are shown in Figure S2, visualized for axial and sagittal views. Strong agreement between the model and data is found in the majority of the brain, with the exception mainly being areas surrounding the skull base and the occipital lobes. Figure 5e shows the corresponding subject-wise distribution of the angles where the angles are centered around zero for all subjects, again showing consistent agreement between the data and model.

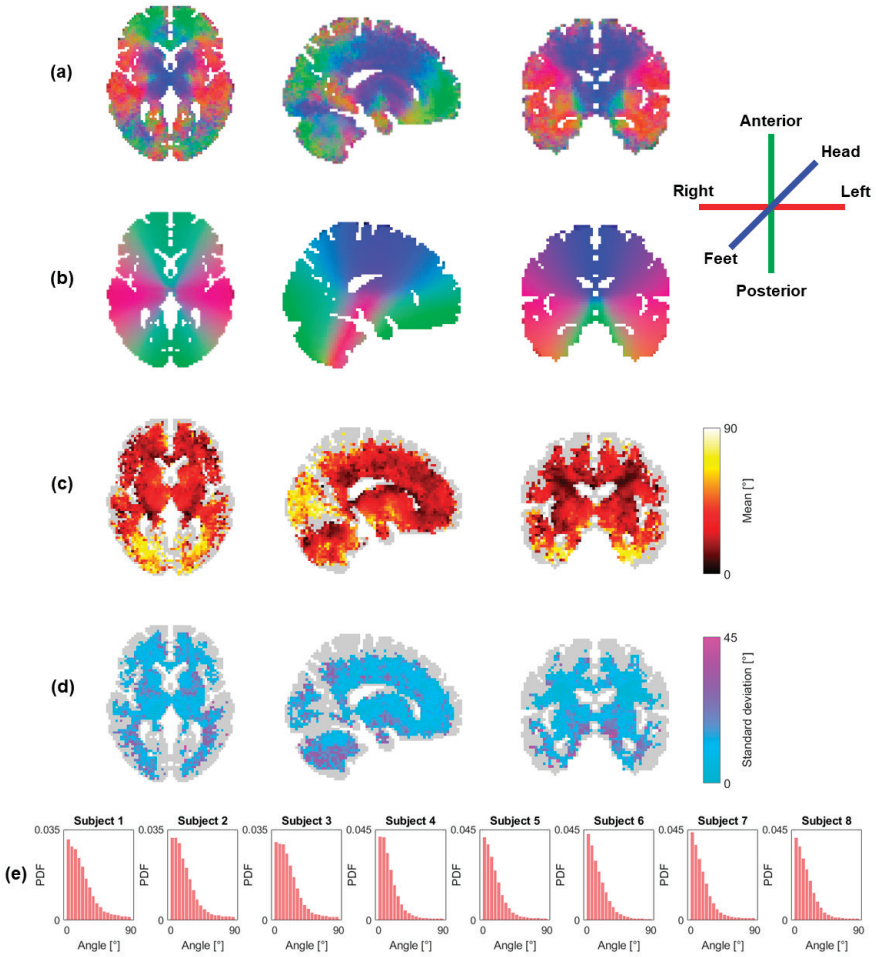


Figure 5: Axial, sagittal, and coronal views of the group-wise mean FPS maps for the measured data (a) and the fitted HFO model (b). The corresponding angles between the FPS directions and HFO model are shown in (c). Lower angles correspond to higher agreement between model and data. Generally low angles are found between the data and model for the majority of the brain, with the main exception being the back of the head. Standard deviation maps are shown in (d), and the subject-wise distributions of angles are shown in (e).

3.3 Analysis of third principal strain directions

3.2.1 Effects of subselection and regional masking

Based on simulations, Figure 6b shows an axial, coronal, and sagittal view of heatmaps displaying the number of measurements per voxel for each subselection based on the angle between the simulated FPS direction and the measured DTI directions. The ICBM 2009c T1-weighted template (Figure 6a) is included for anatomical reference. The number

of measurements per subselection increases following what is described in section 2.4.2, such that the mean voxels per subject is $N_{high\text{-}bias}$ = 15800 ± 1190, $N_{medium\text{-}bias}$ = 43240 ± 2870, and $N_{low\text{-}bias}$ = 59110 ± 4060 for the full brain. The histograms on the right-hand side of the heatmaps display the resulting distribution of angles between the TPS and the DTI. Here, the effects of the subselection-projection technique clearly can be seen for both the data and random strains as the distributions are shifted towards higher angles, particularly for the medium and high-bias subselections. Meanwhile, in low-bias regions the histogram shows a nearly flat distribution, meaning that the subselection-projection method has a minimal effect on the resulting distributions. Figure 6c shows the equivalent heatmaps and histograms as in Figure 6b, where the ICBM 2009c white matter mask has been applied to the heatmaps. Here it can be seen that for the given (measured) DTI orientations, a regional subselection of structured white matter has a negligible effect on the shape of the distributions for random strains compared to the whole brain, indicating that such a subselection does not bias the results.

Based on TPS measurements, Figure 6d displays the equivalent heatmaps and histograms as in Figure 6b for the measured TPS orientations. The black line represents the mean distribution of simulated random strains shown in Figure 6b for direct comparison, where the shaded area indicates the 95% confidence interval. Similar distributions are found in Figure 6b and Figure 6d for the high and medium-bias subselections, however, slight deviation can be seen in the low-bias subselections. Figure 6e shows the equivalent heatmaps and histograms as in (d), where the ICBM 2009c white matter mask has been applied to the heatmaps. The black line represents the mean distribution of simulated random strains shown in Figure 6c for direct comparison, where the shaded area indicates the 95% confidence interval. Here, the histograms of the high- and medium-bias subselections display very similar distributions as in Figure 6d while the low-bias subselection displays a stronger tendency for higher angles between the TPS and the DTI.

Figure 6(f,g) shows the equivalent results as Figure 6(d,e) but for the FPS measurements. Unlike the TPS, the FPS angle distributions relative to DTI showed no considerable or consistent deviation from the simulated strains in the low bias case. For this reason, more detailed results for the TPS directions relative to DTI are presented in the next section, while the corresponding results for the FPS directions are provided in Figure S3 of the supplementary material.

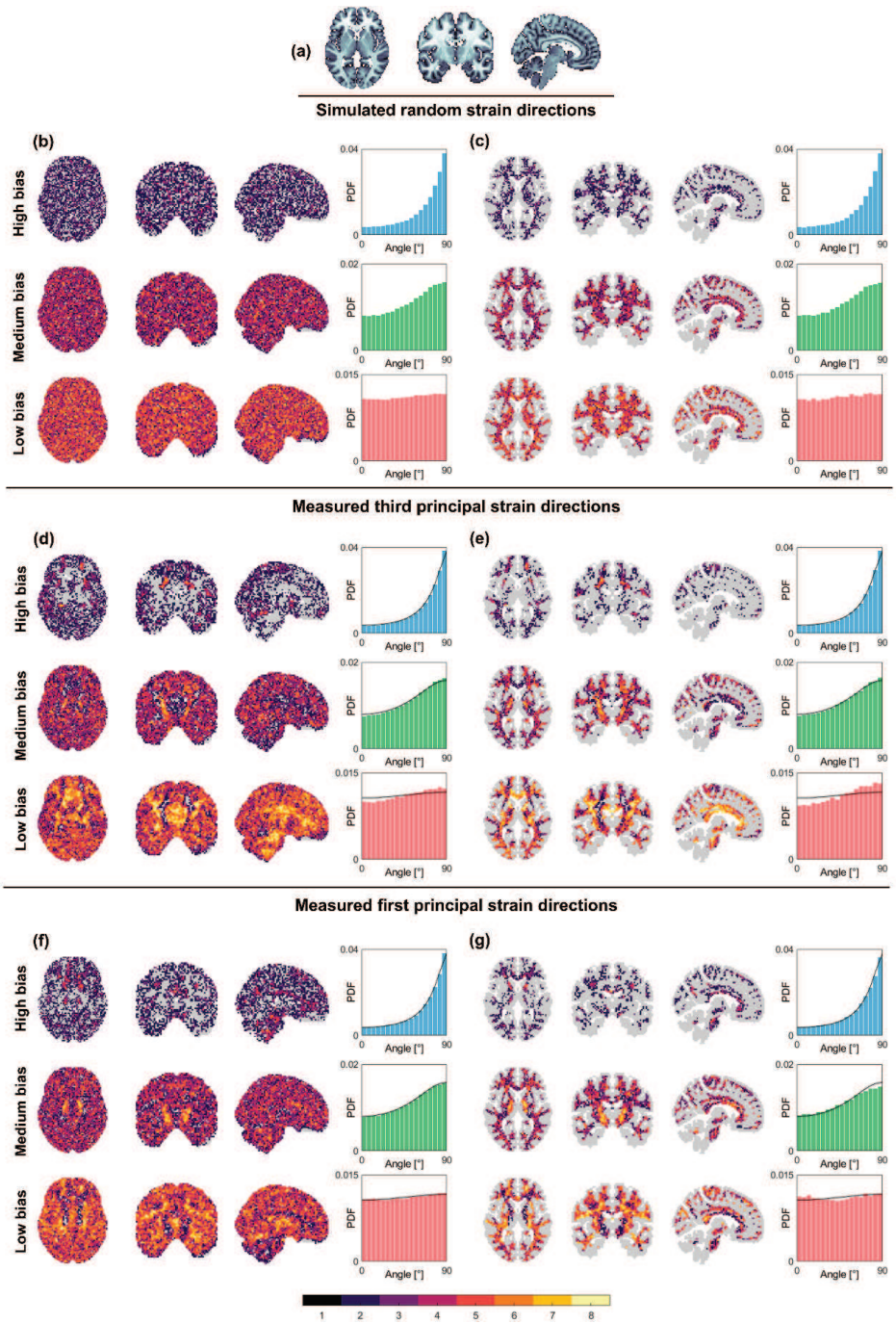


Figure 6: Axial, coronal, and sagittal view of heatmaps displaying the number of measurements per voxel for each subselection based on the angle between the FPS and DTI. The ICBM 2009c T1-weighted template used for registration to MNI space is included for anatomical reference (a). The histograms on the right-hand side of each heatmap show the distribution of angles between the

TPS and the DTI in the selected voxels. The results are shown for random strains (b), random strains with the ICBM 2009c white matter mask (c), measured TPS (d), measured TPS with the ICBM 2009c white matter mask (e), measured FPS (f), and measured FPS with the ICBM 2009c white matter mask (g). The black lines in the histograms in (d-g) indicate the mean simulated random strain distributions, (d-g) respectively, where the shaded area indicates the 95% confidence interval, which in this case is very narrow and may be difficult to discern.

3.2.2 Regional analysis

Figure 7a shows an axial, coronal, and sagittal view of heatmaps displaying the number of measurements per voxel for the low-bias subselection as was also shown in the bottom row of Figure 6e. Here we show a more detailed analysis of white matter (Figure 7b), gray matter (Figure 7c), voxels where FA > 0.8 (Figure 7d), and in the brainstem (Figure 7e). The number of voxels per region is presented in Table S3 in the supplementary material. The ICBM 2009c T1-weighted template used for registration is displayed in Figure 7a for anatomical references. Here, the white and gray matter masks were created from probability distributions generated from T1-weighted images and applied to each subject separately. The histograms on the right-hand side illustrate the distributions of angles between the TPS and DTI within the selected regions for all subjects. The black line represents the mean distribution of simulated random strains subjected to the same selections, where the shaded area indicates the 95% confidence interval. In white matter and high FA regions, there is a consistent tendency for higher angles, meaning that the TPS tends to align perpendicularly to the DTI. Conversely, in gray matter regions, no such tendency is found, and the measured strains behave similarly to the simulated random strains. In the brainstem, the opposite behavior is observed, where there is a tendency for the TPS to be aligned with the DTI.

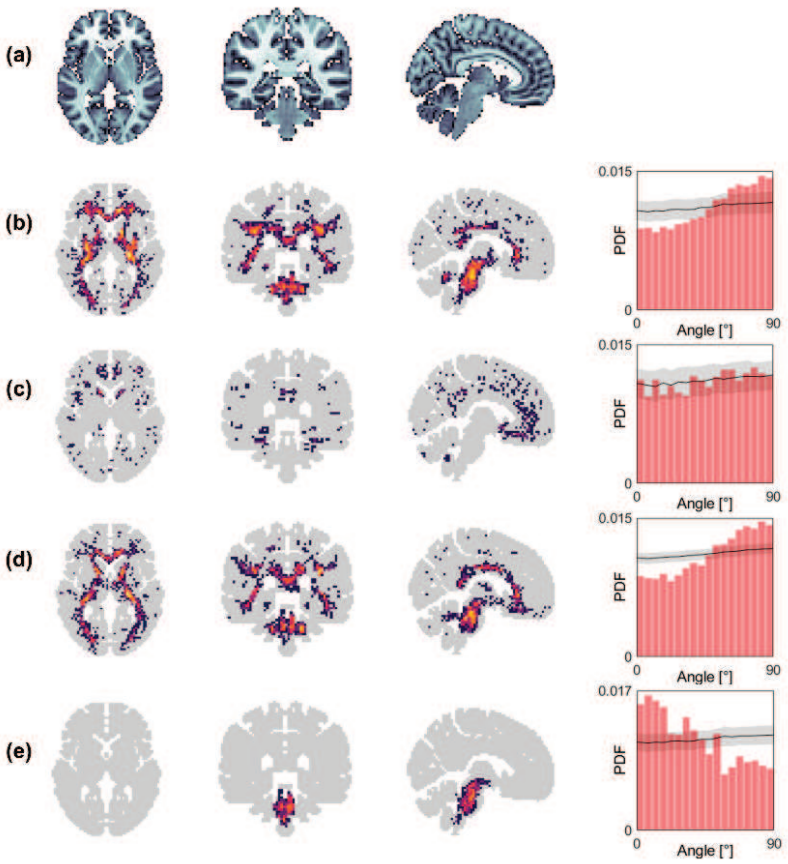


Figure 7: Axial, coronal, and sagittal views of heatmaps displaying the number of measurements per voxel in different regions for the low bias subselection based on the angle between the FPS and the DTI. The ICBM 2009c T1-weighted template used for registration to MNI space is included for anatomical reference (a). The histograms on the right-hand side of each heatmap show the distribution of angles between the TPS and the DTI in the selected voxels. The results are shown for white matter (b), gray matter (c), voxels where FA > 0.8 (d), and for the brainstem (e). The black line represents the mean distribution of random strains subjected to the same selections, where the shaded area indicates the 95% confidence interval.

4 Discussion

This work helps develop a deeper understanding of brain mechanical behavior by quantitatively characterizing the brain's mechanical response to systolic pulsations. Two conceptual models were compared: one capturing global boundary conditions (the HFO model) and the other representing local microstructure, based on DTI data. The HFO model was found to largely describe the measured principal strains, indicating that the first principal strain directions are mostly related to the global boundary conditions.

Conversely, the measured third principal strains tended to align perpendicularly with the DTI orientations, indicating that the third principal strain directions may be more related to the local microstructure. Meanwhile, the HFO model correlated poorly with the third principal strain directions, and no tendencies for alignment between the first principal strain directions and the DTI orientations were observed.

The observed directionality patterns in the FPS maps were to a large extent well described by a model which only takes the global boundary conditions of the brain into account, as evidenced by the distributions of angles between the data and model being centered around 0°, with low variance, along with a high mean R^2 value. The angle maps displayed some regions of disagreement, particularly surrounding the skull base and the occipital lobes. The majority of disagreement at the skull base likely arose due to the shape of the skull being approximated with brain masks obtained from T1-weighted image segmentation, therefore not capturing the complex geometry of the skull base. Similarly, for the occipital lobes, both the tentorium cerebelli and the falx cerebri restrict motion induced by cerebral arterial pulsations, which likely explains the large disagreement in both regions. While the model could be updated to account for these structures, it is not essential for this study and is thus deemed to be outside of the scope. The fact that the FPS data can largely be explained by this simple model, which captures only a few fundamental concepts related to the global boundary conditions, suggests that these conditions likely play a key role in defining the measured FPS directions. This is further reflected in the fact that no clear tendencies for the FPS to align with the DTI were observed in any of the regions of interest (see supplementary material). Meanwhile, the tissue microstructure seemingly contributes as a second-order effect in the TPS directions, which only have a degree of freedom in planes of which the normal is parallel to the FPS direction.

We included simulated random strains for three reasons. First, to evaluate the impact of the subselection-projection technique on the shape of the angle distributions. Second, to verify that further regional selections were valid and did not introduce additional bias given the spatially distinct DTI and FPS orientations. Third, to ensure that any observed deviations in the angle distributions of the measured strains, compared to the simulated random strains, are due to genuine structural effects, distinguishing real structural characteristics from analysis artifacts. A clear deviation from randomness was found in the angle distributions between the TPS and the DTI in the low-bias subselection. This was observed in the entire brain but partially in the white matter where there was a higher prevalence of higher angles between TPS and DIT main orientation. Meanwhile, no such effects were observed in the random strain distributions, meaning that the tendency towards higher angles observed in the angle distributions between the TPS and the DTI should correspond to consistent structural characteristics.

The regional analysis was conducted only after ensuring that a regional subselection would not introduce bias into the resulting angle distributions. A clear tendency for high angles between the TPS and DTI was observed in white matter after applying subject-wise white matter masks and stringent tissue masks, which limited the analysis to regions with well-defined strains. The main direction of shortening thus seemingly tends to occur across the main fiber direction. This effect is even more pronounced in high FA regions, where the directionality of white matter tracts is also well-defined. Meanwhile, no such tendencies were found for gray matter, indicating that the structural anisotropy present in the microstructure of white matter plays a crucial role in dictating the observed directional strain patterns. Interestingly, the brainstem exhibits the opposite behavior as is observed in general white matter and high FA regions, where the TPS tends to align with the DTI. Meanwhile, there was a strong tendency for the FPS direction to occur across the fiber direction, as shown in the mirror analysis (see supplementary material). Thus, the brainstem was shortened along its main direction and stretched perpendicularly to it, demonstrating the Poisson effect. This could indicate a distinction in mechanical behavior between the brainstem and general white matter tracts. More plausibly, it reflects the different force fields to which the brain and the brainstem are subjected due to the brainstem being pushed out of the Foramen Magnum, leading to compressional loading forces.

The results indicate that the main direction of tissue lengthening is governed by global boundary conditions, while the principal direction of shortening tends to align with the underlying microstructure. One possible interpretation of this behavior is that the FPS directions reflect the primary loading direction induced by brain pulsations, whereas the TPS directions represent the passive Poisson response to this loading. As far as we are aware, there are no direct measurements of pulsatile hemodynamic loading in the human brain, so the FPS directions serve as an *in vivo* proxy for these forces. We believe this is reasonable given the small strains and corresponding small loadings in the system. Computational modeling work (Causemann et al., 2022) and a computational model estimating interstitial pressure gradients based on our brain deformation measurements (McGarry et al., 2025) both show pressure fields that would correspond to generally inwardly pointing, smooth force fields. Although this supports the interpretation that the FPS largely reflect the loading forces, more research and validation is clearly warranted.

Assuming that the FPS reflects homogenously directed loading, the preference of the TPS directions to be perpendicular to the primary diffusion directions supports the idea that white matter is mechanically anisotropic. Still, it is conceivable that the TPS tends to align perpendicular to the diffusion direction due to heterogeneously directed loading. Here we use the term heterogeneously directed loading to refer to a loading pattern that would give rise to anisotropic strains in a mechanically isotropic material. If the loading

would be heterogeneously directed on the scale of the measurements, while the tissue simultaneously exhibits isotropic properties, a pattern in the angle distribution between TPS directions and the primary diffusion direction could arise if the loading directions align with the diffusion directions (i.e. with the fiber orientations). One conceivable source of such heterogeneously directed loading could be vascular structures. However, a study focusing on the venous vessels reported only limited alignment with these vessels and main white matter orientation in many regions (Schilling et al., 2025). The overall pattern of arterial supply is outside-in and does not seem to be related to fiber orientation either.

Regardless, it is hard to imagine loading conditions that would produce spatially coherent FPS directions alongside spatially heterogeneous TPS directions, unless the underlying material exhibits mechanical anisotropy. Therefore, the observed directional preference of the TPS would be challenging to explain under isotropic material properties, making Occam's Razor favor the hypothesis of mechanical anisotropy in white matter. In particular, the tendency of the TPS to align perpendicularly to the DTI orientations could imply that white matter is stiffer along the tract direction than across, consistent with tensile anisotropy. This interpretation is in line with recent MR elastography studies that also suggest tensile anisotropy in white matter (Smith et al., 2022; Wang et al., 2023), further supporting the notion that anisotropy emerges *in vivo* under physiological loading conditions. However, an alternative or contributing explanation could be the presence of residual stress in white matter. Recent work in mice and minipigs has shown that white matter is under tensile stress along the fiber axis, while gray matter exhibits compressive stresses (Balouchzadeh et al., 2025). Such pre-tension may be related to, and is difficult to disentangle from, intrinsic material anisotropy. Although these findings have so far only been demonstrated in animal models, they suggest that residual stress could contribute to the directional patterns observed here.

If indeed the preferentially perpendicular alignment of the TPS with DTI reflects anisotropic behavior as a second-order effect via the Poisson effect, our results may help reconcile the ongoing debate on whether the brain is mechanically isotropic or anisotropic. Broadly speaking, white matter behaves in a largely mechanically isotropic manner, as the FPS is primarily dependent on the global boundary conditions rather than the underlying tissue microstructure. Mechanical anisotropy only emerges as a second-order effect in the TPS. It is therefore plausible that both effects can be exhibited depending on the experimental conditions, as shown by the disagreement in the literature. Notably, these results are obtained non-invasively, *in vivo*, while the brain is in its natural state. We therefore avoid many of the challenges faced in traditional mechanical testing and provide a novel perspective that more accurately represents the true functional conditions of the brain. It is, however, important to note that this study is observational in nature. All reported directional patterns in the principal strain maps are directly derived from *in vivo* measure-

ments, without requiring assumptions about underlying material properties. While we present interpretations consistent with mechanical anisotropy, the observational results stand independently of these assumptions.

Due to the necessity of the subselection strategy to avoid bias in the TPS directions, approximately half of the voxels were excluded from the analysis, potentially leading to uncertainty about whether the excluded regions exhibit similar anisotropic effects. Despite this limitation, voxels were sampled from most regions of the brain thanks to the inclusion of multiple subjects, as demonstrated in the heatmaps in Figure 7. The excluded regions are visible in the 0-30° and 30-60° selection heatmaps, where specific tract structures with principal strains and DTI within these angle ranges stand out. These exclusions also appear as gaps in the 60-90° selection heatmap. The number of voxels that were analyzed was also further reduced by applying stringent masking which assures more well-defined strains. While most regions were reduced to contain roughly half their initial number of voxels, the gray matter was reduced from approximately 8961 ± 4407 to 1147 ± 637 voxels, which is particularly visible in the heatmaps. However, angle distributions obtained with and without stringent masking showed high similarity, and the decreased number of voxels was deemed a necessary trade-off in all other regions.

Several factors could diminish the impact of the observed anisotropic effects. One limitation is the relatively large resolution of 3 mm isotropic, leading to considerable partial volume effects. As gray matter was shown here to exhibit low to no anisotropic properties, this lessens the observed effect in white matter regions bordering gray matter. The large voxel size also affects the principal strain and DTI measurements, as finer structural details and subtle variations within the white matter are averaged out, potentially obscuring the true extent of anisotropy. It also is known that most voxels contain multiple fiber orientations even at higher resolutions (Jeurissen et al., 2013), the larger voxel size used in this analysis exacerbates this issue, further contributing to increased ambiguity. While the voxel size in the DENSE measurements was optimized for single-voxel SNR, previous studies (Adams et al., 2019, 2020) have shown that a voxel size of approximately 2 mm^3 is achievable. Future work could therefore consider higher-resolution DENSE data, at the expense of single-voxel SNR. While our study provides direct *in vivo* observations of brain strain patterns under physiological loading, it does not in itself disentangle the underlying constitutive properties of brain tissue. Our use of phenomenological models has been intended to summarize and interpret the observed strain directionality rather than to provide mechanistic explanations. Instead, advanced computational models are likely required to gain deeper insight into the nature of brain mechanics. Examples of simulations that work towards the required complexity are e.g. the work of Linninger et al., (2019), and more recent works by Causemann et al., (2022) and McGarry et al., (2025). The authors are open to sharing data for the purpose of developing such models.

5 Conclusion

In this study, we explored to what extent principal strain directions that arise due to cerebral arterial pulsations can be explained by the global boundary conditions and local microstructure. We found that our model, incorporating two phenomenological principles related to the global boundary conditions, largely explains the measured FPS direction patterns. This suggests that the stretch directions primarily depend on the global boundary conditions, consistent with isotropic mechanical properties of brain tissue. Meanwhile, a tendency for the TPS to align perpendicular to the principal diffusion direction was observed, suggesting that compression effects preferably occur across white matter tracts and that the local microstructure thus leads to some form of mechanical anisotropy. As these findings suggest that mechanical anisotropy emerges as a second-order effect in the TPS, they may help resolve the ongoing debate on mechanical isotropy in the brain.

References

Aletras, A. H., Ding, S., Balaban, R. S., & Wen, H. (1999). DENSE: displacement encoding with stimulated echoes in cardiac functional MRI. *Journal of Magnetic Resonance (San Diego, Calif. : 1997)*, *137*(1), 247–252. https://doi.org/10.1006/jmre.1998.1676

Almudayni, A., Alharbi, M., Chowdhury, A., Ince, J., Alablani, F., Minhas, J. S., Lecchini-Visintini, A., & Chung, E. M. L. (2023). Magnetic resonance imaging of the pulsing brain: a systematic review. *Magma (New York, N.Y.)*, *36*(1), 3–14. https://doi.org/10.1007/s10334-022-01043-1

Balouchzadeh, R., Kroenke, C. D., Garcia, K. E., & Bayly, P. V. (2025). Measurement of Residual Stress in the Brain. *Journal of Biomechanical Engineering*, *147*(9). https://doi.org/10.1115/1.4068879

Budday, S., Ovaert, T. C., Holzapfel, G. A., Steinmann, P., & Kuhl, E. (2020). Fifty Shades of Brain: A Review on the Mechanical Testing and Modeling of Brain Tissue. *Archives of Computational Methods in Engineering*, *27*(4), 1187–1230. https://doi.org/10.1007/s11831-019-09352-w

Budday, S., Sommer, G., Birkl, C., Langkammer, C., Haybaeck, J., Kohnert, J., Bauer, M., Paulsen, F., Steinmann, P., Kuhl, E., & Holzapfel, G. A. (2017). Mechanical characterization of human brain tissue. *Acta Biomaterialia*, *48*, 319–340. https://doi.org/10.1016/j.actbio.2016.10.036

Budday, S., Steinmann, P., & Kuhl, E. (2014). The role of mechanics during brain development. *Journal of the Mechanics and Physics of Solids*, *72*, 75–92. https://doi.org/10.1016/j.jmps.2014.07.010

Causemann, M., Vinje, V., & Rognes, M. E. (2022). Human intracranial pulsatility during the cardiac cycle: a computational modelling framework. *Fluids and Barriers of the CNS*, *19*(1), 84. https://doi.org/10.1186/s12987-022-00376-2

El Sayed, T., Mota, A., Fraternali, F., & Ortiz, M. (2008). Biomechanics of traumatic brain injury. *Computer Methods in Applied Mechanics and Engineering*, *197*(51–52), 4692–4701. https://doi.org/10.1016/j.cma.2008.06.006

Eskandari, F., Shafieian, M., Aghdam, M. M., & Laksari, K. (2021). Structural Anisotropy vs. Mechanical Anisotropy: The Contribution of Axonal Fibers to the Material Properties of Brain White Matter. *Annals of Biomedical Engineering*, *49*(3), 991–999. https://doi.org/10.1007/s10439-020-02643-5

Feng, Y., Lee, C.-H., Sun, L., Ji, S., & Zhao, X. (2017). Characterizing white matter tissue in large strain via asymmetric indentation and inverse finite element modeling. *Journal of the Mechanical Behavior of Biomedical Materials*, *65*, 490–501. https://doi.org/10.1016/j.jmbbm.2016.09.020

Feng, Y., Murphy, M. C., Hojo, E., Li, F., & Roberts, N. (2024). Magnetic Resonance Elastography in the Study of Neurodegenerative Diseases. *Journal of Magnetic Resonance Imaging : JMRI*, *59*(1), 82–96. https://doi.org/10.1002/jmri.28747

Feng, Y., Okamoto, R. J., Namani, R., Genin, G. M., & Bayly, P. V. (2013). Measurements of mechanical anisotropy in brain tissue and implications for transversely isotropic material models of white matter. *Journal of the Mechanical Behavior of Biomedical Materials*, *23*, 117–132. https://doi.org/10.1016/j.jmbbm.2013.04.007

Fonov, V., Evans, A. C., Botteron, K., Almli, C. R., McKinstry, R. C., & Collins, D. L. (2011). Unbiased average age-appropriate atlases for pediatric studies. *NeuroImage*, *54*(1), 313–327. https://doi.org/10.1016/j.neuroimage.2010.07.033

Fonov, V., Evans, A., McKinstry, R., Almli, C., & Collins, D. (2009). Unbiased nonlinear average age-appropriate brain templates from birth to adulthood. *NeuroImage*, *47*, S102. https://doi.org/10.1016/S1053-8119(09)70884-5

Giordano, C., Cloots, R. J. H., van Dommelen, J. A. W., & Kleiven, S. (2014). The influence of anisotropy on brain injury prediction. *Journal of Biomechanics*, *47*(5), 1052–1059. https://doi.org/10.1016/j.jbiomech.2013.12.036

Goriely, A., Geers, M. G. D., Holzapfel, G. A., Jayamohan, J., Jérusalem, A., Sivaloganathan, S., Squier, W., van Dommelen, J. A. W., Waters, S., & Kuhl, E. (2015). Mechanics of the brain: perspectives, challenges, and opportunities. *Biomechanics and Modeling in Mechanobiology*, *14*(5), 931–965. https://doi.org/10.1007/s10237-015-0662-4

Greitz, D., Wirestam, R., Franck, A., Nordell, B., Thomsen, C., & Ståhlberg, F. (1992). Pulsatile brain movement and associated hydrodynamics studied by magnetic resonance phase imaging. The Monro-Kellie doctrine revisited. *Neuroradiology*, *34*(5), 370–380. https://doi.org/10.1007/BF00596493

He, G., Karatza, Z., & Papanicolopulos, S.-A. (2022). Contact orientation distributions for visualisation of granular fabric. *Granular Matter*, *24*(2), 44. https://doi.org/10.1007/s10035-021-01201-7

Hirsch, S., Klatt, D., Freimann, F., Scheel, M., Braun, J., & Sack, I. (2013). In vivo measurement of volumetric strain in the human brain induced by arterial pulsation and harmonic waves. *Magnetic Resonance in Medicine*, *70*(3), 671–683. https://doi.org/10.1002/mrm.24499

Jeurissen, B., Leemans, A., Tournier, J.-D., Jones, D. K., & Sijbers, J. (2013). Investigating the prevalence of complex fiber configurations in white matter tissue with diffusion magnetic resonance imaging. *Human Brain Mapping*, *34*(11), 2747–2766. https://doi.org/10.1002/hbm.22099

Jin, X., Zhu, F., Mao, H., Shen, M., & Yang, K. H. (2013). A comprehensive experimental study on material properties of human brain tissue. *Journal of Biomechanics*, *46*(16), 2795–2801. https://doi.org/10.1016/j.jbiomech.2013.09.001

Karimi, A., & Navidbakhsh, M. (2014). An experimental study on the mechanical properties of rat brain tissue using different stress-strain definitions. *Journal of Materials Science. Materials in Medicine*, *25*(7), 1623–1630. https://doi.org/10.1007/s10856-014-5198-0

Klein, S., Staring, M., Murphy, K., Viergever, M. A., & Pluim, J. P. W. (2010). elastix: a toolbox for intensity-based medical image registration. *IEEE Transactions on Medical Imaging*, *29*(1), 196–205. https://doi.org/10.1109/TMI.2009.2035616

Leemans, A., Jeurissen, B., Sijbers, J., Leemans, A., Jeurissen, B., Sijbers, J., & Jones, D. K. (2009). *ExploreDTI: A graphical toolbox for processing, analyzing, and visualizing diffusion MR data*. http://www.ExploreDTI.com.

Linninger, A., Hartung, G., Badr, S., & Morley, R. (2019). Mathematical synthesis of the cortical circulation for the whole mouse brain-part I. theory and image integration. *Computers in Biology and Medicine*, *110*, 265–275. https://doi.org/10.1016/j.compbiomed.2019.05.004

McGarry, M., Sowinski, D., Tan, L., Weaver, J., Zwanenburg, J. J. M., & Paulsen, K. (2025). In vivo magnetic resonance imaging of the interstitial pressure gradients pgMRI using a pulsatile poroelastic computational model. *Interface Focus*, *15*(1). https://doi.org/10.1098/rsfs.2024.0044

Miller, K., & Chinzei, K. (1997). Constitutive modelling of brain tissue: Experiment and theory. *Journal of Biomechanics*, *30*(11–12), 1115–1121. https://doi.org/10.1016/S0021-9290(97)00092-4

Prange, M. T., & Margulies, S. S. (2002). Regional, directional, and age-dependent properties of the brain undergoing large deformation. *Journal of Biomechanical Engineering*, *124*(2), 244–252. https://doi.org/10.1115/1.1449907

Procès, A., Luciano, M., Kalukula, Y., Ris, L., & Gabriele, S. (2022). Multiscale Mechanobiology in Brain Physiology and Diseases. *Frontiers in Cell and Developmental Biology*, *10*, 823857. https://doi.org/10.3389/fcell.2022.823857

Rashid, B., Destrade, M., & Gilchrist, M. D. (2012). Mechanical characterization of brain tissue in compression at dynamic strain rates. *Journal of the Mechanical Behavior of Biomedical Materials*, *10*, 23–38. https://doi.org/10.1016/j.jmbbm.2012.01.022

Reese, T. G., Feinberg, D. A., Dou, J., & Wedeen, V. J. (2002). Phase contrast MRI of myocardial 3D strain by encoding contiguous slices in a single shot. *Magnetic Resonance in Medicine*, *47*(4), 665–676. https://doi.org/10.1002/mrm.10111

Schilling, K. G., Newton, A., Tax, C. M. W., Chamberland, M., Remedios, S. W., Gao, Y., Li, M., Chang, C., Rheault, F., Sepherband, F., Anderson, A., Gore, J. C., & Landman, B. (2025). The relationship of white matter tract orientation to vascular geometry in the human brain. *Scientific Reports*, *15*(1), 18396. https://doi.org/10.1038/s41598-025-99724-z

Sloots, J. J., Biessels, G. J., de Luca, A., & Zwanenburg, J. J. M. (2021). Strain Tensor Imaging: Cardiac-induced brain tissue deformation in humans quantified with high-field MRI. *NeuroImage*, *236*, 118078. https://doi.org/10.1016/j.neuroimage.2021.118078

Smith, D. R., Caban-Rivera, D. A., McGarry, M. D. J., Williams, L. T., McIlvain, G., Okamoto, R. J., Van Houten, E. E. W., Bayly, P. V., Paulsen, K. D., & Johnson, C. L. (2022). Anisotropic mechanical properties in the healthy human brain estimated with multi-excitation transversely isotropic MR elastography. *Brain Multiphysics*, *3*, 100051. https://doi.org/10.1016/j.brain.2022.100051

STREETER, D. D., SPOTNITZ, H. M., PATEL, D. P., ROSS, J., & SONNENBLICK, E. H. (1969). Fiber Orientation in the Canine Left Ventricle during Diastole and Systole. *Circulation Research*, *24*(3), 339–347. https://doi.org/10.1161/01.RES.24.3.339

Toussaint, N., Stoeck, C. T., Schaeffter, T., Kozerke, S., Sermesant, M., & Batchelor, P. G. (2013). In vivo human cardiac fibre architecture estimation using shape-based diffusion tensor processing. *Medical Image Analysis*, *17*(8), 1243–1255. https://doi.org/10.1016/j.media.2013.02.008

Tyler, W. J. (2012). The mechanobiology of brain function. *Nature Reviews. Neuroscience*, *13*(12), 867–878. https://doi.org/10.1038/nrn3383

Velardi, F., Fraternali, F., & Angelillo, M. (2006). Anisotropic constitutive equations and experimental tensile behavior of brain tissue. *Biomechanics and Modeling in Mechanobiology*, *5*(1), 53–61. https://doi.org/10.1007/s10237-005-0007-9

Wagshul, M. E., Eide, P. K., & Madsen, J. R. (2011). The pulsating brain: A review of experimental and clinical studies of intracranial pulsatility. *Fluids and Barriers of the CNS*, *8*(1), 5. https://doi.org/10.1186/2045-8118-8-5

Wang, S., Guertler, C. A., Okamoto, R. J., Johnson, C. L., McGarry, M. D. J., & Bayly, P. V. (2023). Mechanical stiffness and anisotropy measured by MRE during brain development in the minipig. *NeuroImage*, *277*, 120234. https://doi.org/10.1016/j.neuroimage.2023.120234

6 Supplementary Material

6.1 Global boundary condition analysis

Table S1: The fitted weights from nonlinear least-squares optimization, shown as their squared and normalized values (scaled such that the largest equals 1). These weights minimize the angle difference between the HFO model and FPS directions.

	Sub. 1	***Sub. 2***	***Sub. 3***	***Sub. 4***	***Sub. 5***	***Sub. 6***	***Sub. 7***	***Sub. 8***
w_n	1	1	1	1	0.94	1	1	1
w_f	0.86	0.80	0.95	0.95	1	0.79	0.90	0.91

Table S2: The fitted weights from nonlinear least-squares optimization, shown as their squared and normalized values (scaled such that the largest equals 1). These weights minimize the angle difference between the HFO model and TPS directions.

	Sub. 1	***Sub. 2***	***Sub. 3***	***Sub. 4***	***Sub. 5***	***Sub. 6***	***Sub. 7***	***Sub. 8***
w_n	0.85	0	1	0	1	0	0	1
w_f	1	1	0	1	0	1	1	0

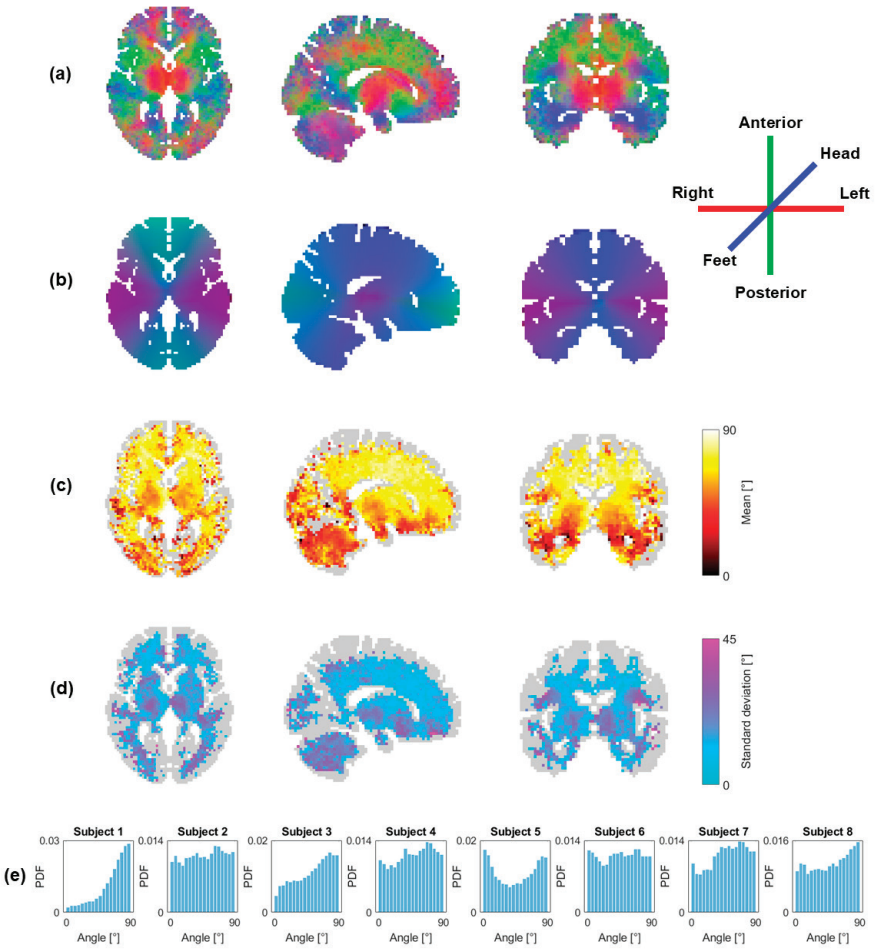


Figure S1: Axial, sagittal, and coronal views of the group-wise mean TPS angle maps for the measured data (a) and the fitted HFO model (b). The corresponding angles between the TPS directions and HFO model are shown in (c). Lower angles correspond to higher agreement between model and data. Standard deviation maps are shown in (d), and the subject-wise distributions of angles are shown in (e).

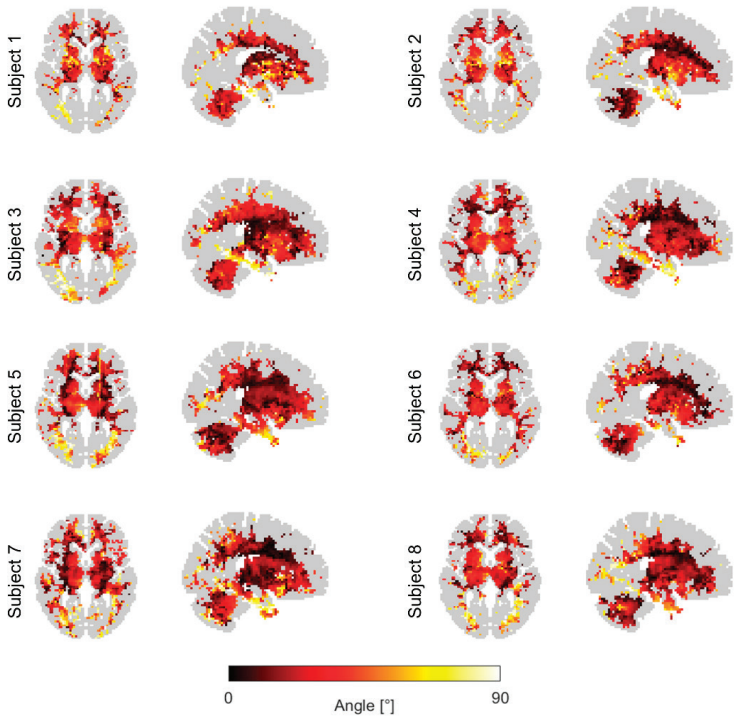


Figure S2: Axial and sagittal views of the voxel-wise angles between the HFO model and FPS direction data for each subject. Lower angles correspond to higher agreement between model and data. The model shows good agreement with the data for the majority of the brain, with the exception for mainly the back of the head. Similar spatial patterns can be observed between subjects, with much overlap between regions of disagreement. Stringent masking of CSF was performed to ensure minimal partial volume effects from CSF in the strain maps. Each angle map has been registered to the MNI152 ICBM 2009c non-linear symmetric template.

6.2 Relationship between TPS and DTI

Table S3: The number of voxels per region with and without applying stringent masking which ensures well-defined strains.

	No stringent mask	***With stringent mask***
White matter	9973 ± 3705	5506± 1777
Gray matter	8961± 4407	1147± 637
High FA regions	6746± 846	4161± 720
Brainstem	778± 181	372± 109

6.3 Relationship between FPS and DTI

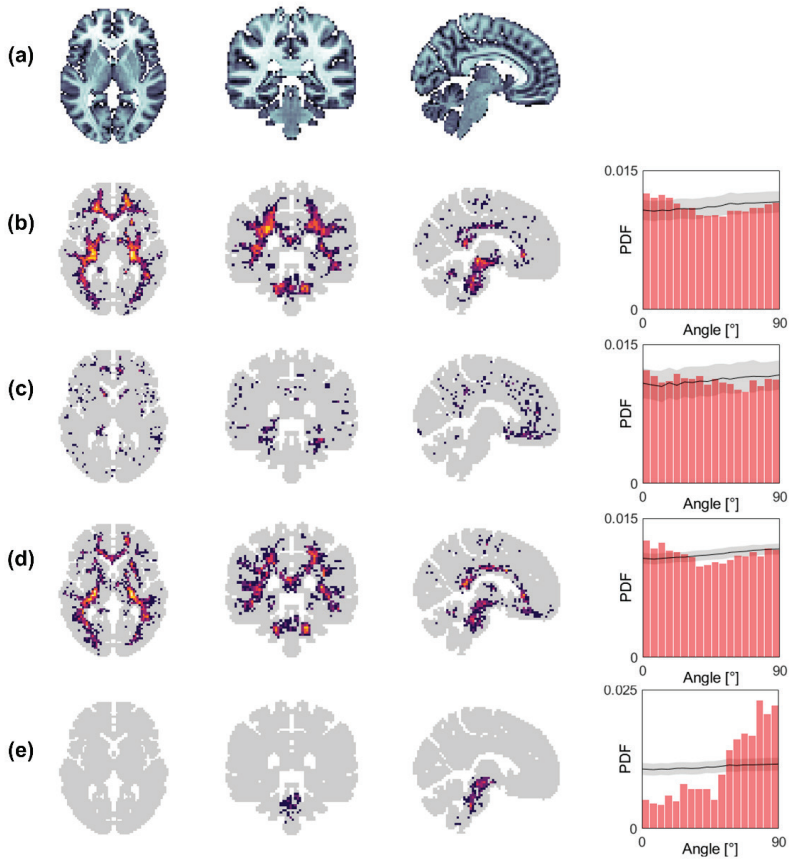


Figure S3: Axial, coronal, and sagittal view of heatmaps displaying the number of measurements per voxel in different regions for the low bias subselection based on the angle between the FPS and the DTI. The ICBM 2009c T1-weighted template used for registration to MNI space is included for anatomical reference (a). The histograms on the right-hand side of each heatmap show the distribu-

tion of angles between the FPS and the DTI in the selected voxels. The results are shown for white matter (b), gray matter (c), voxels where FA > 0.8 (d), and for the brainstem (e). The black line represents the mean distribution of random strains subjected to the same selections, where the shaded area indicates the 95% confidence interval.



Chapter 7

General discussion

In recent years, it has become increasingly clear that the brain's mechanical state plays a crucial role in both neural function and dysfunction, and consequently in overall health and disease. Because of the protective nature of the skull and the fragile structure of the brain, its mechanical state has for long been inaccessible. Only recently, with the advent of specialized MRI techniques, has it become possible to probe the brain's mechanical properties non-invasively *in vivo*. Consequently, many mechanical aspects of brain physiology and function remain unknown - not only in healthy cases, but also in pathological or injured conditions. This gap in knowledge makes the study of brain mechanics a field rich with potential, offering new avenues to understand, diagnose, and treat a wide range of disorders.

The overall aim of this project was two-fold. First, to develop intrinsic Magnetic Resonance Elastography (iMRE) using precise measurements of brain pulsations enabled by the increased sensitivity of the DENSE sequence, and to assess its performance. Second, to explore underlying biological and physiological mechanisms in relation to mechanical property measurements to better understand their role in brain function and pathology. This chapter summarizes and discusses the studies presented in this thesis, drawing together their implications, insights, and future perspectives.

Part I: Advancing and evaluating intrinsic MR elastography

At the onset of this project, iMRE was largely unexplored. The first experiment using cardiac-induced brain pulsations to estimate mechanical properties was performed by Weaver and colleagues in 2012 (Weaver et al., 2012), employing an angiographic phase-contrast sequence to measure tissue displacements. The technique posed several intriguing benefits compared to traditional MR elastography (MRE). As outlined in **Chapter 1**, iMRE enabled mechanical property estimates without external equipment, overcame the problem of poor shear wave penetration through the skull, and captured the brain's natural mechanical state rather a state subjected to artificially external vibrations. Despite these benefits, the technique saw limited further exploration, likely due to substantial noise in the property maps of the initial attempts and the absence of coherent, realistic spatial property distributions. Accurate estimation of mechanical properties critically depends on precise displacement measurements. Early attempts relied on phase-contrast techniques optimized for other purposes, with sensitivities on the order of centimeters (Weaver et al., 2012; Zorgani et al., 2015). Consequently, these measurements were inherently noisy - analogous to attempting to measure micrometer-scale displacements with a ruler calibrated in centimeters. Figure 1 displays examples of stiffness maps obtained using early attempts of iMRE, alongside a representative map obtained in Chapter 2.

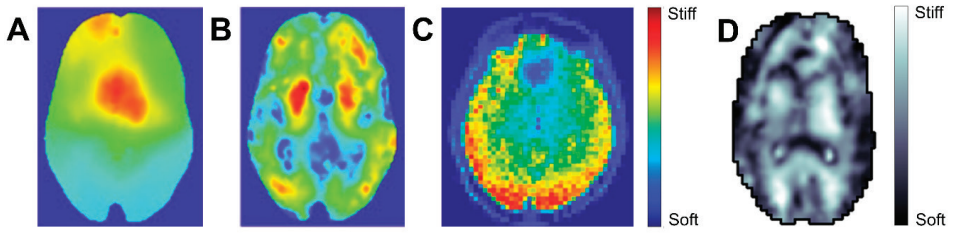


Figure 1: Stiffness maps obtained from early iMRE approaches: (A) linear elastic model, (B) poroelastic model by (Weaver et al., 2012), and (C) seismic noise correlation by (Zorgani et al., 2015). Panel (D) shows a representative shear stiffness map using a viscoelastic model from Chapter 2, demonstrating improved anatomical detail and clearer delineation of brain structures compared to previous methods.

In this light, the Displacement Encoding with Stimulated Echoes (DENSE) MR sequence represented a critical advancement for iMRE by enabling measurement of displacements induced by cardiac brain pulsations. Despite an inherent twofold loss in signal-to-noise ratio (SNR) compared to spin-echo techniques, the extended interval between motion encoding and decoding enabled substantial signal accumulation, which was crucial for accurately characterizing sub-voxel brain tissue motion (Adams et al., 2020). This development laid the foundation for the work presented in **Chapter 2**, where notable improvements in accuracy were observed. First, the shear stiffness maps exhibited improved anatomical detail and clearer delineation of brain structures compared to earlier attempts. Second, test-retest reliability (hereafter referred to as repeatability) approached that of standard 3 T MRE, which is remarkable given the complete absence of external actuation, traditionally considered an essential feature of MRE. Third, the spatial sensitivity was comparable to standard MRE, enabling detection of consistent regional stiffness differences not only across the group of eight subjects but also at the level of individual subjects. Furthermore, the spatial stiffness distribution obtained with iMRE closely resembled that of standard MRE, further supporting its validity. Some regional differences were observed between iMRE and standard MRE, which is unsurprising given that different brain regions experience varying degrees of stiffening under higher-frequency actuation (Weickenmeier et al., 2018) and the differences in the behavior of the brain's fluid component between the two frequency regimes (M. McGarry et al., 2019).

The differences in regional stiffness between iMRE and standard MRE highlight an important feature of iMRE that was briefly touched on before; iMRE measures the brain in its natural, unperturbed state. The spatial stiffness distribution obtained with iMRE therefore reflects the intrinsic mechanical properties of brain tissue under physiological conditions, capturing the influence of local fluid dynamics, vascular perfusion, and tissue microstructure without the confounding effects of externally applied vibrations. This topic will be explored further later in this chapter.

Despite its strengths, the proposed iMRE technique had several limitations. First, the damping ratio exhibited lower repeatability and spatial resolution compared to stiffness, reflecting a data-model mismatch when applying a viscoelastic model at low actuation frequencies (M. McGarry et al., 2019; M. D. J. McGarry et al., 2015). Second, displacement measurements were contaminated by signals from fluid flow, including CSF and larger blood vessels, producing artifacts in the mechanical property maps. Third, Lamé's first parameter (here referred to as λ-modulus), representing compressional stiffness, could not be adequately modeled in a viscoelastic framework. Instead, only a global mean estimate could be determined. Finally, at low actuation frequencies, force imbalances between elastic and inertial components prevent objective determination of viscoelastic properties. This leads to measurements that are arbitrarily scalable, an effect known as non-uniqueness[1]. For this reason, lower stiffness bounds of 100 Pa were imposed to restrict the non-linear inversion (NLI) scheme from producing what at the time was considered to be non-physical solutions.

Chapter 2 demonstrated the feasibility of measuring the mechanical behavior of brain tissue using the commonly employed viscoelastic model, highlighting both its strengths and limitations. However, most of these limitations could be largely or entirely overcome by moving to poroelastic modeling, a more elaborate mechanical model that is less common in MRE, which naturally represented the next step in advancing the methodology. This work, presented in **Chapter 3,** investigated the performance of poro(visco) elastic while using the viscoelastic model as a benchmark. By employing both poroelastic and poroviscoelastic models, fluid flow artifacts were reduced, unique solutions were achieved, and data-model mismatch was minimized. The λ-modulus could be reliably captured, enabling voxel-wise measurement of compressional stiffness. The poroelastic property of fluid permeability, reflecting fluid movement through the porous matrix and tissue-fluid interactions, could additionally be estimated on a voxel-wise basis.

Successfully modeling λ-modulus and fluid permeability represented an important step toward a more complete characterization of brain mechanics. In standard viscoelastic MRE, where the brain is treated as a continuous incompressible medium, λ-modulus is typically assigned a very large value to enforce incompressibility. In contrast, poroelastic models treat the individual constituents - the solid matrix and fluid - as incompressible, but the drained solid matrix itself must be compressible to allow fluid motion in response

1 **Non-uniqueness** occurs when a given set of data can be explained by more than one possible solution. In such cases, the available information is insufficient to uniquely determine the underlying parameters (such as stiffness). This often happens in complex systems where different factors influence the outcome in similar ways. In such cases, the relative spatial distribution of the estimated values may still be meaningful, but their absolute magnitudes are not uniquely defined and can be arbitrarily scaled. By contrast, a **unique** solution is one in which the data constrain the model strongly enough, such that only a single set of parameter values fits the observations. In this case, the estimated parameters can be interpreted as objective, physically meaningful values that are directly comparable across subjects, conditions, or studies.

to volumetric strain. Consequently, λ-modulus is no longer arbitrarily set to a large value; instead, it becomes a parameter of interest, reflecting the resistance of the *drained* tissue matrix to volumetric changes in the absence of vascular or extracellular fluids. As such, λ -modulus provides a complementary perspective to shear stiffness, offering additional insight into brain mechanical properties. Similarly, shear stiffness in poroelastic models represents the shear properties of the drained solid matrix rather than those of a continuous medium. Together, these parameters capture intrinsic characteristics of the brain parenchyma, independent of confounding vascular or fluid effects.

Successful reconstruction of the fluid permeability marked an important technical achievement for many reasons. First, the ability to characterize fluid behavior in the brain and its interaction with the surrounding tissue allows decoupling of the contributions of solid and fluid components to the brain's overall mechanical response. This separation shows how interstitial and vascular fluids influence brain deformation, pressure dynamics, and tissue stiffness - helping to disentangle tissue and vascular components in pathological alterations to brain structure. Second, fluid permeability has traditionally been fixed to a global constant in poroelastic MRE due to limited data quality. This oversimplification can distort the estimation of other parameters, since permeability strongly influences local fluid-solid interactions. Third, the choice of fluid permeability had a strong scaling effect on the resulting shear stiffness maps, meaning that inaccurate assumptions could mask the true mechanical properties of the tissue. This point proved crucial in this thesis, as reconstructing λ-modulus removed a major source of arbitrary scaling and uncovered the brain's intrinsically ultra-soft character (see Chapter 4).

The transition to poro(visco)elastic modeling resolved many of the limitations inherent in viscoelastic iMRE approaches while introducing several new advantages. Overall, the poro(visco)elastic property estimates exhibited comparable or improved repeatability relative to the viscoelastic model. In addition, the poroviscoelastic framework can capture more complex tissue behavior, providing a more comprehensive representation of brain mechanics. The poroviscoelastic model generally yielded higher repeatability and symmetry than the purely poroelastic model, while simultaneously providing additional insight into the viscous behavior of the brain's solid matrix. This represents a notable advantage, as recent work has shown that viscous effects govern short-term relaxation dynamics, whereas porous effects dominate over longer timescales (Greiner et al., 2024). Allowing the model to account for viscous effects therefore enables a more accurate characterization of the brain's time-dependent mechanical behavior. Furthermore, the ability to produce unique solutions in the iMRE inversion process represented another key advantage, which had major implications and laid the foundation for the work that is presented in **Chapter 4**.

However, while promising on many fronts, poroelastic iMRE faced a major limitation related to pressure field boundary conditions. These conditions are unknown and cannot be measured *in vivo* due to the skull's protective nature and the fact that direct pressure measurements require invasive procedures. Consequently, they are typically assumed rather than obtained empirically - most often by setting them to zero (as done in **Chapter 3)**. However, this assumption introduces errors that propagate throughout the analysis, particularly affecting pressure-dependent properties such as the λ-modulus and fluid permeability.

The ability of the poroelastic models to yield unique solutions provided a new vision of the brain's stiffness in its natural, unperturbed state. Since its inception, nearly all MRE literature has reported brain stiffness values in the kilopascal range; these estimates were corroborated both by measurements obtained with external actuation - which artificially increases stiffness - and by post-mortem mechanical testing, where the extent of tissue alteration after death remains uncertain. Thus, the recovery of global stiffness values of approximately 5-6 Pa in **Chapter 3** was unexpected and initially raised questions about the ability of the poroelastic models to yield unique solutions. Previous studies employing poroelastic models in intrinsic MRE reported global stiffness values in the range of 2-3 kPa - almost two orders of magnitude higher (M. McGarry et al., 2019; M. D. J. McGarry et al., 2015; Solamen et al., 2021). However, in all such cases, either the λ-modulus or the fluid permeability was fixed to global mean values, chosen to reproduce the stiffness magnitudes that were considered typical at the time, and ubiquitously reported in MRE literature (Hiscox et al., 2020; McIlvain et al., 2022; Murphy et al., 2013; Sack et al., 2009). At the same time, a study investigating the frequency dependence of the brain's viscoelastic properties showed a strong decrease in stiffness at low frequencies. Using wavelength analysis with intrinsic activation steady-state MRE, they estimated a global brain stiffness of approximately 21 Pa at 1 Hz, which is much more consistent with our findings (Herthum et al., 2021).

Together, the work presented in Chapter 3 and that of Herthum et al. (2021) represent, to the best of our knowledge, the first demonstrations of brain stiffness estimation using entirely intrinsic actuation and without the imposition of fixed global parameters that could artificially scale the results. In both cases, the results pointed towards the brain being ultra-soft, exhibiting almost fluid-like properties. This is not an entirely far-fetched idea, as the brain is both suspended in fluid and permeated by interstitial and vascular fluids. Furthermore, at low frequencies, these fluids have sufficient time to redistribute in response to deformation, effectively reducing the tissue's mechanical resistance. These observations underscore that, at low frequencies, the brain's mechanical behavior cannot be fully captured by traditional viscoelastic models alone; rather, its almost fluid-like

response reflects the dynamic interplay between tissue structure and fluid redistribution, particularly at physiologically relevant timescales.

The observation that the brain may be considerably softer than previously believed in turn challenged previous assumptions. In **Chapter 2**, a lower boundary of 100 Pa was imposed in the NLI scheme in accordance with the assumption that the brain is much stiffer, which consequently constrained the resulting stiffness distributions to remain above this limit. As a result, even if the viscoelastic model could converge to the 5-6 Pa values measured above, the imposed lower bound would prevent the solutions from fully reflecting this ultra-soft behavior. Furthermore, the claim that the viscoelastic model produced non-unique solutions was predicated on a force imbalance between elastic and inertial forces (M. McGarry et al., 2019). However, a nearly two-order-of-magnitude reduction in brain stiffness also implies a corresponding reduction in elastic forces, which may restore the elastic-to-inertial force balance and allow the model to converge to unique solutions. These insights sparked the investigation presented in **Chapter 4**, where we report multiple lines of evidence supporting the ability of the viscoelastic model to yield unique solutions. Moreover, by examining the brain's viscoelastic behavior at 1, 2, and 3 Hz, the model was shown to produce physically meaningful solutions that closely matched the frequency-dependent behavior reported by Herthum et al. (2021). These observations demonstrate the ability of the viscoelastic model to yield unique solutions at the frequencies of the cardiac pressure pulse and show that the brain indeed exhibits ultra-soft mechanical properties. The implications of this will be re-visited later in this chapter.

Part II: Understanding the underlying mechanisms of brain strain

By leveraging the DENSE sequence to obtain precise displacement fields, iMRE provides rich insight into the brain's mechanical behavior under physiologically natural conditions. The same displacement measurements can also be used to characterize the brain's dynamic behavior through Strain Tensor Imaging (STI) (Sloots et al., 2021). STI is a DENSE-based MRI protocol optimized to reconstruct the full 3D strain tensor on a voxel-wise level, with sufficient signal-to-noise ratio. It quantifies strain-derived metrics, rather than just displacements, offering a complementary perspective on brain mechanics. However, because it is relatively new, the underlying physiological and biological drivers contributing to these metrics remain largely unknown.

Brain stiffness has been hypothesized to influence strain metrics such as volumetric and octahedral shear strain by Adams et al. in 2019. However, at the time, accurate character-

ization of brain stiffness was largely limited to standard MRE, which requires specialized equipment. Moreover, as noted earlier, standard MRE assesses the brain under externally applied vibrations, altering tissue stiffness and thereby confounding the relationship between intrinsic stiffness and strain behavior. The development of iMRE, as discussed in Part I, overcame these limitations and enabled direct assessment of these relationships under physiological conditions. In addition, cerebral blood volume (CBV) - a proxy for the degree of vascularization - has been proposed to contribute to volumetric strain, consistent with observations that white-to-gray matter ratios are similar across both metrics (Adams et al., 2020). Finally, because brain pulsations arising from the cardiac cycle generate the measured strains, we hypothesized that pulse pressure also plays a key role as a driving factor.

The role of these drivers in volumetric and octahedral shear strain was explored and assessed in **Chapter 5**, providing insights into the physiological mechanisms underlying brain tissue deformation. It was found that volumetric and octahedral shear strain reflected distinct yet interrelated physiological processes. Volumetric strain was more strongly associated with cerebral blood volume, indicating a vascular origin, while octahedral shear strain correlated with tissue stiffness. Both metrics exhibited dependences on the pulse pressure, confirming our initial hypothesis. At the same time, it appeared that both metrics result from more complex interplay of factors than previously assumed. The results indicate that neither volumetric nor octahedral shear strain can be attributed to a single factor, such as blood volume or tissue stiffness. Instead, multiple physiological contributors influence each metric, with no single factor dominating.

Given the ultra-soft nature of brain tissue, it is likely that vascular wall compliance plays a major role in shaping volumetric strain, as it directly governs the extent of vessel expansion in response to arterial pulsations, rather than this being primarily determined by the surrounding tissue. The fact that volumetric strain had minimal dependence on tissue stiffness supports this notion. It is also possible that vascular architecture - such as branching patterns or the flow of blood through the vascular network - further influences strain dynamics. For instance, as conductance through the vascular network decreases, resistance increases, potentially leading to greater energy dissipation and consequently modulating the observed strain.

In this context, it would be particularly interesting to compare volumetric strain measurements with vascular compliance. However, vascular compliance is exceedingly difficult to measure directly, and is therefore typically inferred through indirect proxies. As volumetric strain depends on similar metrics, direct comparisons would likely be confounded by shared dependencies. For this reason, alternative approaches to estimating vascular compliance, including non-confounding imaging proxies or advanced modeling techniques

(e.g. as proposed by (Gao et al., 2025)), are needed to interpret this relationship. For example, hemodynamic models that explicitly relate vessel wall motion to intraluminal pressures could allow estimation of compliance or related physiological parameters, such as local pulse pressure or intracranial pressure, providing a more mechanistic interpretation of the strain measurements.

While functional MRI techniques provide in vivo measurements of perfusion and oxygenation, they offer a limited perspective on the mechanical behavior of the brain's microstructure. Similarly, structural MRI (such as diffusion-weighted imaging) can detect subtle tissue changes and correlations with early brain damage before overt lesions appear (Farias Da Guarda et al., 2025), but provides only indirect information about microvascular mechanics. In contrast, volumetric strain has the potential to directly capture the mechanical properties of the microvasculature, offering complementary insights not accessible through conventional functional or structural MRI.

Our findings show that it correlates with cerebral blood volume, but not with tissue stiffness, implying that it predominantly reflects microvascular properties. While further work is required to confirm this relationship, along with vascular compliance and architecture, the ability to capture microvascular characteristics would be especially relevant for conditions such as cerebral small vessel disease (cSVD), a disorder marked by damage to the microvasculature and surrounding tissue (Shi et al., 2020). Volumetric strain may therefore serve as a sensitive tool to investigate early pathological changes, which could allow detection of microvascular alterations before macroscopic lesions become visible on standard CT or MR imaging. Given that vascular stiffening is linked to increased risk of stroke and cSVD development, assessing these early mechanical changes could provide important insights into disease progression and underlying cerebrovascular physiology (Sloots et al., 2021; Wardlaw et al., 2019). Overall, volumetric strain shows promise as a noninvasive biomarker for cerebrovascular dysfunction, though additional work in clinical validation is needed to further clarify the underlying mechanisms. A potential next step would be a proof-of-principle study to validate volumetric strain in a clinical cohort. This could involve comparing measurements between patients with cSVD and age-matched controls, and assessing correlations with established MRI markers of microvascular damage (Smith et al., 2019).

In addition to the strains discussed above, STI also characterizes principal strain directions. Similar to volumetric and octahedral shear strain, the mechanisms underlying the orientations of the first principal strain (FPS) and third principal strain (TPS) remain largely unknown. However, consistent patterns across subjects have been observed in maps of these strains (Sloots et al., 2021). The FPS maps generally exhibit inwardly directed strains pointing toward the foramen magnum, indicating global effects, whereas TPS maps

displayed locally heterogeneous patterns that may reflect regional brain microstructure. The aim of **Chapter 6** was thus to make sense of these patterns, shedding light on the structural aspects underlying brain deformation by determining the extent to which the measured strain directions reflect global boundary condition effects versus local microstructural influences.

The results showed that the FPS patterns to a very large extent could be explained by two main principles: the swelling vasculature appears to generate an internal force field directed perpendicular to the rigid skull and oriented downward toward the foramen magnum. These findings showed how the shape and boundary conditions imposed by the skull strongly influence the global strain field during brain pulsations. In contrast, the influence of microstructural organization on the FPS patterns appeared negligible. Meanwhile, a tendency for the TPS directions to align perpendicularly to the microstructure was observed, indicating a relationship between TPS directions and the microstructure. This observation provided additional support for the hypothesis and points toward an important insight: the brain may exhibit mechanical anisotropy.

The potential evidence of mechanical anisotropy could carry significant implications. First, accurate computational modeling of the brain depends on realistic characterization of such intrinsic mechanical properties. Second, the degree of mechanical anisotropy in brain tissue remains a topic of debate, with studies providing evidence both for and against it (Budday et al., 2020). Consequently, computational brain models that either include or neglect mechanical anisotropy may yield divergent results. Most studies investigating anisotropy have relied on mechanical testing or computational modeling conducted under diverse experimental conditions - across different species (including porcine, rat, and human brains), various brain regions, measurement scales, and differing experimental setups (Budday et al., 2017; Eskandari et al., 2021; Karimi & Navidbakhsh, 2014; Miller & Chinzei, 1997; Rashid et al., 2012). This all likely contributes to the variability in reported outcomes. Moreover, brain tissue is notoriously difficult to characterize in such experimental conditions due to its ultrasoft, highly fragile, biphasic, and heterogeneous nature (Budday et al., 2020), as well as the additional influence of post-mortem changes in mechanical properties (Weickenmeier et al., 2018). By contrast, our results offer a unique perspective derived non-invasively and *in vivo*, capturing dynamic mechanical behavior under physiological conditions and circumventing many limitations of ex vivo or simulated studies.

One possible interpretation of the observed strain patterns is that the FPS directions reflect the primary loading direction induced by brain pulsations, whereas the TPS directions represent the passive Poisson response to this loading, potentially giving rise to mechanical anisotropy as a second-order effect. This suggests that the influence of an-

isotropy is subtle and may become more pronounced only under specific conditions. This is an important insight, as it could help explain why mechanical anisotropy is detected in some experiments but not in others, thereby offering a possible avenue to reconcile the ongoing debate in the literature. However, while the results are in line the presence of mechanical anisotropy, the observed tendencies could alternatively be attributed to the loading conditions, as discussed in detail in **Chapter 6**. At the same time, mechanical anisotropy could itself play a role in generating such loading conditions.

This illustrates the complexity of brain mechanics, where tissue properties and loading conditions are tightly interdependent, which makes it difficult to establish clear causal relationships. Direct measurements of the underlying force fields are currently infeasible, as no established *in vivo* methods exist. Rather, methods like STI provide a close approximation, reflecting direct effects of the underlying force fields. Similarly, work has been done using DENSE and poroelastic models (similar to those discussed in **Chapter 3**) to estimate the forces driving pulsatile interstitial fluid movement in the brain, offering further insight into the underlying mechanics (M. McGarry et al., 2025). However, these models typically assume mechanical isotropy, emphasizing once again the importance of accurately characterizing anisotropic properties. In this context, recent work by Magdoom et al. (2025) proposes a tensor-based representation of brain stiffness that has the potential to quantify mechanical anisotropy, providing a promising pathway beyond isotropic assumptions.

Bringing it together: overall implications and insights

This thesis has explored a broad range of mechanical aspects of the human brain using iMRE and STI, yielding a deeper understanding of its mechanical behavior under physiological conditions. Notably, the majority of the results and insights discussed here have were enabled by a single MR sequence - the DENSE sequence - demonstrating both the depth and breadth of understanding it has enabled. The ability of a single sequence to generate diverse mechanical information suggests potential utility as a unified approach to studying brain mechanics. While this thesis focused primarily on technical development and the fundamental understanding of the biological and physiological mechanisms underlying the derived metrics, the versatility of the DENSE sequence also points toward important potential clinical applications.

Because it does not rely on any specialized external equipment, both iMRE and STI via the DENSE sequence can be readily integrated into existing MR protocols. This represents a major practical advantage compared to traditional, externally actuated MRE, whose implementation in large-scale clinical studies has been limited by its dependence on additional hardware and experienced personnel. The simplicity and compatibility of iMRE and STI via DENSE makes it well suited for clinical use. Beyond its relative ease of

implementation, DENSE also provides a range of mechanical information within only a few additional minutes of scan time. The resulting imaging metrics have the potential to serve as biomarkers for diseases that alter the brain's mechanical properties. In this thesis, eight such metrics have been explored and discussed: shear stiffness, λ-modulus, fluid permeability, damping ratio, volumetric strain, octahedral shear strain, first principal strain, and third principal strain - each offering unique insight into the brain's mechanical state.

Taken together, the diversity of these parameters effectively forms a "mechanical fingerprint" of the brain, capturing complementary aspects of its mechanical behavior. Such a multidimensional mechanical profile enables more specific and sensitive differentiation between normal and pathological tissue states, analogous to the way multiparametric imaging approaches are used in other MRI modalities (Panda et al., 2017). As outlined in **Chapter 1**, a wide range of pathological processes can alter the microstructure of human brain tissue. Tissue stiffness alone can be affected by multiple processes, such as neuroinflammation, axonal atrophy, loss of oligodendroglial cells, microglial activation, Wallerian degeneration, and microvascular damage, all resulting in microstructural changes, ranging from increased tissue water content to progressive gliosis and loss of volume (Agarwal & Carare, 2021). By combining multiple mechanical metrics, one could gain a more comprehensive perspective on disease processes - one that captures not just isolated changes in stiffness but a more integrated view of the underlying structural and physiological alterations. Furthermore, DENSE can be readily combined with other imaging sequences to provide complementary information. This comprehensive characterization could hold promise for improving disease detection, patient stratification, and monitoring of treatment response in conditions that alter brain biomechanics.

The fact that iMRE measures the brain in a physiologically natural state, rather than relying on externally applied vibrations as in standard MRE, may be of particular relevance. Recent work using wideband MRE, which probes mechanical properties across a frequency range of 5-50 Hz, has shown that age-related brain softening is most pronounced at low frequencies (Schattenfroh et al., 2025, see Figure 2). This finding suggests that higher-frequency actuation may reduce sensitivity to subtle physiological changes by masking low-frequency mechanical effects. However, the specific mechanisms underlying this sensitivity, and the extent to which they influence the observed mechanical metrics, remain largely unknown and represent an interesting direction for future research. Moreover, given the increased sensitivity to age-related brain softening at low frequencies, iMRE could provide a valuable complementary perspective to studies employing higher-frequency actuation, such as those by Sack et al. (2011).

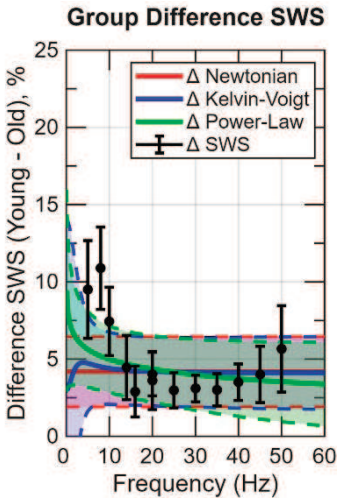


Figure 2: Relative percent differences in shear wave speed (SWS, a measure of stiffness) between a younger group (4 females, 10 males, mean age: 29.7 ± 4.1 years) and an older group (2 females, 8 males, mean age: 56.5 ± 3.8 years) across a frequency spectrum. The difference in stiffness between the two groups is more pronounced at lower frequencies, suggesting greater sensitivity to age-related softening in this range. Figure reproduced from (Schattenfroh et al., 2026), Fig. 4, licensed under CC BY.

The observation that the living brain may operate in an ultra-soft mechanical regime suggests the need for a reconsideration of how cerebral biomechanics are understood. Rather than behaving as a purely viscoelastic solid with fixed material properties, the brain instead seemingly functions as a dynamic, fluid-solid continuum, where its apparent stiffness emerges from the interaction between multiple properties, such as tissue elasticity, pressure, and fluid motion. Evidence for such coupling has already been reported: for instance, Hetzer et al. (2018) demonstrated that brain stiffness is modulated by perfusion. Similarly, **Chapter 3** showed that variations in fluid permeability substantially affect the effective stiffness.

From this perspective, stiffness does not represent an intrinsic constant, but is a context-dependent property reflecting the current physiological state. This reinforces the importance of assessing brain mechanics under physiologically natural conditions - an inherent strength of iMRE. Moreover, the exceptionally low stiffness values revealed by iMRE, together with the factors mentioned above, suggests that the brain's mechanics may be closely linked to its fluid environment. Such ultra-softness could be mechanically sustainable precisely because the brain is enclosed within the rigid skull, which shields it from external loads and allows internal fluid-solid interactions to dominate. One possible implication is that this softness may be important in facilitating efficient and adaptive transmission of pulsatile forces that promotes interstitial fluid movement, contributing to

waste clearance (Xie et al., 2024). As stiffness is frequency-dependent, then lower resting heart rate may correspond to lower effective stiffness, potentially favoring fluid transport. In line with this, a recent population-based cohort study reported that elevated resting heart rate was associated not only with incident dementia, but also with accelerated cognitive decline in older adults, independent of cardiovascular disease (Imahori et al., 2022). While speculative, it is consistent with the notion that the brain's mechanical properties play an active role in maintaining physiological homeostasis, rather than merely providing structural support (Barnes et al., 2017). Taken together, these observations highlight a largely unexplored aspect of the brain, namely the role of the brain's complex fluid-solid structural effects in healthy and disrupted physiology.

Future outlook

The implementation of the poroelastic and poroviscoelastic models in the iMRE framework without the need to rely on assumed global values for the λ-modulus and fluid permeability represented a major advancement. However, as previously discussed, the framework remains limited by a key challenge: the need to assume boundary conditions for the internal pressure fields. This limitation could be addressed by integrating a coupled adjoint field formulation (Seidl et al., 2019) with the pressure forward problem (Tan et al., 2017), which together would eliminate the requirement for prescribed pressure boundary conditions. Notably, a similar implementation has already been developed for the viscoelastic model presented in **Chapter 2**, demonstrating improved performance and robustness (Kurtz et al., 2024). Extending this approach to the poroelastic and poroviscoelastic frameworks therefore represents a promising next step.

Although the poroelastic and poroviscoelastic models provide more accurate representations of the human brain compared to the viscoelastic model, there remains room for further refinement. In their current form, both the vascular and interstitial fluid compartments are modeled as a single fluid domain with shared properties. This is an oversimplification that could be overcome by adopting multiple-network poroelastic models, in which blood and interstitial fluid are treated separately (Guo et al., 2020). This could open up possibilities for more detailed studies on non-invasive, patient specific interstitial fluid flow characterization, a crucial first step towards the development of effective interventions with next-generation therapeutic agents (M. McGarry et al., 2025). Additionally, brain pulsations arise from the periodic inflow and outflow of blood, which in a poroelastic framework is represented by a fluid source term. In current implementations, these sources are typically assumed to be zero - an approximation that may introduce errors, particularly in regions containing larger vessels such as around the circle of Willis. Recent work has shown the feasibility of recovering this fluid source term, albeit under some sim-

plifying assumptions, which may provide an avenue for further improving the poroelastic iMRE framework (M. McGarry et al., 2025). Finally, the potential evidence of mechanical anisotropy presented in **Chapter 6** challenges the current assumptions within the iMRE framework. Although further investigation is required to confirm this effect, incorporating anisotropic properties could provide a basis for more physiologically realistic models.

While a state-of-the-art DENSE protocol was employed for the strain measurements in **Chapters 5** and **6**, the iMRE analysis relied on a dataset acquired with a less optimized DENSE implementation. This difference arose because the most recent approach used a single-shot 2D acquisition (Sloots et al., 2021), which, although it substantially improved the SNR for strain measurements, led to the displacement data being affected by phase wrapping and slice-to-slice inconsistencies due to subject motion. While both issues present significant challenges, preliminary work indicates that they can be effectively mitigated. As iMRE relies heavily on accurate displacement measurements, this advancement could have a considerable impact on all derived metrics and represents an important direction for future development. Furthermore, although this thesis has investigated iMRE at a high field strength of 7 T, lower field strengths such as 1.5 T or 3 T are more clinically feasible. Once the iMRE framework has been fully optimized at 7 T, translating these advances to lower field strengths will be a logical next step. Exploring how the quality of iMRE-derived metrics is affected at these lower fields would therefore be an important step toward clinical translation.

The present iMRE framework yields stiffness values that agree with literature (see **Chapter 4**), however, the framework has not yet been validated on external phantoms. This work is ongoing, involving an agarose-based phantom placed in an actuator setup capable of generating 1 Hz vibrations, thereby mimicking the pulsations produced by the heartbeat. Validation of our framework is achieved if it can accurately characterize the phantom's stiffness using only the measured displacement field, with results confirmed by comparison to stiffness values obtained through mechanical testing. However, standard agarose-based phantoms lack poroelastic properties, meaning that only the viscoelastic model can be validated using this setup. Future work could therefore involve more complex poroelastic phantoms to enable validation of properties such as the λ-modulus and fluid permeability. These efforts are an important step toward ensuring that both viscoelastic and poroelastic property estimates are quantitatively reliable, an important requirement for reliably translating iMRE measurements to *in vivo* studies and, ultimately, clinical applications.

Concluding remarks

This thesis demonstrates that intrinsic MR elastography, particularly when combined with poroviscoelastic modeling, provides a powerful and physiologically grounded approach for characterizing the mechanical behavior of the living human brain. By capturing the brain in its natural, unperturbed state, this approach reveals insights that were previously inaccessible, offering a unique window into its intrinsic mechanical properties. In particular, the work provides novel evidence for the fluid-like, ultra-soft nature of the brain, while also uncovering potential indications of mechanical anisotropy. These findings advance our fundamental understanding of brain biomechanics and open new pathways for exploring how fluid-solid interactions, cerebrovascular dynamics, and tissue microstructure operate in the healthy brain and what role they play in the development of disease. Together, this research lays a foundation for future studies spanning both basic science and clinical translation.

References

Adams, A. L., Kuijf, H. J., Viergever, M. A., Luijten, P. R., & Zwanenburg, J. J. M. (2019). Quantifying cardiac-induced brain tissue expansion using DENSE. *NMR in Biomedicine*, *32*(2), e4050. https://doi.org/10.1002/nbm.4050

Adams, A. L., Viergever, M. A., Luijten, P. R., & Zwanenburg, J. J. M. (2020). Validating faster DENSE measurements of cardiac-induced brain tissue expansion as a potential tool for investigating cerebral microvascular pulsations. *NeuroImage*, *208*, 116466. https://doi.org/10.1016/j.neuroimage.2019.116466

Agarwal, N., & Carare, R. O. (2021). Cerebral Vessels: An Overview of Anatomy, Physiology, and Role in the Drainage of Fluids and Solutes. *Frontiers in Neurology*, *11*. https://doi.org/10.3389/fneur.2020.611485

Barnes, J. M., Przybyla, L., & Weaver, V. M. (2017). Tissue mechanics regulate brain development, homeostasis and disease. *Journal of Cell Science*, *130*(1), 71–82. https://doi.org/10.1242/jcs.191742

Budday, S., Ovaert, T. C., Holzapfel, G. A., Steinmann, P., & Kuhl, E. (2020). Fifty Shades of Brain: A Review on the Mechanical Testing and Modeling of Brain Tissue. *Archives of Computational Methods in Engineering*, *27*(4), 1187–1230. https://doi.org/10.1007/s11831-019-09352-w

Budday, S., Sommer, G., Birkl, C., Langkammer, C., Haybaeck, J., Kohnert, J., Bauer, M., Paulsen, F., Steinmann, P., Kuhl, E., & Holzapfel, G. A. (2017). Mechanical characterization of human brain tissue. *Acta Biomaterialia*, *48*, 319–340. https://doi.org/10.1016/j.actbio.2016.10.036

Eskandari, F., Shafieian, M., Aghdam, M. M., & Laksari, K. (2021). Structural Anisotropy vs. Mechanical Anisotropy: The Contribution of Axonal Fibers to the Material Properties of Brain White Matter. *Annals of Biomedical Engineering*, *49*(3), 991–999. https://doi.org/10.1007/s10439-020-02643-5

Farias Da Guarda, S. N., Zanon Zotin, M. C., Maillard, P., van den Brink, H., Ponciano, A., Oliveira, L. C., Schoemaker, D., Chokesuwattanaskul, A., Greenberg, S. M., & Viswanathan, A. (2025). White Matter Free Water and PSMD as Neuroimaging Biomarkers of Cerebral Amyloid Angiopathy Severity. *Neurology*, *105*(11), e214390. https://doi.org/10.1212/WNL.0000000000214390

Gao, X., Yuan, T., Liao, Z., Yang, Y., Wu, W., Zhan, W., & Dini, D. (2025). Blood–brain mechanics: How brain tissue responds to pulsatile blood flow dynamics. *International Journal of Mechanical Sciences*, *296*, 110278. https://doi.org/10.1016/j.ijmecsci.2025.110278

Greiner, A., Reiter, N., Hinrichsen, J., Kainz, M. P., Sommer, G., Holzapfel, G. A., Steinmann, P., Comellas, E., & Budday, S. (2024). Model-driven exploration of poro-viscoelasticity in human brain tissue: be careful with the parameters! *Interface Focus*, *14*(6). https://doi.org/10.1098/rsfs.2024.0026

Guo, L., Vardakis, J. C., Chou, D., & Ventikos, Y. (2020). A multiple-network poroelastic model for biological systems and application to subject-specific modelling of cerebral fluid transport. *International Journal of Engineering Science*, *147*, 103204. https://doi.org/10.1016/j.ijengsci.2019.103204

Herthum, H., Dempsey, S. C. H., Samani, A., Schrank, F., Shahryari, M., Warmuth, C., Tzschätzsch, H., Braun, J., & Sack, I. (2021). Superviscous properties of the in vivo brain at large scales. *Acta Biomaterialia*, *121*, 393–404. https://doi.org/10.1016/j.actbio.2020.12.027

Hetzer, S., Birr, P., Fehlner, A., Hirsch, S., Dittmann, F., Barnhill, E., Braun, J., & Sack, I. (2018). Perfusion alters stiffness of deep gray matter. *Journal of Cerebral Blood Flow and Metabolism : Official Journal of the International Society of Cerebral Blood Flow and Metabolism*, *38*(1), 116–125. https://doi.org/10.1177/0271678X17691530

Hiscox, L. V., McGarry, M. D. J., Schwarb, H., Van Houten, E. E. W., Pohlig, R. T., Roberts, N., Huesmann, G. R., Burzynska, A. Z., Sutton, B. P., Hillman, C. H., Kramer, A. F., Cohen, N. J., Barbey, A. K., Paulsen, K. D., & Johnson, C. L. (2020). Standard-space atlas of the viscoelastic properties of the human brain. *Human Brain Mapping*, *41*(18), 5282–5300. https://doi.org/10.1002/hbm.25192

Imahori, Y., Vetrano, D. L., Xia, X., Grande, G., Ljungman, P., Fratiglioni, L., & Qiu, C. (2022). Association of resting heart rate with cognitive decline and dementia in older adults: A population-based cohort study. *Alzheimer's & Dementia*, *18*(10), 1779–1787. https://doi.org/10.1002/alz.12495

Karimi, A., & Navidbakhsh, M. (2014). An experimental study on the mechanical properties of rat brain tissue using different stress-strain definitions. *Journal of Materials Science. Materials in Medicine*, *25*(7), 1623–1630. https://doi.org/10.1007/s10856-014-5198-0

Kurtz, S., Wattrisse, B., & Van Houten, E. E. W. (2024). Minimizing Measurement-Induced Errors in Viscoelastic MR Elastography. *IEEE Transactions on Medical Imaging*, *43*(3), 1138–1148. https://doi.org/10.1109/TMI.2023.3329293

Magdoom, K. N., Avram, A. V, Sarlls, J. E., & Basser, P. J. (2025). In vivo palpation of anisotropic human brain tissue using MRI. *BioRxiv : The Preprint Server for Biology*. https://doi.org/10.1101/2025.06.20.660588

McGarry, M. D. J., Johnson, C. L., Sutton, B. P., Georgiadis, J. G., Van Houten, E. E. W., Pattison, A. J., Weaver, J. B., & Paulsen, K. D. (2015). Suitability of poroelastic and viscoelastic mechanical models for high and low frequency MR elastography. *Medical Physics*, *42*(2), 947–957. https://doi.org/10.1118/1.4905048

McGarry, M., Sowinski, D., Tan, L., Weaver, J., Zwanenburg, J. J. M., & Paulsen, K. (2025). In vivo magnetic resonance imaging of the interstitial pressure gradients pgMRI using a pulsatile poroelastic computational model. *Interface Focus*, *15*(1). https://doi.org/10.1098/rsfs.2024.0044

McGarry, M., Van Houten, E., Solamen, L., Gordon-Wylie, S., Weaver, J., & Paulsen, K. (2019). Uniqueness of poroelastic and viscoelastic nonlinear inversion MR elastography at low frequencies. *Physics in Medicine and Biology*, *64*(7), 075006. https://doi.org/10.1088/1361-6560/ab0a7d

McIlvain, G., Schneider, J. M., Matyi, M. A., McGarry, M. D., Qi, Z., Spielberg, J. M., & Johnson, C. L. (2022). Mapping brain mechanical property maturation from childhood to adulthood. *NeuroImage*, *263*, 119590. https://doi.org/10.1016/j.neuroimage.2022.119590

Miller, K., & Chinzei, K. (1997). Constitutive modelling of brain tissue: Experiment and theory. *Journal of Biomechanics*, *30*(11–12), 1115–1121. https://doi.org/10.1016/S0021-9290(97)00092-4

Murphy, M. C., Huston, J., Jack, C. R., Glaser, K. J., Senjem, M. L., Chen, J., Manduca, A., Felmlee, J. P., & Ehman, R. L. (2013). Measuring the Characteristic Topography of Brain Stiffness with Magnetic Resonance Elastography. *PLoS ONE*, *8*(12), e81668. https://doi.org/10.1371/journal.pone.0081668

Panda, A., Mehta, B. B., Coppo, S., Jiang, Y., Ma, D., Seiberlich, N., Griswold, M. A., & Gulani, V. (2017). Magnetic Resonance Fingerprinting-An Overview. *Current Opinion in Biomedical Engineering*, *3*, 56–66. https://doi.org/10.1016/j.cobme.2017.11.001

Rashid, B., Destrade, M., & Gilchrist, M. D. (2012). Mechanical characterization of brain tissue in compression at dynamic strain rates. *Journal of the Mechanical Behavior of Biomedical Materials*, *10*, 23–38. https://doi.org/10.1016/j.jmbbm.2012.01.022

Sack, I., Beierbach, B., Wuerfel, J., Klatt, D., Hamhaber, U., Papazoglou, S., Martus, P., & Braun, J. (2009). The impact of aging and gender on brain viscoelasticity. *NeuroImage*, *46*(3), 652–657. https://doi.org/10.1016/j.neuroimage.2009.02.040

Sack, I., Streitberger, K.-J., Krefting, D., Paul, F., & Braun, J. (2011). The Influence of Physiological Aging and Atrophy on Brain Viscoelastic Properties in Humans. *PLoS ONE*, *6*(9), e23451. https://doi.org/10.1371/journal.pone.0023451

Schattenfroh, J., Meyer, T., Aghamiry, H. S., Jaitner, N., Fedders, M., Görner, S., Herthum, H., Hetzer, S., Estrella, M., Flé, G., Steinmann, P., Guo, J., & Sack, I. (2025). *In Vivo Wideband MR Elastography for Assessing Age-Related Viscoelastic Changes of the Human Brain*.

Schattenfroh, J., Meyer, T., Aghamiry, H. S., Jaitner, N., Fedders, M., Görner, S., Herthum, H., Hetzer, S., Estrella, M., Flé, G., Steinmann, P., Guo, J., & Sack, I. (2026). In vivo wideband MR elastography for assessing age-related viscoelasticity changes of the human brain. *Acta Biomaterialia*. https://doi.org/10.1016/j.actbio.2026.02.002

Seidl, D. T., Oberai, A. A., & Barbone, P. E. (2019). The Coupled Adjoint-State Equation in forward and inverse linear elasticity: Incompressible plane stress. *Computer Methods in Applied Mechanics and Engineering*, *357*, 112588. https://doi.org/10.1016/j.cma.2019.112588

Shi, Y., Thrippleton, M. J., Blair, G. W., Dickie, D. A., Marshall, I., Hamilton, I., Doubal, F. N., Chappell, F., & Wardlaw, J. M. (2020). Small vessel disease is associated with altered cerebrovascular pulsatility but not resting cerebral blood flow. *Journal of Cerebral Blood Flow & Metabolism*, *40*(1), 85–99. https://doi.org/10.1177/0271678X18803956

Sloots, J. J., Biessels, G. J., de Luca, A., & Zwanenburg, J. J. M. (2021). Strain Tensor Imaging: Cardiac-induced brain tissue deformation in humans quantified with high-field MRI. *NeuroImage*, *236*, 118078. https://doi.org/10.1016/j.neuroimage.2021.118078

Smith, E. E., Biessels, G. J., De Guio, F., de Leeuw, F. E., Duchesne, S., Düring, M., Frayne, R., Ikram, M. A., Jouvent, E., MacIntosh, B. J., Thrippleton, M. J., Vernooij, M. W., Adams, H., Backes, W. H., Ballerini, L., Black, S. E., Chen, C., Corriveau, R., DeCarli, C., … Wardlaw, J. M. (2019). Harmonizing brain magnetic resonance imaging methods for vascular contributions to neurodegeneration. *Alzheimer's & Dementia (Amsterdam, Netherlands)*, *11*, 191–204. https://doi.org/10.1016/j.dadm.2019.01.002

Solamen, L. M., McGarry, M. D. J., Fried, J., Weaver, J. B., Lollis, S. S., & Paulsen, K. D. (2021). Poroelastic Mechanical Properties of the Brain Tissue of Normal Pressure Hydrocephalus Patients During Lumbar Drain Treatment Using Intrinsic Actuation MR Elastography. *Academic Radiology*, *28*(4), 457–466. https://doi.org/10.1016/j.acra.2020.03.009

Tan, L., McGarry, M. D. J., Van Houten, E. E. W., Ji, M., Solamen, L., Zeng, W., Weaver, J. B., & Paulsen, K. D. (2017). A numerical framework for interstitial fluid pressure imaging in poroelastic MRE. *PloS One*, *12*(6), e0178521. https://doi.org/10.1371/journal.pone.0178521

Wardlaw, J. M., Smith, C., & Dichgans, M. (2019). Small vessel disease: mechanisms and clinical implications. *The Lancet. Neurology*, *18*(7), 684–696. https://doi.org/10.1016/S1474-4422(19)30079-1

Weaver, J. B., Pattison, A. J., McGarry, M. D., Perreard, I. M., Swienckowski, J. G., Eskey, C. J., Lollis, S. S., & Paulsen, K. D. (2012). Brain mechanical property measurement using MRE with intrinsic activation. *Physics in Medicine and Biology*, *57*(22), 7275–7287. https://doi.org/10.1088/0031-9155/57/22/7275

Weickenmeier, J., Kurt, M., Ozkaya, E., de Rooij, R., Ovaert, T. C., Ehman, R. L., Butts Pauly, K., & Kuhl, E. (2018). Brain stiffens post mortem. *Journal of the Mechanical Behavior of Biomedical Materials*, *84*, 88–98. https://doi.org/10.1016/j.jmbbm.2018.04.009

Xie, L., Zhang, Y., Hong, H., Xu, S., Cui, L., Wang, S., Li, J., Liu, L., Lin, M., Luo, X., Li, K., Zeng, Q., Zhang, M., Zhang, R., & Huang, P. (2024). Higher intracranial arterial pulsatility is associated with presumed imaging markers of the glymphatic system: An explorative study. *NeuroImage*, *288*, 120524. https://doi.org/10.1016/j.neuroimage.2024.120524

Zorgani, A., Souchon, R., Dinh, A.-H., Chapelon, J.-Y., Ménager, J.-M., Lounis, S., Rouvière, O., & Catheline, S. (2015). Brain palpation from physiological vibrations using MRI. *Proceedings of the National Academy of Sciences of the United States of America*, *112*(42), 12917–12921. https://doi.org/10.1073/pnas.1509895112



Appendix

Dutch summary

In de afgelopen jaren hebben wetenschappers ontdekt dat de mechanische eigenschappen van de hersenen (bijvoorbeeld hoe stijf of viskeus ze zijn) een belangrijke rol spelen in hoe de hersenen functioneren en hoe ze veranderen bij ziekten. Omdat de hersenen beschermd worden door de schedel en bestaan uit zeer kwetsbaar weefsel, is hun mechanische conditie lange tijd moeilijk te bestuderen geweest. De ontwikkeling van geavanceerde MRI-technieken heeft het mogelijk gemaakt om deze eigenschappen veilig en niet-invasief in mensen te karakteriseren. Ondanks deze vooruitgang is nog veel onbekend - zowel over het normale mechanische gedrag van de hersenen als over hoe dit verandert bij verschillende ziekten. Het bestuderen van hersenmechanica biedt daarom grote mogelijkheden om ons begrip van hersenaandoeningen te verbeteren en daarmee op termijn hopelijk ook de diagnose en behandeling hiervan.

Het algemene doel van dit project was tweeledig. Het eerste doel was de ontwikkeling van intrinsieke Magnetic Resonance Elastography (iMRE), een techniek die gebruikmaakt van de subtiele pulsaties van de hersenen die veroorzaakt worden door het zwellen van de bloedvaten bij elke hartslag. Deze pulsaties worden vastgelegd met een zeer gevoelige MRI-methode, genaamd Displacement Encoding with Stimulated Echoes (DENSE). De resulterende verplaatsingsvelden worden gebruikt om de stijfheid van hersenweefsel af te leiden, zoals beschreven in **hoofdstukken 2-4**. Het tweede doel was het onderzoeken van de biologische en fysiologische factoren die van invloed zijn op de pulsatiele weefseldeformaties, zoals beschreven in **hoofdstukken 5** en **6**. Meer inzicht in de biologische factoren achter de gemeten weefseldeformaties is nodig. Dit helpt om beter te begrijpen hoe deze samenhangen met hersenfunctie en ziekte. De volgende sectie vat elk hoofdstuk samen.

Aan het begin van dit project was intrinsieke Magnetic Resonance Elastography (iMRE) nog grotendeels onontgonnen terrein. De eerste poging, gepubliceerd in 2012, toonde de haalbaarheid van de techniek aan, maar de resulterende parameterkaarten bevatten weinig gedetailleerde anatomische informatie en veel ruis. Daarom werd iMRE nauwelijks verder ontwikkeld. De beperkte nauwkeurigheid was waarschijnlijk te wijten aan de lage gevoeligheid van de MR-technieken die destijds werden gebruikt, omdat deze niet waren geoptimaliseerd voor het meten van de hersenpulsaties. In **hoofdstuk 2** hebben we dit aangepakt door een geoptimaliseerde DENSE methode toe te passen, die de kleine weefselverplaatsingen veroorzaakt door hersenpulsaties bijzonder gevoelig kan meten. De verhoogde gevoeligheid voor weefselpulsaties bleek cruciaal: het stelde ons in staat de stijfheid van de hersenen nauwkeurig en met hoge resolutie in kaart te brengen. De resultaten lieten zien dat iMRE mechanische eigenschappen in kaart kan brengen zonder externe activering, met een ruimtelijke nauwkeurigheid en betrouwbaarheid die vergeli-

jkbaar is met traditionele MRE, die wel afhankelijk is van externe mechanische activering. Hierbij is belangrijk dat iMRE de hersenen in hun natuurlijke, onaangetaste toestand vastleggen, wat een meer fysiologische kijk op hersenmechanica biedt. Dit hoofdstuk liet zien dat er nog uitdagingen over bleven,- zoals ruis door vloeistofbewegingen, een mismatch tussen de gegevens en het model, en metingen die willekeurig schaalbaar waren (bekend als niet-uniciteit). Desondanks heeft dit werk iMRE succesvol neergezet als een veelbelovend, volledig niet-invasief instrument voor het bestuderen van hersenweefselmechanica bij mensen.

Hoofdstuk 3 bouwde voort op de bevindingen van **hoofdstuk 2**. Met behulp van poro-elastische en poro-visco-elastische weefselmodellen binnen het niet-lineaire inversieschema (NLI) werden belangrijke beperkingen van visco-elastische iMRE aangepakt om de schatting van mechanische eigenschappen te verbeteren. De poro-(visco)-elastische modellen behandelen de hersenen als een combinatie van een poreus vast weefsel gevuld met vloeistof, waardoor meer fysiologisch realistische mechanische eigenschappen kunnen worden geschat. Deze aanpak maakte het mogelijk om de compressiemodulus (lambda-modulus) en hydraulische permeabiliteit per voxel in kaart te brengen, terwijl artefacten door vloeistofstroming werden verminderd. Daarnaast werd ook de mismatch tussen data en model teruggedrongen en leverde deze modellen unieke, betrouwbare oplossingen (d.w.z. waarden die vergelijkbaar zijn tussen proefpersonen in plaats van waarden die alleen relatieve, regionale verschillen binnen één proefpersoon kunnen laten zien). Over het algemeen lieten de poro-elastische en poro-visco-elastische eigenschappen vergelijkbare of verbeterde herhaalbaarheid zien ten opzichte van het visco-elastische model. Het poro-visco-elastische model behaalde met name een hogere herhaalbaarheid en symmetrie dan het puur poro-elastische model, terwijl het ook extra inzicht bood in het viskeuze gedrag van het vaste weefsel van de hersenen. Samen boden deze vooruitgangen een consistenter en uitgebreider beeld van de hersenmechanica. Sommige uitdagingen bleven echter bestaan. Met name de noodzaak om drukrandvoorwaarden aan te nemen introduceert onzekerheid, vooral in de lambda-modulus en hydraulische permeabiliteit. De poro(visco)elastische modellering bleek een goede stap vooruit voor iMRE en leverde, door unieke oplossingen mogelijk te maken, nieuw bewijs van de intrinsiek ultra-zachte aard van de hersenen.

Hoofdstuk 4 bouwde voort op de bevindingen van **hoofdstuk 3** door de implicaties van poro-elastische resultaten voor visco-elastische iMRE te onderzoeken. Het vermogen van de poro-elastische modellen om unieke oplossingen te produceren, onthulde dat de hersenen veel zachter zijn dan tot dusver werd aangenomen, met een globale stijfheid rond 6 Pa - bijna twee ordes van grootte lager dan de kilopascal-waarden die in de meeste eerdere studies werden gerapporteerd. Eerdere schattingen waren gebaseerd op externe activering, die stijfheid kunstmatig verhoogt, of op post-mortem weefsel,

waarin mechanische eigenschappen na de dood ook veranderd zijn. De bevinding dat de hersenen ultra-zacht zijn, suggereert dat ze vloeistofachtig gedrag vertonen bij fysiologisch relevante, lage frequenties en kleine vervormingen. Dit gedrag weerspiegelt waarschijnlijk de herverdeling van interstitiële en vasculaire vloeistoffen als reactie op vervorming.

Deze bevindingen stelden de aannames die eerder gedaan waren in de visco-elastische iMRE ter discussie. In **hoofdstuk 2** was een ondergrens van 100 Pa opgelegd tijdens de berekening van de mechanische eigenschappen, gebaseerd op de veronderstelling dat de hersenen veel stijver waren. Deze beperking verhinderde dat het model het ultra-zachte gedrag van de hersenen kon bepalen. **Hoofdstuk 4** toonde aan dat het visco-elastische model in feite unieke, fysiek zinvolle waarden oplevert die overeenkomen met het frequentieafhankelijke gedrag dat in de literatuur is gerapporteerd. Deze resultaten bevestigen niet alleen de mechanisch ultra-zachte aard van het menselijke brein, maar benadrukken ook het belang van intrinsieke metingen. De resultaten laten daarnaast zien dat voor het begrijpen van weefselmechanica het nodig is om rekening te houden met de specifieke karakteristieken van de dynamica van (poreus) weefsel bij lage frequenties.

Op basis van DENSE MRI metingen van de kleine bewegingen in de hersenen, biedt iMRE gedetailleerd inzicht in hoe de mechanische eigenschappen van de hersenen onder normale, natuurlijke omstandigheden. Door het berekenen van strain-tensor-beelden (STB's) kunnen dezelfde metingen ook worden gebruikt om te bestuderen hoe de hersenen uitrekken en vervormen gedurende de hartslag. STB's bieden een ander perspectief op de hersenmechanica, bijvoorbeeld via metingen die relatieve volumeverandering en octahedrale afschuiving worden genoemd, twee metrische waarden die mogelijk klinische waarde hebben. Omdat nauwkeurige meting van STB's echter een recente ontwikkeling is, begrijpen we de biologische en fysiologische processen achter deze maten nog niet volledig. **Hoofdstuk 5** onderzocht mogelijke onderliggende factoren die bijdragen aan volumetrische rek en octahedrale schuifvervorming. Drie complementaire categorieën van factoren werden beschouwd: effecten van polsdruk, vasculaire en hemodynamische factoren, en weefseleigenschappen. De resultaten gaven aan dat beide maten werden beïnvloed door polsdruk, waarbij de volumetrische rek sterker was gekoppeld aan cerebraal bloedvolume, terwijl octahedrale schuifvervorming meer werd geassocieerd met weefselstijfheid. De bevindingen suggereerden ook dat beide vervormingsmaten voortkomen uit een complexe wisselwerking van factoren, wat het belang van verder onderzoek voor beter begrip van deze relaties onderstreept.

Naast relatieve volumeverandering en octahedrale afschuiving kunnen STB's ook de hoofdrichtingen tonen waarin de hersenen uitrekken en samentrekken, de zogenaamde eerste en derde hoofdrek (EH en DH). Net als bij de bovengenoemde deformatiemetingen

zijn de factoren die ruimtelijke patronen in deze hoofdrichtingen bepalen nog niet volledig begrepen. **Hoofdstuk 6** had tot doel dit te verduidelijken door te onderzoeken of EH en DH voornamelijk worden bepaald door de algemene begrenzingen van de hersenen, zoals de schedel, of door de microstructuur van de hersenen. De resultaten toonden aan dat EH-patronen grotendeels worden bepaald door grens-effecten: tijdens elke hartslag wordt de zwelling van de hersenen beperkt door de stijve schedel, en een deel van de totale uitzetting vindt plaats via het foramen magnum (de grote opening aan de basis van de schedel). Dit suggereert dat de schedel sterk bepaalt hoe de hersenen vervormen. Daarentegen liet de DH een voorkeur zien om zich loodrecht te richten op de hoofdrichting van de microstructuur van de hersenen, wat suggereert dat lokale weefselstructuur de DH in de hersenen beïnvloedt. Dit wijst op een belangrijk idee: de hersenen kunnen mechanische anisotropie vertonen; dat wil zeggen dat hun stijfheid en vervorming afhangen van de richting waarin ze belast worden. Omdat STB de hersenen meet in hun natuurlijke toestand, bieden deze bevindingen een uniek perspectief vergeleken met traditionele tests in dieren of post-mortem weefsel en kunnen ze helpen bij het oplossen van lopende discussies over de richtingsafhankelijke verschillen in mechanische eigenschappen van de hersenen.

Dit proefschrift toont aan dat iMRE, met name in combinatie met poro-visco-elastische modellen, een krachtige benadering biedt om het mechanische gedrag van het levende menselijke brein te bestuderen. Door de hersenen te meten in hun natuurlijke, onaangetaste toestand, levert deze benadering inzichten op die eerder buiten bereik lagen, en onthult het de intrinsieke mechanische eigenschappen van de hersenen. Het werk levert nieuw bewijs dat de hersenen vloeistofachtig en ultra-zacht zijn bij lage frequenties en kleine vervormingen, en suggereert ook de aanwezigheid van mechanische anisotropie. Deze bevindingen verbeteren ons begrip van hersenmechanica en openen nieuwe mogelijkheden om te onderzoeken hoe interacties tussen weefsel en vloeistof, bloedstroom en microstructuur werken in gezonde hersenen en welke rol ze spelen bij het ontstaan van ziekten.

Publications

Peer-reviewed publications

Burman Ingeberg M, Van Houten E, Zwanenburg JJM. Estimating the viscoelastic properties of the human brain at 7T MRI using intrinsic MRE and nonlinear inversion. Hum Brain Mapp. 2023 Dec 15;44(18):6575-6591. doi: 10.1002/hbm.26524. Epub 2023 Nov 1. Erratum in: Hum Brain Mapp. 2024 Dec 15;45(18):e70117. doi: 10.1002/hbm.70117.

Burman Ingeberg M, Van Houten E, Zwanenburg JJM. Evaluating the Performance and Repeatability of Poroelastic and Poroviscoelastic Models in Intrinsic MR Elastography. NMR Biomed. 2025 Jul;38(7):e70073. doi: 10.1002/nbm.70073.

Burman Ingeberg M, Van Houten E, Froeling M, Zwanenburg JJM. Alignment of cardiac-induced brain tissue strain with global boundary conditions and local microstructure: potential effects of anisotropy. J Mech Behav Biomed Mater. 2026 Jan;173:107252. doi: 10.1016/j.jmbbm.2025.107252.

Accepted submissions

Burman Ingeberg M, Van Houten E, Shoykhet A, Zwanenburg JJM. Exploring the role of vascular factors and tissue properties in pulsatile brain deformation. Accepted for publication in NMR in Biomedicine.

Under submission

Burman Ingeberg M, Van Houten E, Zwanenburg JJM. Evidence for the ultra-soft brain provided by uniqueness in intrinsic MR elastography.

Conference abstracts (selection)

Burman Ingeberg M, Van Houten E, Zwanenburg JJM. Estimating brain tissue stiffness from cardiac-induced 7T MRI displacement measurements using 3D subzone-based reconstruction.
Poster presentation, ISMRM Benelux 2022, Maastricht, The Netherlands

Burman Ingeberg M, Van Houten E, Zwanenburg JJM. Estimating brain tissue stiffness from cardiac-induced 7T MRI displacement measurements.
Poster presentation, Brain and Brain PET 2022, Glasgow, Scotland

Burman Ingeberg M, Van Houten E, Zwanenburg JJM. Estimating brain tissue stiffness from cardiac-induced 7T MRI displacement measurements.
Oral presentation, ISMRM Workshop on Magnetic Resonance Elastography 2022, Berlin, Germany

Burman Ingeberg M, Van Houten E, Zwanenburg JJM. Estimating brain tissue stiffness from cardiac-induced 7T MRI displacement measurements.
Oral presentation, Utrecht Brain Conference 2022, Utrecht, The Netherlands

Burman Ingeberg M, Van Houten E, Zwanenburg JJM. Estimating brain tissue stiffness from cardiac-induced 7T MRI displacement measurements.
Poster presentation, ISMRM Benelux 2023, Brussels, Belgium

Burman Ingeberg M, Van Houten E, Zwanenburg JJM. Estimating brain tissue stiffness from cardiac-induced 7T MRI displacement measurements.
Poster presentation, ISMRM and ISMRMT Annual Meeting and Exhibition 2023, Toronto, Canada

Burman Ingeberg M, Van Houten E, Zwanenburg JJM. Estimating the viscoelastic properties of the brain using intrinsic MRE and 7T MRI.
Oral presentation, ICP Network Meeting 2023, Utrecht, The Netherlands

Burman Ingeberg M, Van Houten E, Zwanenburg JJM. Estimating the viscoelastic properties of the brain using intrinsic MRE and 7T MRI.
Oral presentation, ImagO Conference 2023, Utrecht, The Netherlands, **won best presentation award.**

Burman Ingeberg M, Van Houten E, Zwanenburg JJM. Investigating the relation between cardiac-induced brain tissue strain and both global boundary conditions and local microstructure.
Power pitch presentation, ISMRM Benelux 2024, 's-Hertogenbosch, The Netherlands

Burman Ingeberg M, Van Houten E, Zwanenburg JJM. Investigating the relation between cardiac-induced brain tissue strain and both global boundary conditions and local microstructure.
Digital poster presentation, ISMRM and ISMRMT Annual Meeting and Exhibition 2024, Singapore, Singapore

Burman Ingeberg M, Van Houten E, Zwanenburg JJM. The viscoelastic properties of the human brain: what's next?
Oral presentation, ImagO Conference 2024, Utrecht, The Netherlands, **won best article award.**

Burman Ingeberg M, Van Houten E, Zwanenburg JJM. Exploring the relationship between cardiac-induced brain strain and both global boundary conditions and local microstructure.
Oral presentation, International Tissue Elasticity Conference 2024, Lyon, France

Burman Ingeberg M, Van Houten E, Zwanenburg JJM. Evaluating the performance of poroelastic and poroviscoelastic models in intrinsic MR elastography.
Oral presentation, ISMRM Benelux 2025, Hilversum, The Netherlands

Burman Ingeberg M, Van Houten E, Zwanenburg JJM. Evaluating the performance and repeatability of poroelastic and poroviscoelastic models in intrinsic MR elastography.
Poster presentation, ISMRM and ISMRMT Annual Meeting and Exhibition 2025, Honolulu, Hawaii

Burman Ingeberg M, Van Houten E, Zwanenburg JJM. Uniquely soft: evidence of uniqueness in viscoelastic intrinsic MR elastography enabled by the ultra-soft brain.
Poster presentation, ISMRM Benelux 2025, Antwerp, Belgium

Acknowledgements

I would like to begin by expressing my sincere gratitude to my promoters, Eli and Jaco. Thank you for your patient guidance and steady support throughout this journey. You welcomed me as I transitioned from the very different field of particle physics into an entirely new research area, and you gave me the time and space to grow into it. From the fundamentals to the most technical aspects of the project, you supported me as I navigated the many topics and disciplines this work has touched on. I have always greatly valued our discussions. They consistently challenged me, broadened my understanding, and deepened my thinking, while also being extremely enjoyable. I always leave our meetings feelings excited and enthusiastic. It's been an absolute pleasure working with both of you, and I think you both play a massive role in sparking my joy for academia.

Jaco, I often wonder how you manage to balance so many responsibilities and still always able to find time. Despite what must be an incredibly demanding schedule, you have always been available - whether for a quick question, a longer discussion, or support at important moments. I have never taken that for granted. Your feedback on abstracts, papers, and proposals has been consistently thorough and thoughtful and it has played a significant role in my growth over these years. More than just guiding me scientifically, you've also always helped me gain perspective. Your way of thinking about problems, decisions, and academia more broadly has shaped how I approach my own work, and how I want to progress in the future. You bring a sort of effortless wisdom that makes even complex challenges feel manageable.

Eli, even with the challenges of long distance and different time zones for much of my PhD, you were always available whenever I needed guidance. Your feedback and advice have been highly valued, and you consistently offer support in a way that feels both thoughtful and approachable. I have always been impressed by your ability to explain even the most complex topics in a way that is immediately clear and accessible - a skill that has helped me grasp ideas more quickly and confidently. On top of that, your enthusiasm for your work is infectious, making every discussion not only productive but genuinely enjoyable. Working with you has been a constant source of motivation and learning, and I am deeply grateful for your guidance throughout this journey.

I would like to thank the members of my PhD assessment committee, Prof. dr. E.T. van Bavel, Prof. dr. G.J. Biessels, Prof. dr. T. van Leeuwen, Dr. ir. C.M.W. Tax, and Prof. dr. B.K. Velthuis, for their time and effort dedicated for the assessment of this thesis.

A big thank you to the members of my closest research team, Ellen, Lotte, and Merlijn, for their support and collaboration, particularly with scanning and all things scanning-

related, which made a real difference throughout this project. It's been a pleasure working by your sides throughout these years.

I would also like to thank all the people in the Translational Neuroimaging Group, the High Field group, and the Q-hallway for creating such a welcoming and enjoyable work environment, and for all the interesting conversations and support along the way. I am especially grateful to Martijn and Alex for their direct support on my projects and the practical help that made the part of the research possible. I am also particularly thankful for the friendships I have formed during my years in these groups - they have made the journey even more enjoyable, and I know these connections will last well beyond my time here. In particular, I'd like to thank Vanja and Michael for their friendship and support, and for the unforgettable memories we shared, especially our Hawaii trip.

I would also like to thank my office mates over the years: Sarah, Zahra, Pien, Luka, Maaike, and Rumeysa. Sharing an office with all of you made the day-to-day work of the PhD much more enjoyable. I greatly appreciated the friendly atmosphere, the conversations, and the small moments of support along the way. Your company helped create a pleasant and motivating environment to work in.

My dear paranymphs, Thomas and Jamilla, thank you for standing by me during my defense and for helping with the planning and ideas for the day itself. Your support made a huge difference, taking a lot off my plate and allowing me to focus on what mattered. Beyond your role as paranymphs, I want to express my deepest gratitude for your friendship over these years. I truly appreciated the time we've spent together. Everything from quick coffees and lunches to the many adventures we've enjoyed. Above all else, I am grateful to count you as friends. Your presence has meant a lot.

Next, I would like to thank two people whose passion for science was crucial in sparking my own. Linda, I still don't think I've met anyone that expresses as much joy for the natural sciences, mathematics, and teaching in these fields. Your genuine enthusiasm really left an impression on me, and it has inspired me to approach my own work with the same curiosity and excitement. Prof. Franklin, even though our meeting was brief, I was deeply struck by the combination of passion and mastery in physics that you carry. Every topic you touched on became both engaging and understandable, sparking my curiosity in a way I hadn't experienced before. At the time, I was unsure whether I wanted to be a physicist. Meeting you, however, made me realize that not only do I want to be a physicist, but I want to be a physicist that approaches my field with the same mastery and passion as I saw in you.

I would also like to thank all the friends I've made while living in the Netherlands. Your curiosity, encouragement, and support have made this journey much more enjoyable, and I will always treasure the adventures and memorable moments we've shared. You've truly made my time here unforgettable, and you have created a sense of community that made me feel at home in a new country. In particular, friends such as Oscar, Indy, Eleonore, Barbara, Alfred, Nika, Thara, Char, and Khyati - along with so many others - have filled these years with joy, support, and unforgettable experiences, making this chapter of my life all the more special. In the same way, I would like to thank all my friends from home, who have continuously cheered me on from afar. Your encouragement and unwavering support have meant more to me than I can express, and I have always felt your presence even from a distance.

Sist, men inte minst, vill jag tacka min kära familj, Dan, Tine, Alex och Alicia, för er kärlek och oändliga stöd och för allt ni har gjort för att göra denna resa möjlig. Jag kommer aldrig glömma vår husbilsresa och flytt hit, och hur ni utan tvekan gjorde en så stor resa bara för att hjälpa mig starta mitt liv här. Er tillit och trygghet har gett mig modet att våga utmana mig själv och satsa fullt ut, med vetskapen om att ni alltid finns där. Er tro på mig har inte bara gett mig styrka att genomföra detta projekt, utan också modet att följa mina ambitioner på längre sikt. Ni har alltid visat intresse för det jag gör, och fått det att kännas mer meningsfullt. Det hade inte varit möjligt utan er, ni har min tacksamhet för alltid.

Curriculum Vitae



Marius Burman Ingeberg was born on May 6, 1995, in Norrfjärden, Sweden. He grew up with his Parents, Dan and Kristine, and his siblings, Alex and Alicia, in Altersbruk. After completing upper secondary school at NTI Gymnasiet in Luleå, he pursued a Bachelor's degree in Physics at Lund University, followed by a Master's degree in Physics at the same institution. During his master's studies, his interests gravitated towards particle physics, culminating in a master's thesis at the ATLAS detector at the Large Hadron Collider (CERN). Over time, his focus shifted towards the brain and medicine, leading him to the 7T group at UMC Utrecht, where he found an opportunity to combine his passions for physics, biology, and medicine in a single research topic. Since then, he has been a member of the Translational Neuroimaging Group, working under the supervision of Dr. ir Jaco Zwanenburg and Dr. Eli van Houten, focusing on characterizing and understanding the mechanical properties of the brain.

Following the completion of his PhD, Marius will continue his research at UMC Utrecht as a Postdoctoral researcher, where he will further refine the techniques developed during his PhD and work towards their clinical implementation.

